Using plasmonic nanostructures to control electrically excited light emission

Shuiyan Cao

université PARIS-SACLAY

NNT : 2018SACLS042

Thèse de doctorat

UNIVERSITÉ PARIS SUD
Comprendre le monde, construire l'avenir

Using Plasmonic Nanostructures to Control Electrically Excited Light Emission

Thèse de doctorat de l'Université Paris-Saclay
préparée à l'Université Paris-Sud

École doctorale n°572 : Ondes et matières (EDOM)
Spécialité de doctorat : Nanophysique

Thèse présentée et soutenue à Orsay, le 16 Février 2018, par

Shuiyan CAO (曹水艳)

Composition du Jury :

Klaus KUHNKE Directeur de Recherche Nanoscience Department (– Max Planck Institute for Solid State Research)	Président
Olivier PLUCHERY Professeur Institut des NanoSciences de Paris (– Université Pierre et Marie Curie)	Rapporteur
Nordin FELIDJ Professeur ITODYS (– Université Paris Diderot)	Rapporteur
Dai ZHANG Academic with habilitation Institute of Physical and Theoretical Chemistry (– University of Tübingen)	Examinateur
Aloyse DEGIRON Chargé de Recherche Centre de Nanosciences et de Nanotechnologies (– Université Paris-Sud)	Examinateur
Elizabeth BOER-DUCHEMIN Maître de Conférences Institut des Sciences Moléculaires d'Orsay (– Université Paris-Sud)	Directrice de thèse
Gérald DUJARDIN Directeur de Recherche Institut des Sciences Moléculaires d'Orsay (– Université Paris-Sud)	Co-Directeur de thèse
Eric LE MOAL Chargé de Recherche Institut des Sciences Moléculaires d'Orsay (– Université Paris-Sud)	Invité

Université Paris-Saclay
Espace Technologique / Immeuble Discovery
Route de l'Orme aux Merisiers RD 128 / 91190 Saint-Aubin, France

Contents

Chapter 1

Introduction

In this thesis, we use different plasmonic nanostructures to control electrically excited surface plasmon polaritons (SPPs) and light. The electrical excitation is carried out using a scanning tunneling microscope (STM). SPPs are collective oscillations in the electron density at the surface of a metal coupled with electromagnetic waves. Such an excitation can be propagating or non-propagating, thus SPPs can be categorized as propagating surface plasmons or localized surface plasmons. As a major branch of nanophotonics, their interactions with various plasmonic nanostructures are fascinating; exploiting these interactions leads to the control of the emitted light and plasmons.

1.1 A brief history of SPP excitation in chronological order

The existence of surface plasmons (the long wavevector limit of SPPs) was first predicted by Ritchie in 1957 [1]. He theoretically investigated the loss spectra of electron beams undergoing diffraction on thin metallic films. He found that besides the expected volume plasmon excitation at an energy of $\hbar\omega_p$, his study also predicted an additional loss at a lower energy $\hbar\omega_p/\sqrt{2}$. The first experimental demonstration of the existence of surface plasmons was presented by Powell and Swan in 1959 [2], [3] which fully confirmed Ritchie's prediction. In their work, they observed the additional peaks in the electron energy loss spectra of aluminum and magnesium in reflection.

In the above mentioned work, high-energy electrons ($\geq 1\ keV$) are the excitation source. From 1959 to 1964, Turbadar made successive efforts to study the reflected spectra when light is incident at an oblique angle on a glass/metal structure [4]–[7]. He interpreted his results in terms of geometrical optics and did not take the SPP oscillations along the metal film into consideration. Even though his work was less recognized by researchers, in fact he pioneered the approach of exciting SPPs with light since he showed that p-polarized light at a certain oblique incident angle on a metal film from the glass side displayed a sharp decrease in the reflected intensity [5].

In 1968, breakthroughs in the field of far field optical excitation of SPPs were achieved on smooth planar metal surfaces. Otto, and Kretschmann together with Raether, separately proposed two famous configurations to excite SPPs by light [8], [9] which are referred as the "Otto configuration" and the "Kretschmann configuration". In the same year, Ritchie et al., experimentally demonstrated that a grating configuration could also be used to excite SPPs with light [10] (details of these three configurations will be shown in chapter 2).

In 1976, Lambe and McCarthy discovered a new method for exciting SPPs using low-energy electrons ($\sim eV$) [11]. Their device was made of a metal-insulator-metal planar junction with an insulating layer thickness on the order of a few nanometers. When a low voltage difference was applied between the two sides of the junction, broadband light emission was observed. In 1989, light from localized SPPs excited from the nanometer-sized junction formed between the tip of a scanning tunneling microscope (STM) and a metallic surface was obtained [12]. STM provided a method to excite SPPs locally ($\sim 10\ nm$), however, at that time, light was detected only from localized surface plasmons because of the phase mismatch between photons in air or vacuum and SPPs on an air/metal or vacuum/metal interface. More recently,

our group detected and imaged (in the real and Fourier spaces) the light from STM-excited localized and propagating SPPs [13]. This low-energy, local and electrical excitation of SPPs with an STM is what we use in this thesis. In chapter 2, this method will be detailed.

In 1996, a scanning near-field optical microscope (SNOM) was used to excite SPPs [14]. Using a SNOM provides a method to locally ($\sim 30\ nm$) excite SPPs optically. More recently, in 2006, a method using a scanning electron microscope (SEM) with high-energy electrons ($\sim 30\ keV$) to excite SPPs locally ($< 10\ nm$) on a metal film was reported [15]. More details of these two methods will be introduced in chapter 2.

1.2 Interaction of SPPs and plasmonic nanostructures

In 1998, the famous extraordinary optical transmission (EOT) phenomenon was experimentally discovered by T. W. Ebbesen and co-workers [16]. They found that due to the interaction of SPPs with a sub-wavelength array of holes in a silver film, the intensity of the light transmitted through the holes was higher than expected.

This pioneering work revived the field of SPPs and opened up new research directions regarding the interaction of SPPs and plasmonic nanostructures. As a result, during the last two decades, more and more scientists have undertaken the study of the interaction of SPPs and plasmonic nanostructures. Using nanostructures to manipulate light and SPPs has potential applications for future devices. For instance, nanostructures may be used to control SPP propagation or the emission of light. In my thesis, several different structures including a *circular* plasmonic lens, an *elliptical* plasmonic lens, a plasmonic multi-layer stack and an individual triangular plate are used for obtaining controllable light emission.

1.3 STM excitation and the study of the interaction of SPPs with plasmonic nanostructures

Benefiting from the contributions made by researchers in the field of plasmonics, scientific studies of SPPs interacting with plasmonic nanostructures is rising rapidly. However, despite these advances, the study of SPP-matter interactions faces some challenges.

When exploring the interaction of SPPs and nanostructures, the *optical* excitation of SPPs is often used. This includes far field and near field optical excitation. Nevertheless, since a laser

is inevitable for the optical excitation of SPPs, a strong optical background will be present and weak signals might go undetected. As well, the size of the excited area for the far field optical excitation of SPPs is large compared to the nanostructures under investigation due to the diffraction limit. As a result, limited by the size of the source, probing the interactions at the nanoscale may face some difficulties.

Therefore, a truly localized nanoscale source of SPPs with no strong optical background light is needed. As we reviewed before, the local, electrical excitation of SPPs can be realized either with high-energy or low-energy electrons. While several investigations of the interaction of SPPs excited with high-energy electrons and nanostructures exist (e.g.[17]–[19]), nevertheless, in terms of applications in a nanodevice, a major drawback of this approach is that it requires a large high-energy electron generator as well as vacuum conditions. Thus, it appears that such a technique would not be compatible with future on-chip nanodevices.

On the other hand, the tunnel junction excitation of SPPs using low-energy electrons could potentially be combined with nanodevices for future applications. Recently, it was shown in our group that by electrically exciting a plasmonic nanoparticle by STM, active angular control of the emitted light is achieved [20]. This provides insight into light manipulation using low-energy, inelastic tunneling electrons from the STM interacting with various plasmonic nanostructures.

Can we go further and achieve more active control of the emission of light from various plasmonic nanostructures by using the low-energy electrical excitation of the STM? The opportunity for this study lies in two aspects. On the one hand, the versatility of the STM provides the opportunity to explore the interaction between SPPs and plasmonic nanostructures since the local excitation position may be precisely controlled. On the other hand, our STM is combined with an inverted optical microscope with which the light from both localized and propagating surface plasmon may be detected and imaged.

1.4 Outline of this thesis

This thesis focuses on using different plasmonic nanostructures to control the emission of electrically excited light. The electrical emission is from an “STM-nanosource” which uses the inelastic tunnel current between the tip of a scanning tunneling microscope (STM) and a

metallic sample, to locally excite both localized and propagating surface plasmon polaritions. The organization of the chapters is listed below:

In chapter 2, the general theoretical background is introduced. The dispersion relation of SPPs propagating at the Au/air interface is derived. Different methods to excite SPPs will be introduced including the electrical excitation of SPPs by STM which I use in my thesis. Radially polarized light is introduced as well as it is important in light manipulation. Besides, the *electronic* local density of states (*E*-LDOS) and the *electromagnetic* local density of states (*EM*-LDOS) are also introduced. In this chapter, the experimental setup and the general experimental techniques such as leakage radiation microscopy, real and Fourier space imaging are introduced.

In chapter 3, we present the experimental results of the interaction of an STM-nanosource and a *circular* plasmonic lens. By electrically exciting SPPs at the center of the plasmonic lens, a radially polarized microsource with low angular spread ($\approx \pm 4°$) is achieved. We also investigate how the structural parameters influence the angular spread of the resulting beam of light. Additionally, we find that by moving the excitation position of the STM tip, the polarization states as well as the angular spread of the microsource will change. As well, the spectral response of our plasmonic lens to the broadband excitation from the STM tunnel electrons is experimentally investigated.

In chapter 4, we present experiments results of the interaction of an STM-nanosource and an *elliptical* plasmonic lens. When an STM tunnel junction electrically excites SPPs at the focal position of the elliptical plasmonic lens, a directional light beam of low angular spread is achieved. Moreover, we find that by changing the eccentricity from 0 to 0.94 of the elliptical plasmonic lens, the emission angle is varied from 0° to near 40°. It was found that the larger the eccentricity of the elliptical lens, the larger the emission angle.

In chapter 5, we present experimental results of the interaction of an STM-nanosource and a planar plasmonic multi-layer stack structure. When the inelastic tunnel current from an STM tip electrically excites the structure, we can experimentally probe the optical band structure for an Au-SiO_2-Au stack. As well, we find that the thickness of the dielectric layer plays an important role in changing the coupling between the modes. We also compare the results obtained by both laser and STM excitation of the same stack structure.

In chapter 6, we present experimental results of the local electrical excitation of triangular plates ($L \approx 600\ nm$). In this study, the experimental results may be categorized into two parts.

First, by locally exciting SPPs at specific locations on the triangle plates, directional light emission is achieved. The directivity of this emitted light is also measured up to $6.8\ dB$. Second, we investigate the possibility of mapping the *EM*- LDOS with our STM-nanosource.

A conclusion may be found in chapter 7.

This thesis experimentally explores the interaction between STM-excited SPPs and various plasmonic nanostructures. The present results show that the manipulation of light is achieved through SPP-matter interactions. Using nanostructures, we control the collimation, polarization, and direction of the light originating from STM-excited SPPs. These studies may lead to future developments in the field of nanoscale opto-electronic integrated circuits.

[1] R. H. Ritchie, “Plasma Losses by Fast Electrons in Thin Films,” *Phys. Rev.*, vol. 106, no. 5, pp. 874–881, 1957.

[2] C. J. Powell and J. B. Swan, “Origin of the Characteristic Electron Energy Losses in Magnesium,” *Phys. Rev.*, vol. 116, no. 81, pp. 81–83, 1959.

[3] C. J. Powell and J. B. Swan, “Origin of the Characteristic Electron Energy Losses in Aluminum,” *Phys. Rev.*, vol. 115, no. 4, pp. 869–875, 1959.

[4] T. Turbadar, “Complete Absorption of Light by Thin Metal Films,” *Proc. Phys. Soc.*, vol. 73, no. 1, p. 40, 1959.

[5] T. Turbadar, “Complete absorption of plane polarized light by thin metallic films,” *Opt. Acta Int. J. Opt.*, vol. 11, no. 3, pp. 207–210, 1964.

[6] T.Turbadar, “Equi-reflectance Contours of Double-layer Anti-reflection Coatings,” *Opt. Acta Int. J. Opt.*, vol. 11, no. 2, pp. 159–170, 1964.

[7] T. Turbadar, “Equi-reflectance Contours of Triple-layer Anti-reflection Coatings,” *Optcia Acta Int. J. Opt.*, vol. 11, no. 3, pp. 195–205, 1964.

[8] E. Kretschmann and H. Raether, “Radiative decay of non-radiative surface plasmons excited by light,” *Zeitschrift für Naturforsch. A*, vol. 23, no. 2135, pp. 2135–2136, 1968.

[9] A. Otto, “Excitation of Nonradiative Surface Plasma Waves in Silver by the Method of Frustrated Total Reflection,” *Zeitschrift für Phys.*, vol. 216, no. 398, pp. 398–410, 1968.

[10] R. H. Ritchie, E. T. Arakawa, J. J. Cowan, and R. N. Hamm, “Surface plasmon resonance effect in grating diffraction,” *Phys. Rev. Lett.*, vol. 21, no. 22, p. 1530, 1968.

[11] J. Lambe and S. L. McCarthy, “Light emission from inelastic electron tunneling,” *Phys. Rev. Lett.*, vol. 37, no. 14, p. 923, 1976.

[12] J. K. Gimzewski, J. K. Sass, R. R. Schlitter, and J. Schott, “Enhanced Photon Emission in Scanning Tunnelling Microscopy,” *Europhys. Lett.*, vol. 8, no. 5, pp. 435–440, 1989.

[13] T. Wang, E. Boer-Duchemin, Y. Zhang, G. Comtet, and G. Dujardin, “Excitation of propagating surface plasmons with a scanning tunnelling microscope.,”

Nanotechnology, vol. 22, no. 17, p. 175201, 2011.

[14] B. Hecht, H. Bielefeldt, L. Novotny, Y. Inouye, and D. W. Pohl, "Local Excitation, Scattering, and Interference of Surface Plasmons," *Phys. Rev. Lett.*, vol. 77, no. 9, pp. 1889–1892, 1996.

[15] M. V. Bashevoy, F. Jonsson, A. V. Krasavin, N. I. Zheludev, Y. Chen, and M. I. Stockman, "Generation of traveling surface plasmon waves by free-electron impact," *Nano Lett.*, vol. 6, no. 6, pp. 1113–1115, 2006.

[16] T. W. Ebbesen, H. J. Lezec, H. F. Ghaemi, T. Thio, and P. A. Wolff, "Extraordinary optical transmission through sub-wavelength hole arrays," *Nature*, vol. 391, no. 12, p. 3, 1998.

[17] J. Nelayah *et al.*, "Mapping surface plasmons on a single metallic nanoparticle," *Nat. Phys.*, vol. 3, no. 5, pp. 348–353, 2007.

[18] E. J. R. Vesseur, R. De Waele, M. Kuttge, and A. Polman, "Direct observation of plasmonic modes in Au nanowires using high-resolution cathodoluminescence spectroscopy," *Nano Lett.*, vol. 7, no. 9, pp. 2843–2846, 2007.

[19] C. E. Hofmann *et al.*, "Plasmonic modes of annular nanoresonators imaged by spectrally resolved cathodoluminescence," *Nano Lett.*, vol. 7, no. 12, pp. 3612–3617, 2007.

[20] E. Le Moal *et al.*, "An electrically excited nanoscale light source with active angular control of the emitted light," *Nano Lett.*, vol. 13, no. 9, pp. 4198–4205, 2013.

Chapter 2

General considerations and experimental setups

In this chapter, we will introduce some basic knowledge and the experimental setups. For the basic knowledge, surface plasmon polaritons (SPPs) are explained and their dispersion relation is derived. Different ways to excite, detect and image SPPs are described. The concept of Fourier space imaging, radially polarized light and the *electronic* and *electromagnetic* local density of states are also introduced since they are also necessary for later chapters. Lastly, the two employed experimental setups are detailed and compared.

2.1 Surface plasmon polaritons

Propagating surface plasmon polaritons (SPPs) are electromagnetic surface waves coupled to charge oscillations at the interface between a dielectric and metal. Unlike dielectrics, the optical properties of metals are frequency dependent, $\varepsilon_m = \varepsilon_m(\omega)$. Using the Drude-Sommerfeld model and considering only free electrons for the dielectric constant of a metal, we get [1]:

$$\varepsilon_m(\omega)=1-\frac{\omega_p^2}{\omega^2+i\Gamma\omega} \quad (2.1)$$

where, $\varepsilon_m(\omega)$ is the dielectric constant of the metal and ω is the angular frequency. ω_p is the volume plasma frequency, and Γ is the damping term which arises since the electron motion is damped by collisions. This model describes how the electrons oscillate in response to the applied electromagnetic field.

Since SPPs are surface modes, the fields in the direction perpendicular to the interface decay exponentially. In order to obtain such a "bound" state at the interface, the following conditions must be satisfied [1]:

$$\varepsilon_d.\varepsilon_m(\omega)<0 \quad (2.2)$$

$$\varepsilon_d+\varepsilon_m(\omega)<0 \quad (2.3)$$

where, ε_d is the dielectric constant of the dielectric layer. The dielectric constant of a real metal is complex and it may be expressed as:

$$\varepsilon_m(\omega) = \varepsilon'_m(\omega) + i\varepsilon''_m(\omega) \quad (2.4)$$

where $\varepsilon'_m(\omega)$ and $\varepsilon''_m(\omega)$ are respectively the real and imaginary parts of the dielectric constant of the metal.

As for the dielectric layer, its dielectric constant ε_d is real and positive and varies little with frequency. Thus, in order to meet the condition in equation (2.2), $\varepsilon'_m(\omega)$ must be negative. For certain metals, especially noble metals, in the visible and infrared region, $\varepsilon'_m(\omega)$ is negative, $\varepsilon''_m(\omega)$ is positive, and, $|\varepsilon'_m| > |\varepsilon''_m|$. Therefore, to meet the conditions in equation (2.3), we require:

$$|\varepsilon'_m| > |\varepsilon_d| \quad (2.5)$$

Now let us consider what type of mode satisfies the above conditions. Starting with a transverse electric (TE) wave, TE waves only have nonzero components of H_x, H_z and E_y,

where, H_x, H_z and E_y are separately denoted as the (auxiliary) magnetic field in the x direction, the (auxiliary) magnetic field in the z direction and the electric field in the y direction. Each component is shown in Figure 1(a).

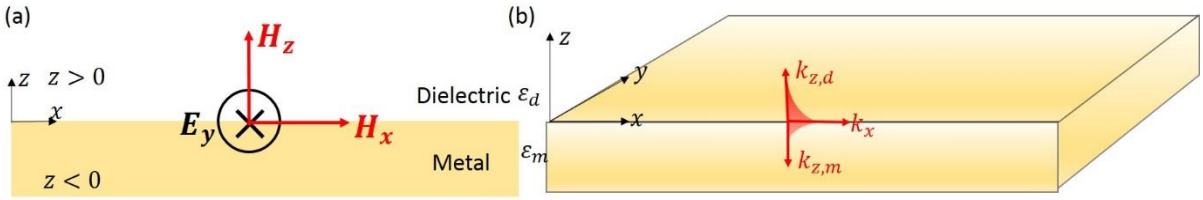

Figure 1. Schematic of the metal (ε_m) /dielectric (ε_d) interface. (a) Schematic illustration of the electric and magnetic field components of a TE wave. (b) Schematic diagram of SPPs propagating at the interface. k_x defines the x component of the wavevector of SPPs and $k_{z,d}$ and $k_{z,m}$ are respectively the perpendicular components of the wavevector in the dielectric and metal layers.

Under the TE condition, the electromagnetic field in the dielectric ($z > 0$) (see Fig. 1) may be described as:

$$H_d = (\tilde{H}_{x,d}, 0, \tilde{H}_{z,d})(e^{ik_x x} e^{ik_{z,d} z} e^{-i\omega t}) \quad (2.6)$$

$$E_d = (0, \tilde{E}_{y,d}, 0)(e^{ik_x x} e^{ik_{z,d} z} e^{-i\omega t}) \quad (2.7)$$

The electromagnetic field in the metal ($z < 0$) may be described as:

$$H_m = (\tilde{H}_{x,m}, 0, \tilde{H}_{z,m})(e^{ik_x x} e^{-ik_{z,m} z} e^{-i\omega t}) \quad (2.8)$$

$$E_m = (0, \tilde{E}_{y,m}, 0)(e^{ik_x x} e^{-ik_{z,m} z} e^{-i\omega t}) \quad (2.9)$$

where, H_d and H_m are the magnetic fields in the dielectric and metal layers respectively and $H_{x,d}$ and $H_{x,m}$ are the x components of the magnetic field in the dielectric and metal ($\tilde{H}_{x,d}$ and $\tilde{H}_{x,m}$ are the amplitudes of the x components of the magnetic field in the dielectric and metal layers). $H_{z,d}$ and $H_{z,m}$ are the z components of the magnetic field in the dielectric and metal ($\tilde{H}_{z,d}$ and $\tilde{H}_{z,m}$ are the amplitudes of the z components of the magnetic field in the dielectric and metal layers). The electric field is defined similarly.

When there are no free currents at the interface, the boundary condition in the x direction requires that: $H_{x,d} = H_{x,m}$ at $z = 0$. The boundary condition in the y direction requires that: $E_{y,d} = E_{y,m}$ at $z = 0$. The boundary condition in the z direction requires that: $H_{z,d} = H_{z,m}$. With these three boundary conditions applied to equations (2.6)-(2.9), as well as the Maxwell-

Faraday and Maxwell-Ampere equations for TE waves ($\frac{\partial E_y}{\partial z} = -i\omega\mu_0 H_x$, $\frac{\partial E_y}{\partial x} = i\omega\mu_0 H_z$, $\frac{\partial H_x}{\partial z} - \frac{\partial H_z}{\partial x} = -i\omega\varepsilon\varepsilon_0 E_y$) assuming harmonic time dependence, we obtain that:

$$k_{z,d} + k_{z,m} = 0 \quad (2.10)$$

In order to have a surface wave, $k_{z,j}$ must be imaginary and $Im[k_{z,j}] > 0$. Thus, equation (2.10) cannot be fulfilled. As a result, SPPs are not TE modes.

Next, we consider a transverse magnetic (TM) wave. In the TM condition, only E_x, E_z and H_y are nonzero. E_x, E_z and H_y are the electric field in x direction, the electric field in the z direction and the magnetic field in the y direction respectively. Each component is sketched in Figure 2 (a).

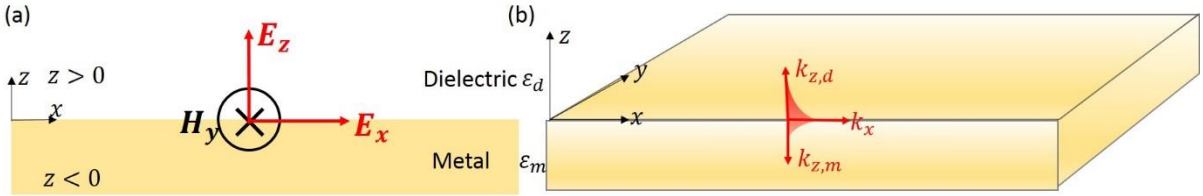

Figure 2. Schematic of the metal (ε_m) /dielectric (ε_d) interface. (a) Schematic illustration of the electric and magnetic field components of a TM wave. (b) Schematic diagram of SPPs propagating at the interface. k_x defines the x component of the wavevector of SPPs and $k_{z,d}$ and $k_{z,m}$ are respectively the perpendicular components of the wavevector in the dielectric and metal layers.

Under the TM condition, the electromagnetic field in the dielectric ($z > 0$) (see Fig. 2) may be described as:

$$H_d = (0, \tilde{H}_{y,d}, 0)(e^{ik_x x} e^{ik_{z,d} z} e^{-i\omega t}) \quad (2.11)$$

$$E_d = (\tilde{E}_{x,d}, 0, \tilde{E}_{z,d})(e^{ik_x x} e^{ik_{z,d} z} e^{-i\omega t}) \quad (2.12)$$

The electromagnetic field in the metal ($z < 0$) can be described as:

$$H_m = (0, \tilde{H}_{y,m}, 0)(e^{ik_x x} e^{-ik_{z,m} z} e^{-i\omega t}) \quad (2.13)$$

$$E_m = (\tilde{E}_{x,m}, 0, \tilde{E}_{z,m})(e^{ik_x x} e^{-ik_{z,m} z} e^{-i\omega t}) \quad (2.14)$$

where, $E_{x,d}$ and $E_{x,m}$ are the x components of electric field in the dielectric and metal ($\tilde{E}_{x,d}$ and $\tilde{E}_{x,m}$ are the amplitudes of the x components of the electric field in the dielectric and metal layers). $E_{z,d}$ and $E_{z,m}$ are the z components of the electric field in dielectric and metal ($\tilde{E}_{x,d}$ and $\tilde{E}_{x,m}$ are the amplitudes of the z components of the electric field in the dielectric and metal layers). The magnetic field is defined similarly.

By applying the boundary conditions of the electromagnetic field, when there is no free charge, the boundary condition in the z direction requires: $\varepsilon_d E_{z,d} = \varepsilon_m E_{z,m}$. When there is no free current, the boundary condition in the y direction requires that: $H_{y,d} = H_{y,m}$. The boundary condition in the x direction requires: $E_{x,d} = E_{x,m}$. According to these three boundary conditions applied to equations (2.11)-(2.14), as well as the Maxwell-Faraday and Maxwell-Ampere equations for TM waves ($\frac{\partial E_x}{\partial z} - \frac{\partial E_z}{\partial x} = i\omega\mu_0 H_y$, $\frac{\partial H_y}{\partial z} = i\omega\varepsilon\varepsilon_0 E_x$, $\frac{\partial H_y}{\partial x} = -i\omega\varepsilon\varepsilon_0 E_z$) assuming harmonic time dependence, we obtain that:

$$\frac{\varepsilon_m}{\varepsilon_d} = -\frac{k_{z,m}}{k_{z,d}} \quad (2.15)$$

Besides $k_x^2 + k_y^2 + k_z^2 = k^2$, $k_y = 0$, and $k = \varepsilon k_0$ then:

In the dielectric layer, we have:

$$k_x^2 + k_{z,d}^2 = \varepsilon_d {k_0}^2 \quad (2.16)$$

In the metal layer, we have:

$$k_x^2 + k_{z,m}^2 = \varepsilon_m {k_0}^2 \quad (2.17)$$

Combined with equations (2.15), (2.16) and (2.17), we can get:

$$k_{SPP} = k_x = k_0 \sqrt{\frac{\varepsilon_m(\omega)\varepsilon_d}{\varepsilon_m(\omega)+\varepsilon_d}} \quad (2.18)$$

The expression in equation (2.18) describes the dispersion relation of SPPs propagating at the interface between a dielectric and a metal.

Figure 3 plots the SPP dispersion relation at an Au/air and an Au/glass interface from equation (2.1) (expression for $\varepsilon_m(\omega)$) and equation (2.18) (SPP dispersion relation). The light line in free space (green dotted line) and in the glass (black dotted line) are also plotted. We can see that for the same energy, the SPP wavevector at an Au/air interface is always larger than that for light in air. Additionally, the wavevector of SPPs at an Au/glass interface and the wavevector of light in glass are always larger than the corresponding wavevectors in air. As a result, if both SPPs and photons are traveling in the same medium, a wavevector mismatch will always exist.

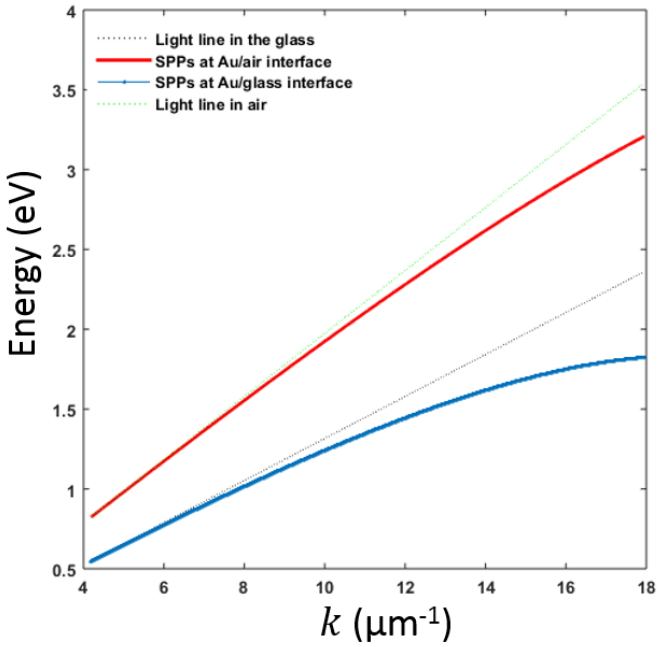

Figure 3. Dispersion relation for SPPs at an Au/air interface (red line) and an Au/glass interface (blue line). Dispersion relation for light in air (green dotted line) and in glass (black dotted line). This graph is obtained using a Matlab program (equation 2.1 and 2.18). For gold, ω_p *is taken as* $13.8 \times 10^{15} s^{-1}$ *and* Γ *is taken as* $1.075 \times 10^{14} s^{-1}$ *[1].*

From the equation (2.4), since the dielectric constant of a metal is complex, the wavevector k_{SPP} is also complex with a real part k'_{SPP} and an imaginary part k''_{SPP}:

$$k_{SPP} = k'_{SPP} + ik''_{SPP} \quad (2.19)$$

The real part k'_{SPP} determines the wavelength of SPPs while the imaginary part k''_{SPP} determines the damping of the SPPs when they propagate along the interface.

From equation (2.18), we can obtain the wavelength of SPPs:

$$k'_{SPP} = \frac{2\pi}{\lambda_{SPP}};\ \lambda_{SPP} = \lambda_0 Re\left[\sqrt{\frac{(\varepsilon_m+\varepsilon_d)}{\varepsilon_m\varepsilon_d}}\right] \quad (2.20)$$

where λ_0 is the wavelength of light in free space.

In the case where the imaginary part of the dielectric function is small i.e. $|\varepsilon''_m| \ll |\varepsilon'_m|$, the propagation length can be approximated as [1]:

$$L_{SPP} = \frac{1}{2k''_{SPP}} = \frac{c}{\omega}\left(\frac{\varepsilon'_m+\varepsilon_d}{\varepsilon'_m\varepsilon_d}\right)^{\frac{3}{2}}\frac{{\varepsilon'_m}^2}{\varepsilon''_m} \quad (2.21)$$

The SPP intensity decreases as the plasmon wave propagates due to ohmic losses of the electrons participating in the SPPs, which results in the heating of the metal [2]. Figure 4 plots

the propagation lengths of SPPs at an Au/air interface for different wavelengths. Figure 4 (a) show the relation by employing the dielectric constant of gold in equation (2.1) and Fig. 4 (b) shows the relation by using the dielectric constant of gold derived from Johnson and Christy [3]. Both of them shown that the propagation length increases with increasing wavelength for this interface and this is due to the loss of gold at longer wavelength becomes smaller.

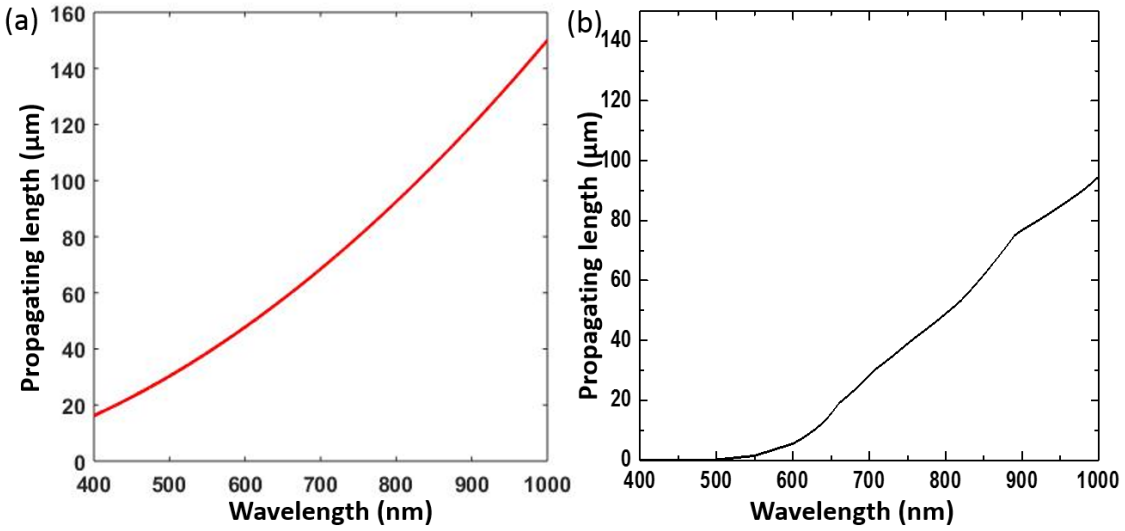

Figure 4. Propagation length of SPPs at an Au/air interface for different wavelengths. The graph is obtained from equation (2.21) using a Matlab program. (a) Dielectric constant of gold is from equation (2.1). (b) Dielectric constant of gold derived from Johnson and Christy [3].

While SPPs propagate in the plane of the interface, their amplitude exponentially decays in the direction perpendicular to the interface. Considering the penetration length along the z axis $d_{z,j} = 1/2\, Im(k_{z,j})$ [1], it defines the energy confinement along the z direction. Here, $k_{z,j}$ can be expressed as:

$$k_{z,j} = \frac{\omega}{c}\sqrt{\frac{\varepsilon_j^2}{\varepsilon_m+\varepsilon_d}} \quad (2.22)$$

where j=m in the metal and j=d in the dielectric. When SPPs propagate at an Au/air interface, the penetration length in Au and air layer can be calculated as $13\,nm$ and $220\,nm$ respectively for $\lambda_0 = 700\,nm$ by employing the dielectric constants from Johnson and Christy [3].

2.2 Methods for SPP excitation

Last section we discussed the basic properties of SPPs. In this section, we will elaborate on the general ways to excite SPPs as well as emphasize the way we use in my thesis. The different methods to excite SPPs may be divided into two categories: *optical* excitation and *electrical* excitation.

2.2.1 Optical excitation

The optical excitation of SPPs includes far field optical excitation and near field optical excitation. SPPs on a flat metal/dielectric interface cannot be directly excited by light beams from the far field, since, as the dispersion curves show in Fig. 3, there is a clear mismatch between the wavevector of SPPs at an Au/air interface and the wavevector of light in air. To compensate this mismatch, prism and grating configurations are proposed to increase the wavevector of light.

Figure 5 (a)-(c) respectively shows the Kretschmann configuration, Otto configuration and grating configuration [4]–[6] which we already mentioned in chapter 1. In the Kretschmann configuration, a thin metal film is evaporated on top of a glass prism. Light impinges from the glass side at an angle greater than the air/glass critical angle of total internal reflection and then the resulting evanescent wave (see below) at the interface can "tunnel" through the metal film and excite SPPs.

For a specific incident angle θ, the evanescent wave can excite SPPs at the metal/air interface only when it satisfies:

$$nk_0 sin\theta = k'_{SPP} \quad (2.23)$$

where n is the refractive index of the glass prism and k_0 is the incident wavevector in free space. k'_{SPP} is the SPP wavevector at a metal/air interface.

In the Otto configuration indicated in Fig. 5 (b), the prism is separated from the metal film by a thin air gap. Similar to the Kretschmann configuration, total internal reflection will take place at the prism/air interface and the evanescent wave can "tunnel" through the air gap. Consistent with what is mentioned above (equation (2.23)), SPPs can also be excited at a metal/air interface by the evanescent wave. Compared with the Kretschmann configuration, the Otto configuration is less popular because it is difficult to control the width of the air gap.

In the grating configuration in Fig. 5 (c), the necessary increase in the photon wavevector to match the SPP wavevector is achieved by adding a reciprocal lattice vector of the grating to the in-plane wavevector. Phase matching takes place whenever the condition below is fulfilled [6]:

$$k_{SPP} = k_0 \sin\theta \pm m\frac{2\pi}{a} \quad (2.24)$$

Here, k_0 is the wavevector of incident light, θ is the incident angle, $\frac{2\pi}{a}$ is the reciprocal vector of the grating, a is the period of the grating, and m is an integer.

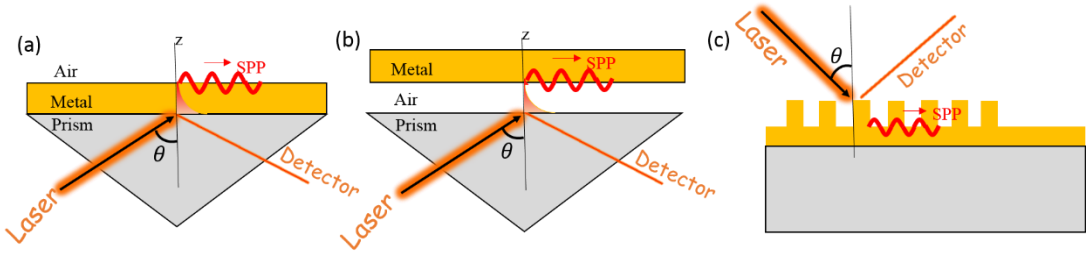

Figure 5. Configurations for the far field optical excitation of SPPs. (a) Kretschmann configuration. (b) Otto configuration. (c) Grating configuration.

To reduce the size of the SPP excitation source, near field optical excitation may be used. Scanning near-field optical microscope (SNOM) excitation [7] is commonly used as a near field optical excitation technique and it is sketched in Fig. 6. The excitation laser is focused through a metalized aperture with a diameter smaller than the excitation wavelength, resulting in an evanescent field. At the same time, the aperture-sample distance is kept less than half the wavelength, therefore, light does not propagate before it interacts with the sample. Confined light fields thus include the evanescent waves with different wavevector components of k_x.

Using the coordinate system of Fig. 2 (a), the evanescent waves decay in the z direction, so that:

$$k_z \cong i|k_z| \quad (2.25)$$

Since $k_0^2 = k_x^2 + k_z^2$, combining this with equation (2.25), we infer that:

$$k_x^2 > k_0^2 \quad (2.26)$$

Since $k_x^2 > k_0^2$, the evanescent wave can excite SPPs at the metal/air interface because as shown from the dispersion curve in Fig. 3, the k_{SPP} wavevector is larger than k_0. Thus a phase matching (momentum matching) condition can be found between an evanescent wave in air and the SPPs at an air/metal interface.

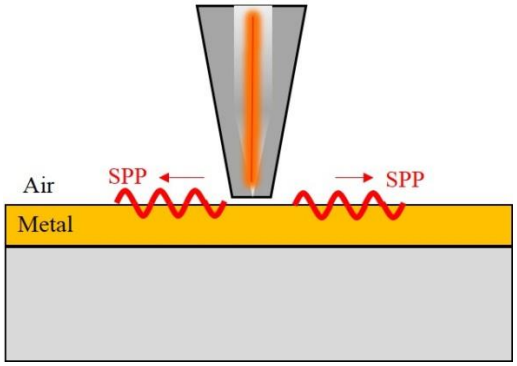

Figure 6. Local excitation of SPPs using near field illumination with a scanning near field optical microscope (SNOM).

Other ways to produce the confined light fields and an evanescent wave that can match the parallel wavevector of SPPs and thus excite them include using subwavelength apertures [7], metallic particles [8], and fluorescent molecules [9].

2.2.2 Electrical excitation

Besides the above-mentioned optical excitation, SPPs can also be excited by high-energy electrons ($\sim keV$), for example, in a scanning electron microscope (SEM) [10]. The main mechanism for the SEM excitation of SPPs in a metal can be explained as follows [11]. When a high-energy electron approaches the metallic surface, it will interact with the free charge in metal, leading to an image charge which has the opposite sign (illustrated in Fig.7 (a)). As soon as the electron reaches the surface, the image charge suddenly disappears and this process may be approximated as a vertical oscillating dipole. The effective dipole either decays as radiation or excites surface plasmon polaritons [12] and this process is sketched in Fig.7 (b).

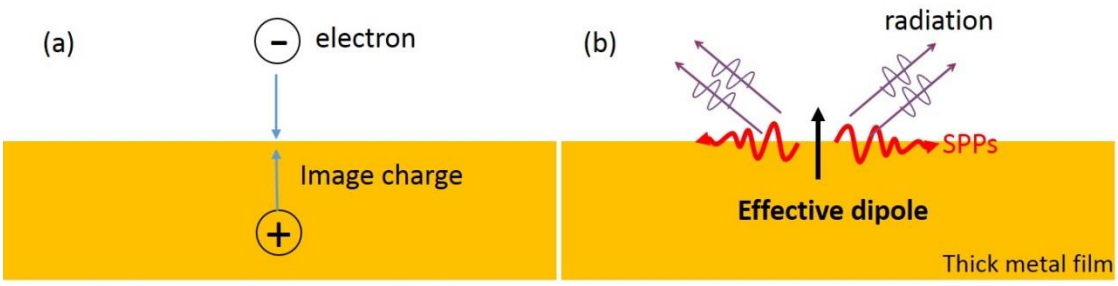

Figure 7. The emission of the light from high-energy electron excitation of Au. (a) The incoming electron induces an image charge in the sample. (b) When the electron crosses the interface the image charge vanishes, leading to an effective dipole that can radiate light or excite surface plasmon polaritons.

Low-energy electrons ($\sim eV$) can also excite SPPs. A tunnel junction is required for the low-energy excitation. When a potential difference is applied between two conductors separated by about a nanometer, electrons will tunnel from one side of the potential barrier to the other. Such a tunnel junction exists, for example, between the tip of a scanning tunneling microscope (STM) and a metallic sample. Most electrons will tunnel elastically i.e., without losing their energy as indicated in Fig. 8 (a). It is proposed that very few electrons (at most $1 \text{in } 100$ electrons) [13] will cross the barrier inelastically and lose all or part of their energy as indicated in Fig. 8 (b). This released energy can lead to radiation into photons or excite a localized gap plasmon in the tunnel junction between the tip and the metal surface. The gap plasmon can radiatively decay or excite propagating surface plasmons. This mechanism may be considered as a oscillating vertical dipole in the cavity formed by the STM tip and the metal surface [14].

Generally, the power spectrum of the emission radiated from a tunnel junction is modeled as the product of a source term given by inelastic tunneling statistics ($\propto(eV - \hbar\omega)$, for $\hbar\omega \leq eV$; 0 otherwise [15]) and an emission term related to the local density of electromagnetic states (*EM*-LDOS) [16]. As a result, the radiation has a broad power spectrum that spreads over the infrared and part of the visible range and falls to zero at energy eV (quantum cutoff). Note that V is the applied voltage.

Using the calculation of *Rendell* & *Scalapino* [17], for a tip radius of $\approx 50\ nm$ and a tip sample distance of $\approx 1\ nm$, the gap plasmon size is on the order of $10\ nm$. Therefore, we can estimate that the size of the STM-nanosource is on the same order as the gap plasmon size.

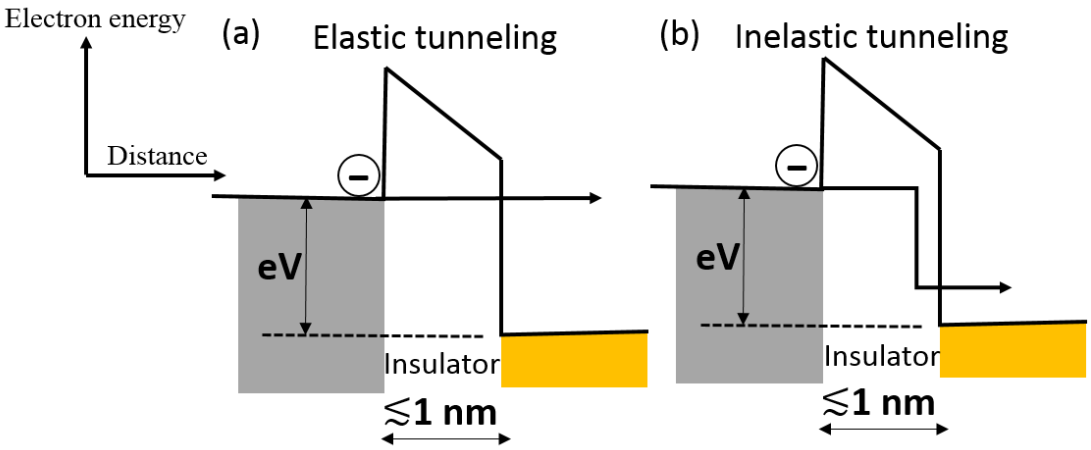

Figure 8. Schematic illustration of electron tunneling. (a) Elastic tunneling: a potential difference V is applied between two conducting layers which are separated by around 1 *nm. From the view of quantum mechanics, the electron can tunnel through this barrier. When the electron has the same energy on both sides of the barrier, we have elastic tunneling. (b) Inelastic tunneling: a small percentage of the tunnel electrons may release all or part of their energy in the barrier. This energy maybe emitted as light or used to excite SPPs.*

In my thesis, I use a scanning tunneling microscope (STM) to excite SPPs. The STM was invented in 1982 by Gerd Binnig and Heinrich Rohrer [18], for which they shared the Nobel Prize in physics in 1986. The first light emission from the STM tunnel junction was observed by Gimzewski et al in 1988 [19].

The basic working principle of STM is illustrated below in Fig. 9. A sharp metallic tip is brought in close vicinity (0.1-1 *nm*) to a conducting sample and when a voltage is applied between the tip and the sample, electrons will tunnel through the gap and the electrical current can be measured. The position of the tip in three dimensions is precisely controlled by the piezo scanner.

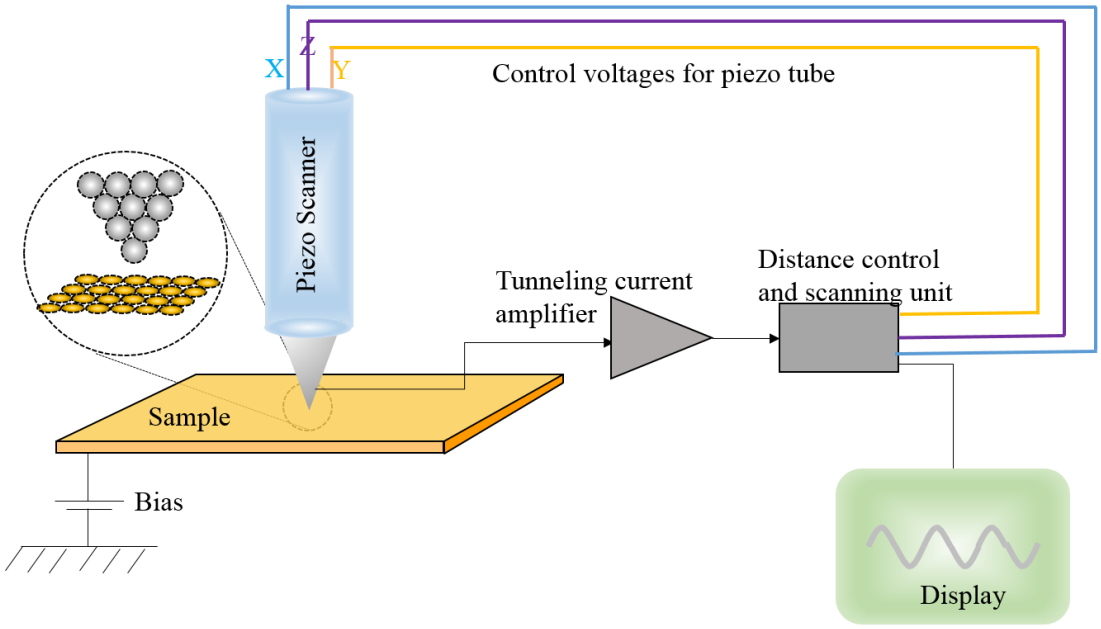

Figure 9. Schematic diagram (inspired by the illustration from the webpage: http://slideplayer.com/slide/6281817/) showing the working principle of STM. A metallic tip is mechanically connected to the piezo scanner and the xyz positioning is realized by this scanner. The sample is positively biased (in our case) so that tunneling current will flow from the tip to the sample when the tip is on the order of 1 *nm from the sample. The tunnel current will be amplified and measured. With the help of the feedback loop of the distance control electronics, the tip-sample distance is adjusted to keep the tunnel current constant. If the tunneling current exceeds the setpoint value, for example, the feedback loop will send a signal to increase the tip-sample separation.*

In the constant current mode, the tip is scanned across the sample while the tunnel current is kept constant by the feedback circuit. In order to keep the current constant, the system continuously adjusts the tip-sample separation by applying a voltage to the applicable piezo (*z* piezo in the figure above). The changes in the voltage applied to the *z* piezo give rise to the topographic image.

2.3 Leakage radiation microscopy

Above, we introduced the basic theoretical background of SPPs, we compared various ways of exciting SPPs and we detailed the electrical excitation of SPPs using an STM. In this

section, we will introduce leakage radiation microscopy (LRM) which may be used for the detection and imaging of SPPs traveling on a thin metal film.

As early as in 1976, the first observations of leakage radiation from SPPs propagating on a thin metal film was reported by Simon et al. [20]. Further progress was obtained by Hecht et al., with the combination of LRM and SNOM [21]. The schematic diagram of LRM is sketched in Fig. 10 (a). Note that a leakage radiation microscope is basically the "inverse" of the Kretschmann configuration. Just as for the Kretschmann configuration, a thin ($\lesssim 70\ nm$ for Au) metal film is deposited on a glass substrate. Excited SPPs couple light into the glass substrate at a certain angle θ_{LR} (leakage radiation angle). The principle of leakage radiation associated with the leakage radiation angle θ_{LR} is illustrated is Fig. 10 (b).

From the dispersion curve in Fig. 3, SPPs can couple light only when the wavevector of the real part of the in-plane wavevector of propagating surface plasmons k_{SPP} at the air/metal surface and the wavevector of the outgoing leakage radiation light k_{LR} passing through the glass substrate are matched (see also equation (2.23)):

$$Re[k_{SPP}] = k_{LR} \sin\theta_{LR} \quad (2.27)$$

$$k_{LR} = n_{glass} k_0 \quad (2.28)$$

where k_0 is the wavevector in free space, n_{glass} is the refractive index of the glass substrate.

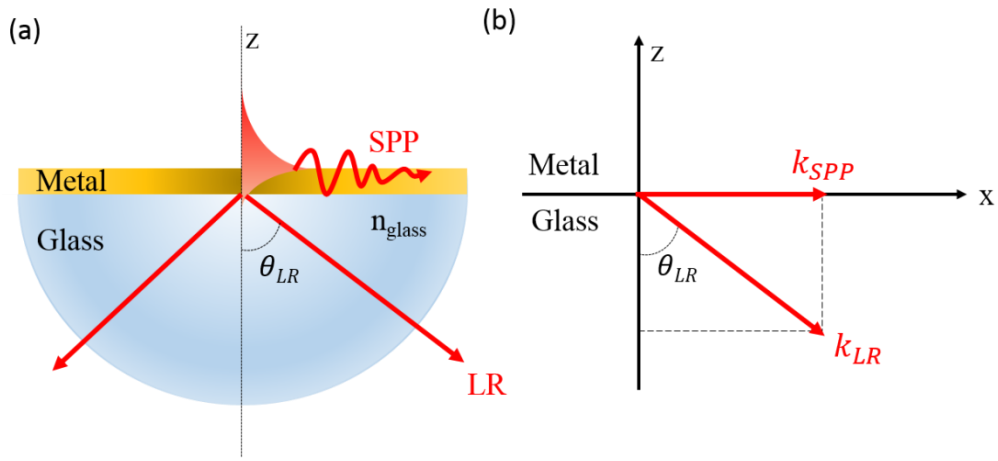

Figure 10. (a) Sketch of the leakage radiation technique. A thin ($\lesssim 70\ nm$ for Au) metal film is deposited on a glass substrate and leakage radiation is emitted directly through the substrate with an angle of θ_{LR}. (b) The principle of leakage radiation.

From the equation (2.27), we see that:

$$\theta_{LR} = \sin^{-1}\left(\frac{Re(k_{SPP})}{n_{glass}k_0}\right) \quad (2.29)$$

The air/glass critical angle $\theta_{critical}$ is equal to:

$$\theta_{critical} = \sin^{-1}\left(\frac{1}{n_{glass}}\right) \quad (2.30)$$

From the equation (2.18), when the dielectric is air, we know that

$$\frac{k_{SPP}}{k_0} = \sqrt{\frac{\varepsilon_m}{\varepsilon_m+1}} \quad (2.31)$$

As $\varepsilon_m < 0$, $|\varepsilon_m| > |\varepsilon_d|$, so $\frac{k_{SPP}}{k_0} > 1$. Then we can infer that:

$$\theta_{LR} > \theta_{critical} \quad (2.32)$$

Note that for an air objective lens, the maximum theoretical acceptance angle is $\theta_{critical}$! For the objective, the acceptance is determined by the numerical aperture (NA). NA is given by:

$$NA = n \sin\theta \quad (2.33)$$

where n is the refraction index of the medium in which the lens is working and if $n = 1$, it is for air. θ defines emission angle (i.e. $NA_{air\,max} = nsin\theta_{max} = sin\theta_{max} = 1$).

Thus an air objective lens cannot collect light emitted at an angle θ_{LR}. To overcome this problem, one solution is to use high refractive index matching oil added below a flat glass substrate and use an oil immersion objective. The refractive index of oil is equal to that of the glass substrate so that leakage radiation is directed through the glass substrate to the objective lens for collection at an angle equal to the emission angle. The LRM with an oil immersion objective is illustrated in Fig. 11. In our case, we use an oil immersion objective with $NA = 1.49$ or 1.45 and $n = 1.52$.

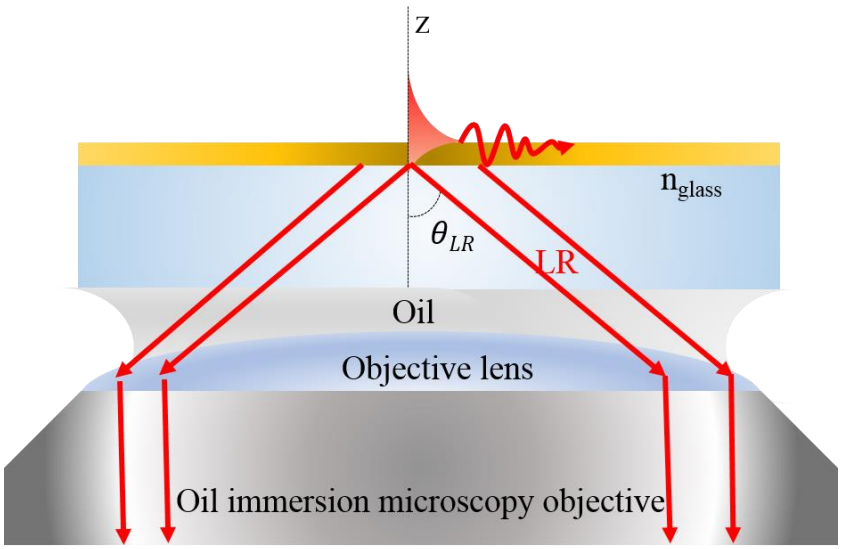

Figure 11. Leakage radiation collected with an oil immersion objective. With an oil immersion objective, the leakage radiation will be directed through the substrate to the objective.

2.4 Fourier and real space imaging

In this section, we will introduce real and Fourier space imaging and especially focus on Fourier space imaging. As we introduced in the previous section, propagating SPPs on an air/metal interface can "leak" through a thin metal film and emit photons in a substrate with higher index of refraction (e.g., glass). This emission is at a well-defined angle in the glass since at this angle the dispersion relation is matched between surface plasmons at meta/air interface and photons at glass substrate. Fourier space imaging provides a way to measure at what angle the light is emitted. Note that the technique of Fourier space imaging may be used not only to measure the leakage radiation angle, but also at what angle light from SPPs is scattered. Fourier space analysis of both leakage radiation and scattered light are carried out in this thesis.

A single thin lens realizes the Fourier transform of the object and the Fourier transform image lies in the back focal plane of the lens. Note that the field distribution in the Fourier plane is the Fourier transform of the field distribution in the object plane. The back focal plane is illustrated in Fig. 12 (see the yellow dotted line). Parallel beams which originate from the object with spatial dimension r (see these light beams with the same emission angle (θ)) will converge at the same point on the back focal plane of the first lens L_1 (e.g. objective lens). For an aplanatic objective, there exists a relationship between the angle of emission θ from the

objective's focus and radius ρ (see in Fig. 12, the radial distance from the optical axis) in the back focal plane of the objective, given by [22]:

$$\rho = f_1 n sin\theta \quad (2.34)$$

where n is the refraction index of the medium in which the lens is working.

In the experiment, from the given equation (2.34), we can measure ρ and determine the light emission angle θ.

Besides, ρ is also given by [23]:

$$\rho = f_1 \frac{k_{\parallel}}{k_0} \quad (2.35)$$

where $k_{\parallel}$ is the wavevector of the emitted light in the direction parallel to the interface and k_0 is the wavevector of light in free space. From equation (2.35), we can derive the relation between ρ and the in-plane wavevector of the emitted light.

Next, we discuss the real space image. After light propagates from the back focal plane, it passes through the second lens L_2 (e.g. the tube lens) and realizes another Fourier transform. An image of the object is formed in the image plane (purple dotted line in Fig. 12). The image at the image plan corresponds to the real space image. Thus, from the real space image, we can obtain the spatial distribution of the emitted light. Note that the real space image of a vertical oscillating dipole (i.e., the STM-nanosource) is that of a "doughnut".

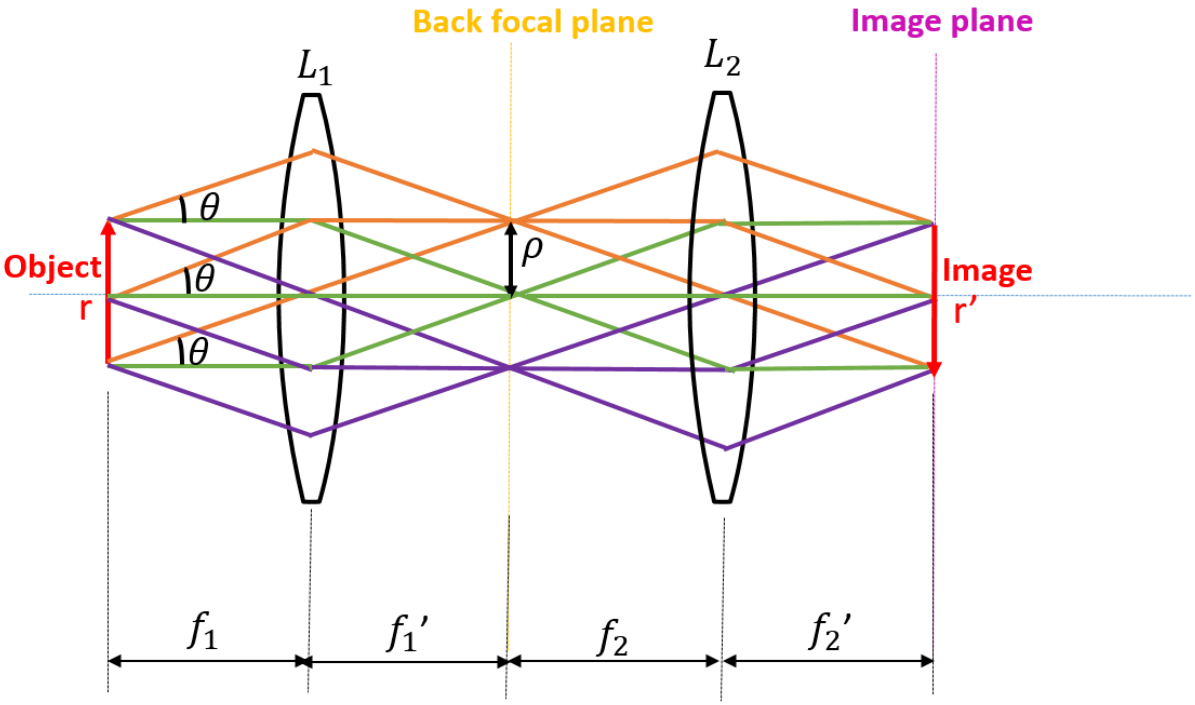

Figure 12. Schematic illustration showing the back focal plane and image plane. Rays that leave the object with the same angle will meet in the objective's back focal plane and then after passing the second lens, an inverted image will be formed on the image plane.

2.5 Radially polarized light

In this section, we will briefly introduce the concept of radially polarized light because in chapter 3, a radially polarized microsource is achieved via the STM excitation of a plasmonic lens.

Radially polarized light beams belong to the family of cylindrical vector beams. Their main characteristic is that their polarization vector is radially oriented with respect to the central axis of the beam (i.e., their polarization spatially varies). The radial vector is drawn from the center of the beam as illustrated in Fig.13 (a). Figure 13 (a) shows a schematic diagram of the radial polarization. Figure 13 (b) shows the polarization of the electric field with respect to the direction of propagation.

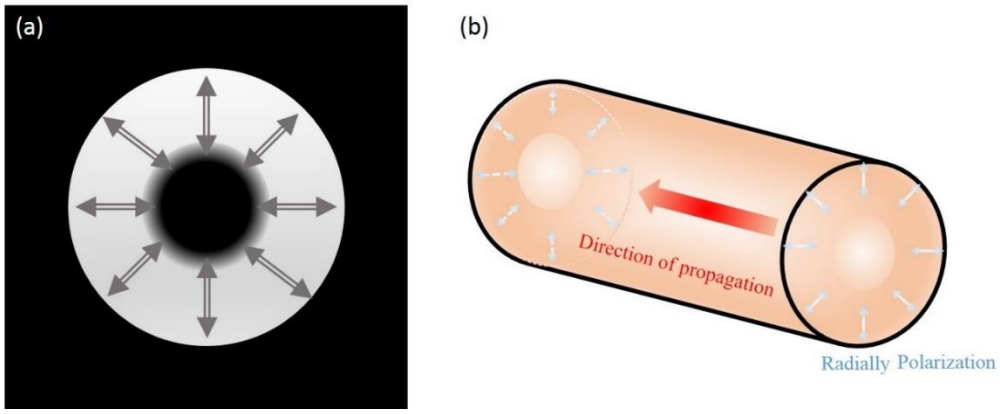

Figure 13. (a) Transverse distribution of intensity and polarization (arrows) in radially polarized light beams. (b) Schematic diagram showing the propagation direction of light.

Radially polarized light has attracted great interest due to the spatial varying orientation of the electric field. Figure 14 compares focusing for a linearly polarized and for a radially polarized beam [24]. In the graph, $\overrightarrow{E_0}$ and $\overrightarrow{k_0}$ respectively represent the electric field vector and wave propagation direction. In Fig. 14 (b), the electric field vectors on opposite sides of the propagation axis are anti-parallel; as a consequence, light rays emerging from the focusing lens at opposite focal angles θ and $-\theta$ have their radial and longitudinal field components interfering destructively and constructively at the focal point, respectively. Thus, the resulting electric field at the focal point is purely axial. However, in Fig. 14 (a), it is the opposite situation, which yields purely lateral electric field at the focal point.

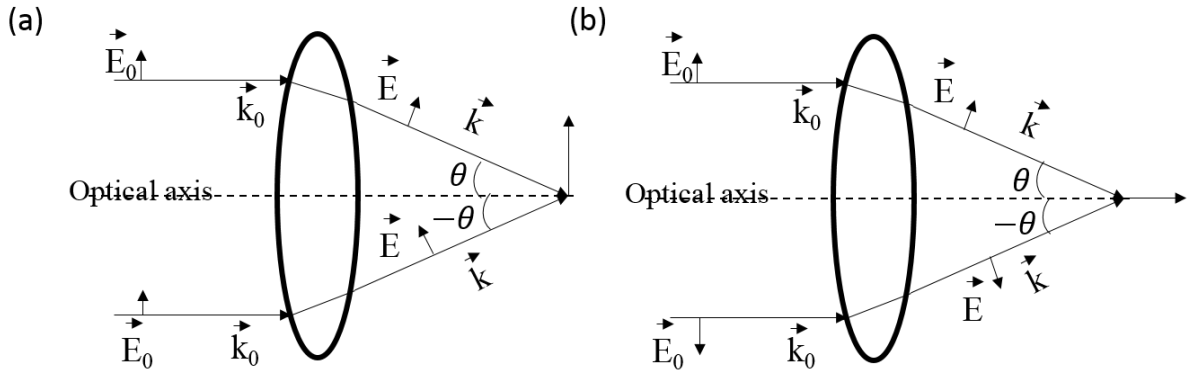

Figure 14. Ray tracing model for the focusing of an incoming collimated light beam in an optical system. $\overrightarrow{E_0}$ and $\overrightarrow{k_0}$ represent the electric field vectors and wave propagation direction, respectively. The optical axis is also shown. (a) Linear polarization. (b) Radial polarization.

Radially polarized beams can be expressed as the superposition of orthogonally polarized Hermite-Gauss HG_{01} and HG_{10} modes [25]:

$$\overrightarrow{E_r} = HG_{10}\overrightarrow{e_x} + HG_{01}\overrightarrow{e_y} \quad (2.36)$$

where $\overrightarrow{E_r}$ is the electric field distribution of radial polarization, and $\overrightarrow{e_x}$, $\overrightarrow{e_y}$ are the unit vectors in the x and y direction.

HG_{01} and HG_{10} are separately plotted in Fig. 15 (a) and (b). The arrows in Fig. 15 describe the polarization direction. Figure 15 (a) shows the y-polarized HG_{01} mode and Fig. 15 (b) shows the x-polarized HG_{10} modes. A radially polarized beam is given by the sum of (a) and (b).

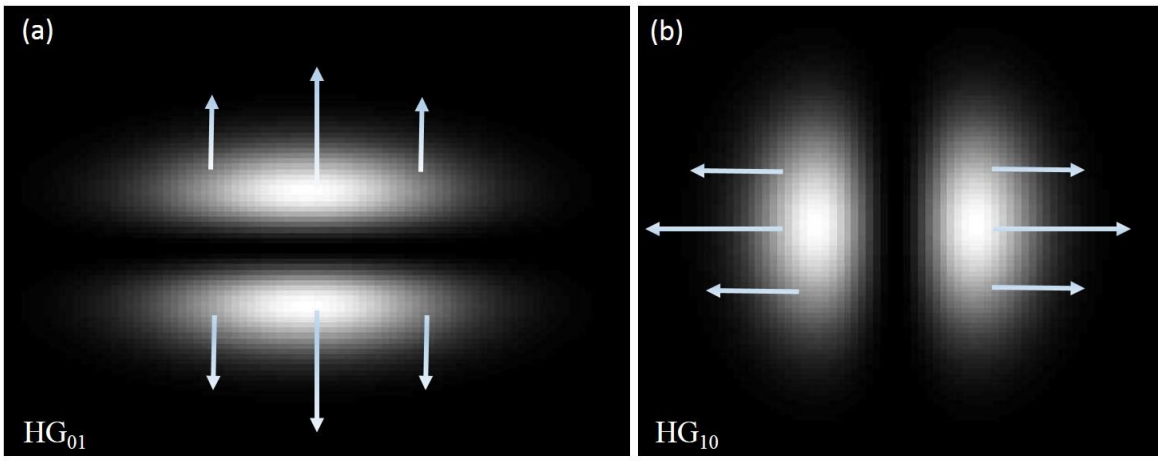

Figure 15. The power density distribution of a Hermite-Gauss conventional mode. (a) y-polarized HG_{01} mode. (b) x-polarized HG_{10} mode. These graphs are plotted using the laser Toolbox in Matlab.

2.6 *Electronic* and *electromagnetic* local density of states

In this section, the *electronic* and *electromagnetic* local density of states will be introduced.

In solid-state physics, the *electronic* density of states (*E*-DOS) describes the number of electronic states per volume per interval of energy. When referring to the *electronic* DOS at a given position, formally it is described as *electronic* local density of states (*E*-LDOS). STM has been shown to measure the *E*- LDOS at the surface of a metal [26]. For the STM, the tunneling current in the low voltage limit is proportional to the *E*-LDOS [27]:

$$I \propto \rho_s(E_F) \quad (2.37)$$

where, I is the tunnel current. E_F is Fermi energy and ρ_s is the *E*-LDOS in the sample.

Similarly, *the electromagnetic* LDOS (*EM*-LDOS) is a sum weighted by the local amplitude of the electromagnetic modes at a particular point in space [28], and in this thesis we refer to it as the *optical* LDOS. In other words, the projected *EM*-LDOS is proportional to the power emitted by a dipole of a particular orientation, while the full *EM*-LDOS describes the emitted power from the three perpendicular dipole orientations. These underlying modes can be photonic or plasmonic. In this thesis, the modes involved are mainly the localized plasmon modes. Measuring the *EM*-LDOS in plasmonic structures is a major issue, since the *EM*-LDOS drives the basic processes of light-matter interactions such as spontaneous emission (fluorescence) and absorption [29].

2.7 Experimental setups

2.7.1 Veeco setup

During my thesis, two experimental setups are employed (their differences will be discussed at the end of this section). The first one is called the "Veeco" setup (named after the STM head supplier). The "Veeco" setup is shown in Fig. 16 and it includes four main parts: a scanning tunneling microscope, an inverted optical microscope, CCD cameras and a spectrometer.

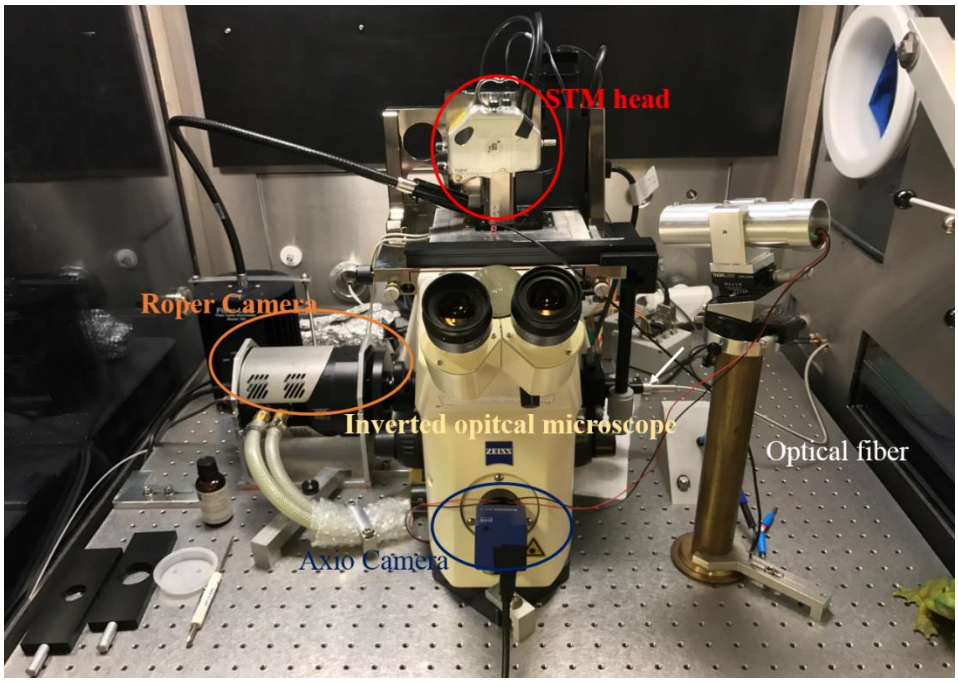

Figure 16. Experimental "Veeco" setup. The STM head is mounted above an inverted optical microscope. The cooled Roper CCD camera is mounted at the left port and Axio CCD camera is mounted at the front port. An optical fiber which is connected to a spectrometer equipped with a cooled camera is mounted at the right port.

2.7.1.1 Scanning tunneling microscope and tips

The STM is the main part in the experiment for exciting SPPs and it is shown as the red circle in Fig. 16. The STM (Veeco Bioscope, hybrid head, NanoScope IVa) can be used either as an STM or as an Atomic Force Microscope (AFM). We have already introduced the working principle of STM in section 2.2.2 and constant current mode is used during all the experiments.

Metallic tips are mounted on the STM head. In our experiment, we use tungsten (W) tips. As we already discussed in section 2.1, $\varepsilon_m<0$ is a requirement for SPPs to exist. In the visible range, the real part of the dielectric constant of W is positive so W tips display dielectric properties rather than metallic optical properties for this frequency range. As a result, W tips are chosen for experiments in order to avoid the impact of a plasmonic response of the tip [30].

The W tips are etched in a 5 mol/L NaOH solution using a direct current electrochemical process [31]. Figure 17 (a) shows a scanning electron microscope (SEM) image of our etched W tip which displays a symmetrical shape and Fig. 17 (b) shows the end of the tip. If we regard the tip end as a sphere, its measured diameter is around 80 nm.

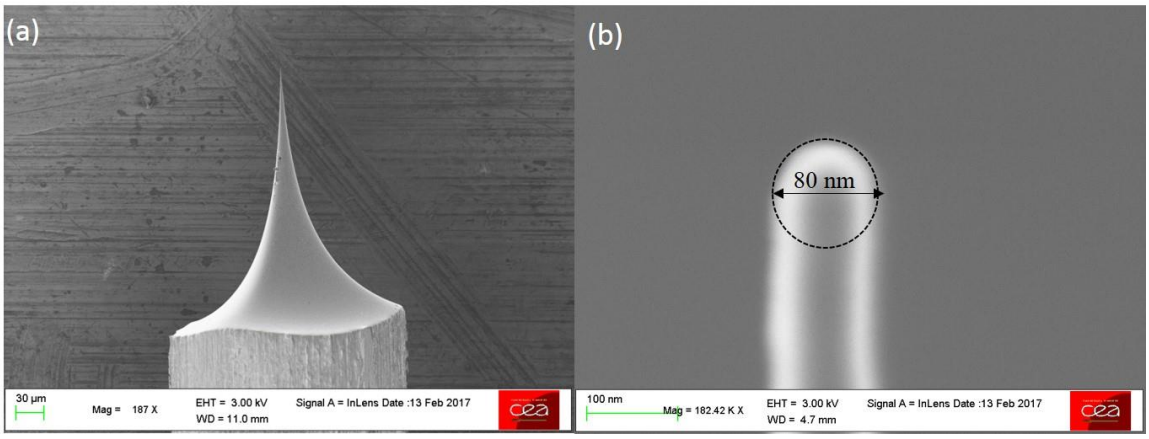

Figure 17. SEM image of our prepared tungsten tip. (a) An overview of the tip which displays a symmetrical shape. (b) A zoom of the end of the tip which shows a round shape. When regarded as a sphere, the measured diameter is close to $80\,nm$*. These SEM images are obtained at CEA Saclay with Sylvie Marguet.*

2.7.1.2 Inverted optical microscope

The STM head is mounted on a Zeiss Axiovert 200 inverted optical microscope. In the inverted optical microscope, three objective lenses are available. Different objective lenses are chosen for conducting different kinds of experiments. The first one is an air objective lens with a magnification of $10\times$ and a numerical aperture (NA) of 0.3. It is used for roughly positioning the sample easily. The second one is an air objective lens with a magnification of $100\times$ and its NA is 0.75. It is used for collecting light originating only from localized SPPs (see section 2.3). The third one is an oil immersion objective with a magnification of $100\times$ and an NA of 1.45. This is mainly used for collecting leakage radiation and scattered light from both propagating and localized SPPs. This oil immersion objective is the one used most frequently.

Below the objective, bandpass filters (e.g., $700/13\,nm$) or polarizers may be added, for example, there is a drawer for such optical elements which is indicated as the yellow circle in Fig. 18. These are used for checking the wavelength dependence of the light emission or verifying the polarization state of the emitted light.

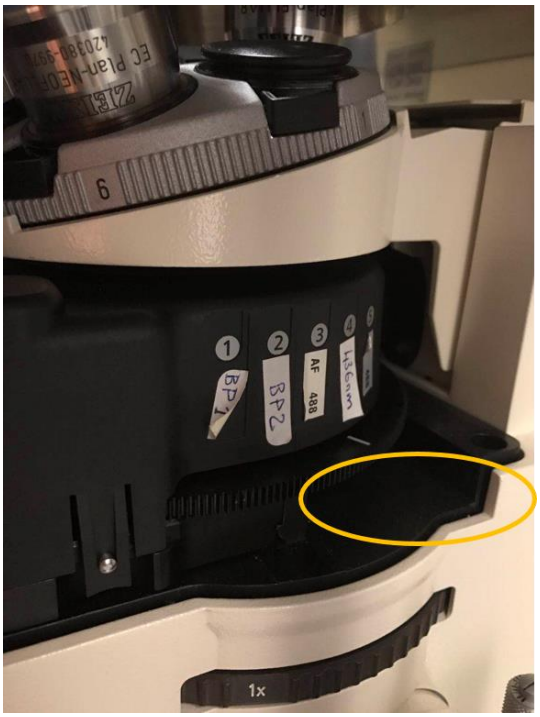

Figure 18. A zoom view on the left port of the inverted optical microscope. It shows a drawer for adding a bandpass filter or polarizer.

2.7.1.3 Light detection systems

As shown in Fig. 16, in the "Veeco" setup, we have three light detectors. The first detector is an uncooled color Axio camera (AxioCam ICc, Zeiss) which is indicated as the blue circle in Fig. 16. It has 1.4 million pixels. The pixel size is $4.65\ \mu m \times 4.65\ \mu m$. If we use the $100\times$ objective, one pixel of the Axio camera in the image plane corresponds to $46.5\ nm$ ($4.65\ \mu m/100$) in the real space image. This camera is used for roughly locating the STM tip position and also as it is colored (could display colored image), from personal experimental experience, by changing the focus, it is easier to distinguish the small nanoparticles deposited on the sample with this camera.

The second detector is a water-circulation cooled CCD (charge coupled device) camera (Roper, Scientific, Princeton Instruments) which is indicated as the orange circle in Fig. 16. It is cooled to $-70°$ for operation. This Roper camera has 1024×1024 pixels and the pixel size is $13\ \mu m \times 13\ \mu m$. This camera is the core equipment in our experiment. With it, the light emitted is collected through the substrate and imaged. Both real space and Fourier space images (introduced in section 2.4) may be recorded. One pixel in the Roper camera in the real space

image corresponds to $130\,nm$ ($13\,\mu m/100$) in the object plane when used with the $100\times$ objective. In the Fourier space image, the resolution is $0.027k_0$ per pixel (The $NA = 1.45$ and in the Fourier space image, light may be collected for a radius up to ≈ 54 pixels and k_0 is the wavevector in free space. Its unit is nm^{-1}).

The third detector is a cooled CCD camera (Symphony LN2) coupled to an optical spectrometer (Triax 190, Horiba-Jobin Yvon). The CCD camera is cooled with liquid nitrogen and operates at $150\,K$. A bundle of 49 optical fibers is used for sending the emitted light to the spectrometer. The spectrometer can be used with two different diffraction gratings or a mirror. The first grating is a blazed grating with a grating density of 300 g/mm (grooves per millimeter). It is designed to operate at a central wavelength of $600\,nm$ and cover a spectral range that is $400\,nm$ wide. The second grating is a holographic grating with a grating density of 150 g/mm. It is designed to operate at a central wavelength of $800\,nm$ and cover a spectral range that is $800\,nm$ wide. Comparing these two gratings, we see that higher groove density results in greater dispersion and higher wavelength resolution but is accompanied by a smaller spectral range.

2.7.2 JPK setup

The second setup used during my PhD will be called the "JPK" setup (the STM head is supplied by JPK Instruments). The "JPK" setup is shown in Fig. 19 and is located on a larger optical table ($1.2\,m \times 1.8\,m$) than the "Vecco" setup. Figure 19 shows a picture of the experiment. Besides the optical elements, the main instruments include: an STM head, an inverted optical microscope, optics for laser excitation (detailed in chapter 5), CCD cameras, an imaging spectrometer, an APD (avalanche photodiode detector).

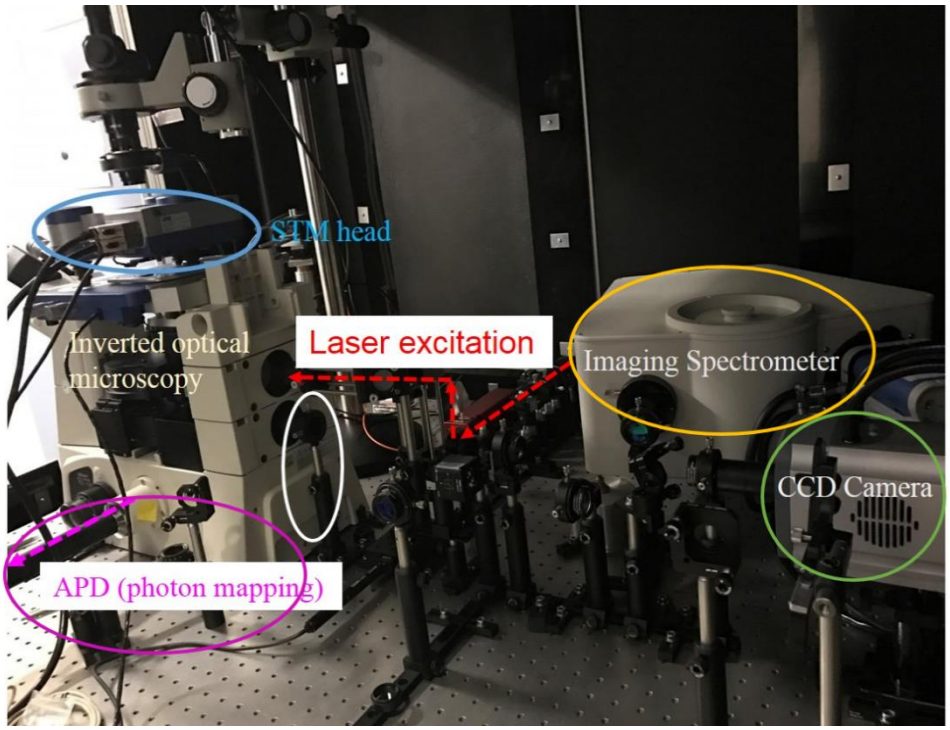

Figure 19. The experimental "JPK" setup is contained in a large box and placed on an optical table ($1.2\ m \times 1.8\ m$*). An STM head is mounted above an inverted optical microscope. A large CCD camera (Andor) is mounted behind the inverted optical microscope on the optical axis of the microscope. With a mirror, the emitted light may also be guided to an imaging spectrometer. Laser excitation is provided via an optical fiber which is coupled to a He-Ne laser (*$633\ nm$*) located outside of the box. An avalanche photodiode detector is also mounted on the right port of the inverted optical microscope.*

2.7.2.1 STM head and inverted optical microscope

For the STM head, we use the Nanowizard®3NanoScience head from JPK Instruments. Similar to the "Veeco" setup, it also can be used for both AFM and STM. Tungsten tips are also used in this set-up.

The inverted optical microscope is an Eclipse Ti-U from Nikon. The main objective lens we used is an oil immersion objective with magnification of $100\times$ and an NA of 1.49.

2.7.2.2 Light detection systems

From Fig. 19, we see that there are three different detectors. The first light detection device is a CCD camera which is a liquid cooled Andor camera (iKon-M, Andor Technology) and it is shown as the blue circle in Fig. 19. The camera uses Peltier cooling and chilled water air circulation to reach a temperature of $-90°C$. The Andor camera has 1024×1024 pixels and the pixel size is $13\ \mu m \times 13\ \mu m$. Here, unlike the "Veeco" setup, the tube lens (with focal length of $f_T = 200\ mm$) inside the microscope is not used to form the image on this CCD camera. Instead, another tube lens (indicated as the white circle in Fig. 19) with a focal length of $f_{T'} = 300\ mm$ is mounted externally. Thus, when the CCD records the image, the magnification is $150 \times (f_{T'}/f_O)$ rather than $100 \times (f_T/f_O)$. As a result, one pixel in the image plane of the Andor camera corresponds to $86\ nm$ $(13\ \mu m/150)$ in the object plane. In the Fourier space image, the resolution is calculated as $0.01k_0$ per pixel (The $NA = 1.49$ and in the Fourier space image, light is collected up to a radius of ≈152 pixels). Compared with the "Veeco" setup, the "JPK" setup has better resolution in both the real and Fourier space images.

However, in terms of the diffraction limit for microscope, according to "Abbe diffraction limit" for light with vacuum wavelength λ_0, traveling in a medium with refractive index n, the smallest distance between two distinguishable objects is:

$$d = \frac{\lambda_0}{2nsin\theta} \quad (2.37)$$

According to equation (2.37), d is around to $200\ nm$ for $\lambda_0 = 600\ nm$ for both the "Veeco" and "JPK" setups. Thus for the "JPK" setup, with 1 pixel per $86\ nm$ in the object plane, the *Shannon Criterion* is met and the spatial resolution of the imaging system is not limited by the pixel size.

The second light detection system (shown as the yellow circle in Fig. 19) is an imaging spectrometer which is from Horiba Instruments. It combines an iHR320 spectrometer with a Synapse CCD detector. This spectrometer also contains two gratings and a mirror inside it. The first grating has a groove density of 600 g/mm. The second grating has a groove density of 150 g/mm. The CCD is cooled to $-80°C$ and it has 1024×256 pixels. The pixel size is $26\ \mu m \times 26\ \mu m$.

All the spectra in this thesis are acquired using this spectrometer. The acquired spectra must be corrected for the spectral response of the different parts of the experiment, i.e., the transmission efficiency of the objective, the spectral efficiency of the grating and the quantum efficiency of the CCD detector. Figure 20 presents that the spectral response to each element

and the total detection efficiency of the spectrometer as a function of wavelength. Here, all the data are provided by the company of our instrument. We can see that the maximum total efficiency is only around 50% at around $\lambda = 500\ nm$. Note that the collection efficiency is not taken into account here.

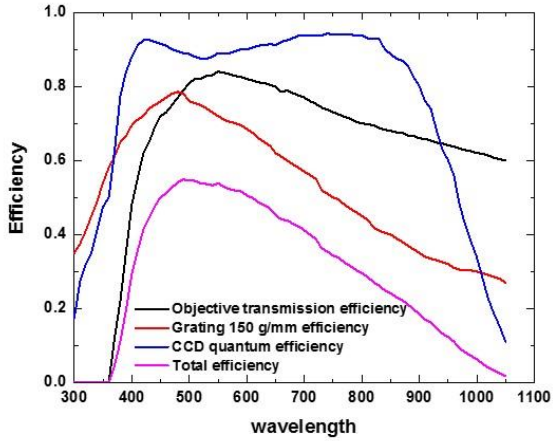

Figure 20. The shape of the acquired spectra is influenced by the spectral dependence of the transmission efficiency of the objective, the spectral grating as well as the quantum efficiency of CCD detector. Each curve separately shows the corresponding efficiency and the total efficiency is also given.

The third light detecting device (shown as the purple circle in Fig. 19) is a single photon counting detector. This device detects all the light emitted from around a $50\ \mu m^2$ area of the image plane within its sensitivity range ($400 - 100\ nm$). The photons are detected using an APD (avalanche photodiode, Excelitas). The TTL output signal from the photodiode is integrated by the STM controller (JPK Vortis ™ Advanced-fully digital SPM Control Station). The APD works for the wavelength range of $400\ nm$ - $1060\ nm$ and the highest photon detection efficiency is 70% at a wavelength of around $700\ nm$.

Our APD is superior in terms of its dark count. Generally, the lowest dark count for other Excelitas APDs is about 25 counts per second. With our APD, however, we can reach 5 counts per second with no illumination. Figure 21 shows an experimental test where the APD signal is recorded as a function of time while it is in the dark. The measured dark count rate is 6 counts per second.

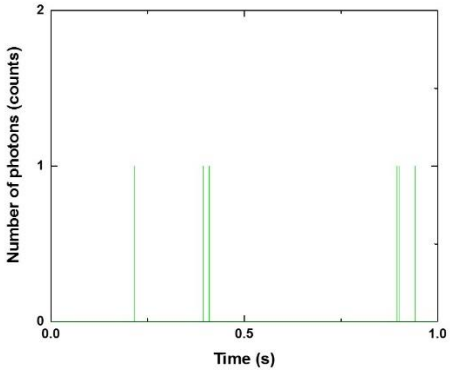

Figure 21. Experimental test for recording the dark count of our APD. The APD signal is recorded while all sources of light are off. The shown image is taken from a continuous time acquisition. The measured dark count is 6 photons per second.

2.7.3 Comparison between the "Veeco" and "JPK" setups

To conclude this section, we will compare the two setups that have been introduced. The differences between these two setups lie mainly in the light detection systems.

First, we will compare the differences in the setups for real and Fourier space imaging. Figures 22 (a) and 22 (b) show ray tracing diagrams for real space imaging for the "Veeco" and "JPK" setups respectively. In both systems, the objectives are infinity corrected, or in other words, the image after the objective is at infinity (i.e., the light rays are parallel). In the "Veeco" setup (Fig. 22 (a)), after the objective lens, there is a tube lens (inside the microscope) which focuses the image on the CCD camera. In the "JPK" setup (Fig. 22 (b)), there are two more lenses L_1 and L_2. The advantage of having two more lenses is that now the image and Fourier planes may be replicated outside the microscope. For example, position B in Fig. 22 (b) represents the Fourier space image location, and if we add a mask at this location to block certain emission angles, the filtered real space image (made up of e.g., only light emitted at $\theta > \theta_c$) can be recorded.

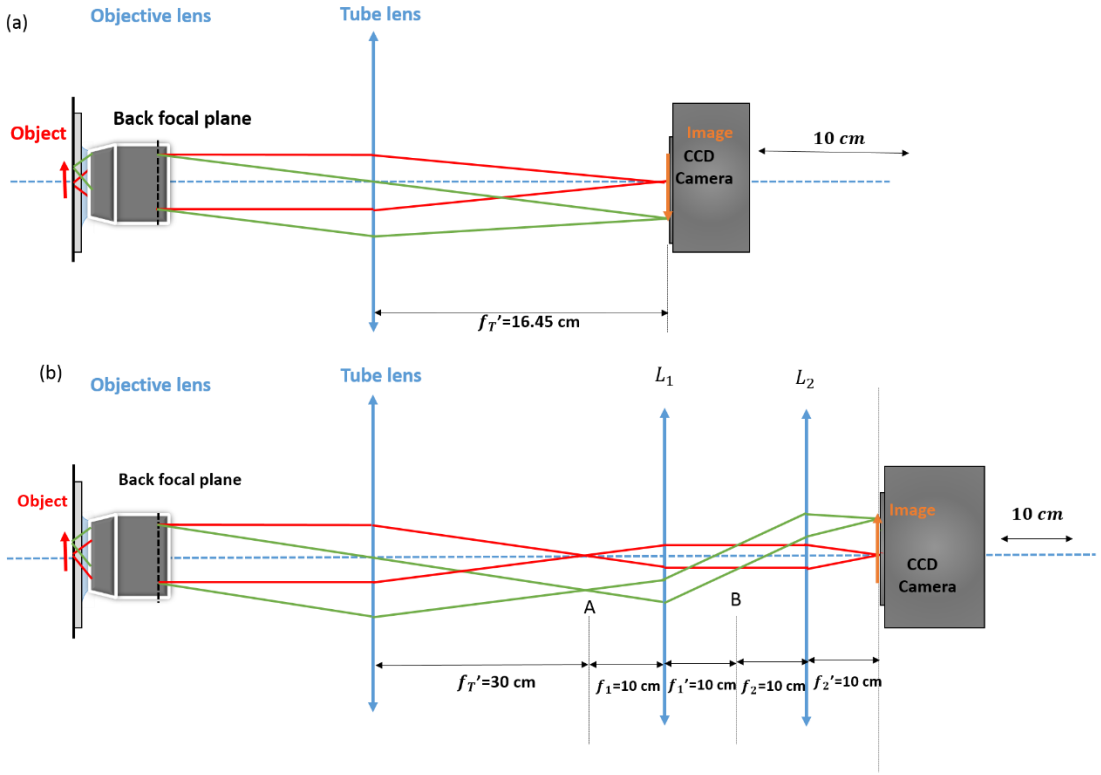

Figure 22. Ray tracing diagrams for real space imaging for the two setups. (a) Veeco setup. (b) JPK setup.

Figures 23 (a) and 23 (b) illustrate the ray tracing diagrams for Fourier space imaging for the "Veeco" and "JPK" setups, respectively. In the Fourier space imaging technique, both setups have the same number of lenses. However, for the "JPK" setup, an intermediate real space image is formed at position A (image plane of the tube lens). So at position A, a mask may be added to block the light emitted from certain locations and thus, the CCD camera can record a filtered Fourier space image acquired with light emitted from only specific locations on the sample.

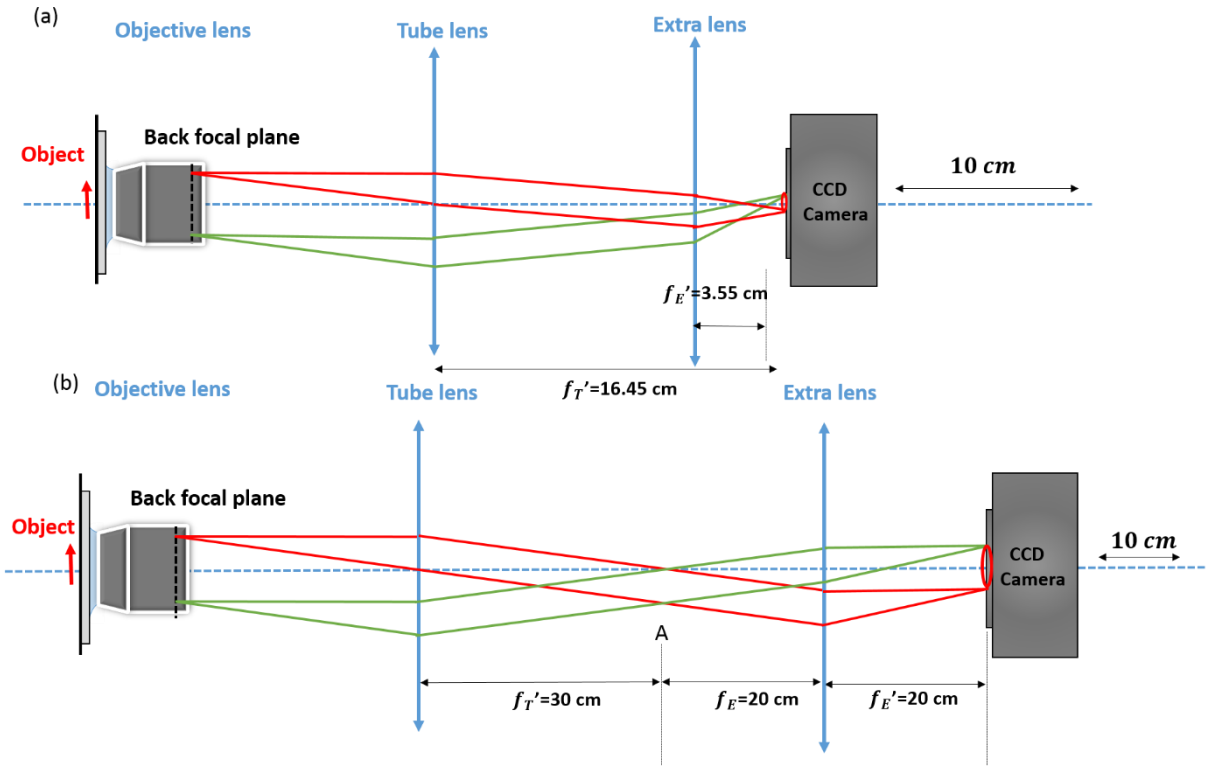

Figure 23. Ray tracing diagrams for Fourier space imaging for the two setups (a) Veeco setup. (b) JPK setup.

Another advantage of the "JPK" setup is that the imaging spectrometer can record angularly resolved spectral images by projecting the Fourier space image on the entrance of the spectrometer. This technique will be detailed in chapter 3.

An advantage of the "Veeco" setup is that it is installed in a glove box that can be filled with nitrogen, which allows the study of oxygen-sensitive systems.

2.8 Conclusion

In conclusion, in this chapter, the theoretical background related to SPPs is described. It is seen that SPPs are TM waves. We also derive the SPP dispersion relation. Different optical and electrical techniques for exciting of SPPs are detailed. The STM excitation of SPPs, which is the principal technique in this thesis, is also detailed and emphasized. We introduce the detection and imaging of SPPs via leakage radiation microscopy. Fourier space imaging, and radially polarized light are also introduced. Lastly, the experimental setups, i.e., the "Veeco"

and “JPK” setups, are detailed and the differences between these two setups are discussed. This chapter lays the foundations for the rest of the manuscript.

[1] L. Novotny and B. Hecht, *Principles of Nano-Optics*. Cambridge University Press, 2006.

[2] S. A. Maier, *Plasmonics: Fundamentals and Applications*. Springer, 2006.

[3] P. B. Johnson and R. W. Christy, "Optical constants of the Noble Metals," *Phys. Rev. B*, vol. 6, no. 12, pp. 4370–4379, 1972.

[4] E. Kretschmann and H. Raether, "Radiative decay of non-radiative surface plasmons excited by light," *Zeitschrift für Naturforsch. A*, vol. 23, no. 2135, pp. 2135–2136, 1968.

[5] A. Otto, "Excitation of Nonradiative Surface Plasma Waves in Silver by the Method of Frustrated Total Reflection," *Zeitschrift für Phys.*, vol. 216, no. 398, pp. 398–410, 1968.

[6] H. Raether, *Surface Plasmons on Smooth and Rough Surfaces and on Gratings*. Berlin, Heidelberg: Springer-Verlag, 1988.

[7] B. Hecht, H. Bielefeldt, L. Novotny, Y. Inouye, and D. Pohl, "Local Excitation, Scattering, and Interference of Surface Plasmons," *Phys. Rev. Lett.*, vol. 77, no. 9, pp. 1889–1892, 1996.

[8] J. R. Lakowicz, "Radiative decay engineering 3. Surface plasmon-coupled directional emission," *Anal. Biochem.*, vol. 324, no. 2, pp. 153–169, 2004.

[9] H. Ditlbacher *et al.*, "Fluorescence imaging of surface plasmon fields," *Appl. Phys. Lett.*, vol. 80, no. 3, pp. 404–406, 2002.

[10] T. Coenen, B. J. M. Brenny, E. J. V. Vesseur, and A. Polman, "Cathodoluminescence microscopy: Optical imaging and spectroscopy with deep-subwavelength resolution," *MRS Bull.*, vol. 40, no. 4, pp. 359–365, 2015.

[11] F. J. García De Abajo, "Optical excitations in electron microscopy," *Rev. Mod. Phys.*, vol. 82, no. 1, pp. 209–275, 2010.

[12] M. Kuttge *et al.*, "Local density of states, spectrum, and far-field interference of surface plasmon polaritons probed by cathodoluminescence," *Phys. Rev. B*, vol. 79, no. 11, pp. 2–5, 2009.

[13] P. Johansson, “Light emission from a scanning tunneling microscope: Fully retarded calculation,” *Phys. Rev. B*, vol. 58, no. 16, p. 10823, 1998.

[14] P. Bharadwaj, A. Bouhelier, and L. Novotny, “Electrical excitation of surface plasmons,” *Phys. Rev. Lett.*, vol. 106, no. 22, p. 226802, 2011.

[15] D. Hone, B. Mühlschlegel, and D. J. Scalapino, “Theory of light emission from small particle tunnel junctions,” *Appl. Phys. Lett.*, vol. 33, no. 2, pp. 203–204, 1978.

[16] K. Joulain, R. Carminati, J. P. Mulet, and J. J. Greffet, “Definition and measurement of the local density of electromagnetic states close to an interface,” *Phys. Rev. B*, vol. 68, no. 24, p. 245405, 2003.

[17] R. W. Rendell and D. J. Scalapino, “Surface-Plasmons Confined by Microstructures on Tunnel-Junctions,” *Phys. Rev. B*, vol. 24, no. 6, pp. 3276–3294, 1981.

[18] G. Binnig, H. Rohrer, C. Gerber, and E. Weibel, “Surface studies of Scanning Tunneling Microscopy,” *Phys. Rev. Lett.*, vol. 49, no. 1, pp. 57–61, 1982.

[19] J. K. Gimzewski, B. Reihl, J. H. Coombs, and R. R. Schlittler, “Photon emission with the scanning tunneling microscope,” *Zeitschrift für Phys. B*, vol. 72, no. 4, pp. 497–501, 1988.

[20] H. J. Simon and J. K. Guha, “Directional surface plasmon scattering from silver films,” *Opt. Commun.*, vol. 18, no. 3, pp. 391–394, 1976.

[21] B. Hecht, D. W. Pohl, H. Heinzelmann, and L. Novotny, “Tunnel near-field optical microscopy:TNOM-2,” *Ultramicroscopy*, vol. 61, no. 1, pp. 99–104, 1995.

[22] L. Dai, I. Gregor, I. von der Hocht, T. Ruckstuhl, and J. Enderlein, “Measuring large numerical apertures by imaging the angular distribution of radiation of fluorescing molecules.,” *Opt. Express*, vol. 13, no. 23, pp. 9409–9414, 2005.

[23] A. Drezet *et al.*, “Leakage radiation microscopy of surface plasmon polaritons,” *Mater. Sci. Eng. B*, vol. 149, no. 3, pp. 220–229, 2008.

[24] S. Quabis, R. Dorn, M. Eberler, O. Glöckl, and G. Leuchs, “Focusing light to a tighter spot,” *Opt. Commun.*, vol. 179, no. 1, pp. 1–7, 2000.

[25] Q. Zhan, “Cylindrical vector beams: from mathematical concepts to applications,” *Adv.*

Opt. Photonics, vol. 1, no. 1, pp. 1–57, 2009.

[26] J. Li, W. D. Schneider, and R. Berndt, "Local density of states from spectroscopic scanning-tunneling-microscope images: Ag(111)," *Phys. Rev. B*, vol. 56, no. 12, pp. 7656–7659, 1997.

[27] C. J. Chen, *Introduction to Scanning Tunneling Microscopy Second Edition*. Oxford University Press, 2008.

[28] R. Carminati *et al.*, "Electromagnetic density of states in complex plasmonic systems," *Surf. Sci. Rep.*, vol. 70, no. 1, pp. 1–41, 2015.

[29] K. H. Drexhage, "Influence of a Dielectric Interface on Fluoresence Decay Time," *J. Lumin.*, vol. 1, no. 2, pp. 693–701, 1970.

[30] E. Le Moal *et al.*, "Engineering the emission of light from a scanning tunneling microscope using the plasmonic modes of a nanoparticle," *Phys. Rev. B*, vol. 93, no. 3, p. 35418, 2016.

[31] Benoit Rogez, "Excitation électrique local de nanostructures plasmoniques par la point d'un microscope à effect tunnel," Université Paris Sud, 2014.

Chapter 3

Using a circular plasmonic lens to control the emission of electrically excited light

In this chapter, the production of a radially polarized microsource of light with a small angular spread is demonstrated using the electrical excitation of a plasmonic lens. This chapter is based on the articles [1]–[3].

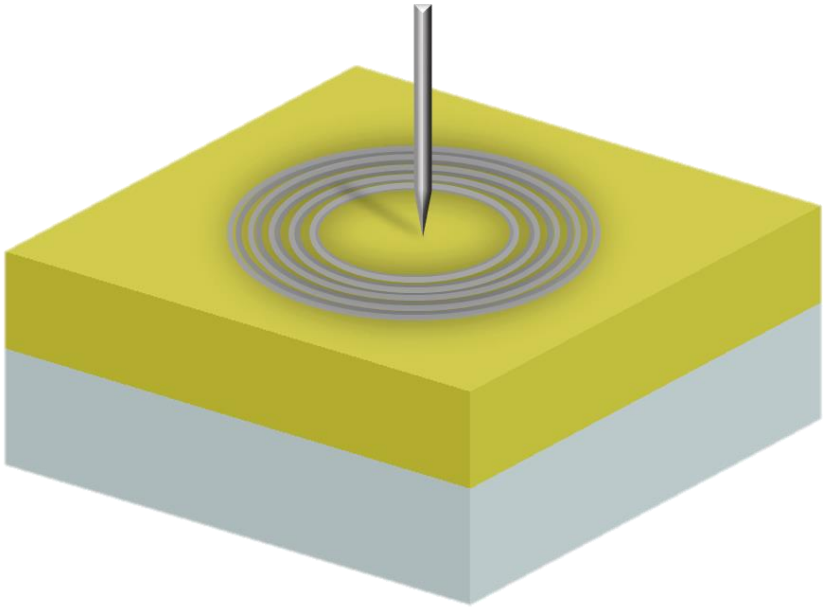

3.1 Introduction

The excitation of surface plasmon polaritons (SPPs) on metallic nanostructures opens up new routes for the manipulation of light at the nanoscale. Just as light may be manipulated using glass elements, the propagating of SPPs may be controlled using a plasmonic lens [4]. Such a lens may be constructed from a series of concentric circular slits etched in a thick metal film. The first plasmonic lens was proposed by Zhang's group in 2005 [5]. They showed that when a circular slit etched in a thick metallic film is irradiated with linearly polarized light, it can act as a planar lens for plasmons that focuses SPPs and concentrates the electromagnetic field at the focal point. Later, in 2009, Zhan's group reported that by using a radially polarized laser beam to illuminate a circular plasmonic lens, they found that the excited plasmons were focused in the center of the near field of the lens for an area whose size was below the diffraction limit [6]. Other examples of plasmonic lenses have also been demonstrated where a propagating light beam is transformed into a focused plasmon spot [7]–[11].

More recently, plasmonic lenses have found a new application as an optical component which not only converts light to a focused SPP spot but also transforms SPPs into collimated light. Thus, such a lens behaves as an optical antenna, linking the optical near and far fields. The Brongersma [12] and Rapaport groups [13] both reported that a nanoscale emitter such as a quantum dot located at the focus of a plasmonic lens may transfer energy via near field coupling to SPPs, which propagate and scatter at the circular slits into an outgoing light beam.

Here, we show a novel method to couple a plasmonic lens structure with a local, electrical source of SPPs. The local, electrical source of SPPs may be achieved with high-energy electrons in a scanning electron microscope (SEM) [14], [15], or with low-energy electrons in a scanning tunneling microscope (STM) [16]–[19]. Due to the disadvantage of large high energy electrons generators, low-energy electrical excitation of SPPs may provide more possibilities for the integration of plasmonics with electronics.

In this chapter we discuss our work where we electrically excite a plasmonic lens using the inelastic tunnel current between an STM tip and the metallic sample and obtain a radially polarized microsource of light of low angular spread (around ($\pm 4°$)). We compare the resulting emission from an STM-excited plasmonic lens and for an unstructured thin Au film on glass. The dependence of the low angular spread on the lens structural parameters of the emitted light will be discussed. We also present how a plasmonic lens responds to the broadband excitation of the STM-nanosource.

3.2 Sample preparation

The plasmonic lenses are prepared by *Jean-François Motte* at the NanoFab facility, Institut Néel in Grenoble. The structures are prepared using the Focused Ion Beam (FIB) etching of an Au film, 200 nm in thickness, that has been thermally evaporated on a glass coverslip coated with a 100 nm-thick layer of indium tin oxide (ITO). Here, the ITO is used for acting as a good conductor in case that the tip is moved to the slit. A dual beam FIB and SEM (scanning electron microscope) system is used for preparation.

The design of the plasmonic lens is either a 5-slit circular grating, 3-slit circular grating or a single circular slit, with the following parameters: slit width $w = 300\ nm$, etch depth 200 nm, and grating period of varying parameters $P = 600, 700,$ and $800\ nm$. Structures with central disks of inner diameters $D = 1, 2, 3, 4, 5,$ and $6\ \mu m$ are examined. Figure 1 (a) illustrates schematically the structure of our plasmonic lens and Fig. 1 (b) presents the side view and parameter definitions. N is the number of slits, D is the inner diameter, w is the slit width and P is the period of the structure. Figure 1 (c) shows a scanning electron microscope image of the prepared plasmonic lens.

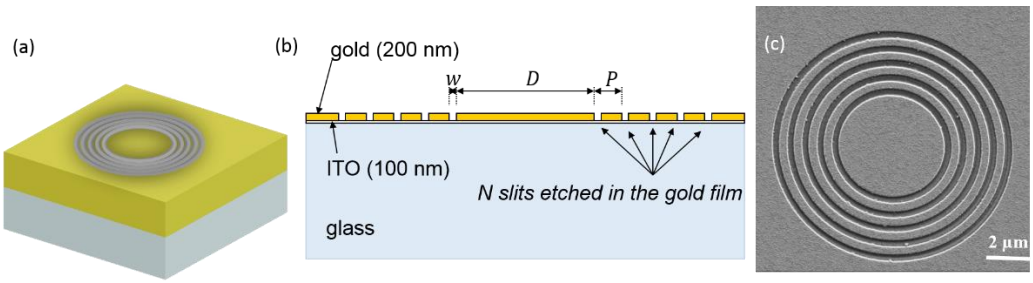

Figure 1. Plasmonic lens structure. (a) Schematic representation of the structure of our plasmonic lens, a series of concentric slits etched on a thick Au film on a glass coverslip coated with ITO. (b) Side view and definitions. N is the number of slits, D is the inner diameter, w is the slit width and P is the period of the structure (c) Scanning electron microscope (SEM) image of a plasmonic lens. It has 5 slits and the inner diameter $D = 5\ \mu m$. The slit grating period is $P = 700\ nm$.

Our plasmonic lens structures are also characterized by optical transmission imaging. White light is used to illuminate the structures from above and the resulting image is obtained by collecting the transmitted light below the substrate. Examples of transmission images of

different plasmonic lenses are shown in Fig. 2. Figure 2 (a) shows the transmission image of the plasmonic lens with $N = 5$, $D = 6\ \mu m$, $P = 700\ nm$. Figure 2 (b) shows the transmission image of the structure with $N = 3$, $D = 4\ \mu m$, $P = 700\ nm$. Figure 2 (c) shows the transmission image of the structure with $N = 1$, $D = 6\ \mu m$. Note that slight imperfections in the fabrication may be identified by the dark spots seen along the white illuminated slits.

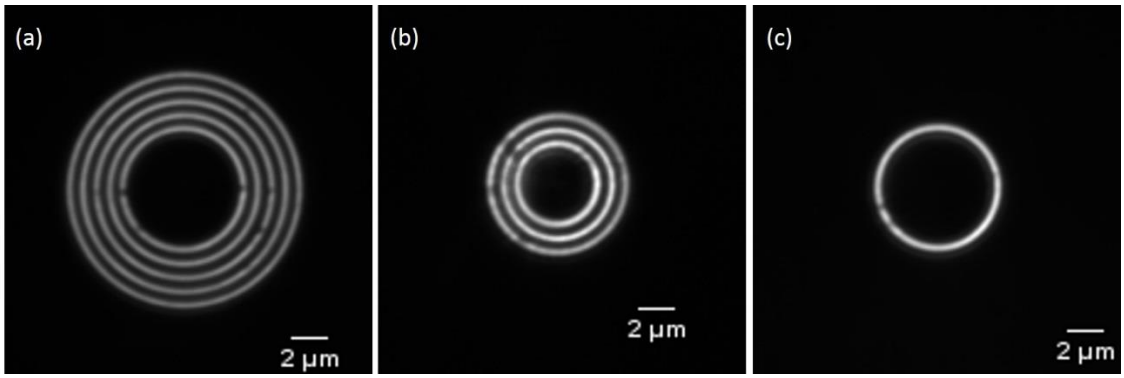

Figure 2. Transmission image of the plasmonic lenses. (a) Transmission image of the plasmonic lens with $N = 5$, $D = 6\ \mu m$, $P = 700\ nm$. (b) Transmission image of the structure with $N = 3$, $D = 4\ \mu m$, $P = 700\ nm$. (c) Transmission image of the structure with $N = 1$, $D = 6\ \mu m$,

3.3 Comparison of the emission patterns obtained when a plasmonic lens and a thin Au film are electrically excited

3.3.1 Real space image comparison

First, we compare the spatial distribution of the emitted light generated through the local electrical excitation of a plasmonic lens (5-slit circular grating etched in a $200\ nm$-thick Au film) and of a thin, planar, Au film (50-nm thick, thermally evaporated in vacuum on a glass coverslip after deposition of $2\ nm$ of chromium). Electrical excitation is achieved using the tunnel current from the STM on the "JPK setup" (see section 2.7.2, chapter 2). The plasmonic lens has a grating period of $P = 700\ nm$ and inner diameter $D = 5\ \mu m$. Due to the two different Au film thickness, only scattering light at the slits is detected in the case of the plasmonic lens, whereas only SPPs leakage radiation is observed in the case of the thin, planar, Au film [20]. Figures 3 (a) and 3 (b) schematically illustrate the experiment. Here, the STM tip is centered on the plasmonic lens. Figure 3 (c-f) show the resulting real space images, recorded

without (c, d) and with (e, f) a linear polarizer in front of the CCD camera. The polarization axis is oriented as shown in (e, f).

Compared with the results obtained on an Au film as shown in Fig. 3 (d), from Fig. 3 (c), we see that light from the plasmonic lens is emitted only from the five slits as expected. Besides, we find that there is a much stronger contribution from the inner slit of the plasmonic lens as compared to the outer slits. This is expected since the SPPs which scatter at the slits are a 2 D circular outgoing wave that isotropically propagates away from the center of the structure. Moreover, the SPP intensity decays very quickly when SPPs propagate through the grating due to the scattering into photons. On the unstructured Au film, a 2 D circular outgoing wave also propagates away from the tip location, yet with a comparatively much longer propagation length, since there is no scattering. High intensity is observed from below the tip, due to the excitation of localized gap plasmon mode that radiatively decays into the glass substrate (see chapter 2).

From Figs. 3 (e) and 3 (f), we see that the intensity cancels out along the axis perpendicular to the polarizer transmission axis. This denotes that we obtain a radial polarized microsource and a radially polarized light cone (The polarization of the light emission will be verified in Fourier space images later).

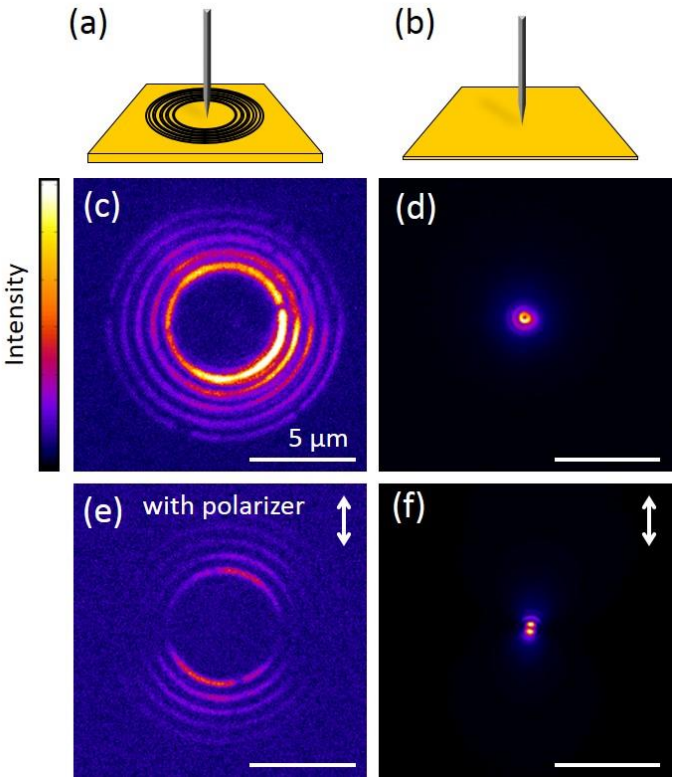

Figure 3. Comparison of the light emitted from a plasmonic lens and a thin Au film after STM excitation. (a) and (b) schematically illustrate the two kinds of excited structures and the tip excitation position. (c) Real space image from the excited plasmonic lens. (d) Real space image from the excited thin Au film. (e) Real space image of the plasmonic lens with a linear polarizer in front of the detector. The orientation of the axis of the polarizer is indicated by the arrow. (f) Real space image of the thin Au film with a linear polarizer in front of the detector. The orientation of the polarizer is indicated by the arrow. The sample is biased to $2.8\,V$ *while the tip is grounded. The setpoint tunnel current is in the range of* $1-6\,nA$*. Acquisition time is* 200 *seconds.*

3.3.2 Fourier space image comparison

Next we compare the angular distribution of the light emitted from a plasmonic lens and a thin Au film when excited by the STM-nanosource. Fourier space image results are shown in Figure 4. Figures 4 (a) and 4 (b) present the schematic illustration of the experiment. In Fig. 4 (c), we see a small and intense doughnut-shaped spot in the center of the Fourier plane. The dotted white circle indicates the numerical aperture (maximum acceptance angle) in Fourier space. A white dashed line passing through the center is drawn and the polar emission pattern obtained along this line is shown in Fig. 4 (e). Here, we see that the emitted light is almost collimated. The angular spread is defined as the half width at half maximum (HWHM) of this intensity profile. From Fig. 4 (e), we measure an angular spread of around $\pm 4°$. Conversely, a wide emission cone is observed for the excitation of SPPs on a thin, planar, gold film. The emitted leakage radiation from SPP-light resonant coupling is measured at the expected leakage radiation angle around $\pm 42.5°$.

If for both kinds of sources, the emission pattern may be modeled as a light cone, the solid angle can be calculated as $\Omega = 2\pi(1-\cos\theta)$, where $2\,\theta$ is the aperture angle of the cone (θ is the angular spread). Thus, the light emitted in the substrate upon electrical excitation of SPPs is characterized by a solid angle of $\Omega = 1.69$ sr for the thin Au film ($\theta = 42.5°$) and 1.38×10^{-2}sr for the plasmonic lens ($\theta = 4°$). Thus, we obtain that the solid angle for the plasmonic lens is more than two orders of magnitude lower than that for the unstructured Au film.

Comparing Figs. 4 (g) and 4 (h) which indicate the situation with the result in Fourier space when a polarizer is placed in front of the camera, we find that in the direction perpendicular to

the polarizer transmission axis, there is no light in both cases. These results confirm that an STM-excited plasmonic lens produces a nearly collimated radially polarized beam of light while in STM-excited thin Au film produces a light cone which is radially polarized.

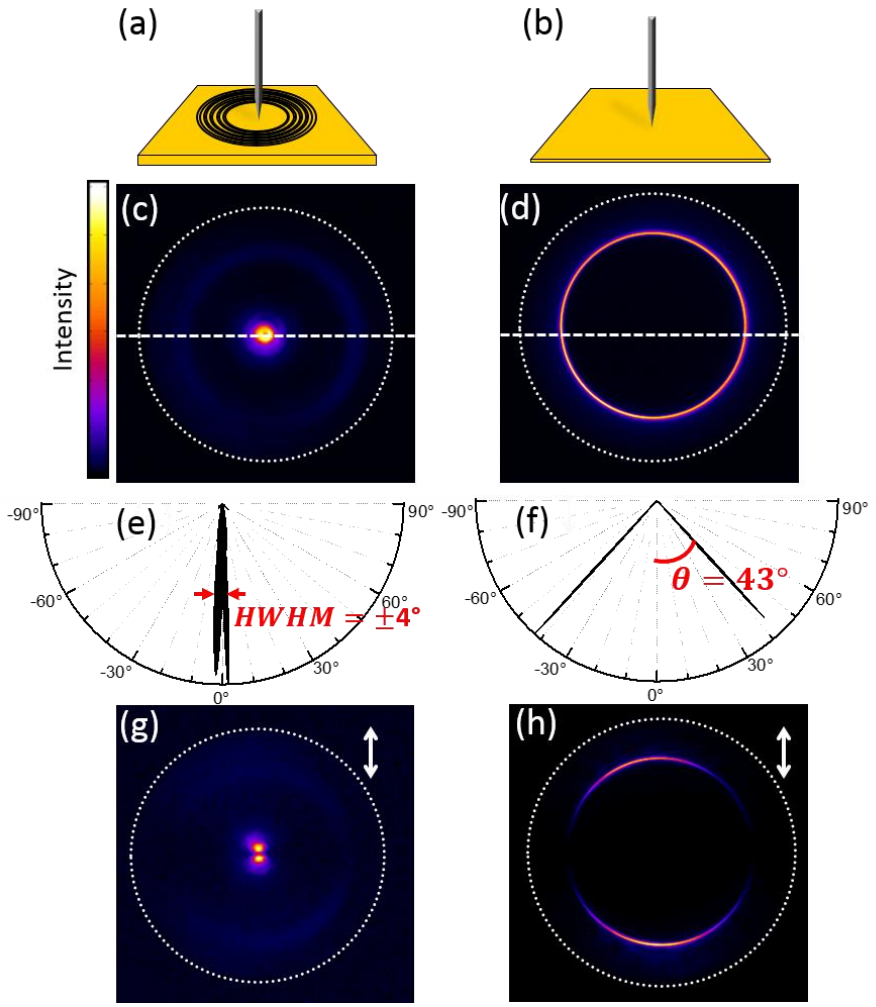

Figure 4. Comparison of the Fourier space images from a plasmonic lens and a thin Au film after STM excitation. (a) and (b) schematically illustrate the two kinds of excited structures and the tip excitation position. (c) Fourier space image from a STM-excited plasmonic lens. (d) Fourier space image from an STM-excited thin Au film. (e) Polar emission pattern obtained from the intensity profile along the white dashed line in (c). (f) Polar emission pattern obtained from the intensity profile along the white dashed line in (d). (g) Fourier space image of the plasmonic lens with a linear polarizer in front of the detector and the orientation of the polarizer transmission axis is indicated by the arrow. (h) Fourier space image of the thin Au film with a linear polarizer in front of the detector. The orientation of the polarizer transmission axis is indicated by the arrow. The sample is biased to $2.8\,V$ *while the tip is grounded. The setpoint tunnel current is in the range of* $1-6\,nA$*. Acquisition time is* 200 *seconds.*

Thus, in this section, we compare the real and Fourier space images obtained when a plasmonic lens and a thin Au film are excited by the inelastic tunnel current from an STM. We find that a nearly collimated radially polarized microsource of light is achieved from the plasmonic lens structure.

3.4 Effect of lens parameters on angular spread

3.4.1 Experimental results

In this section, we discuss the effect of varying the geometrical parameters of the plasmonic lens, namely the inner diameter D, the number of slits N and the slit period P. First, we focus on the experimental dependence of the angular spread of the emitted light beam on these parameters.

Figure 5 (a) shows the variation of the angular spread (HWHM in Fourier image) versus the inner diameter D for three plasmonic lenses of different periods P. The lowest angular spread is systematically achieved for $P = 700\,nm$ as compared to the results with $P = 600\,nm$ and $P = 800\,nm$. This can be generally understood by considering the emission spectrum shown in Fig. 5 (c), which is measured on a thin Au film ($50\,nm$ in thickness). This data gives insight into the energy distribution of the surface plasmon nanosource when the tip is made of tungsten and the sample is made of Au [17], [21]. This distribution exhibits a peak centered at about $\approx 720\,nm$ (photon wavelength in vacuum). The beaming effect from our structure is due to the constructive interference of the light emitted from the slits when the slit period equals the SPP wavelength of around $675\,nm$ (which is calculated from equation (2.20) in chapter 2); therefore, more of the source energy is converted into a collimated light beam when the energy of maximum emission matches the slit period of the plasmonic lens (The detailed wavelength dependence will be discussed later).

The origin of the beamed emission also explains the effect of the number of slits. The experimental Fourier space images are also shown in Fig. 6 for direct observation and comparison. As shown both in Fig. 5 (d) and Fig. 6, the higher the number of slits, the lower the angular spread of the emitted beam. The slits behave as a coherent light source that interferes in the far field; thus, the more numerous these sources, the sharper the features in the

interference pattern. Interestingly, at a fixed inner diameter D, increasing N from 1 to 3 strongly enhances the collimation of the emitted beam, whereas adding another two rings ($N = 5$) yields only subtle improvement. This suggests that near-optimal beaming is achieved for $N = 3$. Indeed, SPP scattering at the slits decreases their propagation length; as a result, the emission from the slits is comparatively low beyond the third one.

Additionally, a general feature emerging from Fig. 5 is that the larger the inner diameter, the better the collimation of the emitted beam and this could also be observed in Fig. 6. The reason is that the wavevector k distribution of the electric field in the far field (whose squared modulus is the Fourier image) is the Fourier transform of its spatial distribution in the sample plane (whose squared modulus is the real plane image). As a consequence, larger structures will have narrower angular radiation distribution. To account for this, we plot in Figs. 5 (b) and 5 (e) the data discussed above as a function of the outer diameter, which is $L = D + 2[(N-1)P + w]$ (w is the width of the slit) and which indicates the actual size of the light source. This way of plotting the data reveals that a single ring structure provides an interesting tradeoff between the dimension of the source and the angular spread of the emitted beam, which may be crucial if integration within a device imposes size requirements and if angular spread is the only criterion for beam collimation. Indeed, the occurrence of secondary lobes (shown in Fig. 6)) in the angular radiation pattern mainly have a strong impact on the performance of the light source, depending on the targeted applications.

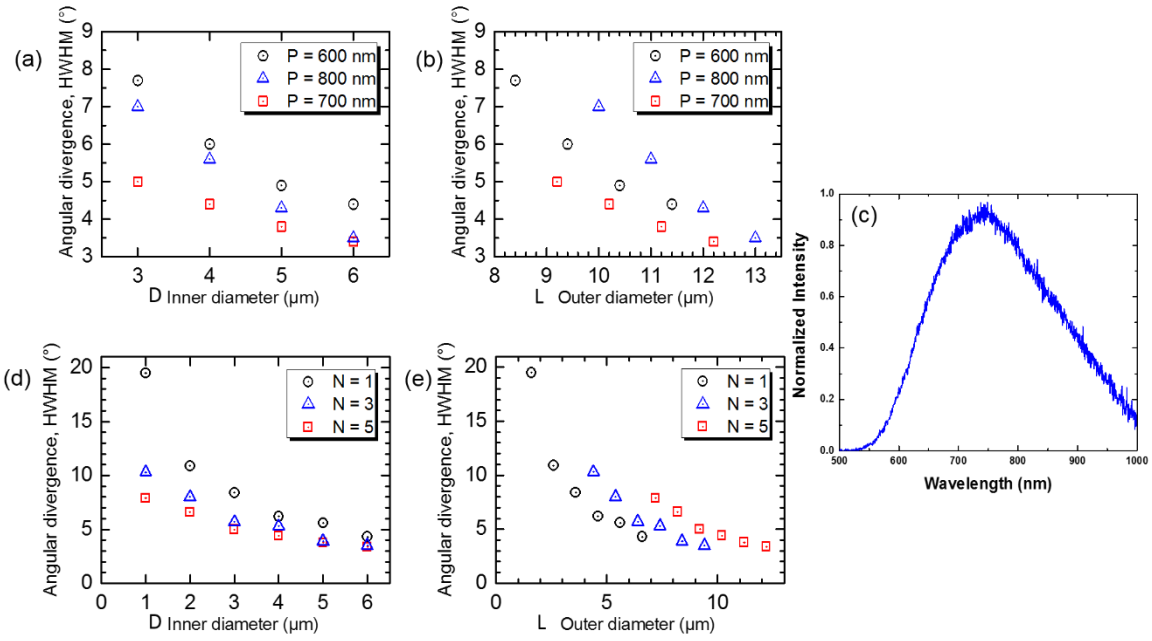

Figure 5. Effect of the geometrical parameters of the plasmonic lenses on the angular spread of their emission. Plasmonic lenses of different inner diameters D, slit grating periods P and numbers of slits N are electrically excited with the STM tip located at the central position. Angular spread is retrieved from the half width at half maximum (HWHM) of the doughnut shaped spot in the Fourier space images and plotted versus either (a, d) the inner diameter D or (b, e) the outer diameter $L = D + 2[(N-1)P + w]$ of the plasmonic lens. (c) Emission spectrum, which spreads over the low-energy part of the visible range and the near infrared. The emission is spectrally centered at $\lambda_0 \approx 700\ nm$. The sample is biased to $2.8\ V$ while the tip grounded. Setpoint tunnel current is in the range of $1 - 6\ nA$.

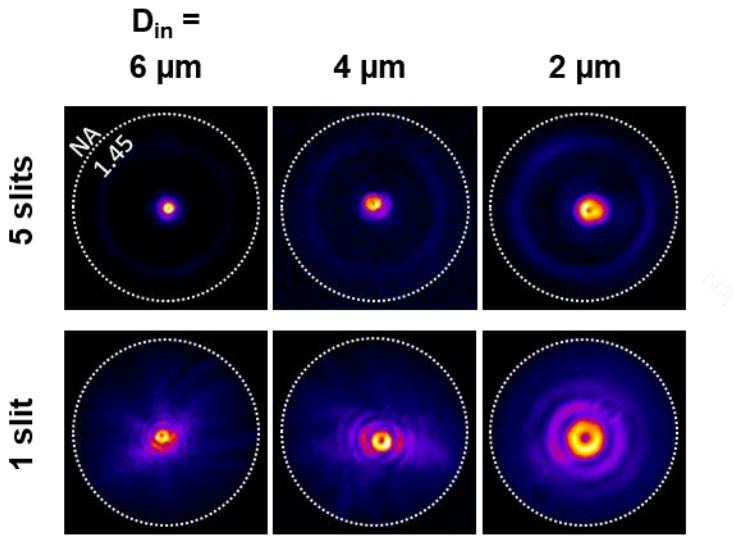

Figure 6. Effect of the inner diameter and the number of the slits in the plasmonic lens. (a) Experimental Fourier space images of the light from a 5 slit circular grating (top row) and a single circular slit (second row) of inner diameters $D = 6\ \mu m, 4\ \mu m$ and $2\ \mu m$, when the STM excitation is centered on the plasmonic lens. The dotted white circular indicates the maximum acceptance angle (NA=1.45).

3.4.2 Simulation results

In the previous subsection, we showed our experimental results demonstrating how the angular spread varies when the structural parameters change. In this subsection, we will show the corresponding simulation results. Our simulations are done by *Aurélien Drezet* at the Institut Néel in Grenoble. In his simulation, he uses an analytical model to determine the Fourier space images from which the theoretical angular spread of the emitted light may be obtained. The

SPP scattering into photons at the slits is modeled as the radiation of a series of electric dipoles located along circles of the same diameter as the circular slits. The complex electric field vector of these dipoles in the far field is calculated. Due to the subwavelength width of the slit, it is assumed that only the in plane radial field component is scattered toward the substrate; hence the dipoles in the model are horizontally oriented along the radial direction. When the excitation is centered, all the dipoles along each circle emit in phase and with the same amplitude. In the model, a relative weight on the contribution of the five circles that exponentially decreases with their diameter is also set.

Figure 7 shows the simulation results of Fourier space images for plasmonic lenses of inner diameters D varying from 1 to 6 μm and consisting of a single slit or a 5 slit grating of period $P = 700\ nm$. This series of images confirms the following: first, the larger the inner diameter, the lower the angular spread; second, for a given D, the angular spread is much lower with five slits than with one.

In addition, Figure 7 reveals the appearance of numerous side lobes around the central lobe at larger emission angle in the case of a single slit structure. For the five slit structure, the emission pattern essentially consists of a single lobe. This is due to the destructive interference of the light emitted from the multiple slits in off axis directions, thus canceling out the side lobes. Hence, if not only low angular spread is required for a specific application, but also the absence of side lobes, then a 5 slit lens is to be favored.

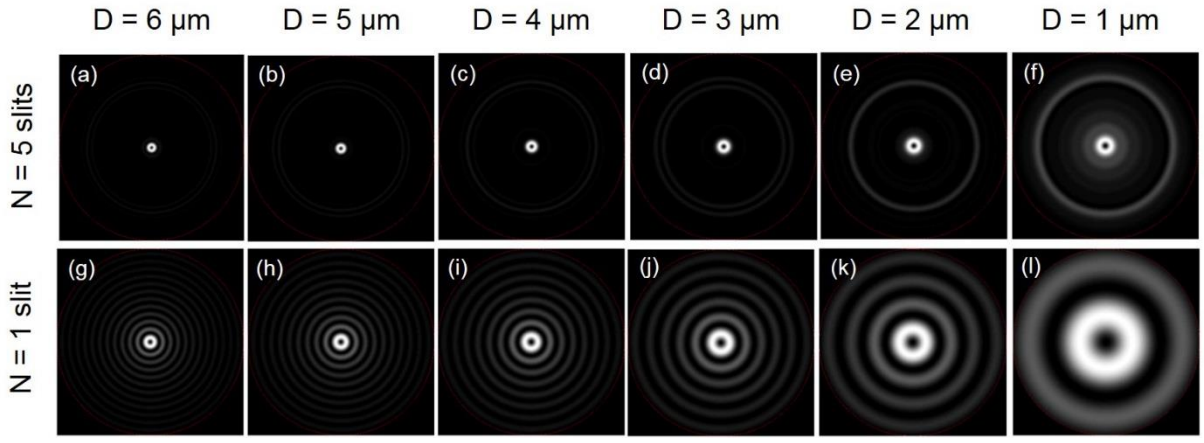

Figure 7. Simulated Fourier space images obtained from a monochromatic dipole excitation ($\lambda_0 = 700\ nm$) for (a to f) a 5 slit and (g to l) a single slit plasmonic lens of inner diameters of 6 to 1 μm. Excitation at the center of the plasmonic lens is assumed. In panels a to f, the slit grating period is $P = 700\ nm$.

Figure 8 shows the good agreement between the experimentally and theoretically obtained angular spread of the light emitted from a 5 slit circular grating and a single circular slit. We see, however, that the simulation overestimates the angular spread for single circular slits with smaller central disk diameters, probably because the width of the slit (not taken into account in the simulation) becomes non-negligible as compared to the diameter of the structure.

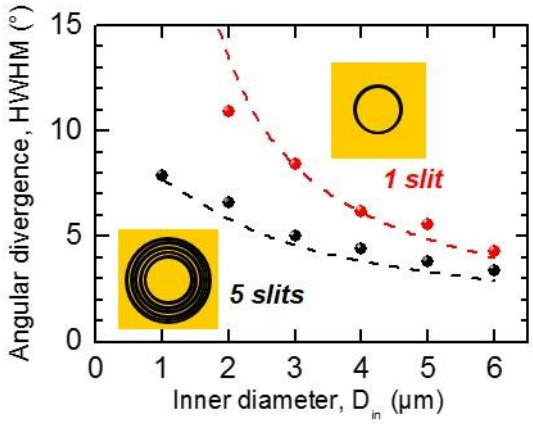

Figure 8. Experimentally and theoretically obtained angular spread of the emission from a 5 slit circular grating and a single circular slit, versus the inner diameter of the central disk D (STM excitation in the center; solid spheres: experimental data; dashed lines: simulation results).

In conclusion, in this section, we have shown how the angular spread depends on the different parameters of the plasmonic lens structure. Good agreement exists between the simulation and experimental results.

3.5 STM excitation is off-centered on the plasmonic lens

3.5.1 Experimental results

In the last two sections, we showed the real and Fourier space image results when the excitation is centered on the plasmonic lens. In this section, we will show the results when the STM excitation is no longer in the center of the lens structure (the experimental results shown here are performed on the “Veeco” setup)

Using the same structure as in section 3.3 ($P = 700\ nm$, $N = 5$, $D = 5\ \mu m$), Figure 9 (a) illustrates the STM excitation experiment with the excitation off-centered and x denotes the radial axis along which the tip position is changed. Fourier space images in Fig. 9 (b)-(e) show the angular distribution of the light emitted below the substrate in the experiment. The lateral position of the STM tip with respect to the center of the disk of the plasmonic lens is varied as $0.5\ \mu m$, $0\ \mu m$, $-1.2\ \mu m$ and $-1.8\ \mu m$ respectively. The corresponding polar emission patterns are shown in Fig. 9 (f)-(i). We also obtain Fourier space images under similar conditions but with a linear polarizer in front of the CCD camera, the polarizer transmission axis is shown by the arrow in Fig. 9 (j)-(m).

When the tip is $0.5\ \mu m$ from the center, the emitted light beam is tilted by $2°$ from the normal and its collimation and radial polarization are preserved (see Figs. 9 (b) and 9 (j)). With the tip at $-1.2\ \mu m$ from the center (Fig. 9 (d)), a tilt of $10°$ is obtained. The beam becomes slightly asymmetric with a minimum angular spread of $\pm 4°$ in one direction and a maximum angular spread of $\pm 6°$ in another. When beam collimation is the desired result, this technique provides a method to electrically generate a narrow beam from a microscale light source, and the ability to control the emission direction within a $0° - 10°$ polar range. Since the structure is symmetrical, we also have $360°$ control azimuthally. However, Fig. 9 (e) reveals that the polarization state is no longer radial when the tip is moved substantially from the center. Since light now is seen in the direction perpendicular to the polarizer transmission axis. This is even more obvious with the tip at $-1.8\ \mu m$ (i.e., only $0.7\ \mu m$ from the inner edge of the first slit). In Fig. 9 (e), the emission is highly divergent, with a strong contribution above the critical angle. As well, the polarization-filtered image of Fig. 9 (m) reveals a quite intricate polarization pattern.

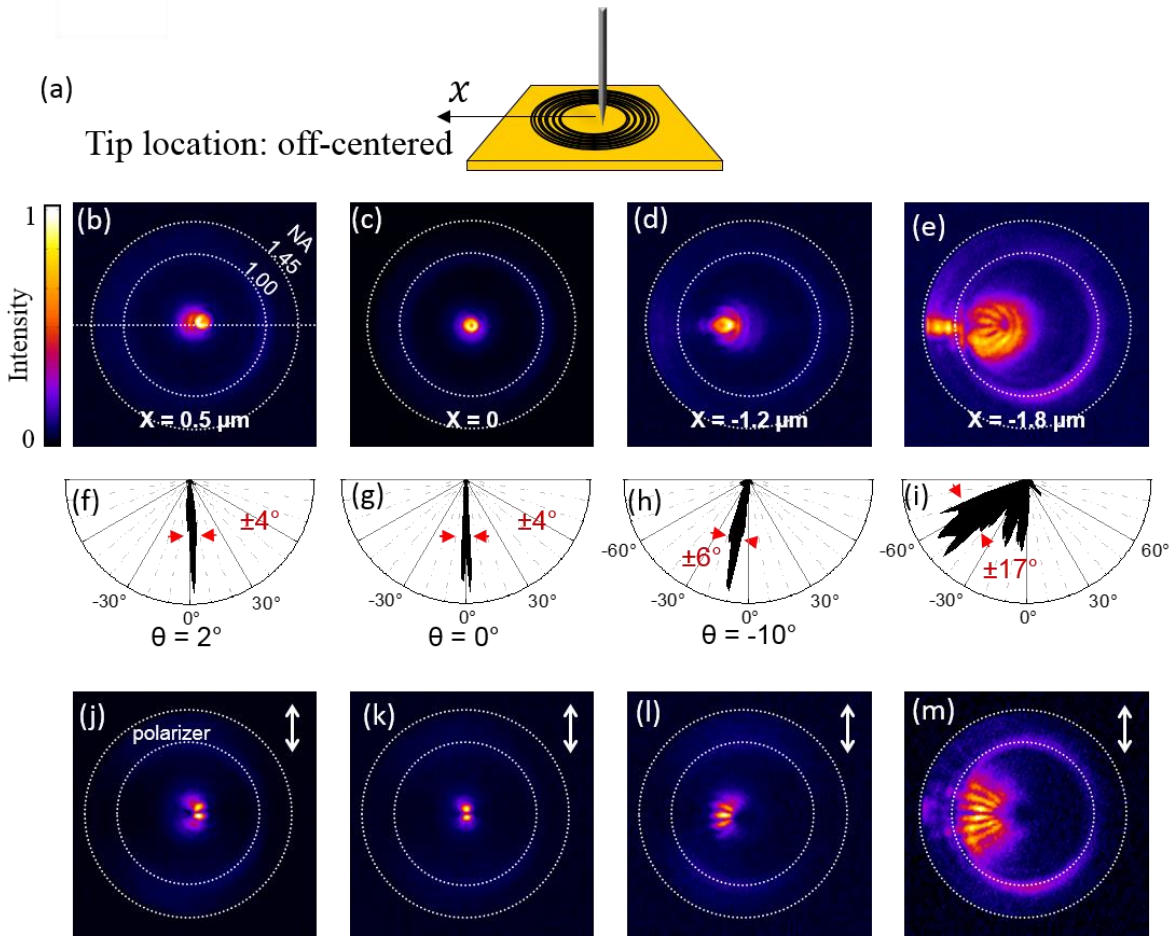

Figure 9. Angular distribution of the emitted light for off-centered excitation. (b)-(e) Fourier space optical images of the light detected from the same 5 slit circular grating plasmonic lens. These results are obtained under the same conditions, but for different lateral positions of the STM excitation on the central disk region. x is the distance from the center of the plasmonic lens. Dotted white circles indicate the maximum acceptance angle ($NA = 1.45 \approx 73°$) and the air/glass critical angle. The polar plot below each Fourier space image is obtained by measuring the intensity profile along the horizontal axis (white dotted line in (b)). In the polar plots (f)-(i) are indicated the polar angle of emission θ and the angular spread of the beam, defined as the HWHM. Parts (j)-(m) are the same as (d)-(e) but filtered with a linear polarizer (the white arrow indicates the transmission axis).

3.5.2 Simulation results

Using the same method described in section 3.4.2, simulated Fourier space images results are calculated by *Aurélien Drezet* to investigate the emitted beam collimation and the radial

polarization for off-center excitation. Figure 10 shows the simulation results for the case of pronounced off-centered excitation, where the effects on the emission properties are obvious. Here, the same structure is used as for the experimental results of Fig. 9. In Fig. 10 (a)-(c), the calculated excitation location is $-1.2\ \mu m$ away from the center. The theoretical Fourier image reveals an intricate angular distribution of the emission, with several lobes instead of the single doughnut shaped spot observed for the tip position close to the center. Theoretical images with a polarization filter also indicate the loss of the radial nature in the emission polarization as in the experimental. In Fig. 10 (d), we examine the case where the STM tip is located closer to the inner edge of the first slit than to the center of the structure (tip is off-centered by $-1.8\ \mu m$). The experimental image Fig. 10 (e) (which is also shown in Fig. 9 (m)), is compared with Fig. 10 (d). We see that the more off-centered the tip, the more intricate the angular and polarization distribution of the emitted light.

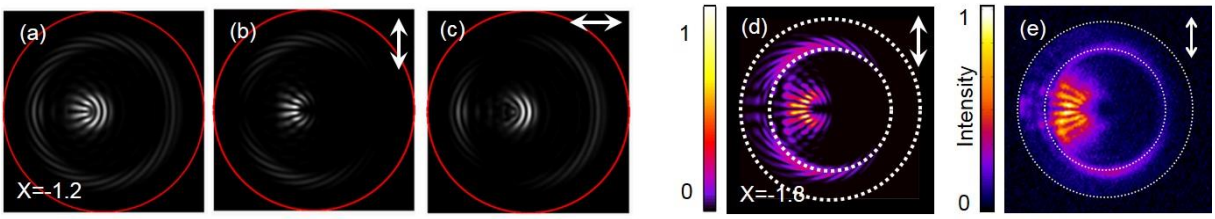

Figure 10. Simulated Fourier space images obtained from a monochromatic dipole excitation ($\lambda_0 = 700\ nm$) for a 5 slit plasmonic lens of inner diameter $D = 5\ \mu m$ and off-centered excitation $x = -1.2\ \mu m$ along the x axis of the plasmonic lens ($x = 0$ is the center of the structure). (a) Intensity image and (b, c) polarization filtered images with the polarizer along (b) the y axis or (c) the x axis. The outer circle (red line) delineates the accessible region of Fourier space. (d) Same as (b) but for $x = -1.8\ \mu m$ and (e) is the corresponding experimental image. The dotted white circles indicate the critical angle at an air-glass interface and the maximum acceptance angle of the objective lens.

In conclusion, in this section, we have shown experimental results when the excitation is off centered on the plasmonic lens. The simulation model also works well for off centered excitation.

3.6 Angular spread as a function of wavelength

In this section, we will investigate the angular spread as a function of emission frequency/wavelength for a certain plasmonic lens structure.

The observation of the beam collimation seen above seems surprising since electrical SPP excitation by inelastic electron tunneling is known to be broadband [22] (see chapter 2); thus, the phase condition mentioned above is only met for a narrow part of the emission spectrum while the full spectrum of the collected light is used to obtain the Fourier image shown in Fig. 11 (a) (It is the same experiments as in Fig. 4 (a), here shown again for easy comparison). The system formed by a tungsten tip and an Au film with a junction bias of $V = 2.8\,V$ is known (see Fig. 5 (c)) to produce an emission maximum with a photon wavelength around $\lambda_0 = 720\,nm$ ($\approx 1.7\,eV$ in energy) and a full-width-half-maximum (FWHM) of $\Delta\lambda_0 \approx 200\,nm$ ($\approx 0.5\,eV$) [18]. Nevertheless, we demonstrate below that the spectral response of the excitation is advantageously broad, thus preserving this beaming effect for a large portion of the power spectrum of the electrical SPP source. In our study, we investigate the spectral response of the plasmonic lens for a broadband wavelength range $\lambda_0 \approx 550 - 1000\,nm$.

Figure. 11 (c)-(j) separately show the spectrally filtered Fourier space images acquired with bandpass filters in front of the camera. The filters have the following central wavelengths/bandwidths: $550/88\,nm$, $600/14\,nm$, $650/13\,nm$, $700/13\,nm$, $750/40\,nm$, $800/40\,nm$, $850/40\,nm$, $900/40\,nm$. The plasmonic lens is the same as the one used in Fig. 11 (a) and the STM excitation is again located in the center of the structure. Intensity profiles taken from the Fourier space images are shown below each image as a polar emission plot. For these images, light is collected using an oil objective lens of $NA = 1.45$ on the "Veeco" setup.

From Fig. 11 (c)-(j), we see that all the images of this series exhibit a doughnut-shaped spot centered on the Fourier space origin; yet the size of this spot varies as a function of the detection wavelength. The spot is smallest for a detection wavelength of $700\,nm$. As well, the polar plots below the images show that the angular spread is the largest at the extrema of the investigated spectra range.

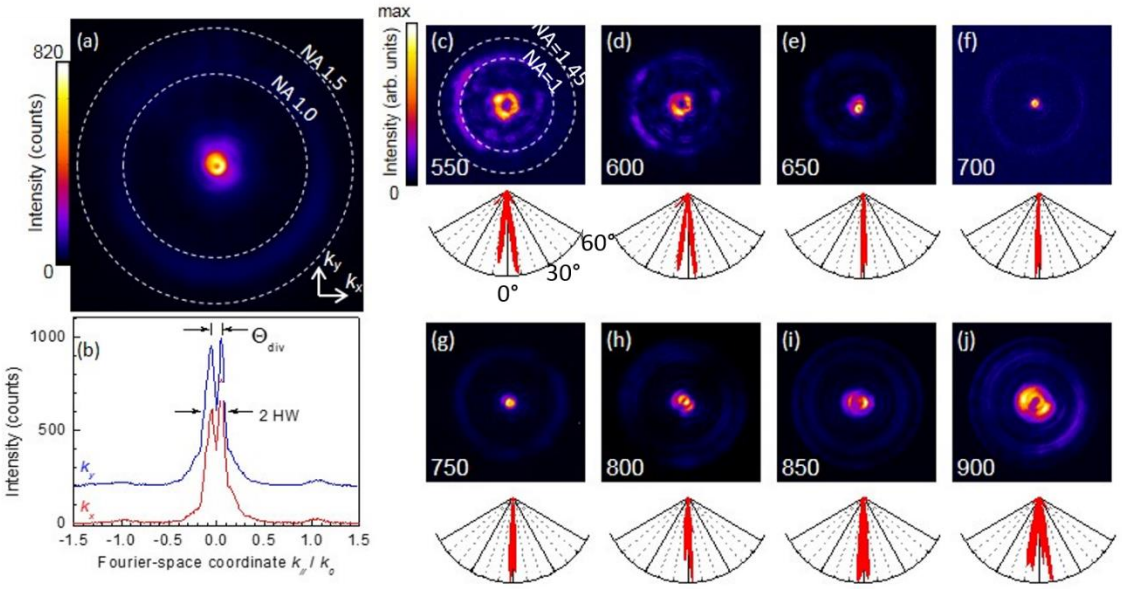

Figure 11. Imaging the angular emission pattern at different energies for an STM-excited plasmonic lens. (a) Fourier space optical image, revealing the angular emission pattern in the substrate. The plasmonic lens is a five slit circular grating period with $700\ nm$ *and inner diameter* $5\ \mu m$ *(For this image, light is collected using an oil objective lens of* $NA = 1.49$*. The STM bias is set at* $2.8\ V$*, the current setpoint is* $6\ nA$ *and the acquisition is* $600\ s$*). (b) Intensity profiles taken from the Fourier image in (a), along the direction of the Fourier space vector* k_x *and* k_y*. The profile along* k_y *is vertically offset for clarity. The Fourier space coordinates (*$k_{\parallel}$ *stands for* k_x *or* k_y*) are normalized by the wavevector corresponding to the spectral peak wavelength in free space* k_0*. (c)- (j) Spectrally filtered Fourier space images. The collected light is filtered using bandpass filters that have the following central wavelengths/bandwidths: (c)* $550/88\ nm$*, (d)* $600/14\ nm$*, (e)* $650/13\ nm$*, (f)* $700/13\ nm$*, (g)* $750/40\ nm$*, (h)* $800/40\ nm$*, (i)* $850/40\ nm$ *and (j)* $900/40\ nm$*. Intensity profiles taken from the Fourier images are shown below each image in a polar plot. For these images, light is collected using an objective lens of* $NA = 1.45$ *and the acquisition time is* $300\ seconds$*.*

From Fig. 11, we see that the smallest angular spread angle occurs for a collection wavelength of $700\ nm$ for the plasmonic lens whose period P equals $700\ nm$. To investigate if this is the case for other structures, we perform another series of experiments with different bandpass filters for plasmonic lenses whose periods equal $P = 600\ nm$ and $P = 800\ nm$, and with an inner diameter of $D = 6\ \mu m$. All the experimental parameters are the same as before

(Fig. 11 (c)-(j)). Figure 12 and Fig. 13 separately show the filtered Fourier space images for different collection wavelengths.

Figure 12 (a)-(h) are the corresponding Fourier space images with different bandpass filters for the $P = 600\ nm$ structure. From this data, we can determine that the smallest angular spread occurs around a wavelength range near $600\ nm$. For a wavelength far away from $600\ nm$, we see that the angular spread is clearly larger.

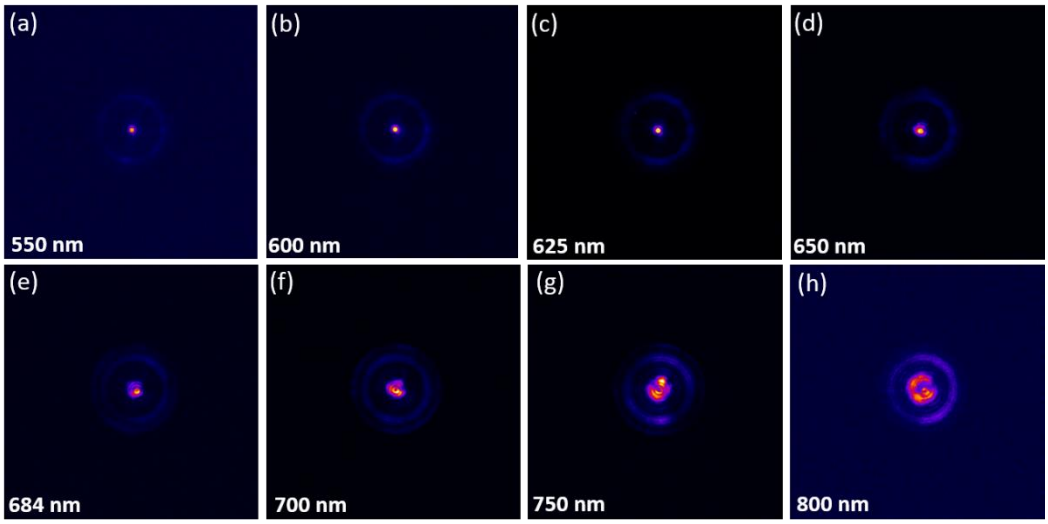

Figure 12. Spectrally filtered Fourier space optical image for a plasmonic lens of $P = 600\ nm$ *and inner diameter* $D = 6\ \mu m$. *The collected light is filtered using bandpass filters that have the following central wavelengths/bandwidths: (a)* $550/88\ nm$, *(b)* $600/14\ nm$, *(c)* $625/26\ nm$, *(d)* $650/13\ nm$, *(e)* $684/24\ nm$, *(f)* $700/13\ nm$, *(g)* $750/40\ nm$ *and (h)* $800/40\ nm$. *The STM bias is set at* $2.8\ V$, *the current setpoint is* $6\ nA$. *For these images, light is collected using an objective lens of* $NA = 1.45$ *and the acquisition time is* $300\ seconds$.

Similarly, Figure 13 (a)-(h) are the corresponding Fourier space images with different bandpass filters for the $P = 800\ nm$ structure. From these, we can determine that the smallest angular spread occurs around a wavelength range near $800\ nm$. For shorter wavelengths, we see that the angular spread become larger.

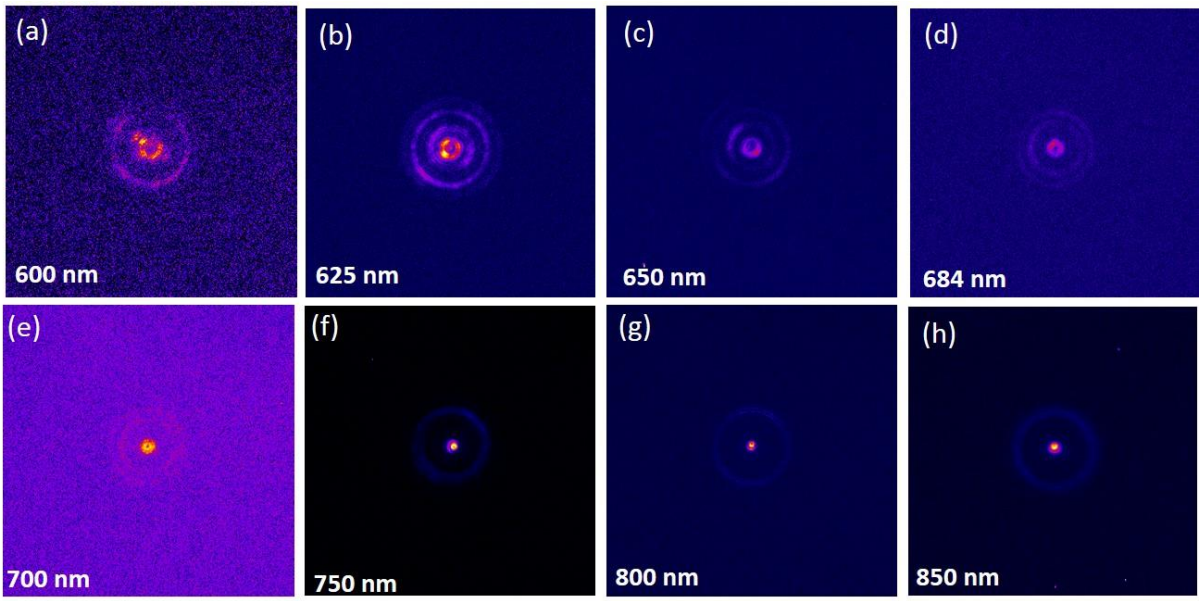

Figure 13. Spectrally filtered Fourier space optical image for a plasmonic lens of $P = 800\ nm$ *and inner diameter* $D = 6\ \mu m$. *The collected light is filtered using bandpass filters that have the following central wavelengths/bandwidths: (a)* $600/14\ nm$, *(b)* $625/26\ nm$, *(c)* $650/13\ nm$, *(d)* $684/24\ nm$, *(e)* $700/13\ nm$, *(f)* $750/40\ nm$, *(g)* $800/40\ nm$ *and (h)* $850/40\ nm$. *The STM bias is set at* $2.8\ V$, *the current setpoint is* $6\ nA$. *For these images, light is collected using an objective lens of* $NA = 1.45$ *and the acquisition time is* $300\ s$.

To confirm these observations, we determine the angular spread of the light beam from the Fourier space images (Fig. 11, Fig. 12 and Fig.13), and plot it versus the emission wavelength as shown in Fig. 14 (b)-(d). Taking the structure with a period of $700\ nm$ as an example, from Fig. 11 (c)-(j), the angular spread minimum is found to be 3.2° at the collection wavelength $\lambda_0 = 700\ nm$. For the energy corresponding to a photon wavelength of $\lambda_0 = 700\ nm$ in vacuum, the SPP wavelength on an ideal smooth Au/air interface is $\lambda_{SPP} \approx 675\ nm$, which is indeed close to the period of the circular slit grating. Interestingly, the angular spread remains lower than 4° within a $100\ nm$ wide wavelength range around $700\ nm$, and lower than 7° until $\lambda_0 = 850\ nm$. In order to explain this effect, we use a simple two slit interference model (see details below) to determine the spectral dependence of the angular spread.

Figure 14 (a) illustrates the principle of the simple $2D$ scalar model used. We consider only two adjacent slits, which scatter the incoming SPPs into light in the substrate, and model these slits as two coherent point sources, separated by the slit grating period P. The emission from these two points sources is assumed isotropic in the glass. Thus, the light in the far field is

expected to be the most intense at an angle where constructive interference occurs between the waves emitted from the two slits. Consequently, a maximum in the emission of light in the direction orthogonal to the interface only occurs if the two source are in phase, i.e., $P = \lambda_{SPP}$. Otherwise, SPPs will preferentially scatter in the direction where the optical path difference in glass δ compensates the phase shift between the two sources. Within this simple representation, we assume that the energy dependent SPP wavelength is that of SPPs propagating on the interface between infinite Au and vacuum half spaces. This reads as:

$$n'_{SPP}P - n_g\delta = \lambda_0 \quad (3.1)$$

where $n_g = 1.52$ is the refractive index of the glass substrate, λ_0 is the photon wavelength in vacuum, and n'_{SPP} is the effective index (for more details see chapter 5) of the SPPs propagating at the Au/air interface. n'_{SPP} is defined as the real part of the wavevector ratio between SPPs and photons in vacuum, as follows:

$$n'_{SPP} = \sqrt{\frac{\varepsilon'_m}{\varepsilon'_m+1}} = \frac{Re(k_{spp})}{k_0} \quad (3.2)$$

Where, we discussed in chapter 2, ε'_m and ε''_m are the real and imaginary parts of the dielectric constant of the metal respectively. This expression holds for $|\varepsilon''_m| \ll |\varepsilon'_m|$. Equivalently, $n'_{SPP} = \lambda_0/\lambda_{SPP}$. From equation (3.1), we see that constructive interference occurs at condition of θ for:

$$n_g sin\theta = \frac{\lambda_0}{\lambda_{spp}} - \frac{\lambda_0}{P} \quad (3.3)$$

Only first order diffraction is considered here. Consequently, SPPs interfere constructively in the forward direction if $P > \lambda_{SPP}$, and in the backward direction if $P < \lambda_{SPP}$. Now come back to the $3D$ problem where SPPs scatter on the circular slits and, as a first step, we ignore the effects of the finite size of the slit grating. Thus, we find that the emitted beam has the shape of a cylinder in the far field only if $P = \lambda_{SPP}$. If $P \neq \lambda_{SPP}$, the emitted beam has the shape of a cone in the far field, with a beam angular spread angle θ given by equation (3.3). Figure 14 (b)-(d) show the results of this simple model (see red line) along with the experimental data for the three different slits grating periods mentioned above: $P = 700, 600,$ and $800\ nm$.

As a second step, we introduce in the model the effect of the finite size of the slits grating by including a lower bound to the angular spread. Within the far-field approximation (Fraunhofer diffraction), the radiation pattern from the source has an angular spread Δk limited

by the source size L through the relation $L\Delta k \gtrsim 2\pi$. Here, light is emitted from the slits etched in the thick Au film; thus the source L is the outer diameter of the N slits circular grating, i.e., $L = D + 2(N-1)P + 2w$, where w is the slit width. Light is mainly emitted orthogonally to the Au film, i.e., along the optical axis of the microscope; therefore, Δk is equivalent to the width of the doughnut shaped spot observed in the Fourier space images. The above relation thus leads to a lower bound for the angular spread of the emitted beam from the plasmonic lens:

$$Ln_g sin\theta k_0 \gtrsim 2\pi \quad (3.4)$$

Then we can get:

$$\theta \gtrsim \arcsin\left(\frac{\lambda_0}{n_g L}\right) \quad (3.5)$$

Equation (3.5) is also plotted in Fig. 14 (b)-(d) (black solid line). The simple model based on equation (3.3) and equation (3.5) reproduces the main trends of the experimentally determined spectral dependence of the angular beam divergence sufficiently. Thus the desired optimum operating frequency range and size of the plasmonic lens as well as the required angular spread may be simply obtained by choosing specific geometric design parameters (inner diameter, grating period, number of slits). Such simple control over the plasmonic lens characteristic is crucial for its future integration with a broadband excitation nanosource. Neither the model nor the spectrally filtered Fourier space images (which are not intensity normalized with respect to each other) provide the power spectrum of the emitted light versus its angular distribution, however. To obtain this key information, angle-resolved optical spectroscopy is necessary where the angular and spectral dependence are revealed in one single image.

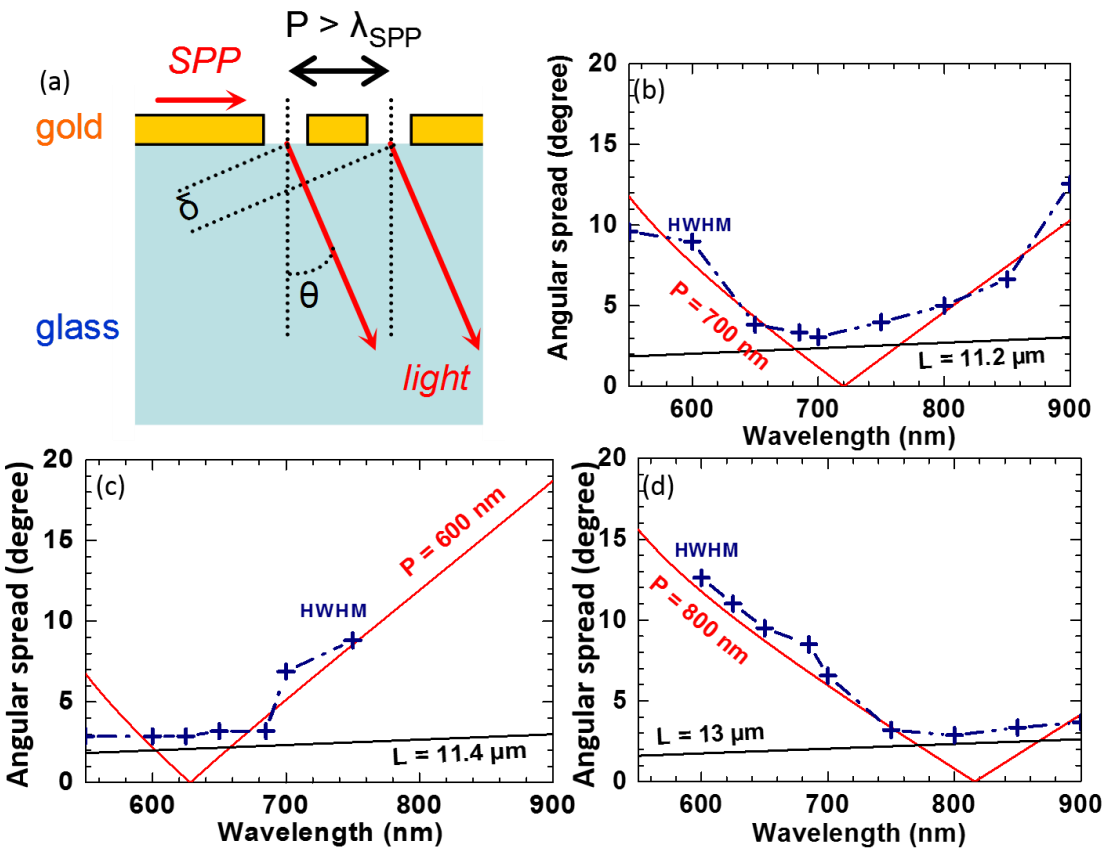

Figure 14. Spectral variation of the angular beam divergence: a simple model and the experimental results. (a) Sketch of the scattering of SPPs into light at two slits etched in a thick Au film on glass. The SPPs propagate from the left hand side of the figure. The light emitted in the substrate from the two slits interferes constructively in the direction denoted by the angle θ. δ is the optical path difference for the light emitted at θ at the two slits. If the period P of the slit grating is longer than the SPP wavelength λ_{SPP}, then the SPPs scattered into light interfere constructively in the forward direction. For $P < \lambda_{SPP}$, constructive interference is in the backward direction. Only first order diffraction is considered here. (b)-(d) The experimental values of the angular spread measured for three different five-slit circular gratings are compared with the angle of constructive interference θ (red line) calculated using the model shown in (a). (b) The grating period is $P = 700\ nm$, (c) $P = 600\ nm$ and (d) $P = 800\ nm$. Angular spread is measured from the filtered Fourier space images in Fig. 11, Fig. 12 and Fig. 13. The theoretical lower bound for the angular beam divergence due to the finite size of the slit grating is shown by the black line. L is the outer diameter of the plasmonic lens.

3.7 Angularly resolved spectral imaging of the light emitted from an STM-excited plasmonic lens

Aangularly-resolved spectral imaging is possible with our imaging spectrometer on the "JPK" setup (see in chapter 2). Figure 15 shows the setup for conducting angularly resolved spectral imaging. This technique is introduced here and will be used again in chapter 5.

Thanks to an added mirror (see Fig. 15), the emitted light is diverted from the optical axis to the imaging spectrometer (iHR320 spectrometer with a CCD detector). An extra lens (see Fig. 15) has the same focal length and position with respect to the tube lens and spectrometer as the mentioned extra lens in front of the Andor camera when it used for Fourier space imaging on the Andor camera (see Fig. 19 in chapter 2). Thus the Fourier space image will be projected on the entrance slit of the spectrometer. Concave mirrors inside the imaging spectrometer will reflect the light to the grating. When the zero order of the grating is used, the light will be directly reflected as in the case of a mirror and the CCD camera will record the Fourier space image (just as it is projected on the entrance slit).

However, with non-zero grating orders, light will be dispersed and each line perpendicular to the long axis of the entrance slit, representing a position in Fourier space, will be spectrally resolved. The relative position of the projected image is adjusted so that the light entering the entrance slit of the spectrometer is from a line along k_y and crosses the Fourier space origin. Thus, the CCD camera of the spectrometer will display an image with wavelength and Fourier-space coordinates along the horizontal and vertical axes, respectively. When the system exhibits axial symmetry with respect to the optical axis, the angular dependence of the emitted pattern is only radial (not azimuthal); therefore, all information about the energy-momentum dispersion (within the investigated energy range) is contained in the images shown in Fig. 16.

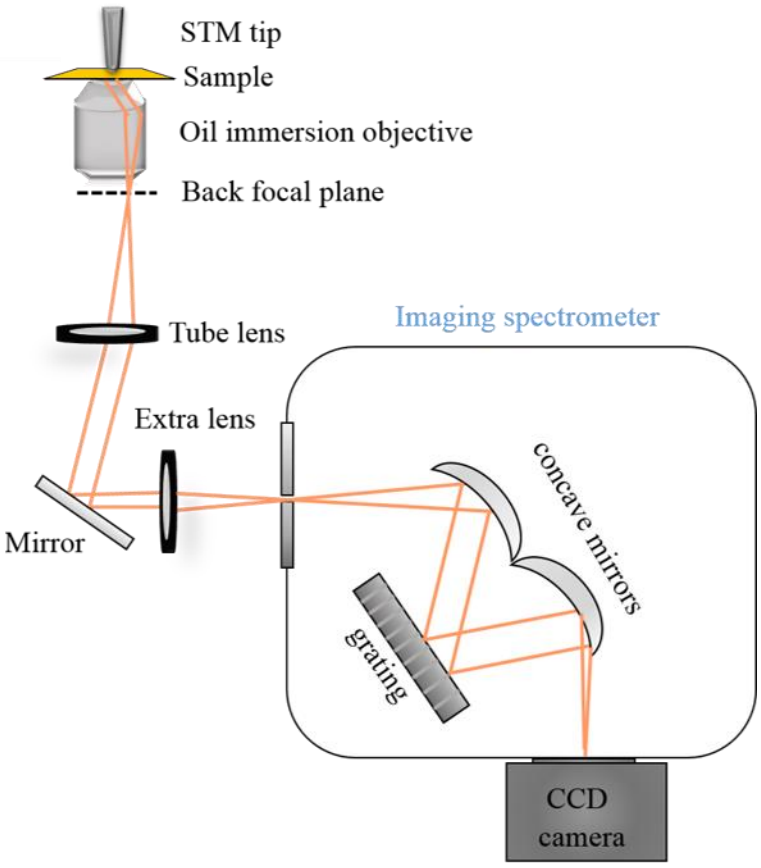

Figure 15. Schematic illustration of the experimental setup for obtaining angularly resolved spectral images.

In Fig. 16 (a), we use a thin $50\ nm$ Au film on glass to calibrate the vertical axis (k_y/k_0) of the Fourier space images. The ring from SPPs leakage radiation (see image on the left) occurs at an angle that is theoretically known from the SPP's dispersion relation ($\frac{k_{SPP}}{k_0} \approx 1.037$ for $\lambda_0 = 700\ nm$). In Fig. 16 (b)-(e), we analyze the light emitted from three different plasmonic lenses under the same excitation conditions as in Fig. 11. These structures are five slit circular gratings, with an inner diameter of $D = 4\ \mu m$ but with different grating periods ($P = 600, 700,$ and $800\ nm$), and a single circular slit with $D = 5\ \mu m$, all etched on in a $200\ nm$ thick Au film on glass.

The general aspect of the energy momentum dispersion image for all four structures may be easily understood by drawing an analogy to Young's double-slit experiment. In the case of a single circular slit, we may assume that the light detected in one direction $k_{\parallel}/k_0$ in Fourier

space results from the interference of the light emitted from two opposite point sources on the slits. Thus, a periodic fringe pattern is expected in Fourier space, with a period varying as the emission wavelength over the slit diameter [23]. This is indeed what is observed in Fig.16 (e).

In a five-slit circular plasmonic lens, five fringe patterns of different periods superimpose in Fourier space and coherently interfere with each other (which we already discussed in section 3.4). Constructive interference in the emission direction orthogonal to the grating only occurs if the slit period is a multiple of the emission wavelength. This explains why the shape of the energy momentum dispersion images seen in Fig. 16 (b)-(d) varies with wavelength and why these bow ties shift in energy as the slit grating period is changed. The angular divergence is lowest and the light emitted in the substrate is most intense at the center of the bow tie. Around this energy value, the angular divergence and the radiated power remain almost constant (and at their optimal values) for a $\approx 0.3\ eV$ wide range.

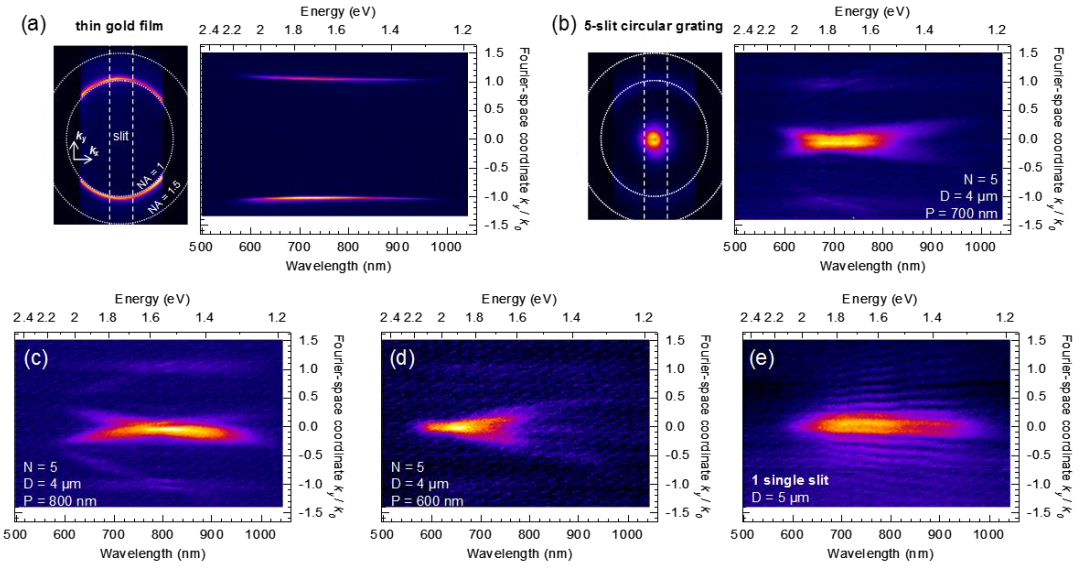

Figure 16. Angle resolved spectroscopy: method and results. Angular and spectral distribution of the light emitted upon STM excitation of (a) an unstructured $50\ nm$ *Au film on glass, (b)- (d) a five-slit plasmonic lens of inner diameter* $D = 4\ \mu m$ *and period (b)* $P = 700\ nm$*, (c)* $P = 800\ nm$*, and (d)* $P = 600\ nm$*, and (e) a single circular slit of inner diameter* $D = 5\ \mu m$*, etched in a* $200\ nm$ *Au film on glass. These experimental data are measured by projecting the Fourier space image of the emitted light on the partly closed entrance slit of the spectrometer. The STM bias is set at* $2.8\ V$*, the current setpoint is at* 3 *to* $4\ nA$ *and the acquisition time is* $300\ s$*. On the left of (a) and (b) are the Fourier space images that are obtained when the spectrometer entrance slit is at its largest width and the image is acquired using the zeroth*

order of the diffraction grating (acquisition time: $100\ s$*). Dashed lines indicate the selected area when the entrance slit is partially closed for spectral measurements.*

We can now explain why the angular spread obtained from the full spectrum Fourier space images shown in Fig. 11 (a) is very close to its lowest value despite the spectral broadness of the electrical SPP nanosource. Two main effects determine the angular beam divergence of our electrical light microsource: the spectral width of the SPP nanosource and the finite size of the structure at which SPPs scatter into light. When the latter dominates over the former, the angular beam divergence remains almost constant over the emission spectrum. Thus the size of the plasmonic microstructure should be decreased to the smallest possible diameter where the angular width of the emitted beam is not limited by the size effect.

Beyond this point, further downsizing of the plasmonic microstructure is inefficient, since it broadens the angular distribution of the emitted light without improving the matching between the spectral response of the plasmonic structure and the power spectrum of the SPP nanosource. Obtaining optimal light beaming while keeping the smallest possible spatial footprint thus requires that the spectral width and size effects contribute equally to the angular beam divergence of the source. From equations (3.3) and equation (3.5) for small $\theta \approx 0$, we evaluate the contributions of these two effects at $\Delta\lambda_0/(n_g P)$ and $\lambda_0/(n_g L)$ respectively, where $\Delta\lambda_0$ and λ_0 are the spectral width and central wavelength of the source (P and L are the period and outer diameter of the slit grating and n_g is the substrate's refractive index). The best tradeoff between narrow light beaming and small spatial footprint is thus obtained when using a plasmonic lens with period to size ratio $P/L \approx \Delta\lambda_0/\lambda_0$.

The data shown in Fig. 16 (b) and 16 (e) also reveal the advantages and drawbacks of increasing the number of slits N of the structure. From Fourier space images, we evaluate the angular divergence of the light beam emitted from the five slits circular grating ($D = 4\ \mu m$ and $P = 700\ nm$) and the single circular ($D = 4\ \mu m$) at 4.4° and 5.6°, respectively (data shown in Fig. 6). Therefore, the latter structure, which is almost half the size of the former ($5.6\ \mu m$ in outer diameter, as compared to $10.2\ \mu m$), has an angular beam divergence that is only $\approx 25\%$ higher. Moreover, using one circular slit rather than five extends the energy range for which optimal beaming and power radiation are obtained. However, the emission pattern obtained from a single circular slit exhibits multiple secondary lobes of non-negligible intensity, which

persist within all the investigated energy range. This off-axis emission represents an important power loss for a light beam source. Furthermore, in an applied context, cross talk issues may occur when several of these sources are used to transfer information to distinct receptors. In this regard, a multiple slit structure is advantageous.

A feature that all images in Fig. 16 have in common is the strong damping of the radiated power at an energy higher than about $2.1\ eV$ (i.e., $\lambda_0 \lesssim 590\ nm$). This is due to the losses in tungsten and Au, i.e., the metals of which the STM tip and the plasmonic lens are made. Generally, the power spectrum of the emission radiated from a tunnel junction is modeled as the product of a source term given by inelastic tunneling statistics ($\propto(eV - \hbar\omega)$, for $\hbar\omega \leq eV$; 0 otherwise [24]) and an emission term related to the local density of electromagnetic states (*EM*-LDOS) [25]. As a result, the radiation has a broad power spectrum that spreads over the infrared and part of the visible range and falls to zero at energy eV (quantum cutoff). Still, the power spectrum radiated by a W-Au tip surface junction is known to rapidly fall beyond $2.1\ eV$ in energy, even when the tunnel junction is biased at $V = 2.8\,V$. This is notably ascribed to interband transitions in gold. In the system that we study here, the dissipative losses in gold play a double role, since they decrease the power emitted by the SPP nanosource and they shorten the SPP propagation length, thus yielding higher propagation losses before SPP scattering from the slits into light in the far field.

3.8 Spectral response: coupling of cavity modes and grating effects

In this section, we discuss spectra obtained using the configuration in Fig. 15 with integrating over the CCD lines before readout (i.e., the signal is integrated over emission angles). In this way, we focus on the total emitted power. Figure 17 (a) shows optical spectra measured for different *single* circular slits with different inner diameters D. The spectra shown in Fig. 17 (a) differ from that of an unstructured thin Au film (a Gaussian pattern see Fig. 5 (c))); instead, they exhibit peaks and dips. When varying the inner diameter D, the peaks and dips shift in energy; therefore, it is unlikely that these features are due to a resonance inside the gap of the slit (the slit width w is always the same). Thus, we infer that the features seen in Fig. 16 (a) are related to the cavity modes of the plasmonic structures, i.e., SPP standing waves formed due to SPP reflection at the circular slit back to the center of the structure.

In order to confirm the origin of the features observed in the experimental spectra, *Jean-Jacques Greffet* from Institut d'Optique and my colleague *Eric le Moal* did a simple calculation to get the "generated" spectra shown in Fig. 17 (b). In this calculation, generated data is obtained in the following way using the simple model illustrated in Fig. 18. With the notations introduced in Fig. 18 (b), where r is the complex amplitude reflection coefficient at the cavity boundary and k_{spp} is the SPP wavevector, the field at the source location satisfies the following system of equations.

$$A^+ = rA^- \exp\left(ik_{spp}D\right) + A^i \qquad (3.6)$$

$$A^- = rA^+ \exp\left(ik_{spp}D\right) + A^i \qquad (3.7)$$

Thus, the field at the source location reads:

$$A^+ = A^- = \frac{A^i}{1 - r\exp\left(ik_{spp}D\right)} \qquad (3.8)$$

The generated data shown in Fig. 17 (b) corresponds to the featureless spectrum measured upon STM excitation of SPPs on an unstructured thin Au film, spectrally weighted by the squared modulus of the electric field calculated using equation (3.8) for $D = 3, 4, 5$ and 6 μm. In the model, $|r| = 0.4$ and $\arg r = \pi$ are used since the result best fits the experimental data. The asterisks indicating the spectral position of the peaks in Fig. 17 (a) are reproduced in Fig. 17 (b) in order to highlight the agreement between the generated and experimental data.

The model used above is very simplistic since it does not describe the out of plane SPP to photon scattering at the slit; nevertheless, the generated data reproduces the number of peaks, their spectral position and spectral width quite well. The main discrepancy is that the model underestimates the low-energy region of the spectrum, which may be due to the frequency dependent SPP scattering efficiency at the slit. All together, these observations confirm the role played by the cavity modes of the central disk in the spectra response of a single circular slit plasmonic lens upon STM excitation.

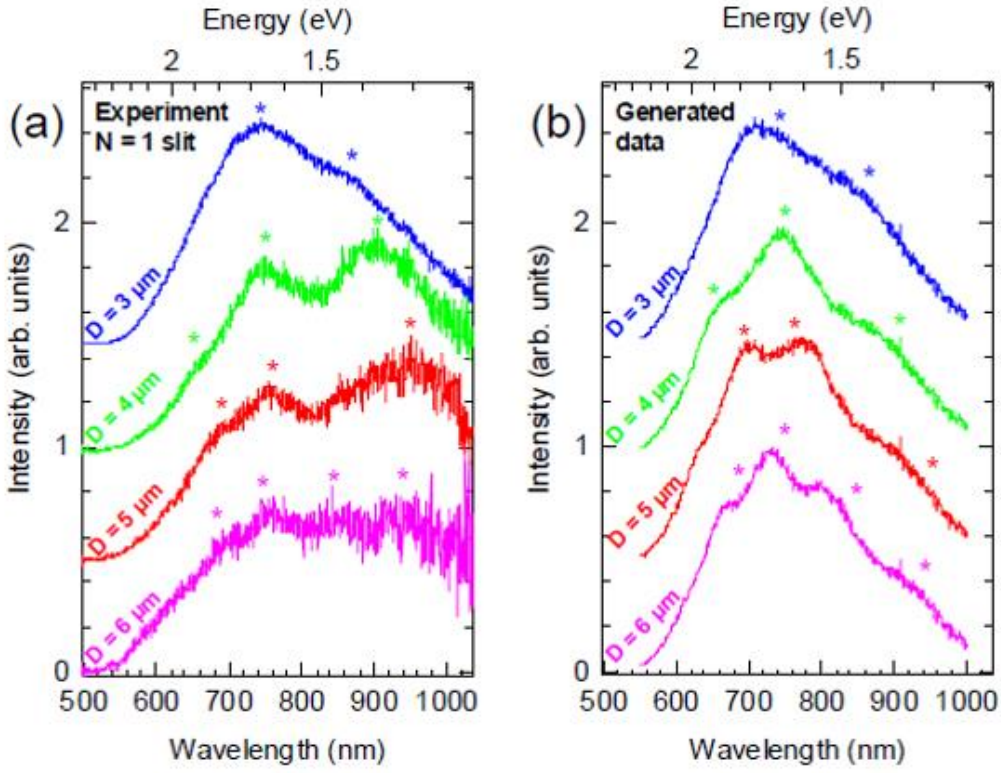

Figure 17. Electrical excitation of a single circular slit: effect of the inner diameter on the spectrum. (a) Spectral distribution of the light emitted upon STM excitation of a single ($N = 1$) circular slit of different inner diameter D, etched in a $200\ nm$ *thick Au film on glass. All spectra are corrected for the spectral response of the instrument, which includes the transmission of the microscope objective, the scattering efficiency of the diffraction grating and the quantum efficiency of the CCD camera used in the spectrometer see chapter 2 section 2.7 (the spectra are vertically offset for clarity).(b) Generated spectra, obtained by multiplying two terms: (i) the squared modulus of the electric field theoretically produced by a point source in one dimension SPP cavity of length D and (ii) the experimental data measured on a thin (*$50\ nm$*) unstructured Au film (see Fig. 5 (c)). The electric field in the SPP cavity is calculated using a simple model described in the text, where the SPP source is located at the center of the cavity. In this model, we use the leakage radiation spectrum measured on the thin Au film as the power spectrum of the SPP source (this is why the generated data shown in (b) exhibits experimental noise). The STM bias is set at* $2.8\ V$*, the current setpoint is* 3 *to* $4\ nA$ *and the acquisition time is* $300\ s$.

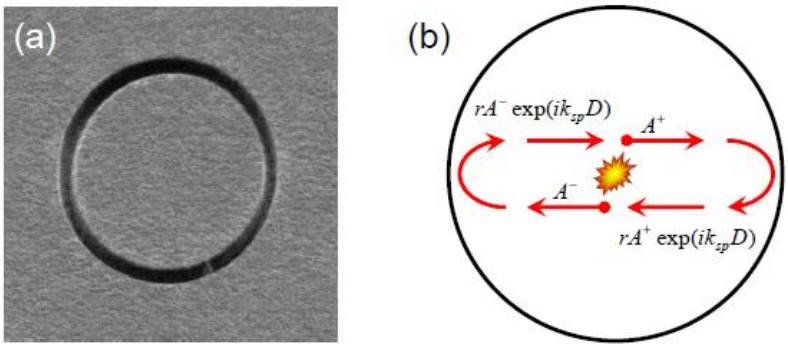

Figure 18. (a) Scanning electron micrograph of a single circular slit plasmonic lens of diameter $D = 5\ \mu m$*. (b) Schematic explanation of the model used to calculate the electric field produced by a point source in an SPP cavity.*

Adding four slits and varying the slit period significantly changes the spectral response of the plasmonic structure, even though the inner diameter D is kept constant (see Fig. 19 (c)). As well, if P remains the same and D is modified (see Figs. 19 (a) and 19 (b)), the peak and dip positions, relative height, and width vary. Since here the detected light is integrated over all the collected angles, the spectral dependence of the emitted light that is observed as a function of slit grating period and diameter cannot be due to the phenomenon seen in Fig. 16. Instead, it is attributed to the effect of the lens parameters on the *EM*-LDOS. Namely, the power of the light beam emitted from the plasmonic lens must be sensitive to the *EM*-LDOS at the position of the SPP nanosource.

The role of the circular slit grating in the spectral response of the plasmonic lens is two fold. The grating, which surrounds the central disk, reflects parts of the outgoing SPP wave back to the center of the disk, and also scatters part of the SPP wave into light in the out of plane direction. Thus, the slit grating and the central disk cavity are coupled through the frequency dependent Fresnel coefficients of the grating. The intensity of the light emitted from the slits depends on both the scattering coefficient of the grating and the intensity of the incident SPPs; the latter, however, depends on the SPP mode density in the central disk cavity, which in turn is determined by the complex amplitude reflection coefficient of the slit grating. Depending on frequency, this grating-cavity coupling may have a strong enhancing or quenching effect on the spectral response of the plasmonic lens.

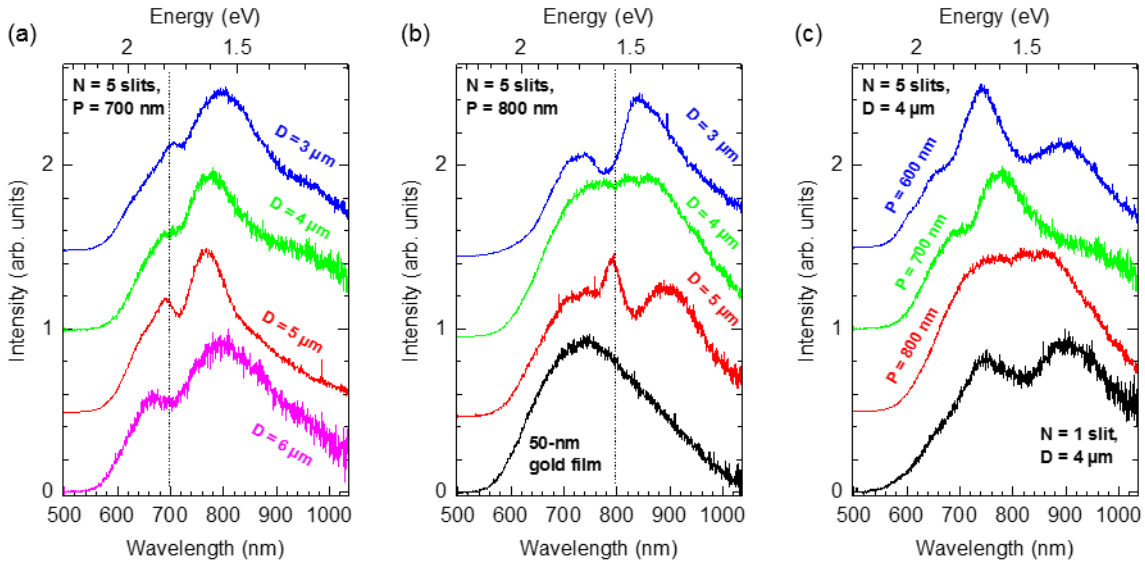

Figure 19. Radiated power spectra: effect of the plasmonic lens parameters. Spectral distribution of the light emitted upon STM excitation of five-slit circular gratings of different inner diameters D and periods P, etched in a $200\ nm$ gold film on glass. The spectral dependence on D with (a) $P = 700\ nm$ and (b) $P = 800\ nm$ is examined (a vertical dotted line indicates $\lambda_0 = P$ to guide the eye). In (c), the effect of varying P while keeping D fixed is studied. For comparison purpose, the spectra obtained for an unstructured $50\ nm$ gold film and for a single ($N = 1$) circular slit etched in a $200\ nm$ gold film are also plotted in (b) and (c) (black lines), respectively. All spectra are corrected for the spectral response of the instrument which is discussed in chapter 2. Spectra are vertically offset for clarity. The bias of STM is set at $2.8\ V$, the current setpoint is 3 to $4\ nA$ and the acquisition time is $300\ s$.

3.9 Conclusion

In conclusion, in this chapter, we demonstrate an electrically driven, microscale light source emitting radially polarized beams at very low angular spread ($\pm 4°$). The basis of this light source is a plasmonic lens, whose SPPs are locally excited through the inelastic tunneling of low-energy electrons from the tip of an STM. The STM-nanosource is ideal for plasmonic structures with radial symmetry. Furthermore, this excitation method may be integrated with current microelectronic technology, since it requires only low voltage ($< 3V$), low current (nA), and may be adapted on a chip as a planar tunnel junction.

We have also shown that in order to optimize the divergence of such a light source, the grating period should match the wavelength of maximum emission of the STM excitation, the

plasmonic lens should consist of at least 3 slits, and the STM excitation must be in the center of the plasmonic lens.

Finally, we also introduce a novel experimental method combining STM, optical microscopy, and optical imaging spectroscopy for carrying out angle-resolved optical spectroscopy measurements. We characterize the spectral response of the plasmonic lens and find that our plasmonic lens is very attractive for building an electrically driven microsource of highly collimated light since its spectral response is broad and optimal within a wide energy range ($650 - 850\ nm$), especially in comparison to other resonant plasmonic structures such as Yagi-Uda nanoantennas [26].

[1] S. Cao *et al.*, "Revealing the spectral response of a plasmonic lens using low-energy electrons," *Phys. Rev. B*, vol. 96, no. 11, p. 115419, 2017.

[2] S. Cao, E. Le Moal, E. Boer-Duchemin, G. Dujardin, A. Drezet, and S. Huant, "Cylindrical vector beams of light from an electrically excited plasmonic lens," *Appl. Phys. Lett.*, vol. 105, no. 11, p. 111103, 2014.

[3] S. Cao *et al.*, "Using a plasmonic lens to control the emission of electrically excited light," in *Proceedings of SPIE, the Interneational Society for Optical Engineering*, 2016, vol. 33, no. 9884, p. 98841Y.

[4] Y. Q. Fu and X. L. Zhou, "Plasmonic Lenses: A Review," *Plasmonics*, vol. 5, no. 3, pp. 287–310, 2010.

[5] Z. Liu, J. M. Steele, W. Srituravanich, Y. Pikus, C. Sun, and X. Zhang, "Focusing Surface Plasmons with a Plasmonic Lens," *Nano Lett.*, vol. 5, no. 9, pp. 1726–1729, 2005.

[6] W. Chen, D. C. Abeysinghe, R. L. Nelson, and Q. Zhan, "Plasmonic lens made of multiple concentric metallic rings under radially polarized illumination," *Nano Lett.*, vol. 9, no. 12, pp. 4320–4325, 2009.

[7] J. M. Steele, Z. Liu, Y. Wang, and X. Zhang, "Resonant and non-resonant generation and focusing of surface plasmons with circular gratings," *Opt. Express*, vol. 14, no. 12, p. 5664, 2006.

[8] A. Yanai and U. Levy, "Plasmonic focusing with a coaxial structure illuminated by radially polarized light," *Opt. Express*, vol. 17, no. 2, p. 924, 2009.

[9] P. Wróbel, J. Pniewski, T. J. Antosiewicz, and T. Szoplik, "Focusing radially polarized light by a concentrically corrugated silver film without a hole," *Phys. Rev. Lett.*, vol. 102, no. 18, p. 183902, 2009.

[10] S. Yue, Z. Li, J. Chen, and Q. Gong, "Ultrasmall and ultrafast all-optical modulation based on a plasmonic lens," *Appl. Phys. Lett.*, vol. 98, no. 16, p. 161108, 2011.

[11] W. Yu *et al.*, "Computational Study of Influence of Structuring of Plasmonic Nanolens on Superfocusing," *Plasmonics*, vol. 6, no. 1, pp. 35–42, 2011.

[12] Y. C. Jun, K. C. Y. Huang, and M. L. Brongersma, “Plasmonic beaming and active control over fluorescent emission,” *Nat. Commun.*, vol. 2, p. 283, 2011.

[13] M. G. Harats *et al.*, “Full spectral and angular characterization of highly directional emission from nanocrystal quantum dots positioned on circular plasmonic lenses,” *Nano Lett.*, vol. 14, no. 10, pp. 5766–5771, 2014.

[14] J. T. Van Wijngaarden, E. Verhagen, A. Polman, C. E. Ross, H. J. Lezec, and H. A. Atwater, “Direct imaging of propagation and damping of near-resonance surface plasmon polaritons using cathodoluminescence spectroscopy,” *Appl. Phys. Lett.*, vol. 88, no. 22, p. 221111, 2006.

[15] F. J. García De Abajo, “Optical excitations in electron microscopy,” *Rev. Mod. Phys.*, vol. 82, no. 1, pp. 209–275, 2010.

[16] Y. Uehara, Y. Kimura, S. Ushioda, and K. Takeuchi, “Theory of Visible Light Emission from Scanning Tunneling Microscope,” *Jpn. J. Appl. Phys.*, vol. 31, no. 8, pp. 2465–2469, 1992.

[17] Y. Zhang *et al.*, “Edge scattering of surface plasmons excited by scanning tunneling microscopy,” *Opt. Express*, vol. 21, no. 12, pp. 13938–48, 2013.

[18] T. Wang, E. Boer-Duchemin, Y. Zhang, G. Comtet, and G. Dujardin, “Excitation of propagating surface plasmons with a scanning tunnelling microscope,” *Nanotechnology*, vol. 22, no. 17, p. 175201, 2011.

[19] P. Bharadwaj, A. Bouhelier, and L. Novotny, “Electrical excitation of surface plasmons,” *Phys. Rev. Lett.*, vol. 106, no. 22, p. 226802, 2011.

[20] A. Drezet *et al.*, “Leakage radiation microscopy of surface plasmon polaritons,” *Mater. Sci. Eng. B*, vol. 149, no. 3, pp. 220–229, 2010.

[21] T. Wang *et al.*, “Temporal coherence of propagating surface plasmons,” *Opt. Lett.*, vol. 39, no. 23, pp. 6679–6682, 2014.

[22] P. Johansson, “Light emission from a scanning tunneling microscope: Fully retarded calculation,” *Phys. Rev. B*, vol. 58, no. 16, p. 16, 1998.

[23] T. Wang *et al.*, “Plasmon scattering from holes: From single hole scattering to Young’s

experiment," *Nanotechnology*, vol. 25, no. 12, p. 125202, 2014.

[24] D. Hone, B. Mühlschlegel, and D. J. Scalapino, "Theory of light emission from small particle tunnel junctions," *Appl. Phys. Lett.*, vol. 33, no. 2, pp. 203–204, 1978.

[25] K. Joulain, R. Carminati, J. P. Mulet, and J. J. Greffet, "Definition and measurement of the local density of electromagnetic states close to an interface," *Phys. Rev. B*, vol. 68, no. 24, p. 245405, 2003.

[26] H. F. Hofmann, T. Kosako, and Y. Kadoya, "Design parameters for a nano-optical Yagi-Uda antenna," *New J. Phys.*, vol. 9, no. 217, pp. 1–12, 2007.

Chapter 4

Controlling the direction and angular spread of light beams using an STM-excited elliptical plasmonic lens

In this chapter, we investigate the interaction between an STM-based nanosource of SPPs and an elliptical plasmonic lens. We focus on controlling the direction and angular spread of the emitted light by varying the parameters of the elliptical plasmonic lens.

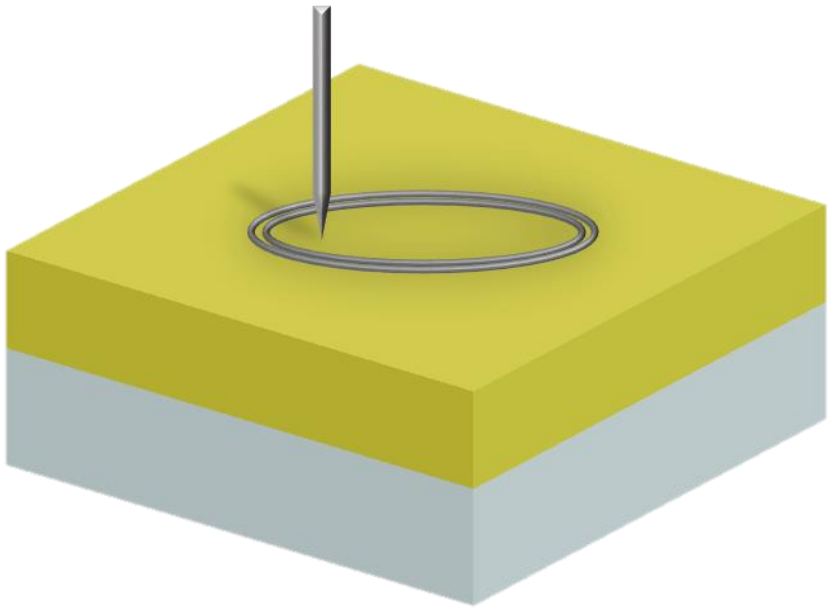

4.1 Introduction

Other important aspects of the transportation of light, apart from speed, include direction and spatial angular spread i.e., the angular width of the beam. These two properties play important roles in describing optical phenomena with nanostructures. Usually, directional and collimated light emission is preferable. Directional means that the light propagates along a certain direction. Collimated light is light whose rays are parallel and therefore the light spreads minimally as it propagates.

So far, many nanostructures have been reported for the creation of directional light emission e.g., Yagi-Uda nanoantennas [1], single cylindrical nanoantennas [2], and single split-ring resonators [3]. Although these structures can achieve directional light emission, they still have some disadvantages, such as the fact that the light emission from these structures has a large angular spread.

The emission of collimated light from nanostructures has been demonstrated. In 2002, Lezec et al., showed that an illuminated "bull's eye" could produce a beaming of light [4]. After that, there was an upsurge in the study of collimated light beams in the field of nano-optics. Several different kinds of structures and methods were proposed to get collimated light beams [5]–[7]. However, few of them provided collimated *and* directional light emission.

In the last chapter, we showed that for a circular plasmonic lens, by moving the excitation position, we control the direction of the emitted light. But there still exists an important drawback for this technique: when our STM excitation moves far off-centered, close to the slits, the collimation is degraded and the angular spread becomes large ($> \pm 17°$).

In this chapter, we propose a novel method to control the direction of collimated light beams by using an elliptical plasmonic lens.

In 2005, Zhang's group showed that an elliptical plasmonic lens can focus SPPs in a way that is similar to a circular plasmonic lens [8]. Later, Lerman et al., demonstrated that upon illumination of an elliptical plasmonic lens with radially polarized light, the electric field distribution on the lens as detected by a SNOM is dependent on the eccentricity of the elliptic structure [9]. In 2012, Schoen et al., used an elliptical cavity as a broadband unidirectional parabolic antenna [10]. They reported that with such an elliptical cavity, directional light emission is achieved.

Inspired by the elliptical cavity which is able to achieve directional light emission, in our work, we use the STM tip to electrically excite different elliptical plasmonic lenses and thus obtain directional collimated light. Interestingly, the elliptical plasmonic lens in our case behaves as an elliptical antenna which can simultaneously direct and collimate light. Different from the elliptical cavity [10], they collected the scattered light emission from the edge of the elliptical cavity in the air but in our case, we collect scattered light from the elliptical slit in the bottom part through the glass substrate.

4.2 Sample preparation

Our elliptical plasmonic lenses are prepared by etching a *single* elliptical shape slit on thick Au film (thickness of $200\ nm$) on an ITO-coated glass substrate using Focused Ion Beam (FIB) etching. The gold film is thick enough to prevent SPP leakage radiation in the glass substrate and the only source of light is the scattering of SPPs into photons at the elliptical slit. Note that as the *elliptical* plasmonic lens mentioned in this chapter only have a single elliptical slit unlike the *circular* plasmonic lens discussed in chapter 3 which have up to 5 slits. So that the fabrication is easier.

Figure 1 (a) is a schematic image of the sample and it shows the definitions of various parameters. D_1 is equal to the minor axis ($2b$) and D_2 is the length of the major axis ($2a$) of the elliptical structure. The etched width w is equal to $300\ nm$. We study different structures with different diameters D_2. The values of D_1 and w are constant. By changing the length of D_2, we get elliptical plasmonic lenses with different eccentricities. Figure 1 (b) shows the SEM image of one structure with $D_1 = 3\ \mu m$,$D_2 = 8.77\ \mu m$ and its eccentricity is calculated as 0.94.

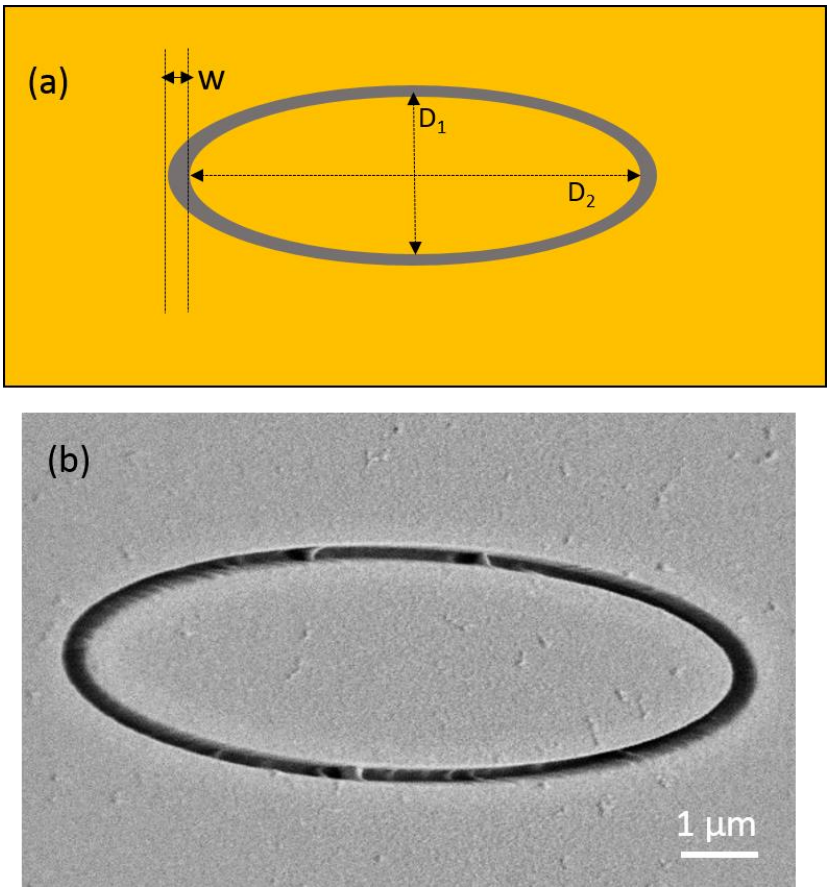

Figure1. Elliptical plasmonic lens. (a) Schematic image of a sample and definition of the parameters. D_1 is equal to the minor axis and D_2 is the major axis of the elliptical structure. (b) SEM image of a structure with $D_1 = 3\ \mu m$,$D_2 = 8.77\ \mu m$. The eccentricity of this structure is 0.94.

4.3 Excitation at a focal point of an elliptical plasmonic lens: collimated light beam

From the previous chapter, we know that the STM excitation of a circular plasmonic lens at its center yields a beam of light whose direction is along the optical axis. This is because the optical path from the center to any point of the circular slit is the same. Thus, SPPs emitted from the center scatter into light at the slit edge in phase. But now, for the elliptical plasmonic lens, when the excitation is centered, since the scattered light along the slit is not in phase, the light emission pattern is expected to change.

We use a circular slit structure with $D_1 = D_2 = 3\ \mu m$ as a reference and an elliptical slit structure with $D_1 = 3\ \mu m$, $D_2 = 8.77\ \mu m$ (see Fig. 1 for the SEM image) is chosen to see the results when excitation is centered on the structure.

Figure 2 (a) schematically depicts the STM excitation centered on a circular plasmonic lens and the experimental result in Fourier space is shown in Fig. 2 (c). In Fig. 2 (c), we see the expected small, intense, doughnut shape spot in the center and since there is only one slit, secondary light rings are present in the Fourier space image. The intensity profile taken along the white dashed line in Fig. 2 (c) is shown in a polar plot in Fig. 2 (e). These results have already been discussed in chapter 3.

Figure 2 (b) shows an illustration of the STM excitation centered on the *elliptical* plasmonic lens and the resulting Fourier space image is presented in Fig. 2 (d). Compared with Fig. 2 (c), now we see a completely different pattern in Fourier space with separated bright spots. It is a more complicated pattern and we will discuss this pattern later in Appendix A. The intensity profile taken along the white dashed line in Fig. 2 (d) is shown in a polar plot in Fig. 2 (f).

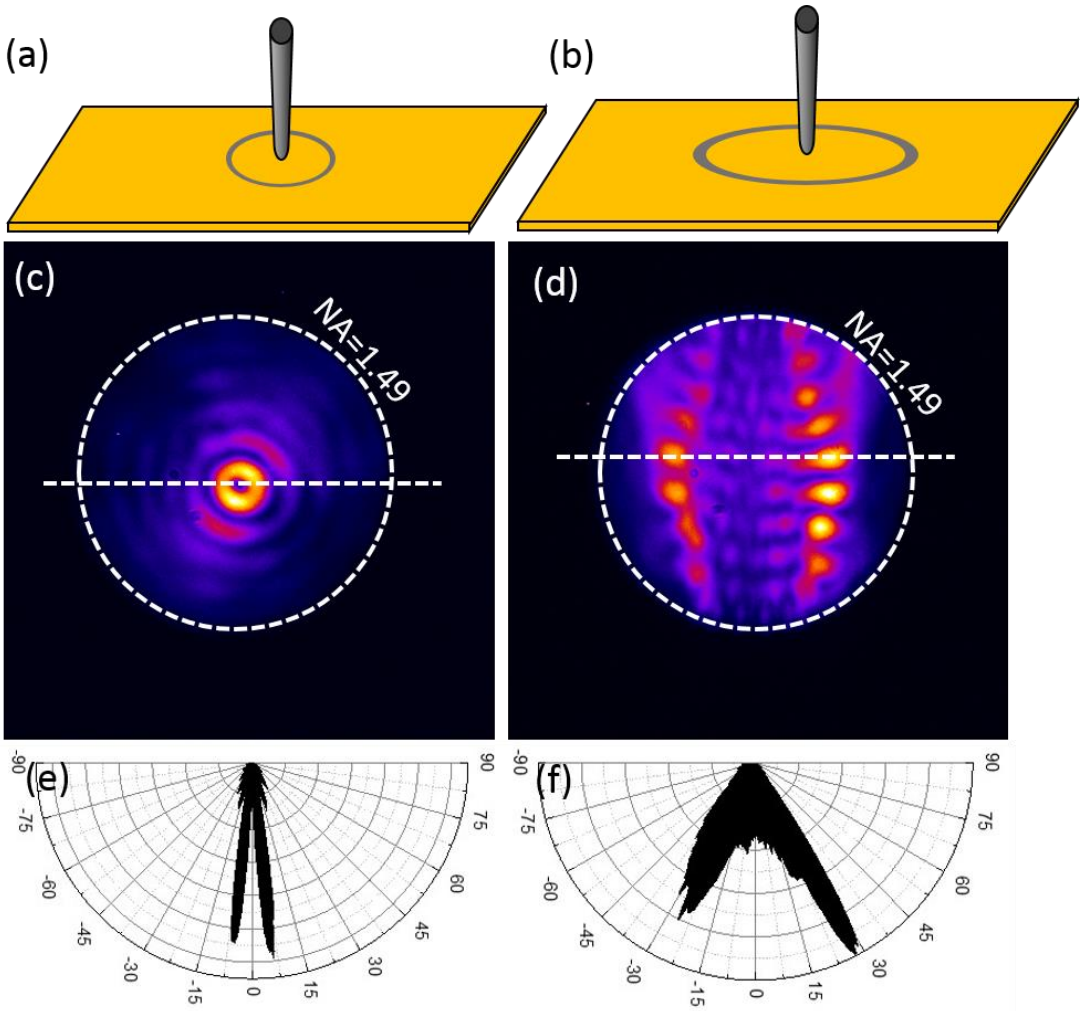

Figure 2. (a-b) Schematic diagram of the tip centered on the circular and elliptical slits. Centered STM excitation of circular and elliptical plasmonic lens with dimensions (a) $D_1 = D_2 = 3\ \mu m$ *and (b) the elliptical slit has* $D_1 = 3\ \mu m, D_2 = 8.77\ \mu m$*. (c-d) Fourier space images when the STM excitation is centered on the slit structures. (e-f) The intensity profile taken along the white dashed lines in (c) and (d) are separately shown in a polar plot. This experiment is performed on the "JPK" setup. The Fourier space image is acquired during 300 seconds. STM bias is set at* $2.8\ V$ *and the setpoint current is* $1\ nA$*.*

For the elliptical plasmonic lens, due to the fact that the light from scattered SPPs is not in phase when the excitation originates from the center, there is not a single direction in which all the light scattered from the slit constructively interferes; therefore, we do not get unidirectional light emission. Then, we move our excitation to the right focal point as depicted in Fig. 3 (a)

and Fig. 3 (c) shows the resulting Fourier space image. The experimental parameters are kept the same as in Fig. 2. In Fig. 3 (c), we see a very intense elliptical spot. This result indicates that the majority of light emitted at this angle constructively interferes; as a result, we get light emission with a low angular spread.

To further explore the beam from an STM-excited elliptical slit, the intensity profile taken along the white dashed line in Fig. 3 (c) is shown in a polar plot in Fig. 3 (e). From Fig. 3 (e), we see that light is emitted in a particular direction, in contrast to Fig. 2 (f). Additionally, compared with Fig. 2 (e) which shows a $0°$ emission angle with regard to the optical axis, now the emission angle is measured at $\approx 38°$. The emission angle is measured as shown in Fig. 2 (e): the red dashed line indicates the position of the center spot. The emission angle θ is measured as the angle of the red dashed line with respect to $0°$ corresponding to the optical axis.

In the same way, we move our excitation to the left focal point of the same elliptical plasmonic lens to observe the same phenomenon of directional light emission with low angular spread. Figure 3 (b) is a schematic of the experiment and Fig. 3 (d) shows the resulting Fourier space image. From Fig. 3 (d), we get a similar pattern as in Fig. 3 (c) except that it points toward the opposite direction. The intensity profile taken along the white dashed line in Fig. 3 (d) is shown in a polar plot in Fig. 3 (f). It also shows the collimated light emission and the measured emitted angle is around $39°$. The emission angle is annotated in Fig. 3 (f) as $-\theta$.

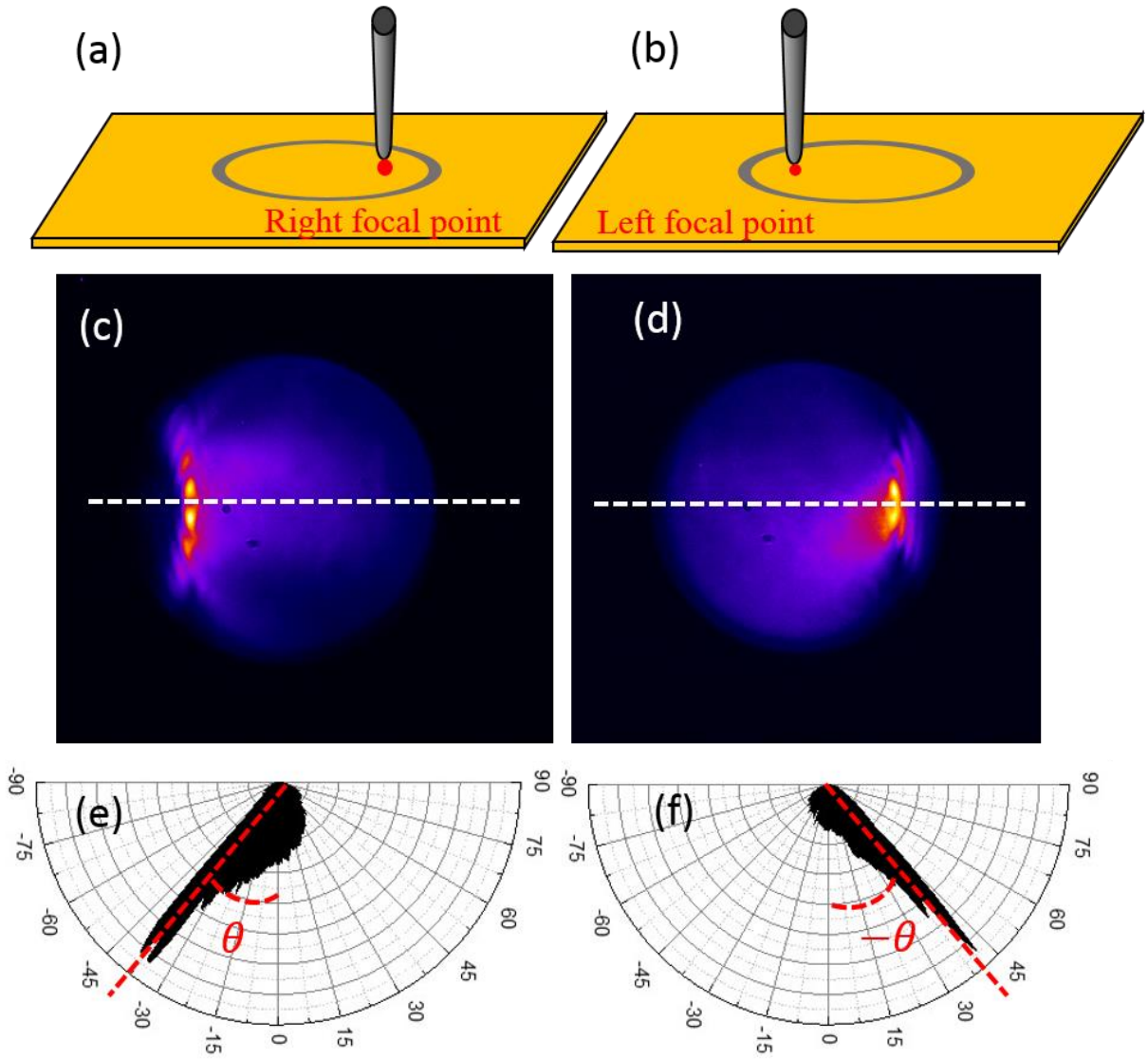

Figure 3. Fourier space images and their corresponding polar emission patterns for an STM-excited elliptical plasmonic lens ($D_1 = 3$ μm,$D_2 = 8.77$ μm). (a-b) Schematic image showing the location of the excitation. (c-d) Fourier space images when the excitation is located at the left or right focal points of the elliptical plasmonic lens. (e-f) The intensity profiles taken along the white dashed line in Fig. 2 (c-d) are separately shown in a polar plot. θ and $-\theta$ stand for the emission angle in two opposite directions. The Fourier space images are acquired during 300 seconds, the bias is set at $2.8\ V$ and the setpoint current is $1\ nA$.

In this section, comparing the STM excitation of *circular* and *elliptical* plasmonic lenses, we find that while the emission of light beams of low angular spread is achieved from a *circular* plasmonic lens when the excitation is *centered* on the structure; however, for an *elliptical* plasmonic lens, it is when the excitation is located on a *focal point*, that we get a collimated

light beam. This collimated light beam is emitted at a specific emission angle with regard to the optical axis.

4.4 Theoretical explanation of collimated light emission when the excitation is located at a focal point of the elliptical plasmonic lens

In this section, we will use two methods to explain why that when the excitation is located at the focal point position of the elliptical slit, we get the emission of light beams of low angular spread.

First, we use a mathematical model. As we mentioned in the introduction, it has been shown that an electrically excited elliptical cavity can produce a beam emitting at a well-defined angle [10]. In this article, D. T. Schoen et al., used a 3 D (three dimension) paraboloid model to explain the directional emission from the 2 D elliptical cavity.

Here, we will also employ this 3 D paraboloid model to explain our directional light emission process. Before showing the 3 D paraboloid model with our structure, we will review some geometrical optics which is related to our model. A vertical cut of a 3 D paraboloid is illustrated in Fig. 4. When light originates from the focal point F, no matter the direction of the light, the reflected light will propagate parallel to the parabolic axis. Additionally, when a plane perpendicular to the optical axis intersects the paraboloid of the focal point, the enclosed area is a circular disc (see the blue area in Fig. 4).

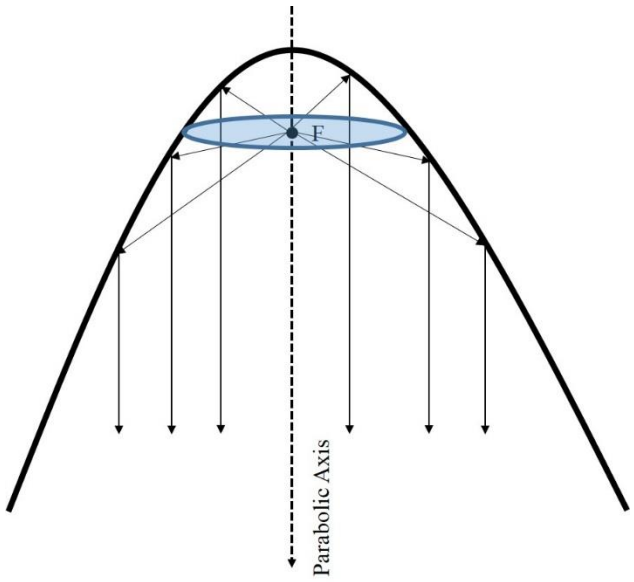

Figure 4. Vertical cut of a 3D paraboloid. Note that the light which originates from the focal point F is reflected parallel to the parabolic axis.

Figure 5 shows how the 3 D paraboloid model relates to the experiment. Figure 5 (a) indicates the case where the parabolic axis is parallel to the optical axis of the experiment. In this case, the center of the plasmonic lens is the focal point of the paraboloid. Since the parabolic and optical axes are parallel, this situation is equivalent to a circular plasmonic lens with the excitation centered. As seen in Fig. 4, since the light originates from the focal point F, if the circular plasmonic lens may be considered equivalent to a $3D$ parabolic mirror, then the emitted beam will be parallel to the parabolic/optical axis. From the experimental results shown in Fig. 2 (c), we have already observed that when the STM excitation is centered on the circular plasmonic lens, light is emitted in the direction of the optical axis with low angular spread.

Next, we will apply our paraboloid model to the elliptical plasmonic lens. Schematically this is shown in Fig. 5 (b). If we tilt our 3 D paraboloid by an angle of θ with respect to the optical axis, the intersection of the paraboloid with a plane perpendicular to the optical axis and passing through the focal point now delineates an *elliptical* area. If the left focal point of the elliptical plane overlaps the focal point of the paraboloid, we could expect that the light is emitted parallel to the parabolic axis. As a result, the light emission is tilted the same angle θ with regard to the optical axis. Thus using this model we can predict the emission angle of an elliptical slit when the excitation is located at a focal point.

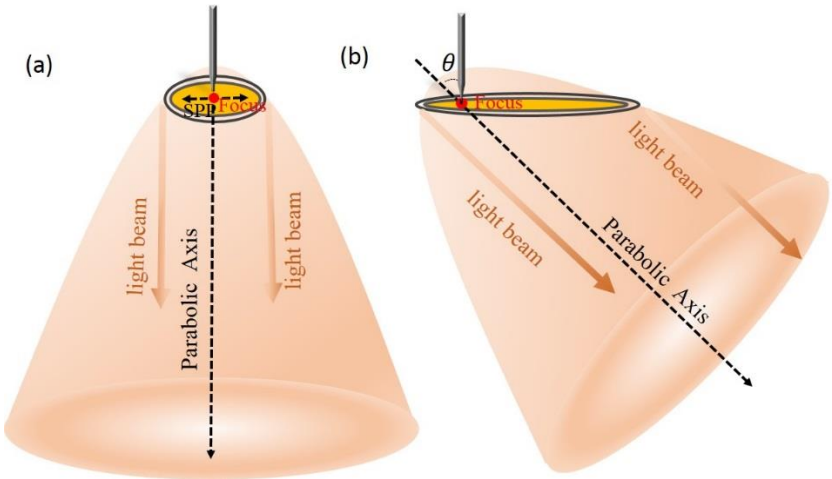

Figure 5. 3 *D paraboloid model schematic diagrams. (a) The model predicts an untilted beam for the circular plasmonic lens excited by the STM in the center. (b) The model predicts a tilted*

beam for the elliptical plasmonic lens when it is excited by the STM at a focal point position. The focal point of the elliptical slit and the focal point of the paraboloid coincide.

With this 3 D paraboloid model, we motivate that only when the STM excitation is located at the focal point position of the elliptical plasmonic lens, we may achieve directional light emission with a tilt angle of θ. From the reference [10], we know that if the focal point of the elliptical plane coincides with the paraboloid, the angle θ should verify:

$$\sin\theta = e \quad (4.1)$$

Here, e is the eccentricity of the ellipse and:

$$e = \sqrt{1 - (\frac{b}{a})^2} = \frac{c}{a} \quad (4.2)$$

where a is the semi-major axis of the elliptical structure and b is the semi-minor axis of the elliptical structure. c is the focal length of the ellipse. In our case, a is equal to $\frac{D_2}{2}$ and b is equal to $\frac{D_1}{2}$.

Thus, from the paraboloid model, we may infer that by changing the eccentricity e of elliptical plasmonic lens, we control the emission angle θ. Figure 6 (a)-(d) show that as the eccentricity is increased from 0 (circular) to larger values, the emission angle θ increases accordingly.

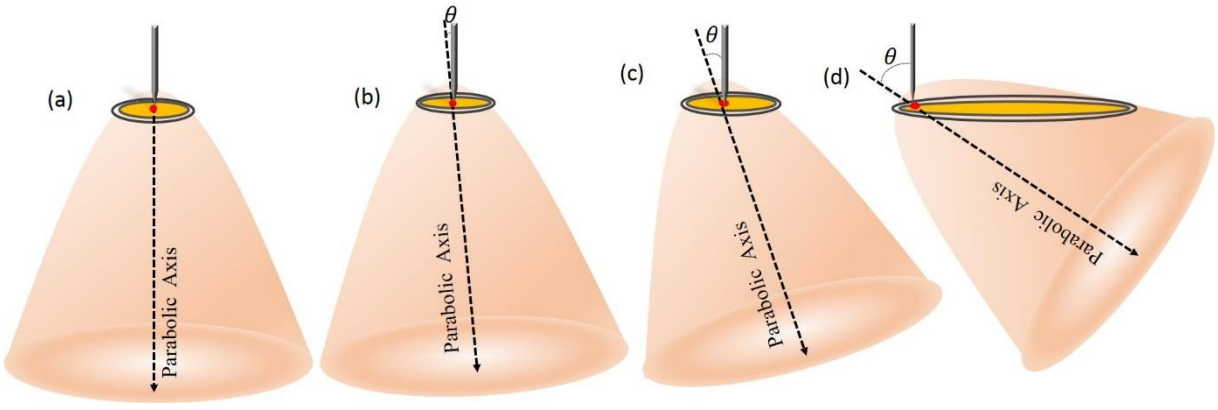

Figure 6. Schematic images of the 3 D paraboloid model showing that by changing the eccentricity of an elliptical slit, we control the emission angle.

In our case, we detect the emission from below the sample and the emission angle in the glass substrate should be calculated as θ' according to Snell's law:

$$\sin\theta = n\sin\theta' \quad (4.3)$$

where θ is the emission angle in air. n is the refractive index in glass and θ' is the emission angle in glass. So θ' can be expressed as:

$$\sin\theta' = \frac{e}{n} \quad (4.4)$$

After elaborating the 3 D paraboloid model, next, we will use a second model (phase relations of scattered light) to explain why that when the excitation is located at the focal point of the elliptical slit, we get a beam of low angular spread.

Figure 7 illustrates a situation when the STM excitation is located at the position F which is the left focal point of the elliptical slit (which satisfies the standard ellipse equation: $\frac{x^2}{a^2} + \frac{y^2}{b^2} = 1$). Position $P\ (x', y')$ denotes an arbitrary point along the elliptical slit. According to the standard equation of the ellipse, the distance r between point F and the arbitrary point P can be expressed as:

$$r = \frac{c}{a}x' + a \quad (4.5)$$

where a, b and c are separately defined as the semi major axis length, semi minor axis length and the focal distance.

Then in terms of optics, the phase change with propagation is φ: $\varphi = k_{spp} \times r$

Thus, combining with the equation (4.5), we have:

$$\varphi\ (x') = k_{spp}(\frac{c}{a}x' + a) \quad (4.6)$$

Equation (4.6) indicates that the phase at different points along the elliptical slit varies linearly with the horizontal coordinate value x' when the excitation originates from the focal point F.

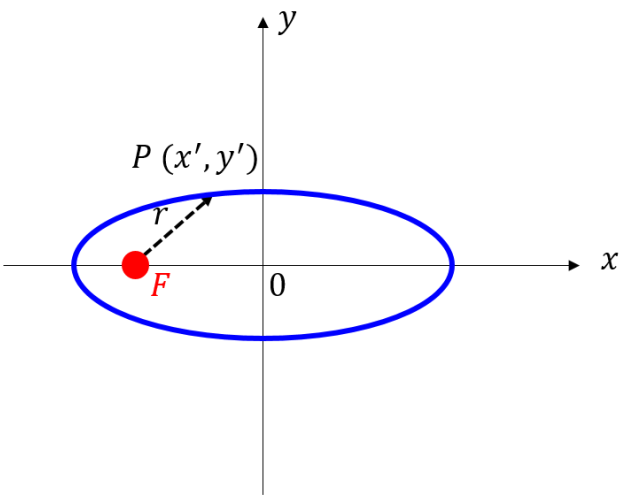

Figure 7. Sketch showing an ellipse with the standard ellipse equation: $\frac{x^2}{a^2}+\frac{y^2}{b^2}=1$. *The STM excitation originates from the left focal point F. For an arbitrary point* $P\ (x', y')$ *on the ellipse, the distance between PF may be expressed as a linear function of* x'.

Now let us approximate the elliptical slit as a simple slit of length 2a, where the phase of the scattered light is equal to $\varphi\ (x')$ and $x' \in [-a, a]$. The linear increase of the phase indicates that the wavefront is in a tilted plane. The wavefront (blue dashed line in Fig. 8) is tilted an angle of θ corresponding to the horizontal direction. Therefore, the emitted light (red line in Fig. 8) is tilted the same angle θ in terms of the vertical direction. This could be another explanation for tilted light beam.

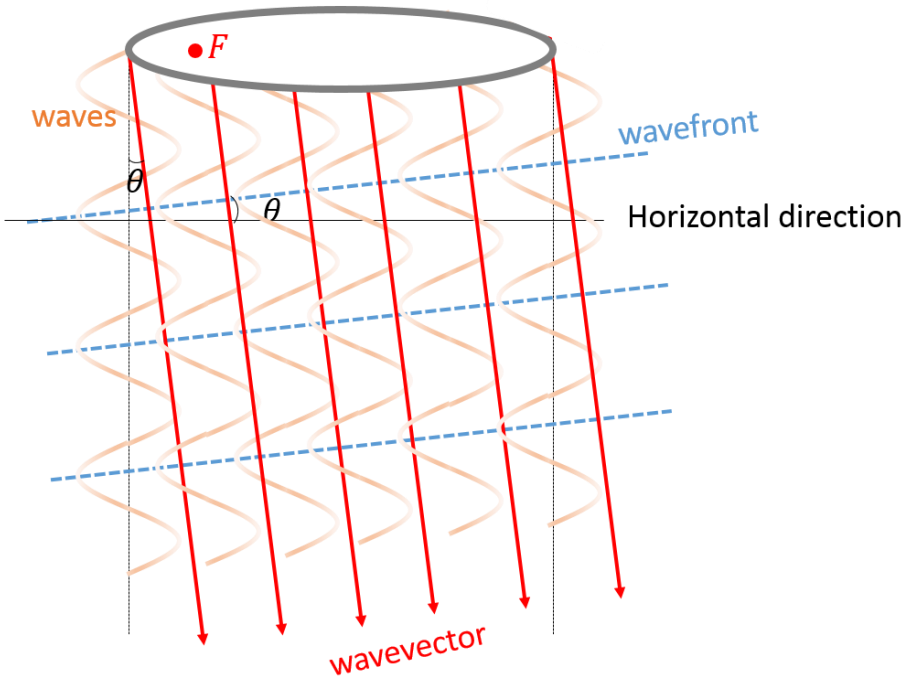

Figure 8. Approximation of the elliptical slit as a simple slits with linear varying phase. Focal point (F in red) represents the excitation position. The orange lines stand for the waves from elliptical slits. The blue dashed lines stand for the wavefront and red lines are the wave propagation direction. In this case, the wavefront is tilted thus the propagation direction is tilted.

Then, in this model, we will derive the light emission angle θ. In Figure 9, F is the focal point with the focal length of c, M is the arbitrary slit point with the coordinate x_i ($-a < x_i < a$) and N is the end point of the slit with the x coordinate of a. When the excitation originates at F, to satisfy the constructive interference of light emitted at the same angle θ, we have :

$$k_{spp}\left(\frac{c}{a}x_i + a\right) + k_{photon}(a - x_i)sin\theta = k_{spp}(a + c) \quad (4.7)$$

where $k_{photon} = nk_0$. n is the refractive index of glass substrate in our case and k_0 is the wavevector in free space.

Thus, from equation (4.7), we have:

$$sin\theta = \frac{k_{spp}}{k_0}\frac{e}{n} \quad (4.8)$$

Therefore, we obtain the similar expression as in equation (4.6) except in this case, we have another term $\frac{k_{spp}}{k_0}$. The absence of the term $\frac{k_{spp}}{k_0}$ in equation (4.6) is due to the fact that the differences in the wavevectors k_{spp} and k_0 are not taken into account. Since $\frac{k_{spp}}{k_0}$ is rather close to 1, equation (4.6) is also applicable.

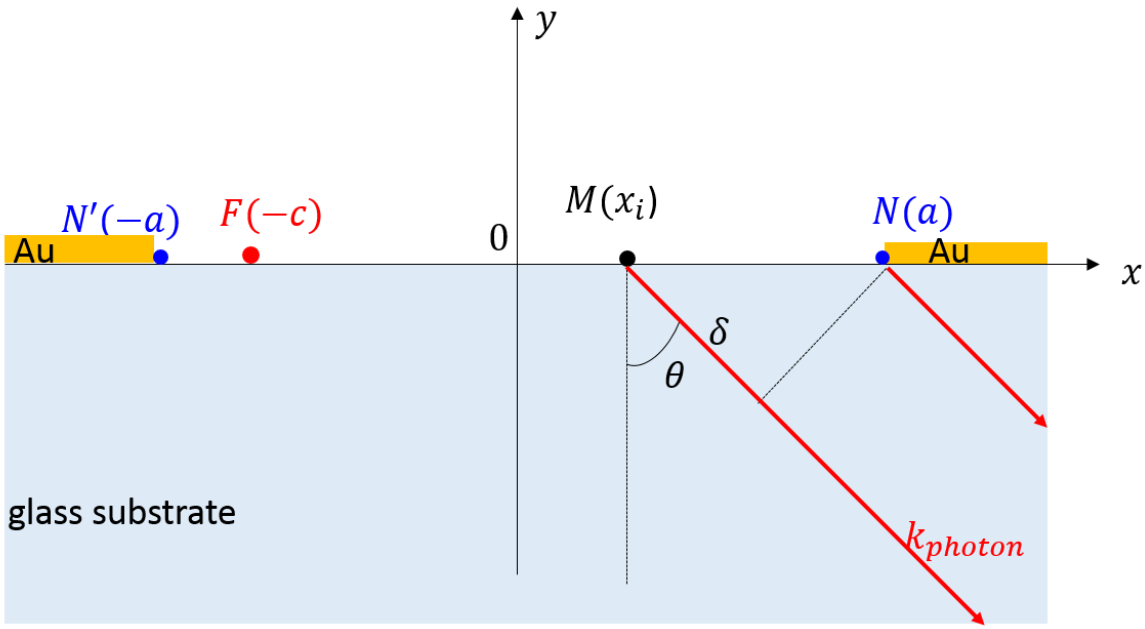

Figure 9. Sketch of the scattering of SPPs into light when the elliptical slit is approximated as a simple slit with linearly phase $\varphi(x')$ (equation (4.6)). The excitation originates at focal point F. The light emitted in the substrate from slit point M and N interferes constructively in the direction denoted by the angle θ.δ is the optical path difference.

In this section, two different methods are applied to explain why only when the excitation originates from the focal point of the elliptical structure, we obtain directional light emission. We also demonstrate that the emission angle is determined by the eccentricity of the elliptical plasmonic lens.

4.5 Experimentally controlling the direction of a collimated light beam using different elliptical plasmonic lenses

In this section, we will experimentally show that by changing the eccentricity of the elliptical plasmonic lens, we can control the direction of the emission of the collimated light beam.

Here, we use 8 different elliptical plasmonic lenses which have the same minor axis length D_1 of 3 µm. By changing the length of major axis D_2, the eccentricity of the elliptical plasmonic lens is varied. The length D_2 is seen in table 4.1 and their corresponding transmission images are respectively shown in Fig. 10 (a_1)-(a_8). These transmission images are recorded by illuminating the structures with white light from above and collecting the transmitted light from below the sample. From these transmission images we clearly see that the structure's shape changes as D_2 is increased and their corresponding eccentricities e are separately calculated shown in table 4.1. We see that a circular slit is gradually varied to an elliptical slit with very high eccentricity.

Structure	1	2	3	4	5	6	7	8
D_2 (µm)	3	3.05	3.2	3.46	3.92	4.67	6	8.77
e	0	0.18	0.35	0.51	0.64	0.77	0.87	0.94

Table 4.1. Parameters of the elliptical slit. D_2 and eccentricities (e).

We have already shown that when the excitation is at the focal point position of an elliptical plasmonic lens, we achieve directional light emission. In these experiments, we locate our excitation at the left focal point of each elliptical slit and for the first circular structure, we position the excitation at the center for comparison. The schematic images of the experiment are shown in Fig. 10 (b_1) - (b_8).

Figure 10 (c_1)-(c_8) show the corresponding Fourier space images. In each image we see that a doughnut shaped spot whose shape changes from circular to elliptical as the eccentricity of the slit is increased. Note also that the position of the spot moves from the center to edge of Fourier space indicating that the emission angle is increasing. These can be seen more intuitively from the polar emission patterns (Figure 10 (d_1)-(d_8)).

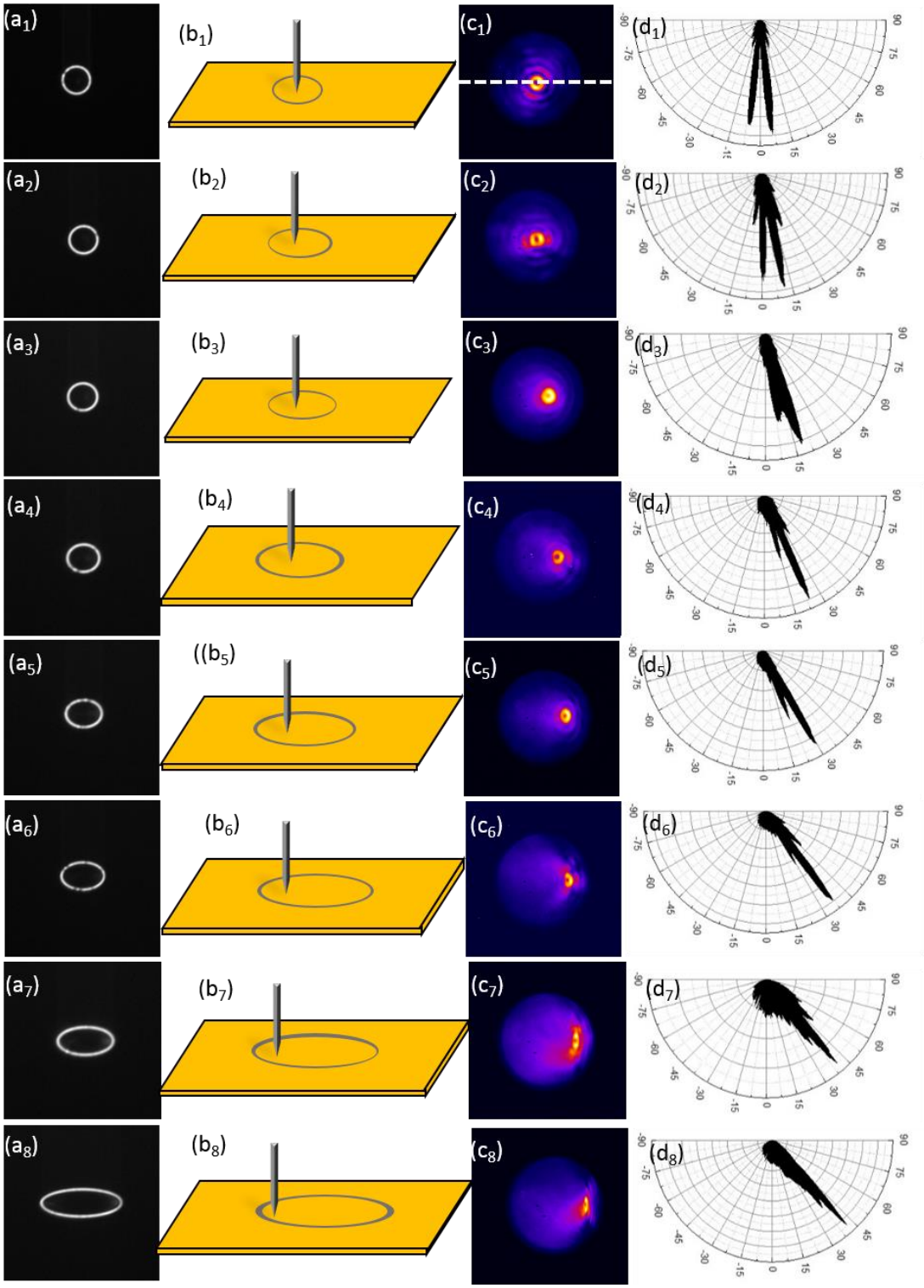

Figure 10. Changing the emission angle by changing the eccentricity of the elliptical slit. (a_1)- (a_8) Transmission images for the structure with constant D_1 of 3 μm and the length D_2 (see table 4.1). (b_1)- (b_8) Schematic diagrams of the excitation position on each structure. (c_1)- (c_8) Corresponding Fourier space images when the excitation is located at the left focal point of the structures. (d_1)- (d_8) Polar emission patterns taken from the central line (see white dashed line

in Fig. 10 (c1)). All these experiments are conducted on the "JPK" setup. The STM bias is set at $2.8\ V$*, the setpoint current is set as* $1\ nA$ *and the acquisition time is* 300 *seconds.*

Figure 11 plots the $sin\theta$ of the emission angle determined from Fig. 10 (d_1)-(d_8) as a function of the eccentricity, as well as the $sin\theta$ of the calculated emission angle determined from equation (4.8) ($sin\theta = \frac{k_{spp}}{k_0}\frac{e}{n}$). Comparing the experimental and calculated results, we find that they fit each other well. Thus, we conclude that by varying the eccentricity of the elliptical plasmonic lens, we vary the phase relation between the SPPs scattered at the elliptical slits, thus leading to a variation in the emission angle by changing the emission from 0° to nearly 40°.

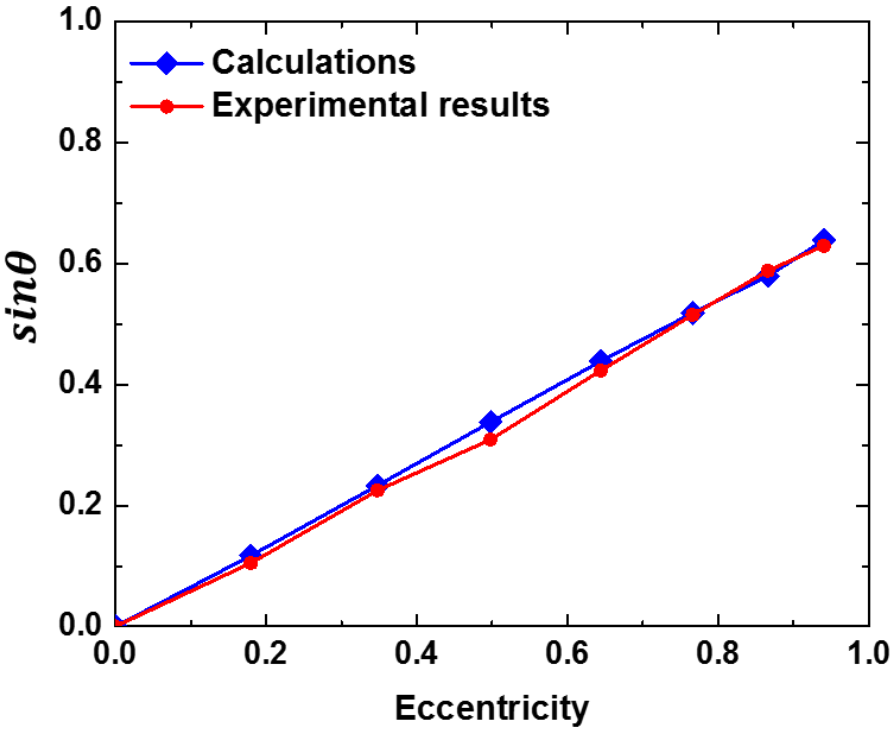

Figure 11. Experimental emission angle as a function of eccentricity: experiment and calculation from a simple model. The experimental results are determined from Fig. 10 (d1)-(d8). The calculation is based on the interference model of equation (4.8) (we use $\frac{k_{spp}}{k_0} \approx 1.037$ *which is for the wavelength of* $700\ nm$ *in free space).*

4.6 Controlling the angular spread of collimated light beams using different elliptical plasmonic lenses

From the above section, we learn that the direction of light emission may be controlled via the eccentricity of the elliptical slit. Next, we will investigate the variation of the angular spread as a function of eccentricity.

First we take the example of the structure in Fig. 10 (a_5) with $D_1 = 3\ \mu m$, $D_2 = 3.92\ \mu m$ and its transmission image is shown in Fig. 12 (a) with marked minor axis length of D_1 and major axis length of D_2. Figure 12 (b) is its Fourier space image which was already shown in Fig. 10 (c_5). We draw two white dashed lines separately passing through the center of the elliptical spot in the horizontal and vertical directions and we define two lines as k_x and k_y. Figure 12 (c) and (d) respectively presents the intensity profile of k_x and k_y. In Fig. 12 (c), the horizontal axis is the angular position with respect to the optical axis and the vertical axis is the normalized intensity. We use HWHM (half width at half maximum) to define the angular spread in Figs. 12 (c) and 12 (d).

The measured angular spread in the k_x direction is equal to $\approx \pm 6.5°$and in the k_y direction, it is equal to $\approx \pm 9.1°$. The angular spread is clearly smaller in the k_x direction than in the k_y direction. This can be due to the diffraction of light, angular spread and source size are related by $L\Delta k \geq 2\pi$ as discussed in chapter 3. This means that the larger the dimension in real space, the more it will be compressed in k space and vice versa. In our case, D_2 is larger than D_1, so as a result, the angular spread in k_x direction will be smaller than in the k_y direction.

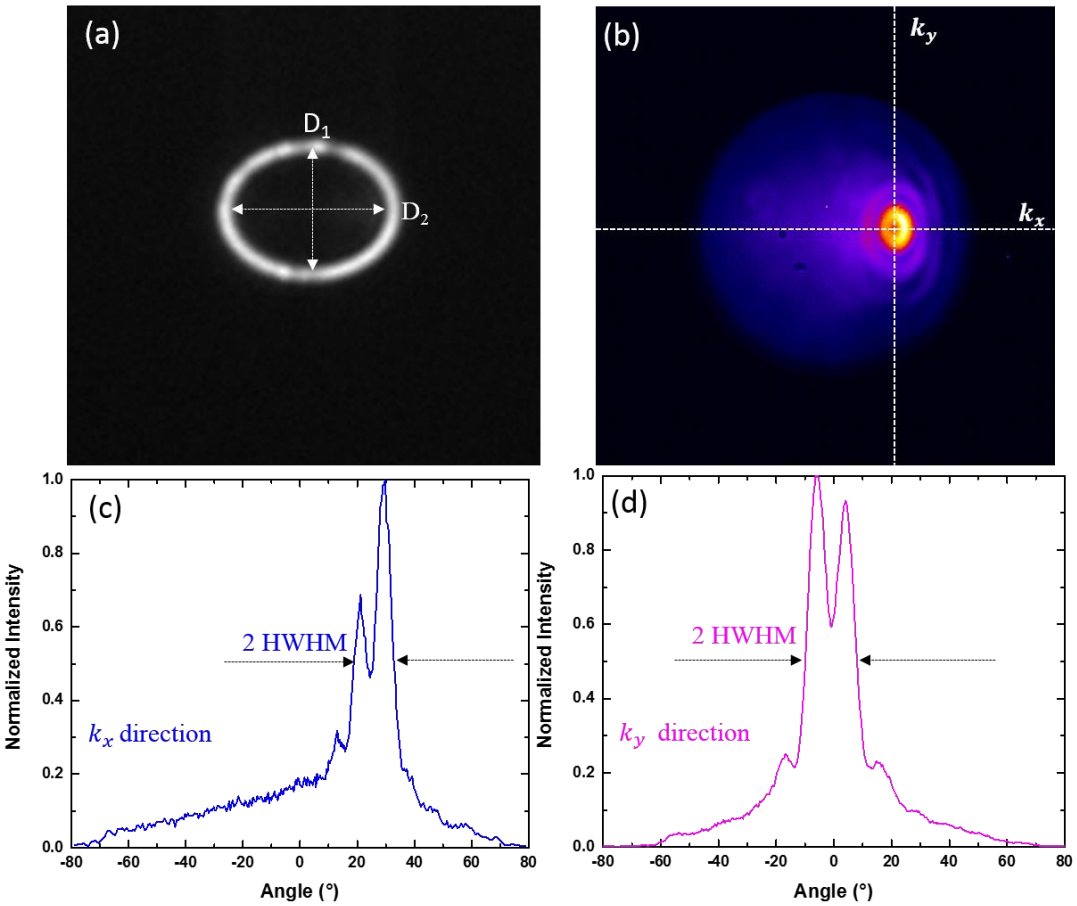

Figure 12. Angular spread of the beam of light resulting from an STM-excited elliptical structure ($D_1 = 3\ \mu m$, $D_2 = 3.92\ \mu m$). (a) The white light transmission image. (b) Fourier space image. (c) Cross section from the image in (b) along the line labeled k_x. (d) Cross section from the image in (b) along the line labeled k_y.

So far, we have shown that the angular spread behavior for only one elliptical structure. As was done in Fig. 12, we measure the angular spread from the Fourier space images in Fig. 10 (c_1)-(c_8). Figure 13 (a) plots the angular spread in the k_x and k_y directions as a function of eccentricity. (For the structures with eccentricities of 0.87 and 0.94 the background is subtracted before the angular spread is measured in the k_y direction (see discussion below).

From Fig. 13 (a), we see that the angular spread in the k_y direction (red line) is stable for all structures since D_1 is set to a constant length of $3\ \mu m$.

However, we find that in the k_x direction (black line), increasing the eccentricity of the elliptical slit leads to a smaller angular spread. For the structures with eccentricities of

0.87 ($D_2 = 6\ \mu m$) and 0.94 ($D_2 = 8.77\ \mu m$), the angular spread is around 4° which is similar to the angular spread for the five-slit circular plasmonic lens ($L = 11.2\ \mu m$) discussed in chapter 3. This is very interesting because we know that the higher the number of slits, the better the collimation. Here we see that a l-slit elliptical structure can achieve a similar beaming effect as that which is found for a multiple-slit circular structure which has even larger size.

Figure 13 (b) plots the ratio of the angular spread in the k_x and k_y directions as a function of eccentricity (purple line) and the ratio between the minor axis length D_1 and the major axis length D_2 as a function of eccentricity (blue line). From the results, we see that the two curves are quite similar. They have the same tendency and the discrepancy is small. This means that the shape of our elliptical spots in Fourier space is the same as the shape of the structure but rotated 90°.

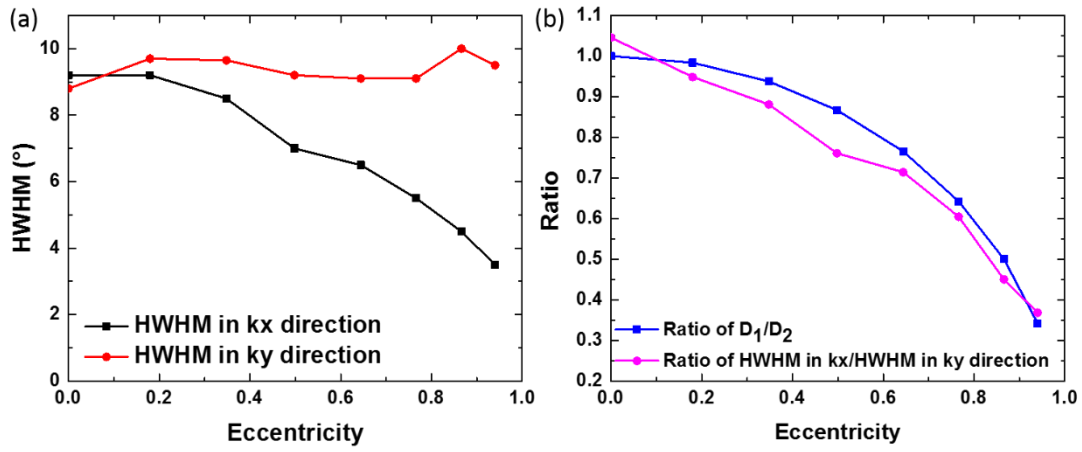

Figure 13. (a) Angular spread in the k_x and k_y directions as a function of eccentricity. (b) Ratio between the dimensions D_1 and D_2 (blue line) and ratio between the angular spread in the k_x direction and k_y directions (purple line) as a function of eccentricity.

Note that the above supports the idea that the origin of the beaming is indeed linearly variation of the phase of the scattered light. We might imagine that when the excitation is at the focal point of the elliptical slit with eccentricity of 0.94 (i.e., that the excitation is much off center), the scattered light is mainly from one side of the slit and in its opposite direction, the intensity is much weaker. Despite the large difference in intensity, in the Fourier space image,

the obtained spot still preserves a small angular spread for the elliptical slit with high eccentricity.

However, the unequal intensity of the emission scattered along the slit will result in decreased visibility of the elliptical spot. This is shown in Fig. 14. Figures 14 (a) and 14 (b) respectively show the experimental and simulation Fourier space images when the excitation is located at the right focal point for the structure $D_1 = 3\ \mu m$, $D_2 = 8.77\ \mu m$ (simulation details and more results are shown in Appendix A). The obtained elliptical spots in both experiment and simulation show that in the k_x direction, the visibility is much lower than in the k_y direction. This is also the reason that when we measure the angular spread in Fig. 13, we subtract the background for the structures with eccentricities of 0.87 and 0.94.

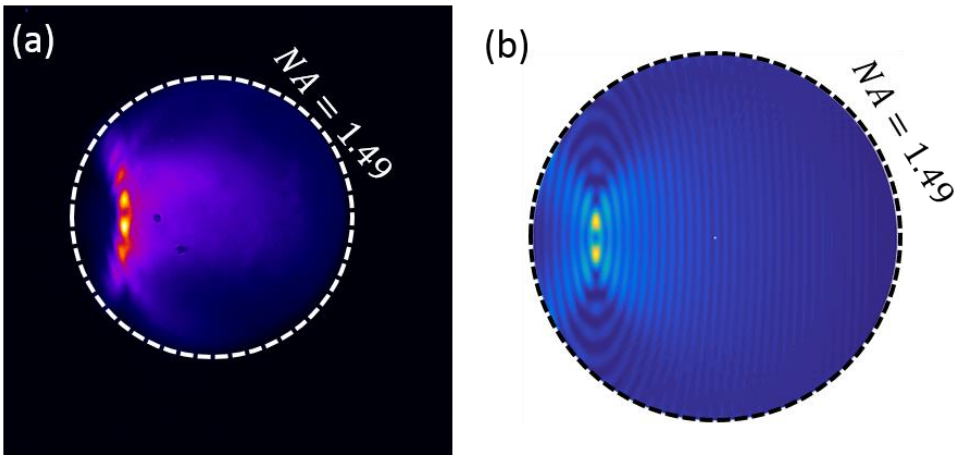

Figure 14. Fourier space images when the excitation is located at the right focal point of the structure ($D_1 = 3\ \mu m$, $D_2 = 8.77\ \mu m$). (a) Experimental result. (b) Simulation result (simulation details in Appendix A)

Directional light emission with low angular spread from an elliptical plasmonic lens is obtained. Since the linear relation for the phase $\varphi = \varphi(x')$ only holds for excitation at the focal point, complicated interference patterns for other excitation positions are expected. These results are shown in Appendix A.

4.7 Conclusion

In summary, a single slit elliptical plasmonic lens electrically-excited with an STM-based nanosource at a focal point can produce a directional beam of light. The direction of the emission is determined by the eccentricity of the elliptical structures. This is explained using a 3 D paraboloid model and motivated by a discussion of the phase relations between the light scattered at different positions on the slit. Changing the eccentricity from 0 to 0.94 leads to a change in directionality of 0° to near 40° with respect to the optical axis. The angular spread of the resulting beam varies from 9° to around 4° in the k_x direction. Our study provides a better understanding of how plasmonic nanostructures such as an elliptical slit can shape the emission properties of electrically excited light.

[1] A. G. Curto, G. Volpe, T. H. Taminiau, M. P. Kreuzer, R. Quidant, and N. F. van Hulst, "Unidirectional Emission of a Quantum Dot Coupled to a Nanoantenna," *Science*, vol. 329, no. 5994, pp. 930–933, 2010.

[2] T. Coenen, F. B. Arango, A. F. Koenderink, and A. Polman, "Directional emission from a single plasmonic scatterer," *Nat. Commun.*, vol. 5, no. 3250, pp. 1–8, 2014.

[3] I. M. Hancu, A. Curto, M. Castro-Lopez, M. Kuttge, and N. F. van Hulst, "Multipolar interference for directed light emission," *Nano Lett.*, vol. 14, no. 1, pp. 166–171, 2014.

[4] H. J. Lezec *et al.*, "Beaming Light from a Subwavelength Aperture," *Science*, vol. 297, no. 2, pp. 820–822, 2002.

[5] D. Z. Lin *et al.*, "Beaming light from a subwavelength metal slit surrounded by dielectric surface gratings," *Opt. Lett.*, vol. 14, no. 8, pp. 836–838, 2006.

[6] B. Lee, S. Kim, H. Kim, and Y. Lim, "The use of plasmonics in light beaming and focusing," *Prog. Quantum Electron.*, vol. 34, no. 2, pp. 47–87, 2010.

[7] H. Aouani *et al.*, "Bright Unidirectional Fluorescence Emission of Molecules in a Nanoaperture with Plasmonic Corrugations," *Nano Lett.*, vol. 11, no. 6, pp. 637–644, 2011.

[8] Z. Liu, J. M. Steele, W. Srituravanich, Y. Pikus, C. Sun, and X. Zhang, "Focusing surface plasmons with a plasmonic lens," *Nano Lett.*, vol. 5, no. 9, pp. 1726–1729, 2005.

[9] G. M. Lerman, A. Yanai, N. Ben-Yosef, and U. Levy, "Demonstration of an elliptical plasmonic lens illuminated with radially-like polarized field," *Opt. Express*, vol. 18, no. 10, pp. 10871–10877, 2010.

[10] D. T. Schoen, T. Coenen, F. J. Garcia de Abajo, M. L. Brongersma, and A. Polman, "The planar parabolic optical antenna," *Nano Lett.*, vol. 13, no. 1, pp. 188–193, 2012.

Chapter 5

Probing the optical band structure of a planar plasmonic multi-layer stack by STM excitation

In this chapter, we demonstrate that the STM-excited nanosource is able to probe the optical band structure of a planar plasmonic multi-layer stack. We also compare the results of laser and STM excitation on the same structure and we find that the STM excitation is more sensitive in terms of signal-to-noise.

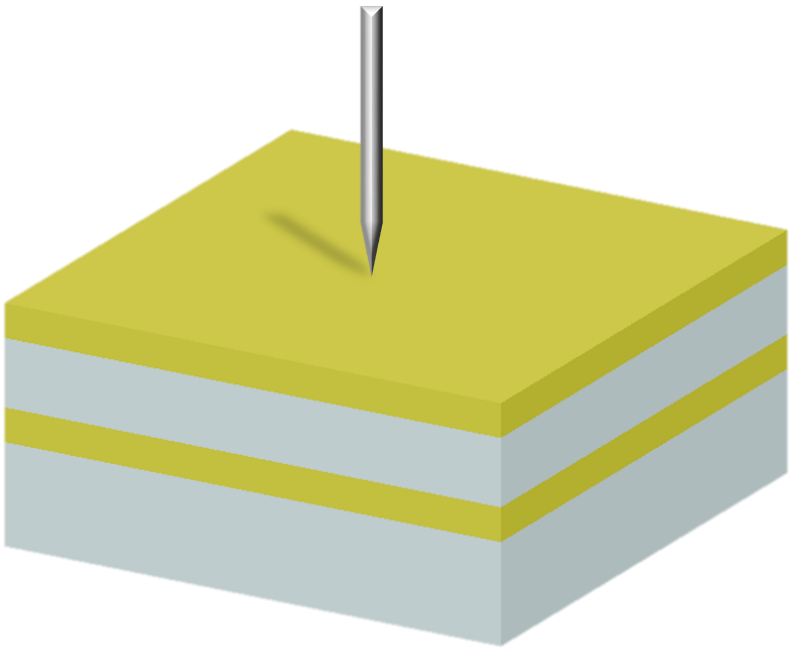

5.1 Introduction

In the previous two chapters, we have discussed the manipulation of light using electrically excited SPPs interacting with plasmonic nanostructures. Through the electrical excitation of a *circular* plasmonic lens using the STM, we produce radially polarized light of low angular spread. Additionally, we find that by changing the excitation position, we control the emission angle. However, when the excitation position is too far from the center of the plasmonic lens, the collimation of the emitted light beam is degraded. To overcome this disadvantage, we proposed an *elliptical* plasmonic lens. By changing the eccentricity of the *elliptical* plasmonic lens, we vary the emission direction when the excitation position is at one of the two focal points of the ellipse. Note also that the emitted light beams have low angular spread, even at comparatively wide emission angles with respect to the normal direction. In this chapter, we continue to explore the interaction between electrically excited SPPs and plasmonic nanostructures and here, we employ a planar plasmonic multi-layer stack structure.

Planar plasmonic multi-layer stacks, such as metal-dielectric-metal and dielectric-metal-dielectric structures, have been widely studied. Such multi-layer stacks can be used as waveguides for propagating surface plasmon polaritons. Continuous efforts have been put forth to achieve long-range propagation and strong spatial confinement of light fields [1]–[7]. Plasmonic multi-layer stack structures have also found applications in absorption switches [8], optical gain switches [9] and in surface plasmon resonance sensors [10]. In the work on surface plasmon sensors by Tien's group [10], they use a polychromatic, radially polarized light beam that they tightly focus on a planar plasmonic multi-layer stack structure (Au (20 nm)-SiO_2 (500 nm)-Au (20 nm)). They spectrally resolve the emitted light as a function of angle. Their Fourier space image, displayed in Fig. 1, shows a rainbow pattern. In other words, the emission angle is different for each wavelength and clearly is resolvable.

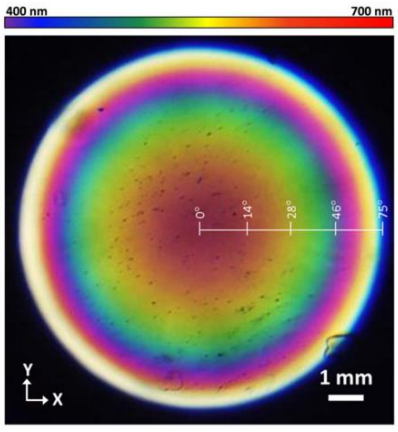

*Figure 1. The illumination of an Au (*20 nm*)-SiO_2 (*500 nm*)-Au (*20 nm*) stack with radially polarized white light leads to rainbow rings at the back focal plane of the objective lens [10].*

Inspired by the results shown above, we have probed the optical bands, namely, explored the dispersion relation of a multi-layer stack with the same configuration. The dispersion relation describes the relation between wavevector and energy. It provides the characteristics of the different waves that are generated in a given structure. The probing of the optical bands has been reported for various structures, such as photonic crystals [11], periodic metal nanoparticle arrays [12], [13], plasmonic circular holes [14] and a plasmonic crystal [15]. The knowledge of the band structure of a system is important as it determines its optical response.

In this chapter, we use our local, electrical excitation method by STM to probe the optical band structure of a plasmonic multi-layer stack in a new way. We also compare the results obtained by both laser and STM excitation of the same structure and the results indicate that the STM technique is more sensitive in terms of signal-to-noise ratio.

5.2 Sample preparation

The experiments are conducted on the "JPK" setup which was introduced in chapter 2. A scanning tunneling microscope operated in air with a metallic tip is mounted above the sample and below is the inverted optical microscope.

The plasmonic multi-layer stack is a metal-dielectric-metal (MIM) system on a glass coverslip (refractive index $n = 1.52$, thickness 170 μm). To better adhere to the substrate, a layer of titanium (3 nm in thickness) is deposited on the substrate before deposition of the MIM layers. The MIM system consists of a silica layer sandwiched between two 30 nm thick gold layers. Three different samples are prepared with different thicknesses of SiO_2: 70 nm, 190 nm and 310 nm. Schematics of the samples are shown in Fig. 2. The sample was fabricated by *Jean-Francois Bryche* at the Centre de Nanosciences et de Nanotechnologies (C2N) in Paris-Sud University.

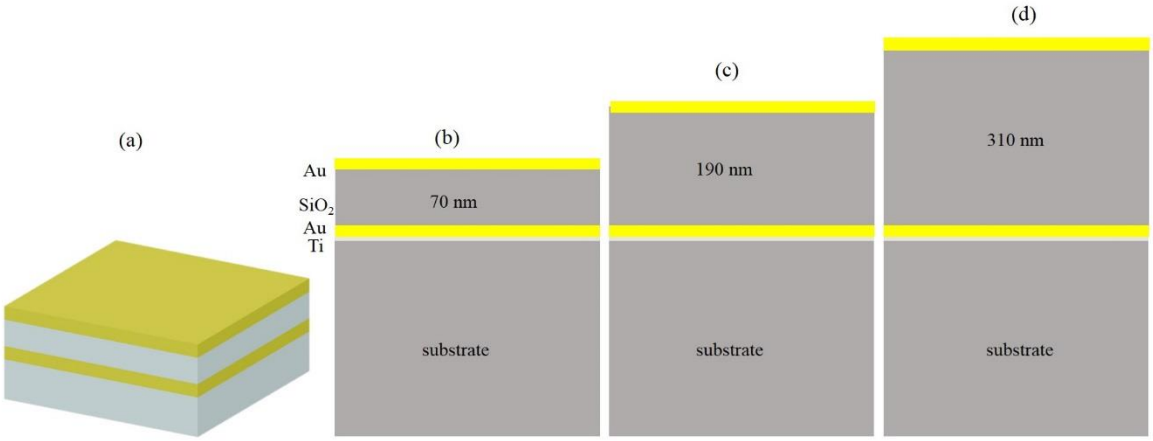

*Figure 2. Schematic diagram of the sample. Au-SiO_2-Au layers are deposited on a glass substrate. (a) The schematic diagram of the sample. Side view of the sample (b) Au (*30 nm*)-SiO_2 (*70 nm*)-Au (*30 nm*). (c) Au (*30 nm*)-SiO_2 (*190 nm*)-Au (*30 nm*). (d) Au (*30 nm*)-SiO_2 (*310 nm*)-Au (*30 nm*).*

5.3 STM excitation of a plasmonic Au (30 nm)-SiO_2 (310 nm)-Au (30 nm) multi-layer stack

5.3.1 Comparison between the STM excitation of the Au (30 nm)-SiO_2 (310 nm)-Au (30 nm) structure and a thin Au film (50 nm)

First, we compare the results in Fourier space for the plasmonic multi-layer stack and a thin Au film. Figures 3 (a) and 3 (b) show schematics of the STM excitation of these two different structures. In the experiments, we use the MIM stack with Au (30 nm)-SiO_2 (310 nm)-Au (30 nm) and for the Au film, the thickness is 50 nm.

Fourier space images are shown in Figs. 3 (c) and 3 (d) and the intensity profiles taken from Figs. 3 (c) and 3 (d) along the white dashed line are presented in Figs. 3 (e) and 3 (f) respectively. The horizontal axis is $k_{\parallel}/k_0$ ($k_{\parallel}$ is the in-plane wavevector component of the collected light and k_0 is the wavevector in free space) and the vertical axis is the normalized intensity. From Figs. 3 (e) and 3 (f), we find that the intensity profiles from the multi-layer stack exhibit the same sharp peak at $k_{\parallel}/k_0 \approx \pm 1.03$ as the gold film (note that Figs. 3 (d) and 3 (f) are reproduced from chapter 3 in Fig. 4(d)) which is the expected wavevector of surface plasmon polaritons (SPPs) propagating at an air/Au interface [16], [17] for $\lambda \approx 700$ nm (i.e.,

the mean excitation wavelength for the STM broadband excitation of an Au film). Thus, it appears that an "SPP-like" mode is excited in the multi-layer structure.

Note also that Fig. 3 (e) displays two additional peaks which are comparatively broad and less intense, annotated with red stars at $k_{\parallel}/k_0 \approx \pm 1.33$. As stated above, the multi-layer stack is M-I-M structure. Since it is made of a dielectric layer between two thin metal films, we can hypothesize what kinds of modes will exist in this structure. Metal-dielectric interfaces are known to support SPP modes (see chapter 2) and dielectric layers can support waveguide modes [18]. Also, it is known that electromagnetic modes of similar energy may hybridize i.e., produce a mode of different energy and of dual nature (e.g., plasmonic and photonic) when they exist in the same structure [19]. Thus, we propose that these resulting hybrid plasmonic-waveguide modes yield additional peaks in the Fourier space image.

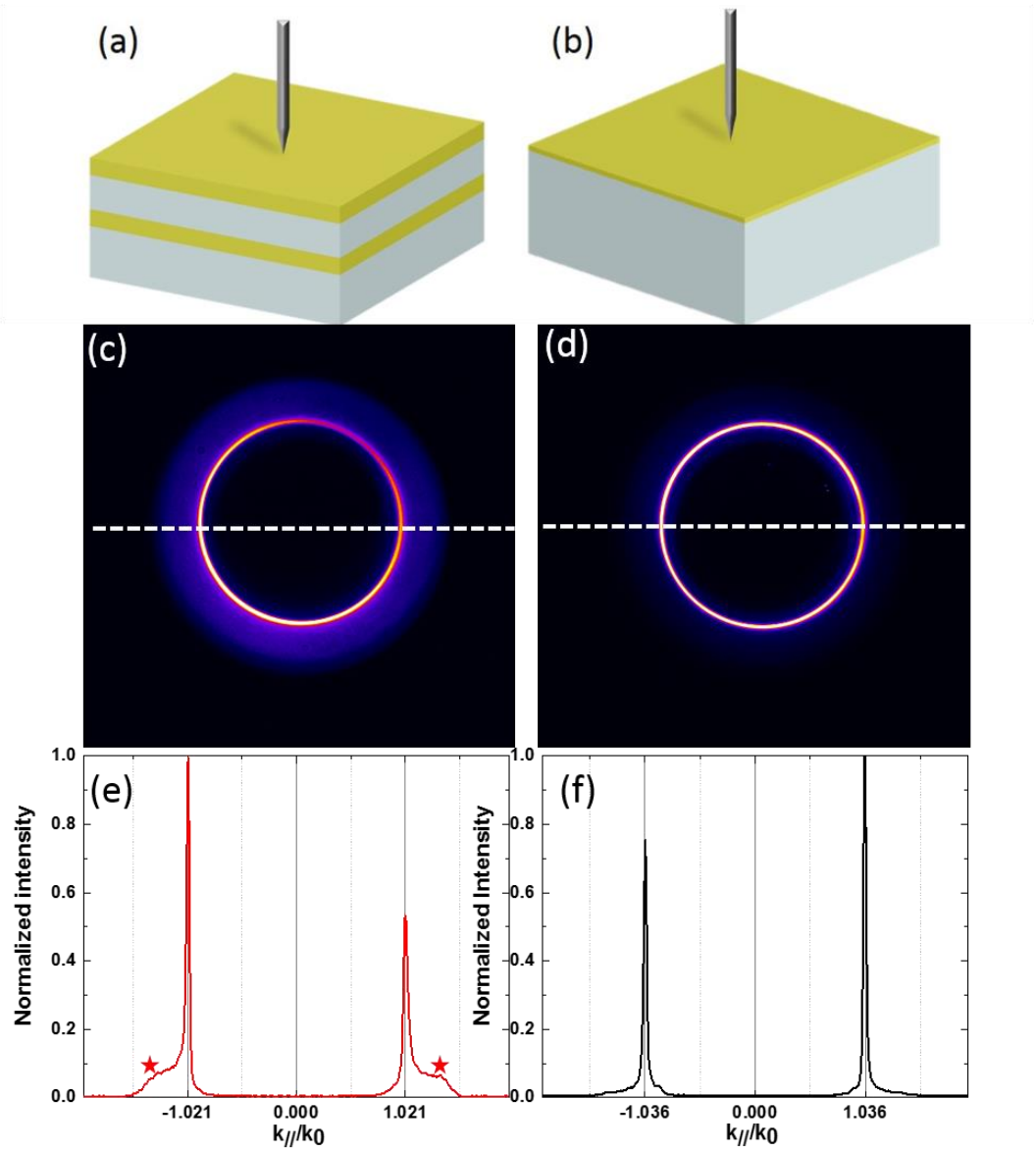

Figure 3. Comparison of Fourier space images obtained upon STM excitation of a plasmonic Au (30 nm) *-SiO_2* (310 nm) *-Au* (30 nm) *multi-layer stack and a thin Au film* (50 nm *in thickness). (a-b) Schematic diagram of the STM excitation of plasmonic wave guide structure and a thin Au film. (c-d) Fourier space image of the STM-excited plasmonic multi-layer stack and a thin Au film. (e-f) Intensity profiles obtained along the white dashed line in (c) and in (d). Bias is set at* 2.8 V *and the tunnel current setpoint is* 1 nA. *Acquisition time is 180 seconds. Experimental error is around* $0.02k_0$.

5.3.2 Fourier space images acquired using different bandpass filters

Next we record the Fourier space images with different bandpass filters in front of the CCD camera (see chapter 2). Figure 4 shows the results obtained with bandpass filters of $625/26\,\mathrm{nm}$, $700/40\,\mathrm{nm}$, $750/40\,\mathrm{nm}$, $800/40\,\mathrm{nm}$, $850/40\,\mathrm{nm}$ and $900/40\,\mathrm{nm}$ and also the intensity profiles taken along the white dashed line in the corresponding Fourier image are shown each below.

From the intensity profiles in Fig. 4 (g)-(l), we clearly see that the position of the inner peaks almost overlaps for different bandpass filters at $k_{\parallel}/k_0 \approx \pm 1.03$ for the "SPP-like" mode. These inner rings appear at the expected wavevector for SPPs propagating at an air/Au interface and this resembles the leakage radiation of the SPP modes launched on the Au film. Therefore, we infer that these hybrid modes have SPP character within this wavelength range.

The wavevector of the outer rings, however, varies with wavelength. As the wavelength increase, the wavevector decreases. When the filter wavelength is $900\,\mathrm{nm}$, the second ring disappears. Later, we will show in more detail how $k_{\parallel}/k_0$ varies upon changing wavelength. We propose that this mode corresponds to a hybrid mode of "waveguide-like" character.

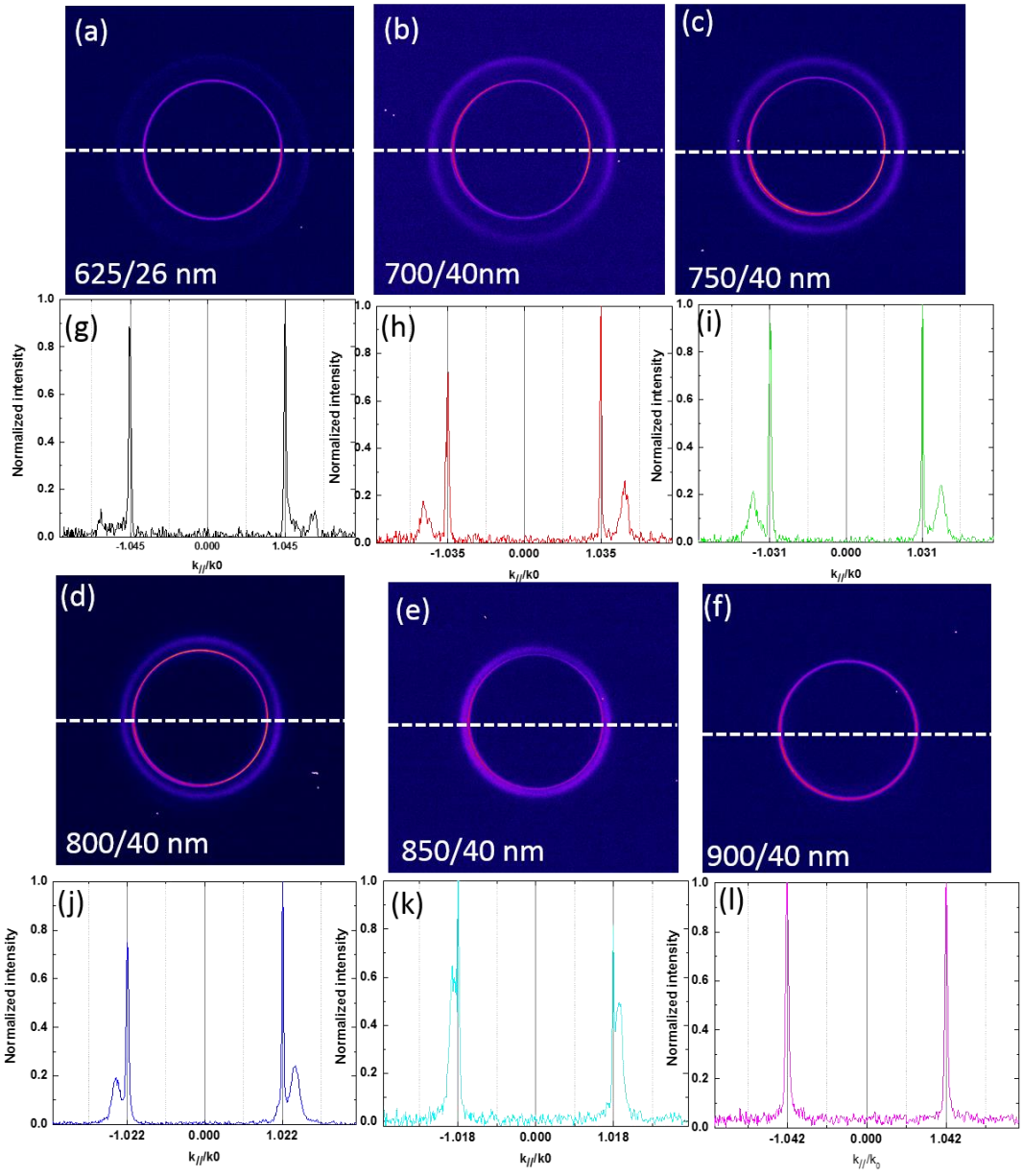

*Figure 4. Fourier space images with different bandpass filters for the Au (*30 nm*)-SiO_2 (*310 nm*)-Au (*30 nm*) structure. Fourier space images with a bandpass filter of (a)* 625/26 nm, *(b)* 700/40 nm, *(c)* 750/40 nm, *(d)* 800/40 nm, *(e)* 850/40 nm, *(f)* 900/40 nm. *Intensity profiles taken from the corresponding Fourier space images along the white dashed line are shown in (g)-(l)). Bias is set at* 2.8 V *and tunnel current setpoint is* 1 nA. *Acquisition time is* 300 *seconds.*

Figure 5 presents the Fourier space results obtained by STM excitation with a polarizer in front of the CCD camera. Figure 5 (a) shows the reference Fourier space image with a bandpass

filter of 750/40 nm and no polarizer. These are the same results as in Fig. 4 (c). The intensity profile is shown in Fig. 5 (d). The Fourier space images with a bandpass filter *and* a polarizer placed before the detector are shown in Fig. 5 (b) (horizontal polarizer) and Fig. 5 (c) (vertical polarizer) respectively. The transmission axis is oriented as shown by the white double arrow in the figure.

Figures 5 (e) and 5 (f) show the vertical and horizontal intensity profiles from Figs. 5 (b) and 5 (c) respectively along the direction perpendicular to the polarizer transmission axis (we normalize the intensity profile by the peak intensity in the images). We can clearly see in both Figs. 5 (e) and 5 (f) that in the direction perpendicular to the transmission axis of the polarizer, there is no light. These results confirm that no TE modes can be excited by STM excitation and that are expected, we can only excite TM modes (see chapter 2 for more on TE and TM modes coupled to SPPs).

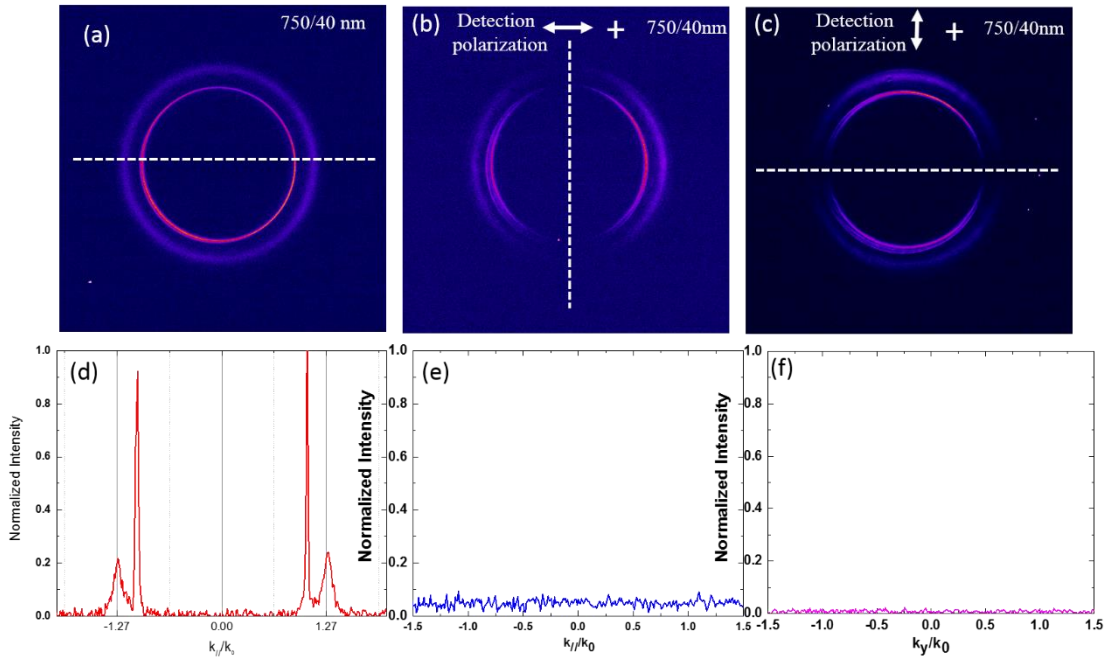

*Figure 5. Fourier space images by STM excitation with a polarizer and bandpass filter in front of the CCD camera for the Au (*30 nm*)-SiO_2 (*310 nm*)-Au (*30 nm*) structure. Fourier space image with (a) no polarizer, (b) a horizontal polarizer in front of the CCD, (c) a vertical polarizer in front of the CCD. All images are acquired with a bandpass filter of* 750/40 nm *in front of the CCD camera. Intensity profiles are obtained along the white dashed lines in the figures above. The bias is set at* 2.8 V *and the tunnel current setpoint is* 1 nA*. Acquisition time is* 300 *seconds.*

In order to look into the details of the proposed "waveguide-like" modes, first we introduce the effective index n_{eff}. The effective index is the ratio of the in-plane wavevector of the collected light to the wavevector in free space, i.e.:

$$n_{eff} = k_{\parallel}/k_0 \quad (5.1)$$

where k_0 is the wavevector in free space and is equal to $\frac{\omega}{c}$ (ω is the angular frequency and c is the speed of light).

In chapter 2, we have already discussed the expression for SPPs propagating at an air/metal interface:

$$k_{spp} = k_0\sqrt{\frac{\varepsilon_m\varepsilon_d}{\varepsilon_m+\varepsilon_d}} \quad (5.2)$$

So the effective index of an SPP mode is equal to: $n_{eff} = \sqrt{\frac{\varepsilon_m\varepsilon_d}{\varepsilon_m+\varepsilon_d}}$ (5.3)

where ε_m and ε_d are the dielectric constants of Au and air respectively in our case.

Figure 6 (a) shows the effective indices of the proposed "SPP-like" and "waveguide-like" modes of our plasmonic multi-layer stack which are determined experimentally from Fig. 4 and plotted as a function of the emission wavelength. From this, we see that in the experiment, the effective index of the "waveguide-like" mode decreases as the wavelength increases and at a longer wavelength of ≈ 900 nm, the "waveguide-like" mode disappears.

In Fig. 6 (a), we also plot the results of a theoretical calculation of the effective index of a "pure" SPP mode propagating at the air/Au interface. In the theoretical calculation, equation (5.3) is used and the optical constants are taken from Johnson and Christy [20]. We see that the theoretical result for a "pure" SPP mode matches the experimental measurements, confirming the "SPP-like" character of the mode with $k_{\parallel}/k_0 \approx \pm 1.03$.

Collaborators from our group, *Moustafa Achlan* and *Georges Raseev*, did a simulation for the MIM structure. Within the simulation, the STM inelastic electron tunneling (IET) is modeled as a vertical oscillating dipole. The oscillating dipole is placed 1 nm above the MIM structure. This dipole emits a spherical electromagnetic wave. Using the Sommerfeld expansion, the spherical waves in momentum space can be divided into two parts: propagating plane waves and evanescent waves. The Fresnel reflection and transmission coefficients are used at each

interface. The transmitted light as a function of angle, i.e., a Fourier space image, is simulated. Therefore, from the simulated Fourier space images, the effective indices $k_{\parallel}/k_0$ of both the "SPP-like" and "waveguide-like" modes may be determined by calculation.

The simulation results are also shown in Fig. 6 (a) with blue and green dots representing the effective indices of the "SPP-like" and "waveguide-like" modes. Good agreement between the simulation and experimental results is found for the "SPP-like" mode. In contrast, for the "waveguide-like" mode, we find that at a wavelength of 700 nm, some discrepancies between the experimental results and simulation exist. At a wavelength of 625 nm, the difference becomes larger. It seems that at short wavelengths, for the "waveguide-like" mode, the discrepancy between the simulation and experimental results is larger than at longer wavelength. The reason could be that the dielectric constants used in the simulation differ from those of the experiments and such a difference may have a stronger effect at short wavelengths.

The data of Fig. 6 (a) may be plotted as a set of dispersion relations. The relation between the wavevector and the energy is thus presented in Fig. 6 (b). The light line in Fig. 6 (b) corresponds to $E(\text{energy}) = \hbar c k_{\parallel}$, and the blue shaded area is the light cone, representing all the possible plane waves in air. It is clear that in the dispersion curves, the SPP dispersion curve lies to the right of the light line. Note also that for the same energy, the wavevector of the "waveguide-like" mode is higher than that of the" SPP-like" mode.

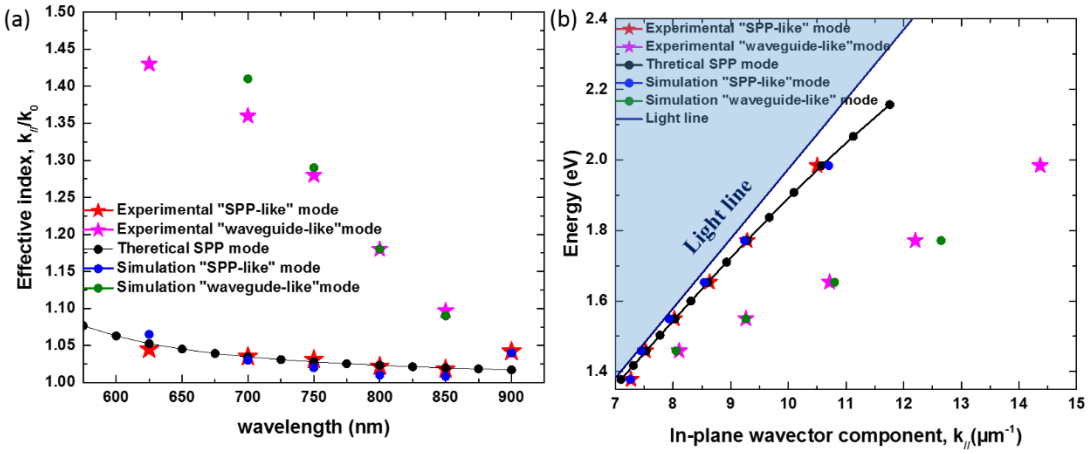

*Figure 6. Dispersion relations of the modes of the plasmonic multi-layer stack of Au (*30 nm*)-SiO_2 (*310 nm*)-Au (*30 nm*). (a) Effective index of the "SPP-like" and "waveguide-like" modes versus wavelength. The effective indices are determined from the radius of the observed rings in the Fourier space images shown in Fig. 4. The theoretical effective index of an SPP at an*

air/Au interface and the simulation results for the "SPP-like" and "waveguide-like" modes are also shown. (b) Dispersion relation between the energy and the in-plane wavevector component $k_{//}$ of the observed modes. The light line in vacuum is also added for comparison.

In this subsection, we discussed the STM excitation results for a plasmonic multi-layer stack of Au (30 nm)-SiO_2 (310 nm)-Au (30 nm). We experimentally derived the optical band structure (dispersion relation) and attributed the identified modes to hybrid guided modes of both SPP and waveguide nature.

5.3.3 Theoretical calculation results

To investigate further the "SPP-like" and "waveguide-like" modes, *Moustafa Achlan* and *Georges Raseev* calculated the intensity distribution of the electric field in the direction perpendicular to the thin layer interfaces (labeled as the z-axis) for the multi-layer structure (air/Au (30 nm)/SiO_2 (310 nm)/Au (30 nm)). In this simulation, a plane wave with wavelength $\lambda = 700$ nm is incident from the substrate at the angle determined by the peak value of $k_{\parallel}/k_0$ from the Fourier space simulation. The results are presented in Fig. 7. The horizontal axis is the electric field intensity $|E|^2$ and the vertical axis is the direction perpendicular to the interfaces (z-axis).

Figure 7 (a) shows the intensity of the electric field along the z direction when the effective index $k_{\parallel}/k_0 = 1.035$ (it is the simulated effective index of the "SPP-like" mode for the Au (30 nm)-SiO_2 (310 nm)-Au (30 nm) structure when $\lambda = 700$ nm). We clearly see that the highest electric field intensity appears at the air/Au interface, and decays exponentially in the air above the structure. This is characteristic of an "SPP-like" mode on an air/Au interface. Note that while quite weak, the electric field intensity is non-zero in the SiO_2 dielectric layer. This suggests that this hybrid SPP-waveguide mode is of SPP character. Therefore, this confirms our previous assignment that for the effective index $k_{\parallel}/k_0 = 1.035$ we have an "SPP-like" mode.

Figure 7 (b) displays the intensity of the electric field along the z direction when the effective index $k_{\parallel}/k_0 = 1.41$ (it is the simulated effective index of the "waveguide-like" mode for the Au (30 nm)-SiO_2 (310 nm)-Au (30 nm) structure when $\lambda = 700$ nm). Here, in contrast to what is shown in Fig. 7 (a), we see that a peak of the electric field intensity is not only

confined to the air/Au interface, but there is also a peak at the Au/SiO_2 and SiO_2/Au interfaces. In fact, the stronger peaks are at the Au/SiO_2 and SiO_2/Au interfaces. This electric field intensity distribution suggests that the two SPP modes at Au/SiO_2 interface have coupled to form a field symmetrical mode which is reminiscent of a waveguide mode. The presence of a symmetrical mode in MIM plasmonic structures has already been shown [6]. Thus, for $\lambda = 700\ \mathrm{nm}$, when $k_{\parallel}/k_0 = 1.41$, the hybrid SPP-waveguided mode in the MIM structure is of both "SPP-like" and "waveguide-like" character.

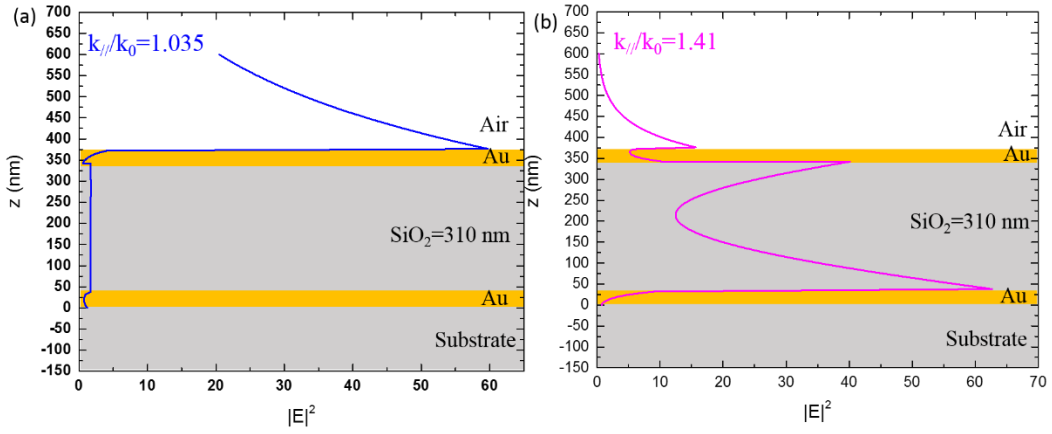

Figure 7. Distribution of the squared modulus of the electric field along the direction perpendicular to the interface (z-direction) for an air/Au (30 nm)/SiO_2 (310 nm)/Au (30 nm)/substrate structure. The horizontal axis is the intensity of the electric field $|E|^2$ and the vertical axis is the z direction. In the calculation, a plane wave with wavelength $\lambda = 700$ nm is incident from the substrate at an angle determined by the peak value of $k_{\parallel}/k_0$ from the Fourier space simulation. The electric field distribution along the z direction when the effective index is (a) $k_{\parallel}/k_0 = 1.035$, (b) $k_{\parallel}/k_0 = 1.41$. Note in (a) the mode is of "SPP-like" character, while the mode in (b) is more of a "waveguide-like" character.

Thus thanks to the simulated results of the electric field intensity distribution in a plasmonic multi-layer stack for different effective indices, we can clearly distinguish the characteristics of the "SPP-like" and "waveguide-like" modes.

5.4 Comparison of STM and laser excitation of the same structure

In this section, we will compare STM and laser excitation of the same sample (plasmonic Au (30 nm)-SiO_2 (310 nm)-Au (30 nm) multi-layer stack) that was discussed in the last section.

Figure 8 depicts the schematic diagram of the laser excitation experiment which is carried out on the "JPK" setup. The linearly polarized He-Ne laser (wavelength of 633 nm) is focused on the sample using an oil objective and incidence is from below the substrate, see Fig. 8 (a). The orientation of the linear polarization may be controlled using a half wave plate. The reflected light beam is collected by the same objective. A beam splitter reflects the incident laser beam towards the sample and transmits the reflected light to the detector (incident and reflected beams go through the same microscope objective). The oil objective lens is used to generate a range of incident wavevector components with various incident angles from the collimated monochromatic light beam. Light is incident from all directions within the numerical angular aperture of the objective and the reflected light is detected on the CCD camera with the same angular restrictions. When the incident angle is larger than the critical angle (total internal reflection), an evanescent wave is induced. In chapter 2, we saw that evanescent waves can excite SPPs at an air/Au interface at a specific incident angle which satisfies the phase-matching condition determined by the dispersion relation. Thus, less light is reflected at this angle. This process is presented in Fig. 8 (a).

Figure 8 (b) is a reminder of the definition of TE (transverse electric) and TM (transverse magnetic) incidence. As illustrated in Fig. 8 (b), when the electric field is parallel to the incidence plane, it is referred to as a TM wave and when it is perpendicular to the incidence plane, it is referred to as a TE wave. The reason why we discuss TE and TM polarization is that while a laser can have both TE and TM wave components, the STM excitation has only a TM component since it is regarded as a vertical oscillating dipole. In other words, as shown in Fig. 5, the STM-nanosource can only excite TM modes. However, with the laser, we also expect to be able to excite TE modes if they exist in the structure.

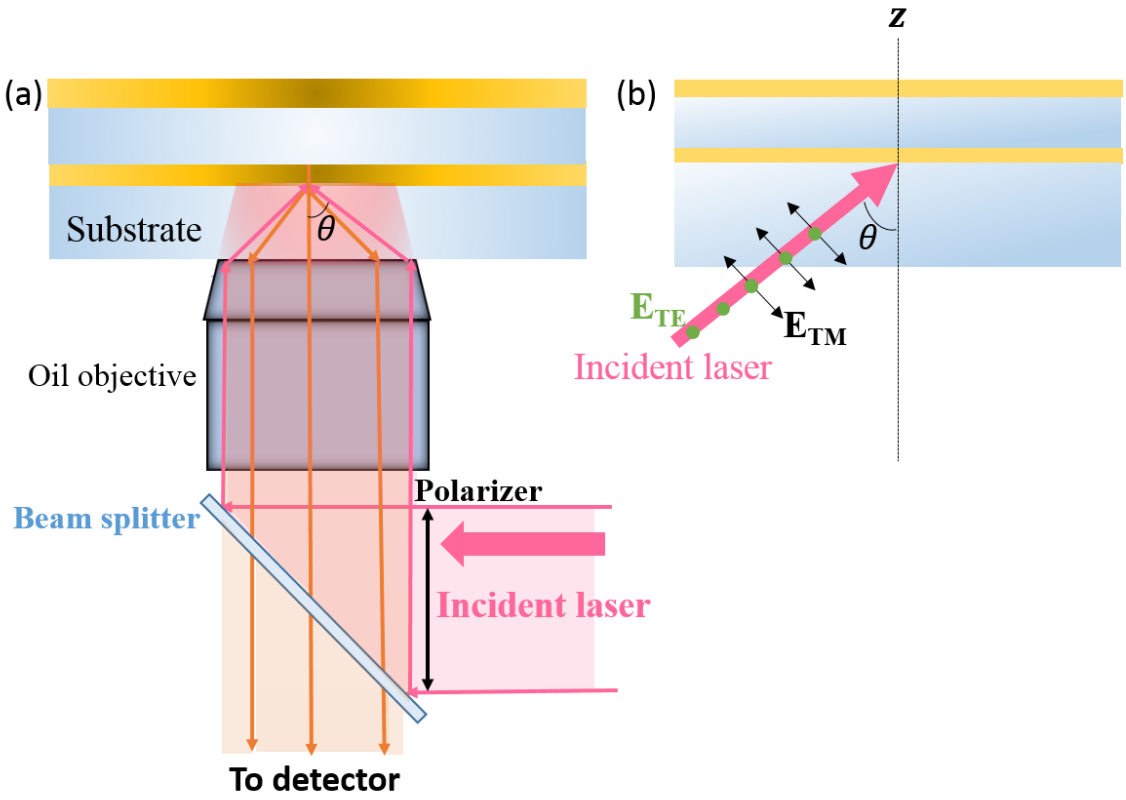

Figure 8. Schematic diagram of laser excitation. (a) A He-Ne laser (wavelength 633 nm*) is incident from below the substrate and is focused on the sample by the oil immersion objective. The sample is a plasmonic multi-layer stack of Au (*30 nm*)-SiO_2 (*310 nm*)-Au (*30 nm*). The reflected light is collected by the same oil immersion objective. (b) Schematic description of TE and TM wave in terms of the incidence plane. The electric field is parallel to the incidence plane for TM waves and perpendicular to the incidence plane for TE waves.*

Figure 9 shows the Fourier space results with the above-described laser excitation. The incident beam has either "*horizontal*" or "*vertical*" linear polarization, where "horizontal" and "vertical" refer to the axes in the CCD images. When the excitation polarization is "horizontal", the incidence is TM along the horizontal axis of the resulting Fourier space image and TE along the vertical axis. The opposite is the case for the "vertical" polarization. The reflected light beam is then recorded in the far-field on the CCD camera. Figures 9 (a) and 9 (b) present the Fourier space images with the "horizontal" and "vertical" polarizations of the excitation respectively.

From Fig. 9 (a), we see that for the "horizontal" polarization, the Fourier space image on the CCD camera shows two groups of dark semi-rings, one is in the horizontal direction and the other is in the vertical direction. Additionally, the diameter of the horizontal semi-rings in the Fourier space is smaller than the diameter of the semi-rings in the vertical direction.

To further investigate these semi-rings, we plot the intensity profiles from the horizontal and vertical axes of Fig. 9 (a). The results are shown in Fig. 9 (c) and 9 (e). We see a dip at $k_{\parallel}/k_0 \approx \pm 1.044$ in Fig. 9 (c). This is the characteristic SPP mode at an air/Au interface for an incident wavelength of 633 nm. Thus we conclude that we are exciting the "SPP-like" mode of the structure. Additionally, the reason why we see a dip rather than a peak is that the incident light with $k_{\parallel}/k_0 \approx 1.044$ couples to propagating surface plasmons at the air/Au interface. As a result, less light is reflected at this angle and there is a dip in the intensity.

As seen in chapter 2, SPP modes may only be excited by TM waves, which is consistent with the excitation direction of the "horizontal" polarization and the result along the horizontal axis of the Fourier space image.

The semi-rings along the vertical axis of Fig. 9 (a) are the result of a TE excitation. This suggests that in this case, the TE excitation couples to a photonic "waveguide-like" mode in the dielectric layer that was not excited with the TM-STM excitation. From Fig. 9 (e), we also measure that the effective index (n_{eff}) of this TE "waveguide-like" mode is around $k_{\parallel}/k_0 \approx 1.19$ for an incident wavelength of 633 nm.

Similarly, with the same method, Fig. 9 (b) shows the Fourier space image obtained for incident light with "vertical" polarization. Figures 9 (d) and 9 (f) show the vertical and horizontal intensity profiles of the Fourier space image from Fig. 9 (b). As expected, the results are consistent with our previous observations.

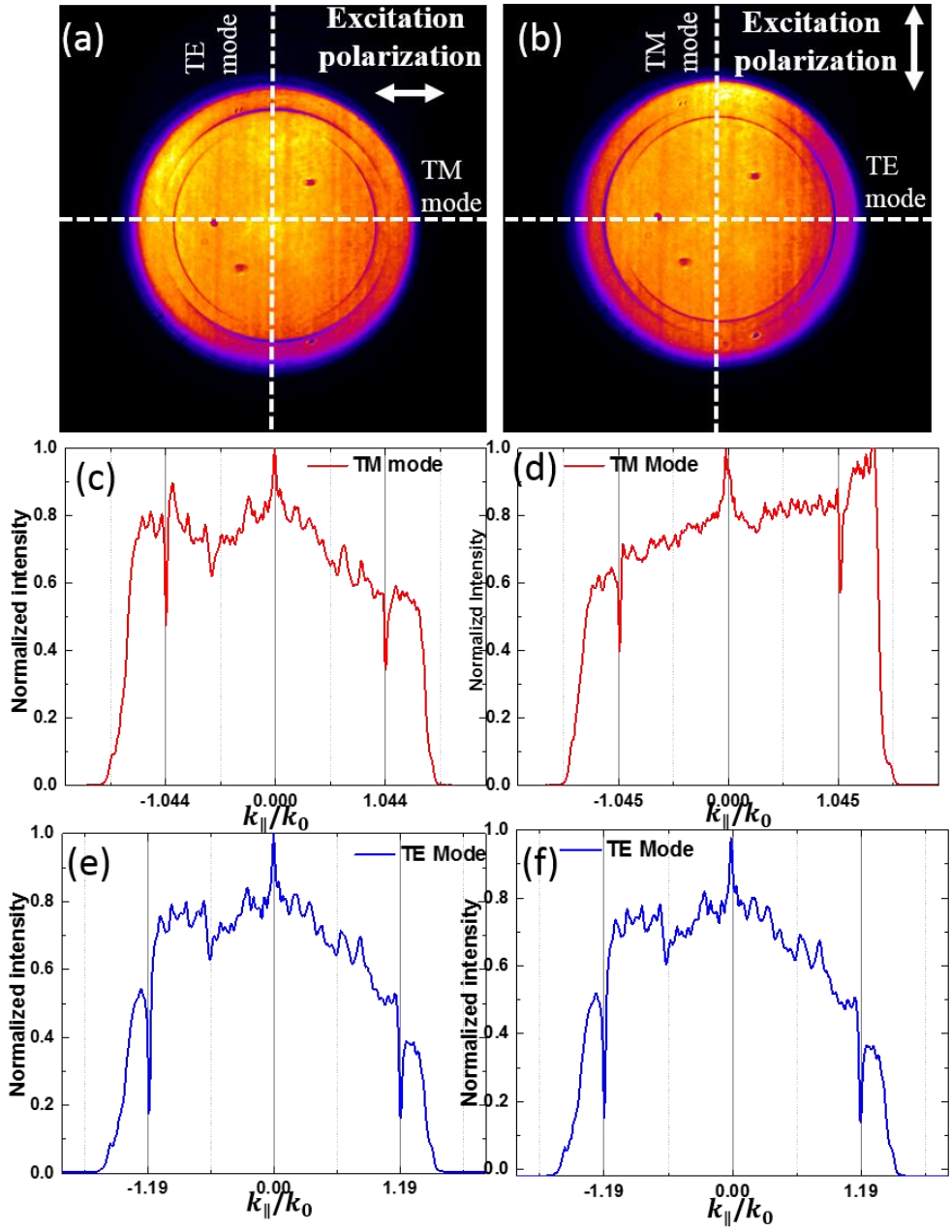

*Figure 9. Fourier space results for the laser excitation of the Au (*30 nm*)-SiO_2 (*310 nm*)-Au (*30 nm*) structure with "horizontal" and "vertical" incident polarization (the wavelength of the He-Ne laser is* 633 nm*). Fourier space image obtained when the incident polarization is (a)"horizontal" or (b)"vertical polarization". (c-d) Intensity profiles of the TM excitation direction. The dip position is* $k_{\parallel}/k_0 \approx \pm 1.044$ *and* $k_{\parallel}/k_0 \approx \pm 1.045$ *and represents the "SPP-like" mode. (e-f) Intensity profiles for the TE excitation direction. The dip positions are both* $k_{\parallel}/k_0 \approx \pm 1.19$ *and represent a waveguide mode. Note that this mode cannot be excited by the STM-nanosource.*

After presenting the results for the laser excitation of a plasmonic multi-layer stack, we will compare them with the results obtained from the STM excitation of the same structure with a bandpass filter of $625/26$ nm in front of the detector, since its transmission band includes the laser wavelength of 633 nm. The comparison is shown in Fig. 10. Figures 10 (a) and 10 (b) show the Fourier space images obtained with the laser and STM excitation respectively (they are the same results as in Fig. 9 (a) and Fig. 4 (a)). Their horizontal intensity profiles are shown in Figs. 10 (c) and 10 (d). We see that the effective index of the "SPP-like" mode in Fig. 10 (c) (which is around ≈ 1.044) is similar to that of the "SPP-like" mode in Fig. 10 (d) (which is around ≈ 1.045). The slight difference is due to the finite bandwidth of the bandpass filter in Fig. 10 (d).

Examining carefully Fig. 10 (d), we find that there exists two secondary peaks (annotated as blue arrows). We have already shown that these second peaks are "waveguide-like" modes. The effective index (n_{eff}) of this "waveguide-like" mode is around $k_{\parallel}/k_0 \approx 1.43$. In the case of laser excitation (Fig. 10 (c)), there appears to be a shallow dip (annotated as blue arrows) and the effective index of this mode is $k_{\parallel}/k_0 \approx 1.49$. In fact, this mode should be the same "waveguide-like" mode observed in Fig. 10 (d). The difference in the effective index might be attributed to the fact that the dip position in Fig. 10 (c) could be shifted due to the rapid decrease of the light intensity at high angles.

Using laser excitation, we may not get accurate effective indices of the "waveguide-like" modes due to the rapid decrease of light intensity at high angle. This rapid decrease of light intensity may be caused by the apodization effect. The amplitude distribution of light at the exit of the objective pupil depends on the apodization of the objective pupil. The apodization factor is termed as [21]:

$$B(\theta, \varphi) = \sqrt{\cos\theta} \quad (5.4)$$

where θ is the angle of emission of the light with respect to the optical axis and φ is the azimuthal angle in the object plane.

According to the apodization factor in equation (5.4), for the same φ, with increasing θ, the value of $B(\theta, \varphi)$ decreases as $\sqrt{\cos\theta}$. This means that at higher emission angles, less light will be collected by the objective.

As a result, in the case of laser excitation, light is collected at all the angles up to the acceptance angle of the objective, and intensity of the collected light will depend on the apodization at high angle. For STM excitation, however, light is only emitted at certain angles, so the apodization will have a lesser effect.

Note then that the dark background in Fig. 10 (b) is flater than the bright background in Fig. 10 (a). This mean that the noise is less for STM excitation than for laser excitation. This is also clear from comparing the background noise in Fig. 10 (c) and in Fig. 10 (d). If we consider the laser excitation experiment as a kind of "absorption measurement" and the STM experiment as an "emission measurement", then from our comparison, we see that the "emission measurement" has a better signal-to-noise ratio than the "absorption measurement". This has been demonstrated before for the emission of light from a single molecule [22], [23]. In the "absorption measurement", the signal-to-background ratio is very weak but in the "emission measurement", it improves.

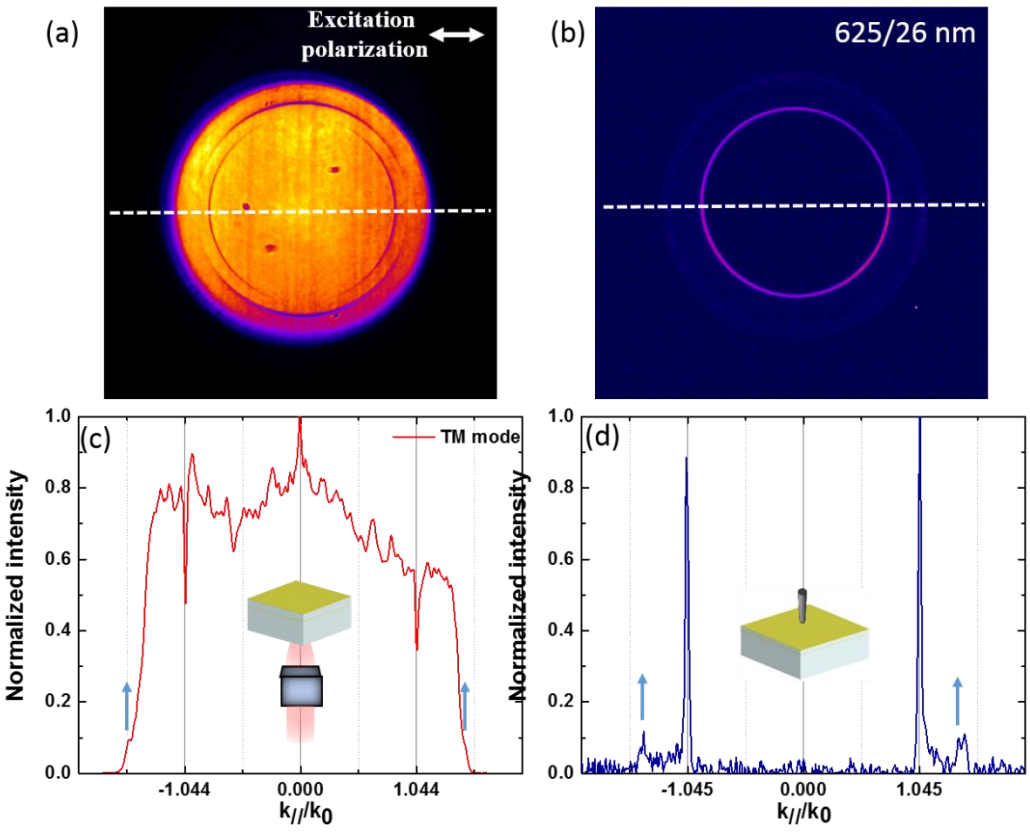

*Figure 10. Comparison of laser and STM excitation of the same Au (*30 nm*)-SiO_2 (*310 nm*)-Au (*30 nm*) structure. (a) Fourier space image obtained with laser excitation (incident wavelength* 633 nm*,"horizontal" polarization). (b) Fourier space image obtained with a*

bandpass filter of $625/26$ nm *in front of the CCD camera. (c) Horizontal intensity profile from (a). (d) Horizontal intensity profile from (b).*

In conclusion, in this section we have shown that we can use laser to probe the TE modes which are inaccessible with the TM-STM excitation. However, improved single-to-noise of the STM "emission measurement", as compared to the laser "absorption measurement" allows us to measure the TM "waveguide-like" mode which is barely visible with laser excitation.

5.5 STM excitation of different plasmonic multi-layer stacks of various SiO_2 thicknesses

5.5.1 Fourier space images of an STM excited Au (30 nm)-SiO_2 (70 nm)-Au (30 nm) multi-layer structure with different bandpass filters

Previously, we detailed the results of the plasmonic Au (30 nm)-SiO_2 (310 nm)-Au (30 nm) multi-layer stack. In this section we will discuss the influence of the thickness of the dielectric layer. Figure 11 shows the Fourier space images achieved from the STM excitation of an Au (30 nm)-SiO_2 (70 nm)-Au (30 nm) structure with different bandpass filters in front of the CCD camera. Unlike the 310 nm thick dielectric layer case, when the thickness is decreased to 70 nm, no "waveguide-like" mode is seen in Fig. 11.

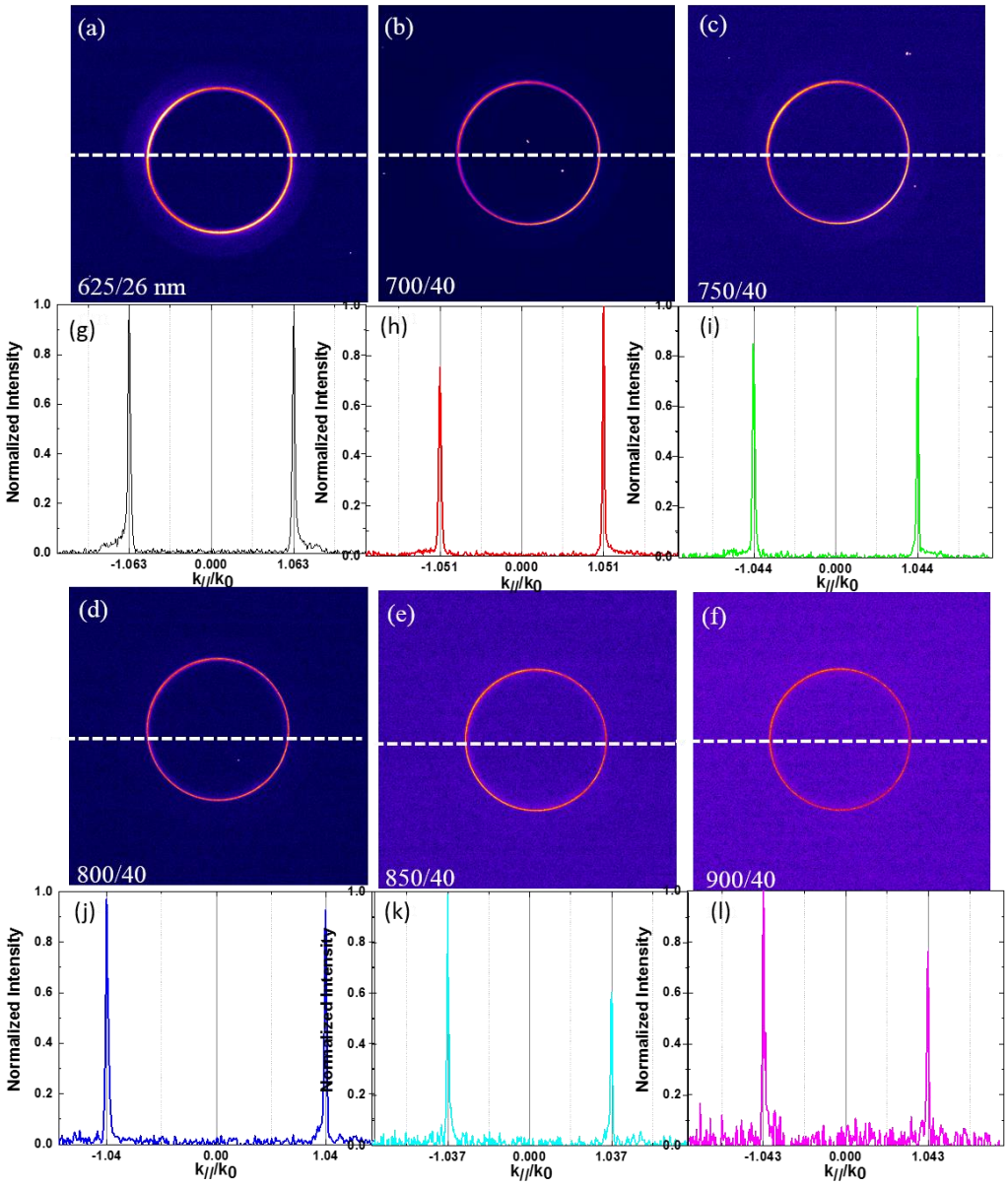

*Figure 11. Fourier space images acquired with different bandpass filters in front of the CCD camera for the Au (*30 nm*)-SiO_2 (*70 nm*)-Au (*30 nm*) structure. Fourier space image with bandpass filter (a)* 625/26 nm, *(b)* 700/40 nm, *(c)* 750/40 nm, *(d)* 800/40 nm, *(e)* 850/40 nm, *(f)* 900/40 nm. *Intensity profiles taken from the white dashed line in each Fourier space images are shown in (g)-(l). Bias is set as* 2.8 V *and tunnel current is* 1 nA. *Acquisition time is* 300 *seconds.*

To further investigate the experimental results of Fig. 11, we plot the effective index as a function of emission wavelength as well as the dispersion relations and results are shown in Fig.

12. Here, we also use the simulation results in the same way as we did in Fig. 6 for comparison. A 50 nm thick Au film without an SiO_2 layer is used as a reference.

From Fig. 12 (b), we see that the experimental dispersion relation for the Au (30 nm)-SiO_2 (70 nm)-Au (30 nm) structure and the Au film (50 nm) are nearly overlapping. Additionally, both of them lie on the line of the theoretical SPP dispersion curve (air/Au interface). The simulation results calculated by *Moustafa Achlan* and *Georges Raseev* show good agreement with the experimental results, except at short wavelengths around 625 nm. This discrepancy was attributed to a possibly incorrect dielectric function which has been already discussed in Fig. 6.

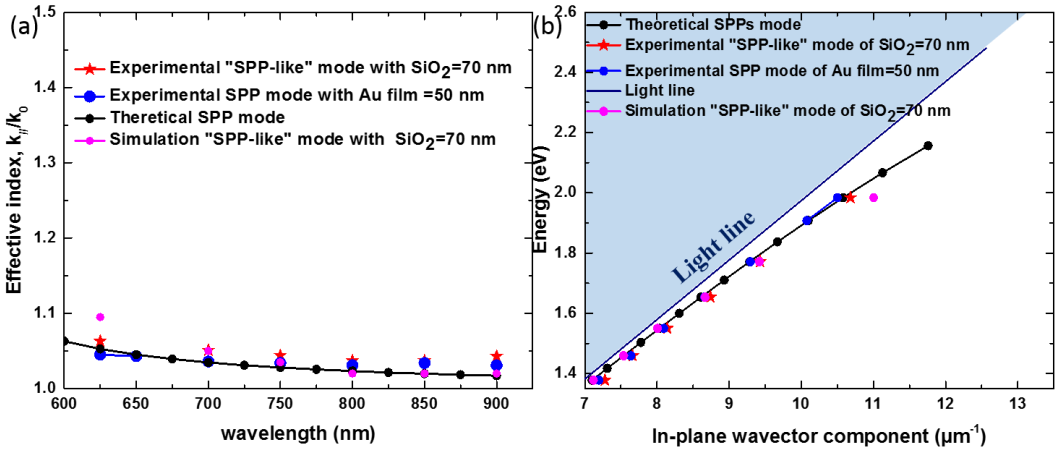

*Figure 12. Dispersion relations for the Au (*30 nm*)-SiO₂ (*70 nm*)-Au (*30 nm*) structure and an Au (*50 nm*) film. (a) Effective index of the "SPP-like" mode of the stack and of an Au film without a SiO₂ layer versus wavelength. The effective index of the "SPP-like" mode is determined from the radius of the inner ring in the Fourier space images shown in Figure 11. The experimental and theoretical effective indices of a "pure" SPP are also shown. (b) Plot of the dispersion relation (energy vs the in-plane wave vector component k//) for the modes of the plasmonic multi-layer stack and an Au film. The light line in the vacuum is also added for comparison.*

From the results shown above, we see that when the thickness of the SiO_2 dielectric layer is decreased to 70 nm, only the "SPP-like" mode is detected. This could mean that any other existing modes have an effective index greater than 1.49, the numerical aperture of our

objective. Thus, the appearance of measurable modes depends on the thickness of the dielectric layer. Below we continue to explore the effect of the thickness of the dielectric layer.

5.5.2 Fourier space images of the STM excitation of an Au (30 nm)-SiO_2 (190 nm)-Au (30 nm) multi-layer structure with different bandpass filters

For the 310 nm thick dielectric layer sample, both an "SPP-like" and "waveguide-like" modes were identified while for the sample where the thickness of the dielectric layer is 70 nm, only the "SPP-like" mode was detected. In the next step, we explore the case of a sample with an SiO_2 layer of intermediate thickness. Figure 13 (a)-(h) show the Fourier space images obtained from the STM excitation of the plasmonic multi-layer stack with Au (30 nm)-SiO_2 (190 nm)-Au (30 nm), using different bandpass filters at the detection. We find that unlike the 70 nm-SiO_2 layer sample, in the 190 nm-SiO_2 structure, the STM excitation excites two different modes (two rings are seen in the Fourier space images for short wavelength ($\lambda \leq$ 650 nm). Also compared to the 310 nm-SiO_2, the second mode appears at shorter wavelengths for the 190 nm structure.

In addition, intensity profiles obtained along the white dashed line in each Fourier space image are also shown in Fig. 13 (i)-(p). An interesting phenomenon is observed in the image where a bandpass filter at $655/40$ nm was used. At this wavelength, there is a strong increase in the intensity of the outer ring in the Fourier space image (see Fig. 13 (j)). This does not occur for the structure with the 310 nm thick SiO_2 layer. These observations suggest that there is a peak in the optical local density of states at this wavelength for this specific thickness, since this corresponds to a gap edge in the optical band structure of the MIM system [24].

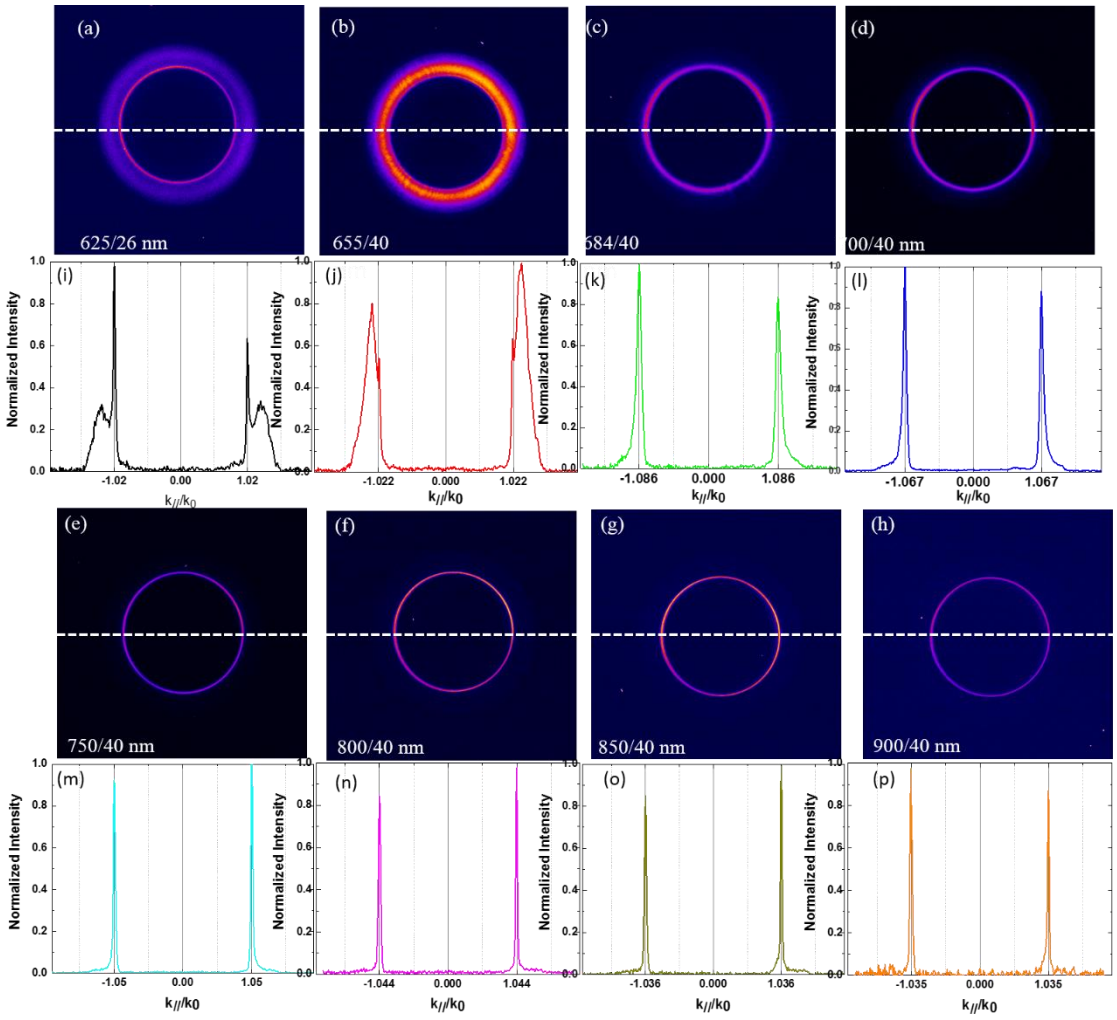

*Figure 13. Fourier space images acquired using different bandpass filters in front of the CCD camera for the Au (*30 nm*)-SiO_2 (*190 nm*)-Au (*30 nm*) structure. Fourier space image with a bandpass filter of (a)* 625/26 nm, *(b)* 655/40 nm, *(c)* 684/40 nm, *(d)* 700/40 nm , *(e)* 750/40 nm, *(f)* 800/40 nm, *(g)* 850/40 nm, *(h)* 900/40 nm . *Intensity profiles obtained along the white dashed line in each Fourier space image are shown in (i)-(p). Bias is set at* 2.8 V *and the tunnel current setpoint is* 1 nA. *Acquisition time is* 300 *seconds.*

Using the same method as previously, the effective indices as a function of the emission wavelength as well as the dispersion relations are plotted in Fig. 14. The two modes identified at wavelengths of 625 nm and 655 nm also exist in the simulation results, except that for the simulation, the modes have higher effective indices. Another interesting point is that at these two wavelengths, unlike for the other two structures, the effective indices of the "SPP-like"

mode are much lower than the theoretical calculation for the SPP mode on an air/Au interface (equation (5.3)). This is also true for the simulation results.

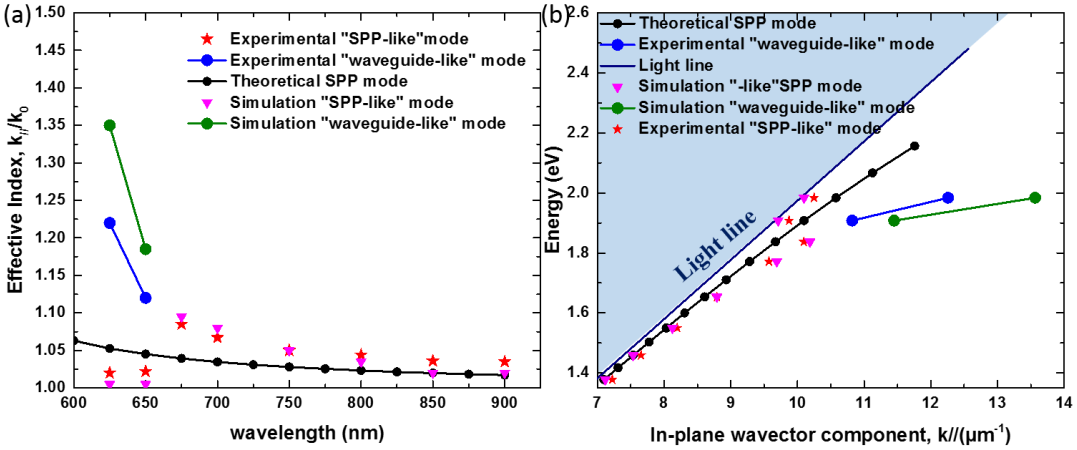

*Figure 14. Dispersion relations of the modes of the plasmonic multi-layer stack Au (*30 nm*)-SiO_2 (*190 nm*)-Au (*30 nm*). (a) Effective indices of "SPP-like" and "waveguide-like" modes versus wavelength. The effective indices are determined from the radius of the rings observed in the Fourier space images shown in Figure 14. The theoretical effective index of SPPs on an air/Au interface is also shown. (b) Dispersion relation between the energy and the in-plane wave vector component $k_{//}$ of the observed modes. The light line in vacuum is also added for comparison.*

To understand why the "SPP-like" modes have lower effective indices at short wavelength, laser excitation and further simulations are performed. Figure 15 (a) presents the Fourier space image acquired by laser excitation with an incident wavelength of 633 nm and "horizontal" polarization (see section 5.4). From Fig. 15 (a), looking only at the TM excitation, we observe the signature of two TM modes along the horizontal axis. Figure 15 (b) shows the STM excitation results with a bandpass filter of 625/26 nm in front of the CCD camera. Figures 15 (c) and 15 (d) plot the horizontal intensity profiles taken from the images in (a) and (b).

From the *laser* excitation experiment (Fig. 15 (c)), we measure that the effective indices of the two TM modes are $\frac{k_{\parallel}}{k_0} \approx 0.99$ and $\frac{k_{\parallel}}{k_0} \approx 1.27$. From the *STM* excitation experiment (Fig.15 (d)), we measure that the effective indices of the two TM modes are $\frac{k_{\parallel}}{k_0} \approx 1.02$ and

$\frac{k_{\parallel}}{k_0} \approx 1.22$. The slight difference in the effective indices measured by these two methods could be attributed to the finite bandwidth of the bandpass filter (used in the STM experiment). Note that the experimental error is estimated at approximately $0.02\ k_0$ per pixel.

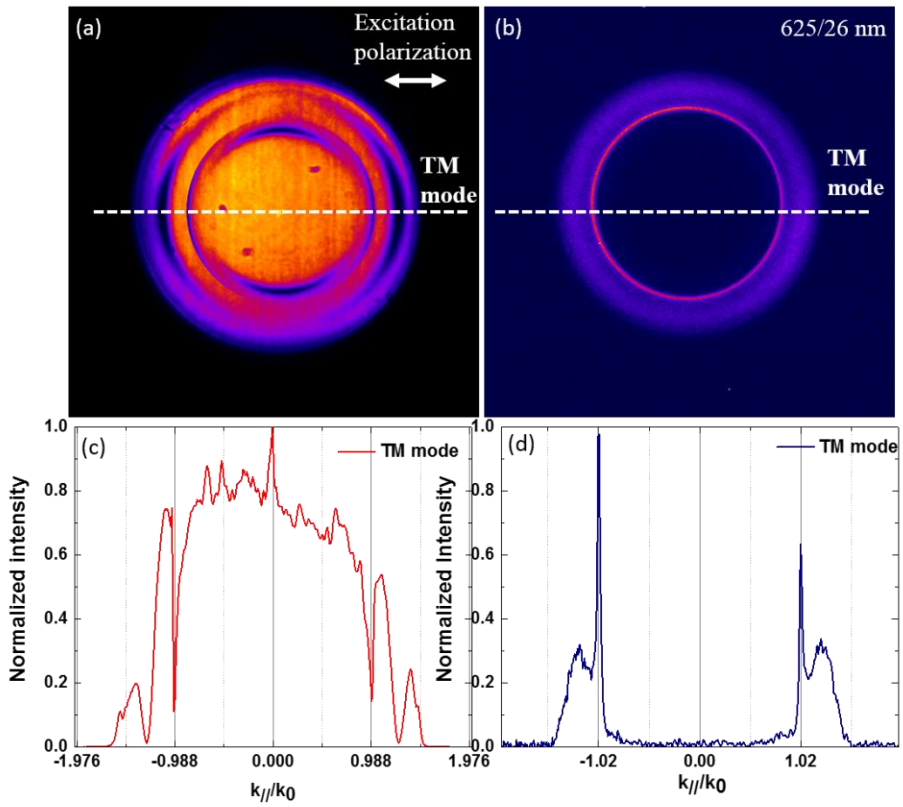

*Figure 15. Comparison of the laser and STM excitation of an Au (*30 nm*)-SiO_2 (*190 nm*)-Au (*30 nm*) structure. For the laser excitation, the incident wavelength is* 633 nm*. For STM excitation, we use the bandpass filter of 625/26 nm. Fourier space images acquired with (a)* ***Laser*** *excitation and "horizontal" polarization, (b)* ***STM*** *excitation and a bandpass filter. (c) Horizontal intensity profile from (a). (d) Horizontal intensity profile view from (b).*

Figure 16 (a) shows the simulated electric field distribution along the direction perpendicular to the interface (z-direction) when the effective index $\frac{k_{\parallel}}{k_0} = 1.0025$ (this is the simulated effective index for the first TM mode of the Au (30 nm)-SiO_2 (190 nm)-Au (30 nm) structure when $\lambda = 633$ nm). In this case, the peak of the electric field intensity in the dielectric layer is comparatively large as compared to that of the electric field intensity at the air/Au interface. As compared to the 310 nm-SiO_2 layer structure, for this structure with a SiO_2 layer

of intermediate thickness (190 nm), the hybrid "SPP-like" mode is of greater photonic or waveguide character. We can then explain the decrease in the effective indices at short wavelength as an increase in the photonic nature of the mode.

Figure 16 (b) shows the electric field distribution along the direction perpendicular to the interface (z-direction) when the effective index $\frac{k_{\parallel}}{k_0} = 1.395$ (this is the simulated effective index for the second TM mode of the Au (30 nm)-SiO_2 (190 nm)-Au (30 nm) structure when $\lambda = 633$ nm). Here, we find that the field distribution is similar to what we have seen for the 310 nm thick SiO_2 layer (Fig. 7 (b)). This is the "waveguide-like" mode.

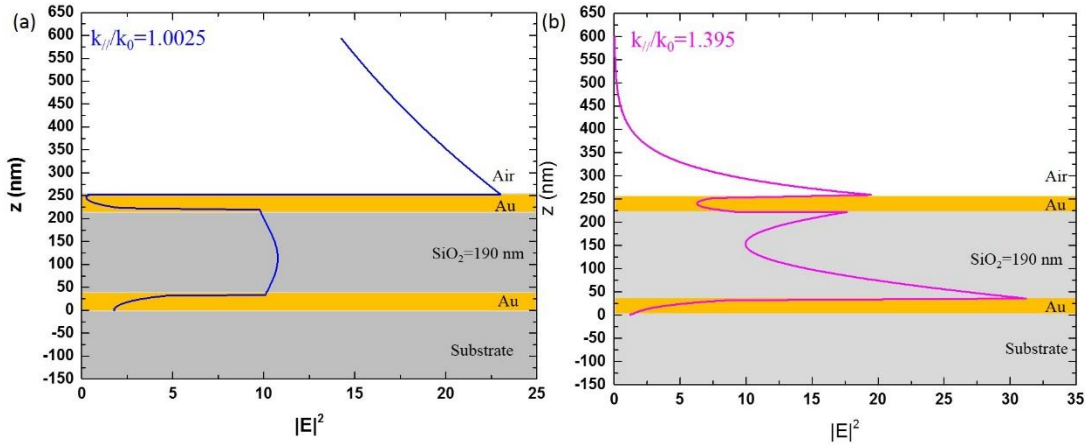

*Figure 16. Intensity distribution or squared modulus of the electric field along the direction perpendicular to the interface (*z*-direction) for an air/Au (*30 nm*)/SiO_2 (*190 nm*)/Au (*30 nm*)/substrate structure. The horizontal axis is the intensity of the electric field $|E|^2$ and the vertical axis is the z direction. In the calculation, a plane wave with wavelength* $\lambda = 700$ nm *was used and is incident from the substrate at angle determined by* $k_{//}/k_0$*. The electric field distribution along the z direction when the effective index is (a)* $\frac{k_{\parallel}}{k_0} = 1.0025$*, (b)* $\frac{k_{\parallel}}{k_0} = 1.395$.

5.5.3 Optical band images and spectra for the three different structures

By measuring the effective indices from the Fourier space images acquired with the STM excitation of the three plasmonic multi-layer stack structures, we have already plotted the dispersion relations of the "SPP-like" and "waveguide-like" modes. But due to the discontinuous wavelengths of the individual bandpass filters used, we do not measure a

continuous curve. In particular, we cannot identify for what "cut-off" wavelength the "waveguide-like" mode begins to exist for a specific SiO_2 layer thickness. In this section, we show the optical band images acquired by angularly-resolved spectroscopy. As shown in chapter 3, by projecting the Fourier-space image on the entrance slit of the spectrometer, we spectrally resolve the emitted light along a line in the Fourier plane. Thus, an image is recorded with spectral and angular coordinates along the horizontal and vertical axes, respectively.

Figure 17 (a)-(c) are the optical band images acquired using STM excitation of the three plasmonic MIM structures discussed above. We clearly see the obvious splitting of the curves when a new mode appears (see Figs. 17 (b) and 17 (c)). The wavelength at which the curve splits is ≈ 670 nm for the 190 nm-SiO_2 layer structure and ≈ 850 nm for the 310 nm-SiO_2 layer structure. As discussed above, no "waveguide-like" mode appears when the thickness is 70 nm-SiO_2 which is confirmed in Fig. 17 (a).

As we introduced in chapter 2, the STM excitation is of broadband nature. Note that through the interaction of the STM excitation with the plasmonic multi-layer stack, the spectrum of the emitted light changes. For the 190 nm structure, the wavelength range of the emission is from 550 nm to 850 nm and for the 310 nm structure, the wavelength range is extended to 1000 nm. This may be explained by realizing that by changing the sample, we change the frequency dependent optical local density of states which in turn then influences the excitation efficiency of the STM-nanosource.

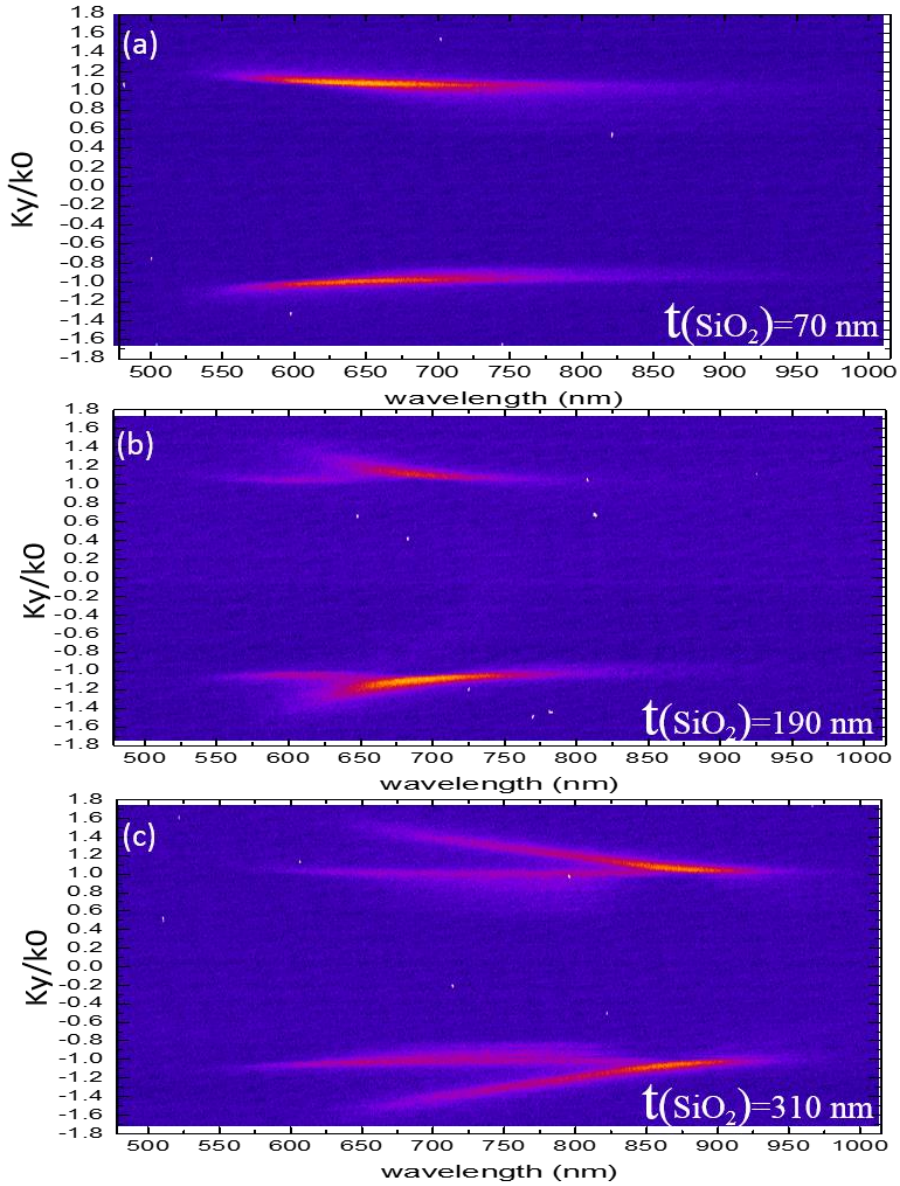

Figure 17. Angle-resolved spectroscopy. Effective index as a function of wavelength acquired by STM excitation of a plasmonic multi-layer stack with an SiO_2 layer of thickness (a) 70 nm*, (b)* 190 nm*, (c)* 310 nm*. These experimental data are measured by projecting the Fourier space image of the emitted light on the narrow entrance slit of the spectrometer. The partially closed entrance slit gives rise to a spectral resolution of about 8 nm (i.e., ≈0.02 eV at λ_0 = 700 nm). Bias is set to* 2.8V*, the setpoint current is* 1 nA *and acquisition time is* 300s*.*

Figure 18 (a) presents the optical spectra measured for the three plasmonic multi-layer stack structures. From Fig. 18 (a), we clearly see that as the thickness of the dielectric layer increases, the spectrum shifts to the red. This confirms the results of Fig. 17.

Another interesting point is that the spectrum for the 190 nm structure displays a comparatively narrow peak. Its FWHM (full-width at half-maximum) is around 125 nm. Note also its shape (a narrow peak at ≈ 740 nm with a shoulder at ≈ 710 nm).

Figure 18 (b) plots the three spectra of Fig. 18 (a) after smoothing. Here, vertical dashed lines are drawn to indicate the peaks or possible minima in each spectrum. The shoulder of the red curve (190 nm structure) may be interpreted as a dip at around 710 nm. For the 310 nm structure, there is also a slight dip at around 854 nm. Note that the "cut-off" wavelengths were identified in Fig. 17 (a) and (c) as ≈ 670 nm (190 nm structure) and ≈ 850 nm (310 nm structure).

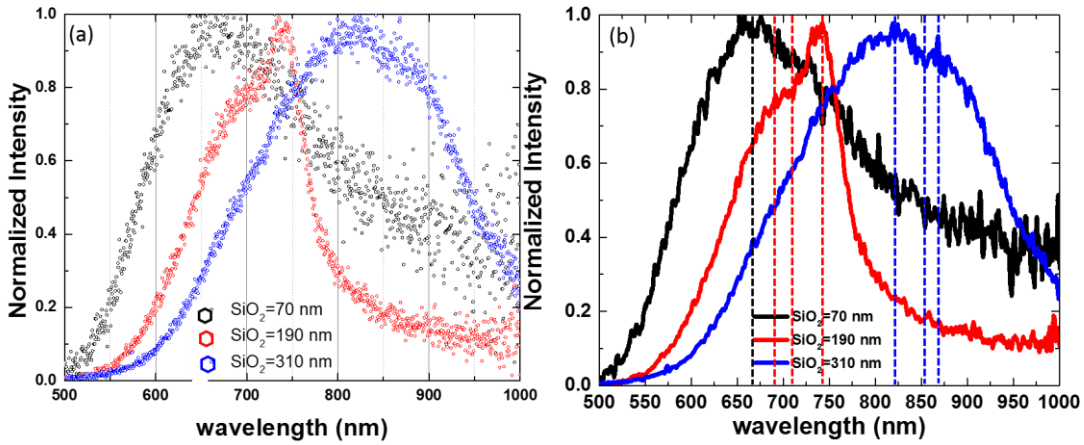

Figure 18. Optical spectra measured for the different plasmonic multi-layer stack structures. (a) Spectra for the structure with an SiO_2 thickness of 70 nm *(black curve),* 190 nm *(red curve),* 310 nm *(blue curve). (b) The spectra after smoothing. The smoothing is done in the Origin file over 10 points. The vertical dashed lines represent the peak and dip positions in each spectrum. Bias is* 2.8V*, the setpoint current is 1 nA and acquisition time is 300 s.*

The observed dip may be due to the strong coupling of the "waveguide-like" and "SPP-like" modes in the plasmonic multi-stack structure. Figure 19 (a) and 19 (b) plot the simulation results for optical band images for the 190 nm and 310 nm structure calculated by *Moustafa*

Achlan and *Georges Raseev*. In both Fig. 19 (a) and 19 (b), we see an anti-crossing which is easiest to see for the 190 nm structure as compared to the 310 nm structure. This is reflected in the experimental results where the dip is more pronounced for the 190 nm structure as compared to the 310 nm structure. Though this phenomenon is not visible in the experimental optical band image (Fig. 17), the dispersion curve for the 190 nm-SiO_2 layer structure (Fig. 14 (b)) is reminiscent of what would be seen for strong coupling.

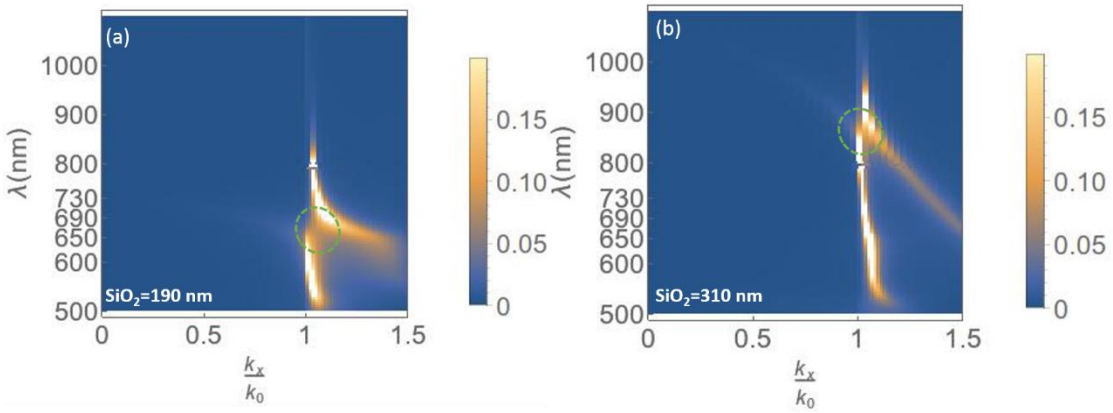

Figure 19. Optical bands simulation results. The horizontal axis is k_x/k_0 *and vertical axis is the wavelength. (a) Optical bands for the (*30 nm*)/SiO₂ (*190 nm*)/Au (*30 nm*) structure. (b) Optical bands for the (*30 nm*)/SiO₂ (*310 nm*)/Au (*30 nm*) structure. Note the anti-crossing behaviour apparent in the circled region.*

5.6 Conclusion

In conclusion, we have probed the optical band structure of a plasmonic Au-SiO_2-Au multi-layer stack using an STM-excited nanosource. The dispersion relations show the existent of an "SPP-like" and a "waveguide-like" mode. By changing the thickness of the dielectric layer, we find that the coupling between the "SPP-like" and the "waveguide-like" modes is varied. A "strong coupling" feature is seen when the thickness of the SiO_2 layer is 190 nm.

Moreover, laser and STM excitation of the same stack is compared. We demonstrate that the STM excitation, which is comparable to an "emission measurement" has a better signal-to-noise ratio than the laser excitation which is analogous to an "absorption measurement".

These findings enhance our understanding of plasmonic multi-stack structures and at the same time highlight the potential of the STM as an optical nanoscopic technique to probe the optical bands of plasmonic nanostructures.

[1] R. C. Word, J. P. S. Fitzgerald, and R. Könenkamp, “Direct coupling of photonic modes and surface plasmon polaritons observed in 2-photon PEEM,” *Opt. Express*, vol. 21, no. 25, pp. 30507–30520, 2013.

[2] A. Pannipitiya, I. D. Rukhlenko, M. Premaratne, H. T. Hattori, and G. P. Agrawal, “Improved transmission model for metal-dielectric-metal plasmonic waveguides with stub structure,” *Opt. Express*, vol. 18, no. 6, pp. 6191–6204, 2010.

[3] H. Ditlbacher *et al.*, “Coupling dielectric waveguide modes to surface plasmon polaritons,” *Opt. Express*, vol. 16, no. 14, pp. 10455–10464, 2008.

[4] A. Sellai and M. Elzain, “Characteristics of a dielectric-metal-dielectric plasmonic waveguide,” *Phys. E*, vol. 41, no. 1, pp. 106–109, 2008.

[5] J. A. Dionne, L. A. Sweatlock, H. A. Atwater, and A. Polman, “Planar metal plasmon waveguides: Frequency-dependent dispersion, propagation, localization, and loss beyond the free electron model,” *Phys. Rev. B*, vol. 72, no. 7, p. 75405, 2005.

[6] J. A. Dionne, L. A. Sweatlock, H. A. Atwater, and A. Polman, “Plasmon slot waveguides: Towards chip-scale propagation with subwavelength-scale localization,” *Phys. Rev. B*, vol. 73, no. 3, p. 35407, 2006.

[7] J. Park and B. Lee, “An approximate formula of the effective refractive index of the metal-insulator-metal surface plasmon polariton waveguide in the infrared region,” *Jpn. J. Appl. Phys.*, vol. 47, no. 11, pp. 8449–8451, 2008.

[8] C. Min and G. Veronis, “Absorption switches in metal-dielectric-metal plasmonic waveguides,” *Opt. Express*, vol. 17, no. 13, pp. 10757–10766, 2009.

[9] Z. Yu, G. Veronis, S. Fan, and M. L. Brongersma, “Gain-induced switching in metal-dielectric-metal plasmonic waveguides,” *Appl. Phys. Lett.*, vol. 92, no. 4, p. 41117, 2008.

[10] T. H. Lan, Y. K. Chung, J. E. Li, and C. H. Tien, “Plasmonic rainbow rings induced by white radial polarization,” *Opt. Lett.*, vol. 37, no. 7, pp. 1205–1207, 2012.

[11] A. F. Koenderink *et al.*, “Near-field optics and control of photonic crystals,” *Photonics Nanostructures - Fundam. Appl.*, vol. 3, no. 2–3, pp. 63–74, 2005.

[12] A. F. Koenderink and A. Polman, “Complex response and polariton-like dispersion

splitting in periodic metal nanoparticle chains," *Phys. Rev. B*, vol. 74, no. 3, p. 33402, 2006.

[13] A. F. Koenderink, R. De Waele, J. C. Prangsma, and A. Polman, "Experimental evidence for large dynamic effects on the plasmon dispersion of subwavelength metal nanoparticle waveguides," *Phys. Rev. B*, vol. 76, no. 20, p. 201403, 2007.

[14] K. Kim, Y. Cho, H. Tae, and J. Lee, "Optical guided dispersions and subwavelength transmissions in dispersive plasmonic circular holes," *Opto-Electronics Rev.*, vol. 14, no. 3, pp. 233–241, 2006.

[15] D. Canneson *et al.*, "Surface plasmon polariton beams from an electrically excited plasmonic crystal," *Opt. Express*, vol. 24, no. 23, p. 26186, 2016.

[16] P. Bharadwaj, A. Bouhelier, and L. Novotny, "Electrical excitation of surface plasmons," *Phys. Rev. Lett.*, vol. 106, no. 22, p. 226802, 2011.

[17] T. Wang, E. Boer-Duchemin, Y. Zhang, G. Comtet, and G. Dujardin, "Excitation of propagating surface plasmons with a scanning tunnelling microscope," *Nanotechnology*, vol. 22, no. 17, p. 175201, 2011.

[18] P. Berini, "Plasmon polariton modes guided by a metal film of finite width," *Opt. Lett.*, vol. 24, no. 15, pp. 1011–1013, 1999.

[19] X. Oulton, R.F.; Sorger, V.J.; Genov, D.A.; Pile, D.F.P.; Zhang, "A hybrid plasmonic waveguide for subwavelength confinement and long-range propagation," *Nat. Photonics*, vol. 2, no. 8, pp. 496–500, 2008.

[20] P. B. Johnson and R. W. Christy, "Optical constants of the Noble Metals," *Phys. Rev. B*, vol. 6, no. 12, pp. 4370–4379, 1972.

[21] Q. Li, "Optimization of point spread function of a high numerical aperture objective lens : application to high resolution optical imaging and fabrication," ECOLE NORMALE SUPERIEURE DE CACHAN, 2014.

[22] W. E. Moerner and L. Kador, "Optical Detection and Spectroscopy of single Molecules in a solid," *Phys. Rev. Lett.*, vol. 62, no. 21, pp. 2535–2538, 1989.

[23] M. Orrit and J. Bernard, "Single pentacene molecules detected by fluorescence excitation

in a p -terphenyl crystal," *Phys. Rev. Lett.*, vol. 65, no. 21, pp. 2716–2719, 1990.

[24] S. Cao *et al.*, "Revealing the spectral response of a plasmonic lens using low-energy electrons," *Phys. Rev. B*, vol. 96, no. 11, p. 115419, 2017.

Chapter 6

STM excitation of surface plasmons on individual Au triangular plates

In this chapter, we discuss the experimental results obtained when the STM is used to excite surface plasmons on isolated Au triangular plates. Two separate investigations are included. In the first section, we demonstrate a directional nanosource of light achieved by correctly choosing the STM excitation position on the triangular plate. In the second section, we investigate whether we can probe the *optical* local density of states (LDOS) of an individual plasmonic object by STM. Note that this is a work in progress and the explanations of the experimental results are preliminary.

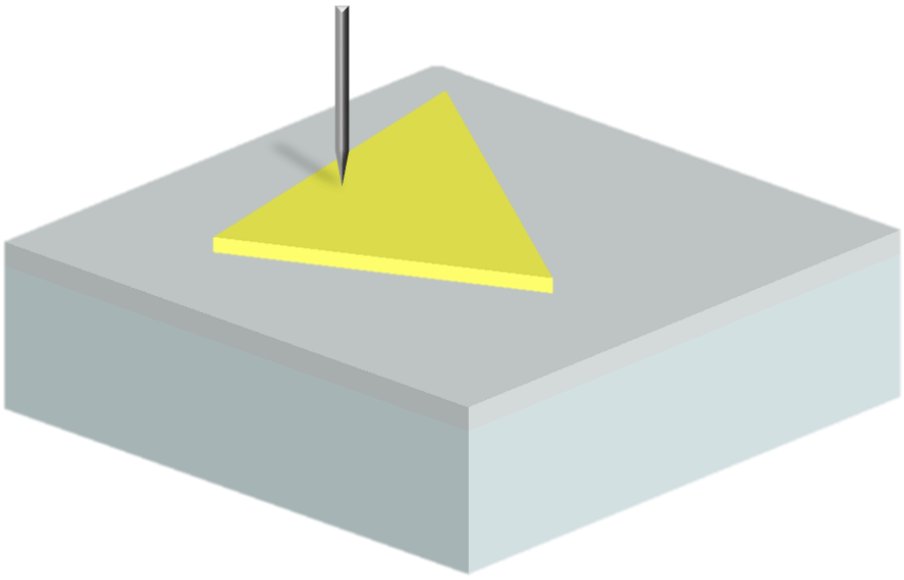

6.1 Directional light emission from an Au triangular plate

6.1.1 Introduction

In previous chapters, we have discussed directional light emission from propagating SPPs scattering into light at slits in a thick gold film (chapter 3 and 4). In this section, we focus on the *localized* surface plasmons of an isolated triangular plate excited by STM. In this way, a directional nanoscale source of light is obtained.

Directional light emission from plasmonic nanoparticles has already been reported for different structures such as Yagi-Uda antennas [1], [2], a single gold nanodisk [3], and U-shape nanoantennas [4]. In this section, we will discuss the directional light emission that arises when a single triangular Au plate is excited by STM.

6.1.2 Sample preparation and characterization

These triangular plates have been synthesized by colloidal chemistry using a widely used protocol, termed seeded growth, in water in the presence of the CTAB surfactant. These nanoplates have been provided by Sylvie Marguet (CEA Saclay) in the context of a collaboration (COSSMET project) following an already published protocol by the Chad Mirkin group in 2005 [5]. Figure 1 shows the Scanning Electron Microscopy (SEM) image of an area of the sample where the Au triangular plates have been dispersed on the ITO (85 nm)-coated glass substrate. Their side lengths range from 600 nm to 900 nm. From Fig. 1, we see that there are also some hexagonal plates on the sample. It is common to obtain a variety of shapes using such synthesis methods [6], [7].

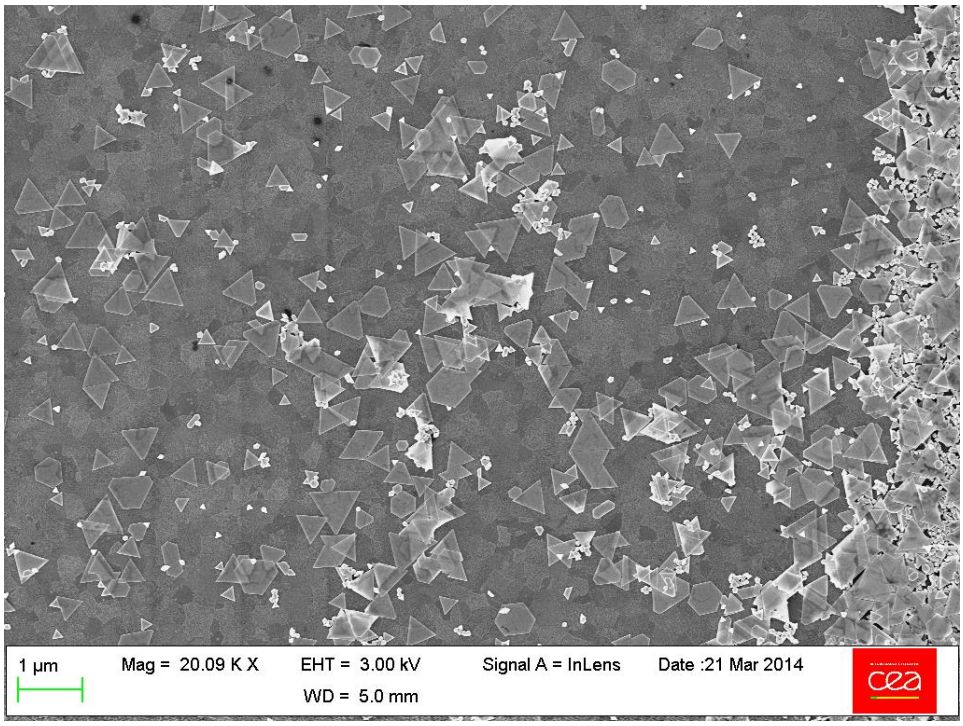

Figure 1. SEM (Scanning Electron Microscope) image of an area on the sample with Au nanotriangular and hexagonal plates. Sample deposited on an 85 nm*-thick ITO layer on a glass coverslip.*

Figure 2 shows two other different ways of characterizing an individual triangular plate. Figure 2 (a) shows the Atomic Force Microscopy (AFM) image of a triangular plate and we measure its side length of around 700 nm. The profile taken along the white dashed line in Fig. 2 (a) is shown in Fig. 2 (b). We measure its height of around 20 ± 3 nm. Figure 2 (c) is the STM image of another triangular plate and its side length is measured near 750 nm and the height is around 22 ± 3 nm. Additionally, its 3D topography image is presented in Fig. 2 (d).

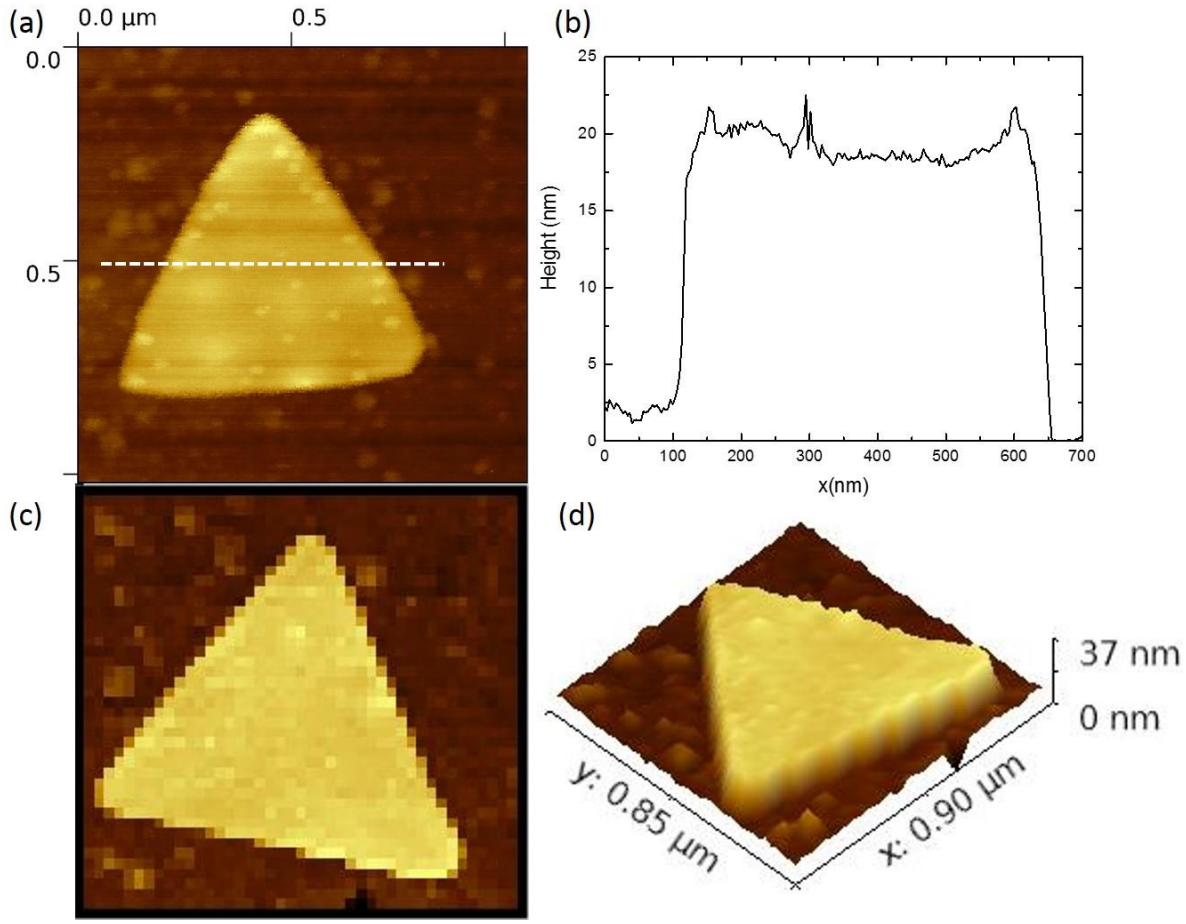

Figure 2. Different ways of characterizing triangular plates. (a) AFM image of a triangular plate with an average side length of ≈ 700 nm. *(b) Height profile along the white dashed line in (a) showing that the height of the triangular plate is* ≈ 20 nm. *(c) STM image of another triangular plate with side length* ≈ 750 nm *and height* ≈ 20 nm. *During the image, the bias is set at* 0.5 V *and tunnel current is at* 0.1 nA. *(d)* 3D *STM topography image of the triangular plate in (c).*

6.1.3 Fourier space images obtained with the STM excitation centered on the triangular plate

In order to study the light emitted when a thin gold triangle is excited by STM, Fourier space imaging will be used. Recall that in Fourier space we measure the emission angle and angular spread of the emitted light. First, our STM excitation is located in the center of a triangular plate. The side length of the plate is L ≈ 700 nm with ≈ 20 nm in thickness. In these experiments, the "Veeco" setup is employed (see chapter 2). Bias is set at 2.8 V so that SPPs emitting in the visible may be excited. The result is shown in Fig. 3 (a). From Fig. 3 (a), we see

that the light is distributed almost homogenously over a ring pattern. The inside radius of the ring corresponds to the critical angle of total internal reflection (NA = 1) and the outside radius is the numerical aperture of the microscope (NA = 1.45). Figure 3 (b) shows three different intensity profiles along the three dashed lines in Fig. 3 (a). From Fig. 3 (b), we see that light is emitted at angles from around 42° to 72° or $1 < n\sin\theta < 1.45$ (where, n is the refractive index of the glass substrate and θ is the emission angle). Note also that some light is also emitted at low angles ($\theta < 42°$).

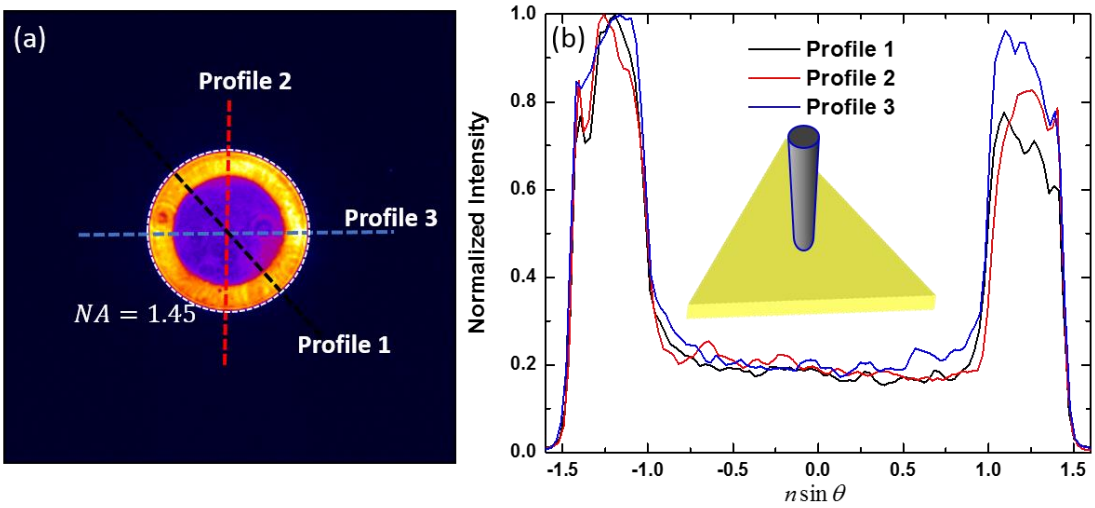

Figure 3. Fourier space image when the excitation is in the center of a triangular plate with side length ≈ 700 nm *and a thickness of* ≈ 20 nm. *(a) The Fourier space image showing that light is distributed over a ring. The white dashed circle denotes the numerical aperture of the collection objective,* NA = 1.45. *(b) Intensity profiles along the three dashed lines in (a). The horizontal axis in the intensity profile is* n sin θ, *where,* n *is the refractive index of the glass substrate and* θ *is the emission angle, and the vertical axis is the normalized intensity. Bias is set at* 2.8 V *and the setpoint is ranging from 1 nA to 4 nA. Acquisition time is* 300 *seconds.*

The specificity of the system being studied is that it is of "intermediate" size. An object whose length $L \gg \lambda$ may be considered similar to a thin film; on the other hand, radiation from a nanoparticle of size $L \ll \lambda$ may be approximated as a dipole. In our case, however, $L \approx \lambda$. This spcificity is confirmed if we examine theoretically the two cases (i) $L \gg \lambda$ (thin film) and (ii) $L \ll \lambda$ (dipole radiation) (calculation seen in Appendix C). From Fig. 4 (a) we see that most

of the radiation from a dipole above a thin (20 nm thick) Au film is emitted as expected at the leakage radiation angle. A dipole above a glass substrate (Fig. 4 (b)) has a peak in its Fourier space image at the air/glass critical angle, but emits comparatively more of its radiation at higher angles than the thin film case. Neither, however, has the same almost "flat" response for $1 < |\mathrm{n}\sin\theta| < 1.49$ which is seen for the STM-excited triangle (Fig. 3 (b)).

Note also that in Figs. 4 (a) and 4 (b) the normalized intensity is ≈ 0 for $-1 < \mathrm{n}\sin\theta < 1$ while it is ≈ 0.2 for the STM-excited triangle (Fig. 3 (b)).

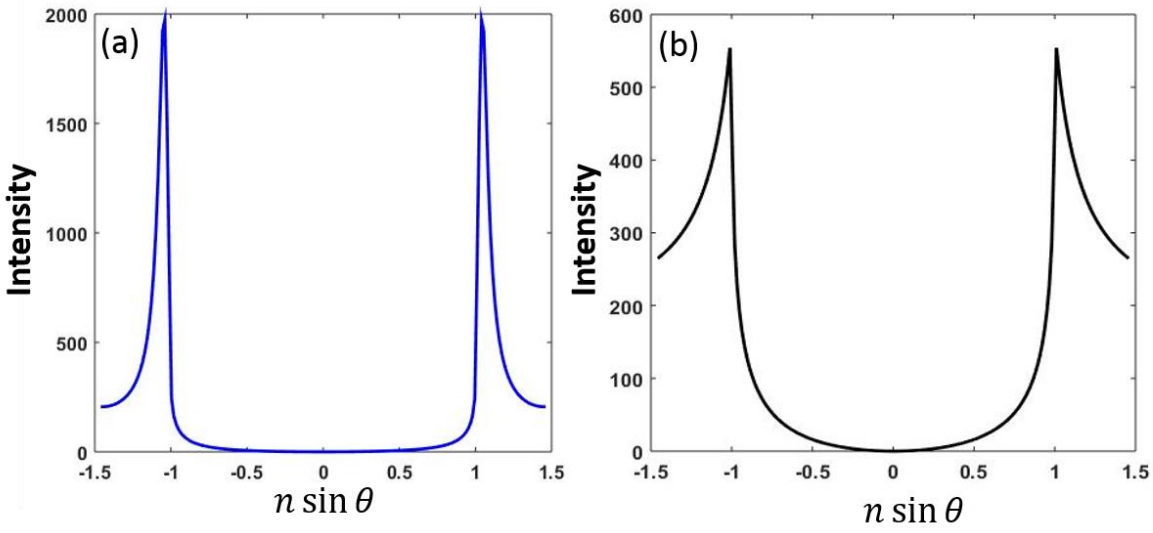

Figure 4. Calculated Foruier space intensity profiles for a vertical dipole above a gold film on glass. The dipole is at the air/gold interface. (a) Dipole above a 20 nm-thick Au film. (b) Dipole above a glass substrate (Au film thickness is 0). The detailed calculation is seen in Appendix C.

From the size of the triangle ($\mathrm{L} = 700$ nm, thickness ~ 20 nm), we do not expect its dipolar modes to be in the visible. Thus, even if they are excited by the STM-nanosource, their emission is not detected. Since the STM-nanosource may be approximated as a vertical oscillating dipole, the Fourier space image of Fig. 4 (b) could be expected if the STM-nanosource did not couple to any modes in the visible. Instead, the pattern displayed in the Fourier space suggests that higher order localized plasmonic modes of a triangular plate are excited by the STM-nanosource. The superposition of the higher order modes could lead to observed broad angular distribution in the Fourier space. The different modes existing on the triangular plates will be discussed in section 6.2.

6.1.4 Fourier space images when the excitation is at the edge of a triangular plate

Now on the same triangular plate, we move our excitation to the center of a side edge and record the Fourier space images seen in Fig. 5. For the Fourier space images, all the experimental parameters are kept the same as those for the excitation in the center of the triangular plate. Figure 5 (a) displays the STM image of our triangular plate and we annotated the three different sides as b, c, and d. Before each Fourier space image, a topography image is obtained in order to locate the next excitation position. The STM excitation is sequentially located at the center of side b, c, and d.

Figure 5 (b)-(d) are the corresponding Fourier space images. Here, we observe that the Fourier space images all show the wide angular distribution patterns which are similar to Fig. 3 (a). But one interesting thing is very different: when we move our excitation to the side edge of the triangular plate, we see that the light distribution is no longer isotropic. In each Fourier space image, there is more light in one direction and less light is in the opposite direction.

Additionally, from Fig. 5 (b)-(d), we find that the direction of the emitted light is away from the excited edge. This means that the excitation position and the orientation of the triangular plate will determine the direction of the light emission.

Figure 5 (e)-(g) respectively show the polar emission patterns obtained along the white dotted lines in Fig. 5 (b)-(d). The white dotted lines are perpendicular to the side edge. The intensities of the polar patterns are normalized. From the polar emission patterns, we see the anisotropy of the emission more directly. Additionally, we also see that the light distribution covers a large range of angles from $\approx 42°$ to $\approx 72°$, i.e., between the critical angle and the maximum acceptance angle of the objective.

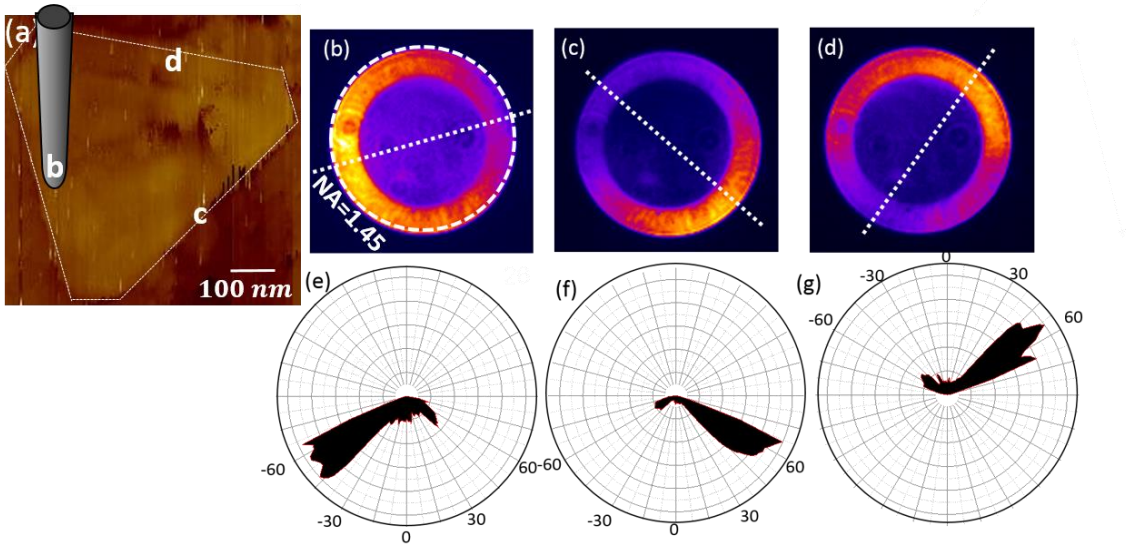

Figure 5. STM electrical excitation of a triangular plate in the center of an edge (positions respectively b, c and d). (a) STM image of a triangular plate with a side length of near ≈ 700 nm *and a thickness* ≈ 20 nm. *The white line indicates the edges of the triangle. (b)- (d) Fourier space images with the STM excitation respectively at the center of each edge b, c and d. (e)- (g) Polar emission patterns obtained along each white dotted line in the Fourier space images. The experiment is performed on the "Veeco" setup. The bias is set at* 2.8 V *and the setpoint current is in the range of* 1 nA *to* 4 nA. *Acquisition time is* 300 s.

In order to quantify the directional emission, we will use a quantity called the directivity. A simple definition of the directivity is the intensity ratio between the point of maximum emitted power (F) and the point on opposite side of Fourier space of emitted power (B) [1]:

$$D = 10\log_{10}\left(\frac{F}{B}\right) \quad (6.1)$$

In this way, we calculate the directivity values for each side b, c and d: 4.3 dB, 6.8 dB and 5.7 dB.

Compared with the Yagi-Uda antenna, we find that using this simple definition for directivity, the highest directivity we achieve from the triangular plate is even slightly higher than that which has been measured for a quantum dot coupled to a Yagi-Uda antenna (6 dB) [1]. Note, however, that while the angular spread in θ direction is similar for both systems, the spread in the φ direcion is about a factor of two smaller for the Yagi-Uda antenna. There are

other advantages of an nanotriangle directional source. First of all, it is complicated to fabricate Yagi-Uda antennas since five nanostructures must be carefully aligned and also its directivity is very sensitive to the excitation location. Secondly, in our case, we achieve different directional light emission by moving the excitation to different sides of the triangular plate, while in the Yagi-Uda antenna case, they need to fabricate differently orientated nanostructures for light emission in different directions. Finally, the Yagi-Uda antenna only works for a small wavelength range. While more experimental work is necessary (i.e., using bandpass filters in front of the CCD camera) the triangular plate appears to work well over a broad wavelength range since our STM-nanosource is broadband.

In order to explore further the possible origins of the directional light emission, we investigate the influence of the particle shape. To understand if the shape of the structure may have an effect on the directivity, a hexagonally shaped plate which also exists on the sample is investigated. We repeat the STM excitation experiment in the center of each edge of the structure. All the experimental parameters are kept the same as for the triangular plate. Here, our hexagonal plate has the same thickness (≈ 20 nm) as the triangular plate. The hexagonal plate has a shortest side length of near ≈ 300 nm and a longest side length of around ≈ 500 nm and its STM image is shown in Fig. 6 (a).

From Fig. 6 (a), we see the six different sides annotated as b to g in sequence. In this case, our STM excitation moves from side b until side g. Fourier space images are recorded on the CCD camera and the results are shown in Fig. 6 (b)-(g). We clearly see that in the Fourier space image, the light is concentrated along one part of the ring. Besides, the direction of light emission in Fourier space is also perpendicular to the side direction for the hexagonal plate as was the case for the triangle.

Figure 6 (h)-(m) show the polar emission patterns obtained along the white lines in Fig. 6 (b)-(g). Compared with the triangle results, the hexagonal plate also presents directional light emission. We use equation (6.1) to calculate the directivity. The directivity values for each side from b to g are respectively 5.6 dB, 4.9 dB, 3.5 dB, 4.7 dB, 3.4 dB and 4.1 dB.

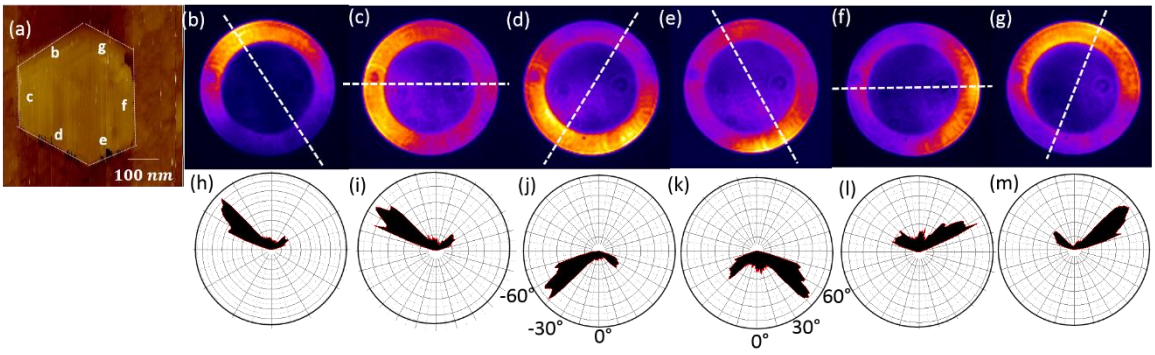

Figure 6. Fourier space images of the STM excitation of a hexagonal plate with the excitation located at different edges annotated from b *to* g. *(a) STM image of a hexagonal plate with a longest side length of near* 500 nm *and a shortest side length of near* 300 nm. *The white lines on the image indicate the edges of the plate. (b)-(g) Fourier space images for different excitation positions b to g. (h)-(m) Polar emission patterns obtained along each dashed white line in (b)-(g). The experiment is performed on the "Veeco" setup. Bias is set at* 2.8 V, *setpoint current is in the range of* 1 -4 nA. *Acquisition time is* 300 s.

From the comparison between triangular and hexagonal plates, we see that the directional light emission obtained does not seem to depend on the shape of the nano-object. The directivity is always perpendicular to the excited edge of the structure.

To understand possible mechanisms for such directional light emission from a single plate when the excitation is on the edge, we conduct another experiment and move the excitation location to the vertex of the same triangular plate as in Fig. 5. Fourier space images are recorded and the results are shown in Fig. 7. Figures 7 (a) and 7 (b) show the Fourier space image when the excitation is at one vertex and at the corresponding edge respectively (a and b in the STM image indicate the excitation positions). From the comparison of Figs. 7 (a) and 7 (b), we see that when the excitation is located at a vertex, the Fourier space image displays a different pattern than when the excitation is at the edge. Now, when the excitation is at the vertex, the direction of light emission is mainly towards its two neighboring sides rather than in line with the vertex (more data can be seen in Appendix C).

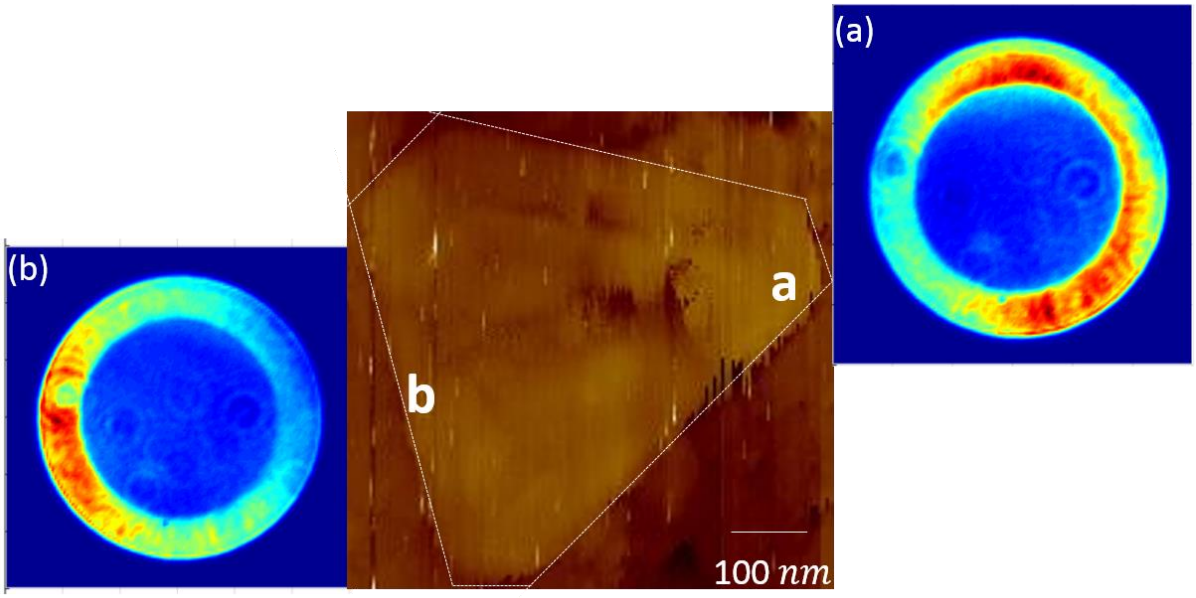

Figure 7. Fourier space images of STM excitation of a triangular plate with the excitation located at a vertex and on an edge. Fourier space image when the excitation position is (a) at the vertex and (b) at the edge of the triangular plate. The experiment is performed on the "Veeco" setup. Bias is set at 2.8 V *and setpoint current is in the range of* 1 nA *to* 4 nA. *Acquisition time is* 300 s.

According to all the above mentioned experimental results, we put forward some ideas which could explain the directional light emission.

(1) First, as we mentioned in the previous subsection, higher order plasmonic modes of the large triangular plate may be excited. Without simulations however, we cannot determine with precision which higher order modes are excited. From the reference [3], we learn that when the excitation by a focused high energy electron beam is off-centered on a nanodisk, directional light emission is also obtained. Their simulation results show that directional light emission is due to the far field interference of different multipole (magnetic dipole and electric quadrupole) moments generated in the disk. So, in our case, by analogy, the directional emission may be due to the interference of the radiation from higher order multipole modes of the triangular plate when the excitation if off-centered. However, since a hexagonal plate has six-fold symmetry and a triangular plate has three-fold symmetry, while some modes in each structure may be similar, but others will be quite different. Thus, it seems surprising

that the directionality is so similar for triangular and hexagonal plates, which have different sizes and symmetries, if the directionality is purely the result of the excitation of higher order modes. More data and a careful look at how the directionality varies as a function of particle shape and size, as well as the corresponding simulations are necessary to clarify this point.

(2) Second, another possibility is that the directional light emission is related to the edge. As illustrated in Fig. 8 (a), when the tip is at the edge of the plate, light will scatter at the edge. It seems possible that more light might be collected at angles in directions away from the metal triangle, since there are losses in the metal. i.e., some of the light in other directions may be absorbed. As a result, we obtain that more light is emitted away from the edge. To confirm this hypothesis, further experiments should be completed. The experiment is sketched in Fig. 8 (b), the sample is an Au film covering, for example, half the substrate. In this case only "film-like" and no "particle-like" modes will exist. STM excitation at the edge of the Au film on glass will then be performed. If we can obtain directional light emission in this experiment, this suggests that our directional light emission from the edge of the triangular plate could be due to an edge effect rather than to the excitation of higher order modes. Using this simplistic argument, however, one would expect to see directional light emission in the direction of the vertex in Fig. 7. Note that the triangle vertices are often truncated (see Fig. 7), so one might think that more light should be emitted in the direction away from the absorbing metal. Thus we may conclude that more work (both experiments and simulations) are necessary to clearly elucidate the mechanisms which are responsible for the observed directional emission of light.

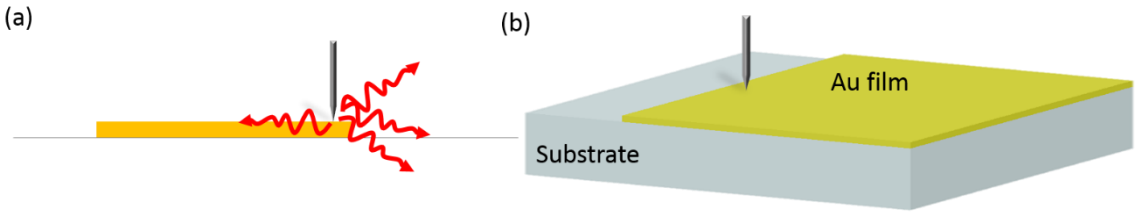

Figure 8. (a) Schematic illustration when the excitation is at the edge of the triangular plate. More light may scatter towards the substrate side because on the other side there is more loss in the Au film. (b) Designed experiment to evaluate the proposed edge effect. In this experiment, the deposited Au film will not cover the whole substrate and the STM excitation will be located

at the edge of the gold film.

6.2 Can we probe the *optical* local density of states of an individual triangular plate with the STM-nanosource?

6.2.1 Introduction

As discussed briefly in chapter 2, the *optical* or *electromagnetic* local density of states influences the local optical behavior (e.g., whether a fluorophore will be quenched or enhanced) [8]. Besides, we noted in chapter 2 that the *electronic* local density of states (*E*-LDOS) is distinct from the *optical* LDOS, and that it is known that the scanning tunneling microscope may be used to resolve the *E*-LDOS with atomic resolution in vacuum.

In this section, we want to explore whether we can resolve the *optical* LDOS using the STM-nanosource. If we can map the *optical* LDOS of a nanostructure, we obtain information about the photonic eigenmodes of the nanostructure.

There are various techniques that may be used to map the *optical* LDOS. Scanning near-field optical microscopy (SNOM) has been used to image the *optical* LDOS in an optical corral [9]. Two-photon luminescence (TPL) microscopy was also shown to be a possibility for the visualization of the *optical* LDOS of a thin gold microcrystal [10]. Additionally, electron energy-loss spectroscopy (EELS) was shown to map the projection in the direction of the exciting high energy electron beam of the *optical* LDOS in nanostructures [11], [12].

Theoretical calculations have suggested that the STM has strong similarities with the scanning near-field optical microscope (SNOM) [13]. While results by *Guillaume Schull* et al., have shown that the STM can *optically* probe the *electronic* LDOS on a triangular Au island [14], a demonstration that the STM can map the *optical* LDOS is still lacking. In this section, we will discuss the experimental results where we investigate the possibility of using the STM-nanosource to map the *optical* LDOS of an individual triangular plate.

Triangular plates of smaller sizes have previously been studied by different techniques. For a small individual triangular plate of side length around ≈ 280 nm, experimental investigations have shown the existence of three eigenmodes at the *vertices*, along the *edges* and in the *center* which cover a wide spectral response from the ultraviolet to near infrared

range [15]. In their work, low-loss energy-filtering transmission electron microscopy (EFTEM) was employed to map the surface plasmon resonances on a single small triangular nanoprism. Figure 9 presents their results for the *(b) vertex, (c) edge* and (e) *center* modes as well as (d) a combination of edge and center modes for this silver triangular structure [15].

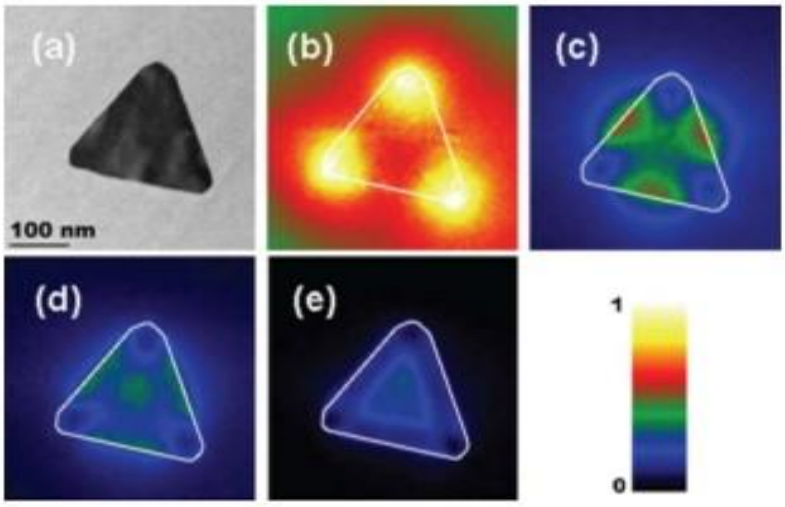

Figure 9. Five EFTEM images acquired on a 276.5 nm *triangular silver nanoprim at (a) 0, (b)* $0.79 - 1.02$*, (c)* $1.34 - 1.57$*, (d)* $1.54 - 1.77$*, and (e)* $1.89 - 2.12$ *eV. For (b) to (e), the outer contour of the nanoparticle is outlined by thick white lines. The intensity scale is common to the four images. Note the existence of (b) corner, (c) edge and (e) center modes as well as (d) a combination of edge and center modes* [15].

Other work has focused on small triangular particles (the side lengths are all smaller than 300 nm). Different techniques such as EELS and cathodoluminescence, have been used to study such small triangle particles. [16], [17].

In our work, we will experimentally study large triangular plates with side lengths of around 600 nm to 900 nm and a thickness of around 20 nm. As the *optical* LDOS is related to the modes of the particle, we will attempt to locally excite these modes with the STM-nanosource and determine whether we can map the *optical* LDOS in this way.

6.2.2 Spectral behavior when the excitation is centered on an individual triangular plate

Since a mode exists at a specific energy, the first step toward local mode mapping is to

measure the spectra when the excitation is on the triangular plate. For the spectral measurements, triangular plates of different side lengths (L) such as 600, 800 and 900 nm have been used (the thickness is near 20 nm). Note that all the spectra are corrected for the instrumental response (see chapter 2).

For the first measurement, we move our excitation to the center of the triangular plate (L = 800 nm) and record a spectrum. The experimental results are shown in Figure 10 (blue curve). We see a strong peak at the wavelength of around 730 nm (energy near 1.68 eV).

In order to verify for the reproducibility of the spectra, we repeat the experiment a second time (see Fig. 10 (red curve)). Comparing the two measurements, we see that the shape of the spectra are very similar. Any slight differences may be due to an effect of the tip (during the excitation on the triangular plate, the tip may change its shape slightly).

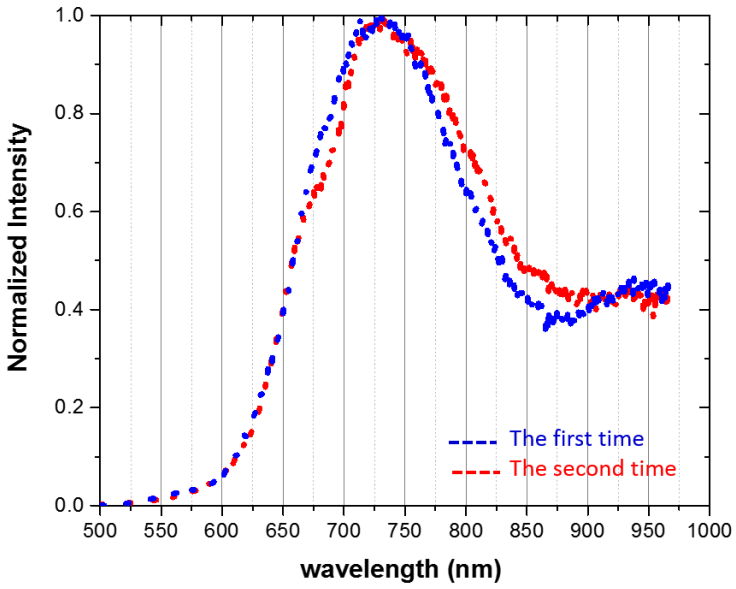

Figure 10. Spectral measurement on a triangular plate with a side length of ≈ 800 nm. *Two consecutive measurements are presented, showing that the measurement is reproducible (no change in the peak position), though slight variations exist (probably due to tip changes).*

Figure 11 shows the acquired spectral results when the STM excitation is centered on a triangle with L1 = 600 nm (red curve) and a triangle with L2 = 800 nm (blue curve). In Fig.

11, the two spectra overlap at the main peak wavelength of ≈ 730 nm (energy ≈ 1.68 eV). This indicates that the size of the triangular plate has little influence on the energy of the main peak.

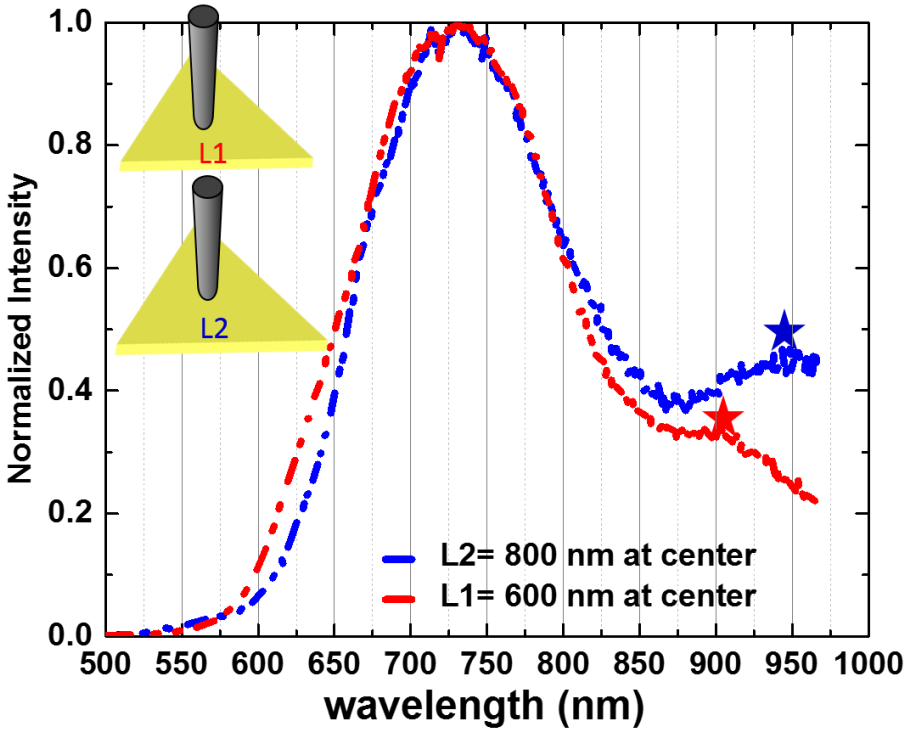

Figure 11. Spectra of two different sizes of triangular plates when the excitation in the center of the plates. One triangle has a side length of near L2 = 800 nm *and the other one has a side length of near* L1 = 600 nm. *Both of them show similar spectral features with a main peak at a wavelength of* 730 nm (1.68 eV*). Note, however, that a secondary peak exists at* λ ~ 900 nm *for the triangle with* L1 = 600 nm *and* λ ~ 950 nm *for the triangle with* L2 = 800 nm *(see stars).*

Since the excitation position is in the center of the particle, we propose that the main peak corresponds to the central mode of the triangular plates (see Fig. 9 (e)). Since the spectra from different structures have the same main peak, the responsible phenomenon depends little on the size of the triangular plate.

However, the two spectra also show a small second peak which is annotated with the blue and red star in Fig. 11. With increasing side length of the triangular plate, these small peaks

shift towards longer wavelengths. Unlike the main peak, this secondary peak shows different spectral behavior with changing side length.

To further understand the spectral features, our collaborators *Mario Zapata*, and *Javier Aizpurua* from the Donostia International Physics Center in Spain and *Andrei Borisov* from ISMO simulated the spectra using COMSOL. In their simulations, the inelastic tunnel current from the STM tip is approximated as a vertical oscillating dipole. Here, for comparison, the dipole in the simulation is located in the center of the triangular plate. The simulated spectra are obtained by integrating over all angles of emission. Note that this is different from the experiment where light is collected only below the substrate with a maximum collection angle of $\approx 72°$ (NA=1.49). In order to take into account the excitation spectrum of the source which depends on the tunneling probability, the flat spectrum of the vertical oscillating dipole is multiplied by $\mathrm{F} = (\mathrm{eV} - \mathrm{E})$ for $\mathrm{E} < \mathrm{eV}$, instead of; $F = 0$ otherwise, where V is the applied voltage and E is the photon energy (see chapter 2). The resulting calculated spectra are shown in Fig. 12 along with the experimental results for triangles with side lengths $\mathrm{L1} = 600$ nm and $\mathrm{L2} = 800$ nm.

Comparing the simulation results for different side lengths, we see that the peak positions change little for shorter wavelengths and shift towards the red for increasing side lengths for the longer wavelengths. This is the same tendency as in the experiment; when the excitation is centered on the triangular plate, the side length has little influence on the spectra except at longer wavelengths.

However, when comparing the simulation and experimental results, there exists a major difference: the spectra from the simulation presented several distinct peaks while in the experimental results, there is only a main peak and a secondary peak. The difference could be due to several factors:

1) The dielectric function of gold that is used for the simulation may be very different from the true value; in particular, the losses may be underestimated.
2) Another reason may be the fact that the dielectric constant of the ITO layer is taken as a real constant ($\varepsilon = 4$). In reality, the dielectric constant of ITO is frequency dependent and has an imaginary part. The imaginary part in the ITO dielectric constant could introduce more loss in the experiment compared with the simulation.
3) All edges are abrupt in the simulation but are rounded in the experiment. This could affect the results, along with non-included sources of loss such as roughness.

4) Finally, there is no STM tip present in the simulation. Since the tip is made of tungsten which is lossy in the considered wavelength range, its presence could be an important source of loss in the experiment, which is not included in the simulation.

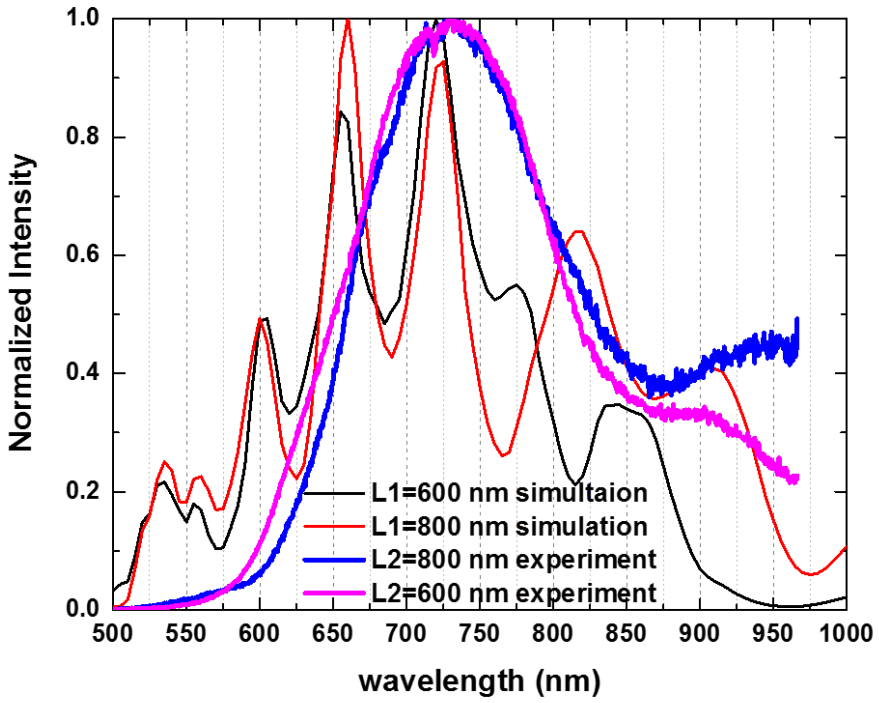

Figure 12. Comparison between experimental and simulated spectra when the excitation is centered on the triangular plate. Two different structures are used with different side lengths of $\mathrm{L2} = 800$ nm *and* $\mathrm{L1} = 600$ nm. *The thickness of the triangular plate is* 20 nm.

6.2.3 Spectral behavior for different triangular plate sizes and excitation at the edge

We have already discussed that when the excitation is centered, the spectrum displays a main peak that changes little with side length and a secondary peak which is side-length dependent. Now we will consider the results when the excitation is at the edge of triangular plates of different side lengths L. We move the excitation to the middle of an edge of the triangular plate, as sketched as tip position 1 in Fig. 13. We measure the spectrum and compare the result with that which is obtained when the tip is centered (tip position 2 in Fig. 13). We find that the spectra are different when the excitation is on the edge or centered on the triangular plate. When the excitation is on the edge of the triangular plate, there are three peaks (wavelengths of ≈ 885 nm, ≈ 766 nm and ≈ 688 nm or energies at ≈ 1.4 eV, ≈ 1.6 eV

and ≈ 1.8 eV for $L = 600$ nm) as opposed to only two peaks (at ≈ 730 nm, ≈ 900 nm or energies at ≈ 1.7 eV and ≈ 1.37 eV) when the excitation is centered.

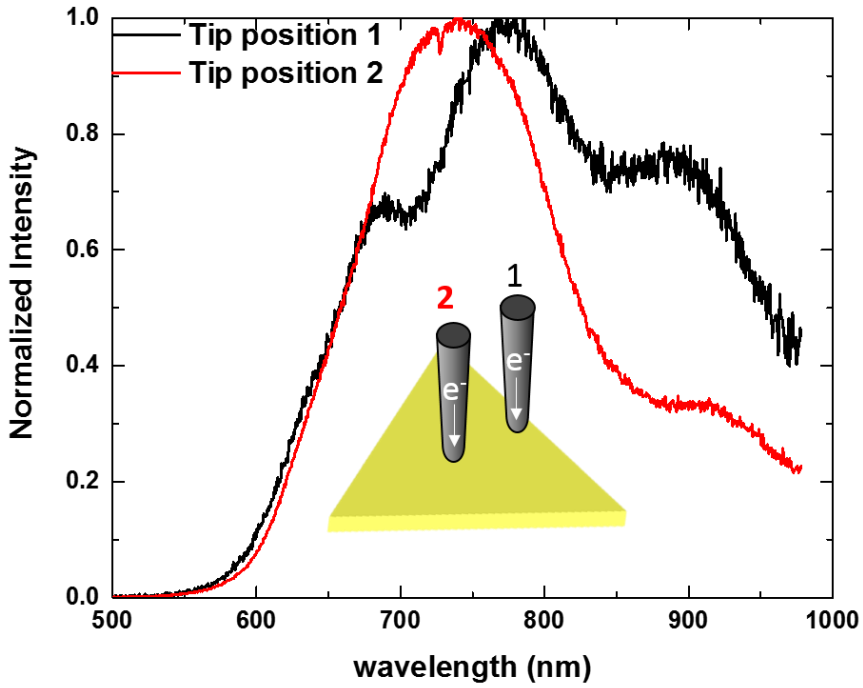

Figure 13. Spectra when the excitation is in the center and on the edge of a triangular plate. The inset shows the tip excitation positions on the triangular plate. The side length of the triangle is around ≈ 600 nm *with a thickness of near* ≈ 20 nm. *We record a spectrum with the excitation at an edge, and in the center of the structure. The black line shows the spectrum when the tip position is at 1 and red line shows the spectrum when the tip position is at 2. We set the bias at* 2.8 V, *tunnel current setpoint at* 0.5 nA *and acquisition time as* 300 *seconds.*

In Fig. 14, we compare the spectra from edge excitation for triangles with $L = 600, 800$ and 900 nm. We see that different sizes of triangles show very different spectral behavior. This is unlike the situation when the excitation is centered on the structure. For the side length around 600 nm, three obvious peaks are seen at the wavelengths of ≈ 675nm, ≈ 760 nm and ≈ 890 nm. Two peaks are seen for the side length around 800 nm at the wavelengths of ≈ 760nm and ≈ 890 nm. Two peaks for the side length 900 nm triangular plate at the wavelengths of ≈ 800 nm and ≈ 925 nm.

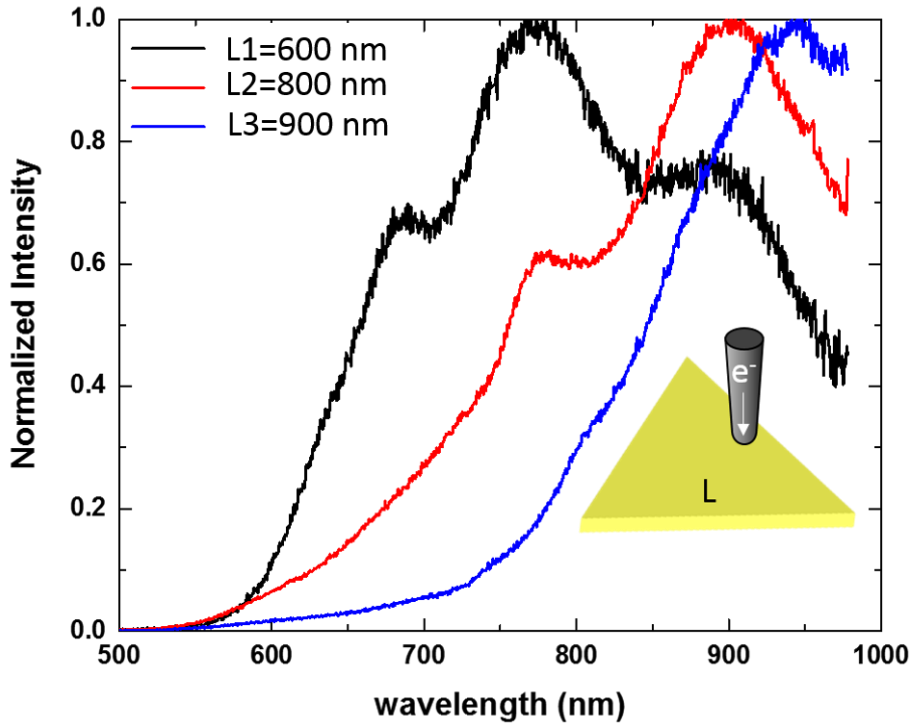

Figure 14. Spectral behavior for differently sized triangular plates when the excitation is at the edge. The triangular plates have side lengths of around L1 = 600 nm, L2 = 800 nm *and* L3 = 900 nm. *In all cases, the STM excitation is at the edge of each triangular plate. We set the bias at* 2.8 V, *tunnel current setpoint as* 0.5 nA *and acquisition time as* 300 *seconds.*

Unlike the case where the excitation is in the center of the triangle, here the whole spectrum seems to red shift with increasing side length of the plates. A similar tendency is seen for aluminum triangular plates of similar size studied with EELS [18]. Since we are exciting on the edge, we expect to excite edge modes most efficiently. We might then tentatively identify these modes as edge modes.

Mario Zapata also simulated the spectra when the excitation is on the edge of the triangular plate. In the simulation, the excitation dipole is now located at the edge of the triangular plate shown in Fig. 15 (red dot defined as Pos2). The spectra are also calibrated as in Fig. 13 and the results are shown in Fig. 15.

Figure 15 shows the experimental and simulation results for triangular plates of different sizes. $P_{2,0}$, $P_{2,1}$, $P_{2,2}$, $P_{2,3}$ and $P_{2,4}$ label the modes which appear in the calculation for the excitation at position 2 (center of the edge). Here, $P_{2,0}$ is a higher order mode since it has the largest energy (lowest wavelength). As seen in the experiment, we observe that by increasing the side length L of the triangular plate, the modes shift toward longer wavelengths (smaller energy).

In Fig. 15, the experimental results are plotted as the dashed curves and simulation results are plotted as the solid curves. Starting with the smallest triangle, the following observations may be made. For $L = 600$ nm and 630 nm, the number of peaks and their relative intensities in the calculation seem to fit quite well with the experimental results, though the $L = 600$ nm data is slightly blue shifted with respect to the simulation. This may be due to the fact that the edges of the triangle are not abrupt but slightly rounded, reducing the effective size of the triangle. A major difference for $L > 780$ nm, is that the $P_{2,0}$ mode is not seen in the experimental results. From the spectra results we observe the following: for an excitation position in the center of the triangle the highest peak in the emission spectrum is at shorter wavelengths than when the excitation is at an edge. This is seen in both experiment and simulation. The fact that the spectrum varies with excitation position is the first indication that the STM-nanosource is sensitive to the *optical* LDOS.

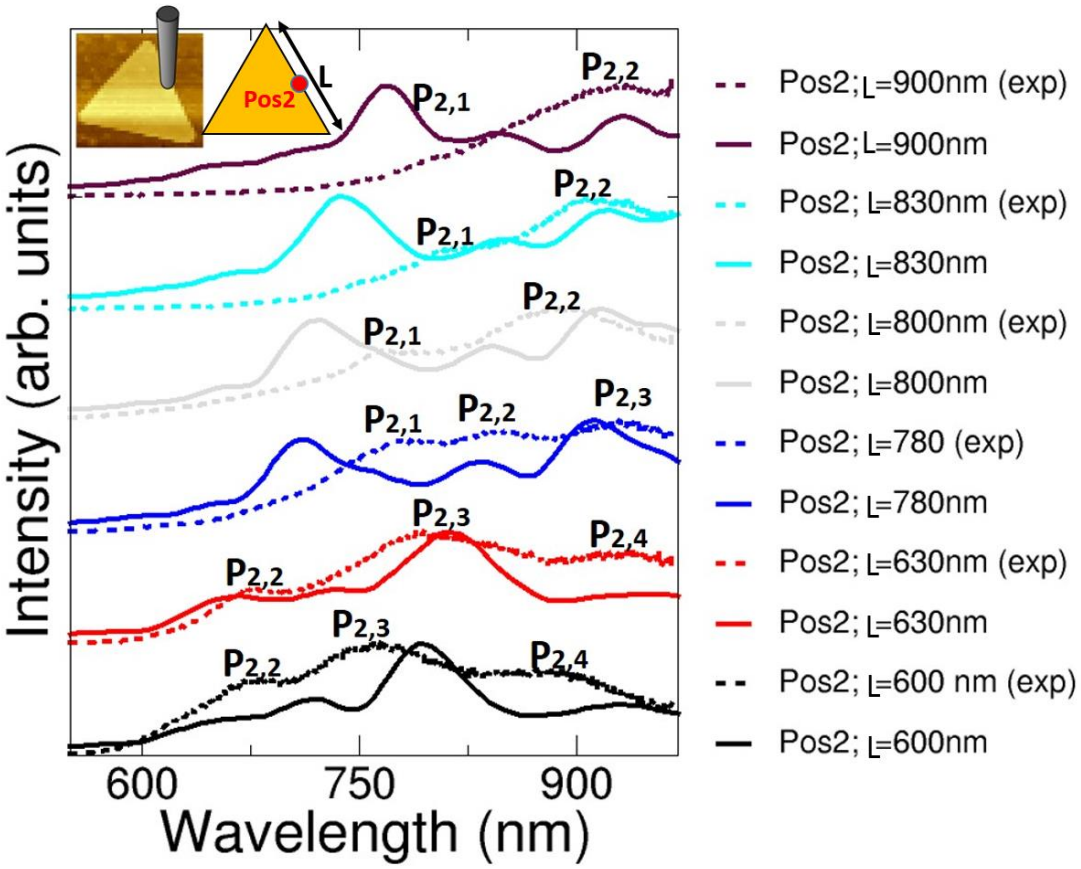

Figure 15. Simulated and experimental spectra when the excitation is on the edge of the triangular plate (Pos2). Six different structures are used with different side lengths of $\mathrm{L} = 600, 630, 780, 800, 830$ *and* 900 nm.*The spectra are all calibrated as in Fig. 13.*

6.2.4 Photon mapping of a triangular plate

As mentioned at the beginning of this section, the main idea of this experiment is to see if we map the *optical* LDOS with the STM-nanosource. To investigate if this is the case, our STM tip will now continuously scan over the triangular plate. When the excitation is at each pixel of the triangular plate image (the total number of pixels is 50×50), all the photons emitted from the $50\ \mu m^2$ area seen by the APD detector (see chapter 2) will be collected. After continuously scanning over the entire triangular plate, a photon mapping image is formed and from the photon mapping image, we directly see at which excitation position on the triangular plate, we acquire more photons. The APD is a single photon detector which produces a TTL signal which is integrated by the STM controller. As a result, we acquire the topography image, tunnel current map image and the photon map image simultaneously.

The ideal system to test if the STM-nanosource can map the *optical* LDOS would be the following: a structure whose modes are well-spaced in energy so that they may be easily separated; and a structure with an easily-resolved mode pattern in the visible. In that case, the photon map generated by the STM-nanosource and *filtered at the energy of the mode* should resemble the mode pattern and *represent the optical* LDOS as in the case of EELS (see e.g., [18]).

Thus, we will performed filtered photon mapping on individual triangular plate to see if there are differences in the photon images as a function of wavelength. Ideally, the filters would correspond to the peaks identified in the spectra, but we have simply used the filters available.

Figure 16 shows all the information obtained from a triangular plate with a side length of $L \approx 630\,\mathrm{nm}$ and a height of around $20\,\mathrm{nm}$. The results shown here are acquired during a photon mapping experiment with a bandpass filter of $900/40\,\mathrm{nm}$.

Figure 16 (a) shows the STM topography image. Bright areas indicate higher topography and darker ones present lower topography. Figure 16 (b) shows the corresponding current map. Bright areas stand for high current and dark areas indicate low current. Both images show the same tendency: the highest topography is at the edge in Fig. 16 (a), as is the highest current (Fig. 16 (b)). The largest number of photon counts is also seen at the edge. Figure 16 (c) shows the photon mapping image (counts per second).

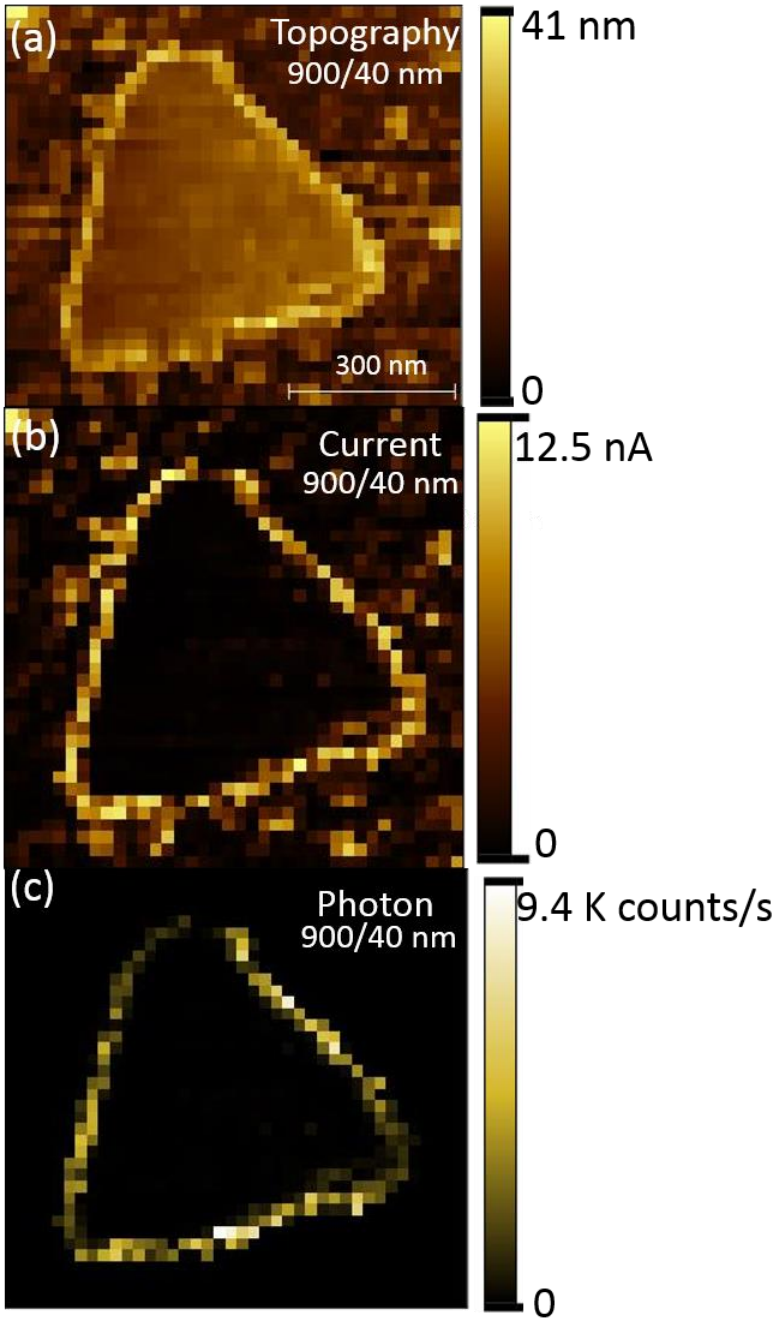

Figure 16. Topography, tunnel current and photon images. The triangular plate has a side length near 630 nm *and is* 20 nm *high. The photon image is recorded with a bandpass filter of* 900/40 nm. *These are all recorded under the bias of* 2.8 V *and a setpoint of* 0.1 nA.

The phenomenon of higher current and higher topography appearing on the edge of the triangular plate appears for all the triangular plates tested with an applied voltage of $V = 2.8$ V. Moreover, this phenomenon is almost absent when imaging at a low voltage (0.5 V). We have

previously shown that the STM tunnel current is unstable when imaging at high (> 2V) applied voltage in air and have attributed this instability to the existence of an electrochemical current [19]. This unstable current (and the associated oscillation of the tip) may be what leads to the above observations. The exact mechanism leading to this artifact, however, is unclear.

For the photon mapping image, one interpretation might be that the bright areas along the edge may simply be due to the increased current. To explore this, we normalize the photon image by the current image, i.e. we divide the photon image of Fig. 16 (c) by the current image of Fig. 16 (b). Figure 17 (a) shows the photon per electron mapping image. The photon/electron image gives the photon yield over the triangular plate which will be referred as the photon yield image later. Figure 17 (b) presents the 3D image of Fig. 17 (a) from which we clearly see that the photons at a wavelength of $900/40$ nm are mainly emitted when the excitation is along the edge of a triangular plate.

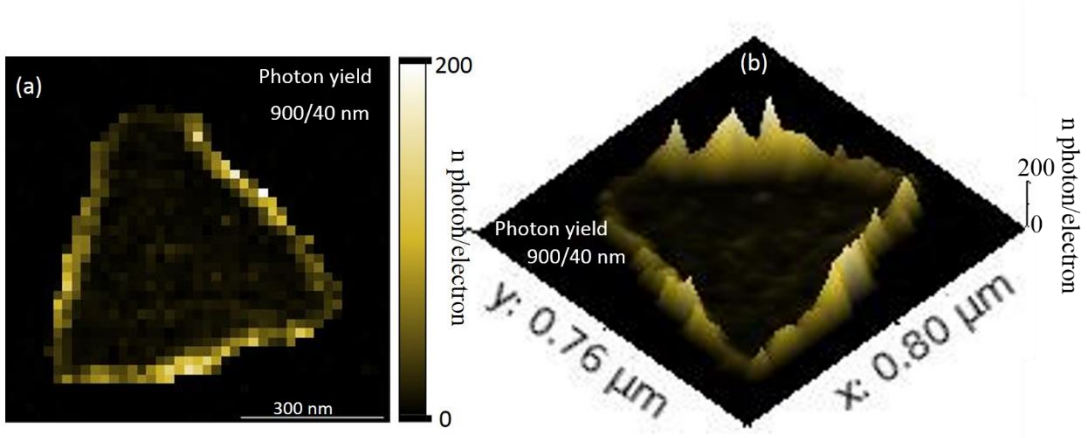

Figure 17. Photon per electron mapping image. (a) The photon mapping image is acquired by dividing the photon image of Fig. 16 (b) the by current map image of Fig. 16 (c). The result shows the photon per electron mapping image. (b) 3D image of (a) in which we clearly see where photons at a wavelength of 900 nm *are excited. The triangular plate has a side length near* 630 nm *and is* 20 nm *high. The photon image is recorded with a bandpass filter of* $900/40$ nm *in front of the detector. The results are recorded under a bias of* 2.8 V *and a setpoint of* 0.1 nA.

The above results are for a bandpass filter of longer wavelength ($900/40$ nm). For comparison, shorter wavelength (≈ 750 nm) photon mapping will be done. Figure 18 presents

topography images, current images, photon images and normalized photon yield images acquired with bandpass filters of $750/40$ nm and $900/40$ nm.

Figures. 18 (e) and 18 (f) show the photon mapping images acquired and Figs. 18 (g) and 18 (h) are the normalized photon yield maps. Interestingly, we find that at different wavelengths, the photon yield distribution over the triangular plate is different. For the bandpass filter of $750/40$ nm (according to the energy range of 1.61 eV to 1.7 eV), we see that there are more photons when the excitation is in the center of the triangular plate. For a bandpass filter of $900/40$ nm (energy range from 1.35 eV to 1.41 eV), however, we see that there are more photons when the excitation is on the edge of the triangle. The fact that very different photon maps are obtained for different collection wavelengths is a second piece of evidence that the STM-nanosource is sensitive to the *optical* LDOS.

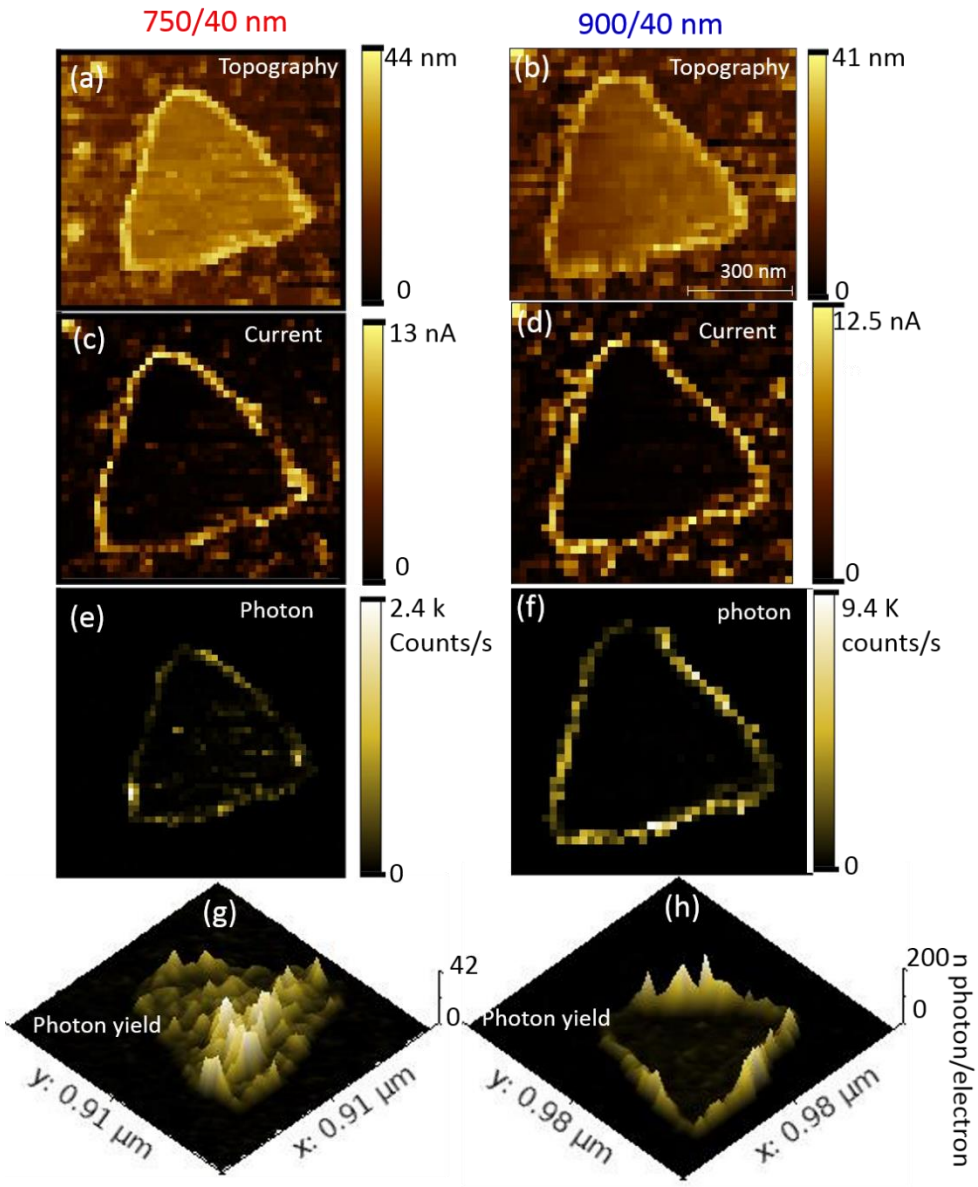

Figure 18. Photon mapping for a triangular plate with side length near 630 nm, *height* ≈ 20 nm *filtered for different wavelengths. The left and right hand columns show the results for a* 750/40 nm *and a* 900/40 nm *band pass filter respectively. STM bias is set at* 2.8 V *and tunnel current is set at* 0.1 nA. *The acquisition time for each image is around* 90 *minutes.*

Additionally, in order to better visualize for which excitation position on the triangular plate, there is the most light, we further analyze the photon yield image for the bandpass filter of 900/40 nm (shown in Fig. 18 (h)) and the results are shown in Fig. 19 (a) and 19 (b). Here, a Matlab program is employed. Figure 19 (a) shows all the points for which the photon yield is

larger than the threshold of 12E-9 photon/electron (the threshold is chosen by us). When the photon yield is smaller than the threshold, the result is plotted in Fig. 19 (b). Comparing Figs. 19 (a) and 19 (b), we see that for the photon yield larger than the threshold, the excitation is mainly on the edge of triangular plate and for the photon yield smaller than the threshold, the excitation is mainly in the interior. The ratio of photon yield per pixel in Fig. 19 (a) is nearly 9 times that of Fig. 19 (b).

Using the same method, the photon yield image for the bandpass filter of $750/40$ nm (shown in Fig. 18 (g)) is plotted with a threshold of 5E-9 photons/electron and the results are shown in Figs. 19 (c) and 19 (d). Here we see that for the photon yield larger than the threshold, the excitation is both on the edge and inside of triangular plate and for the photon yield smaller than the threshold, the excitation is mainly seen along the edge of the triangular plate. The ratio of photon yield per pixel in Fig. 19 (c) is near 3 times that of Fig. 19 (d).

Therefore, according to this analysis of the photon maps, we may conclude that at large wavelength of 900 nm (low photon energy), the best excitation position to see more photons is on the edge of the triangular plate. For small wavelength of 750 nm (high photon energy), the best excitation position to see more photons is in the center part of the triangular plate. The difference between the edge and center part for photon occurrence is more pronounced at the wavelength of 900 nm (9 times different) than at 750 nm (3 times different). Another series of mapping results for more bandpass filters may also be found in Appendix C.

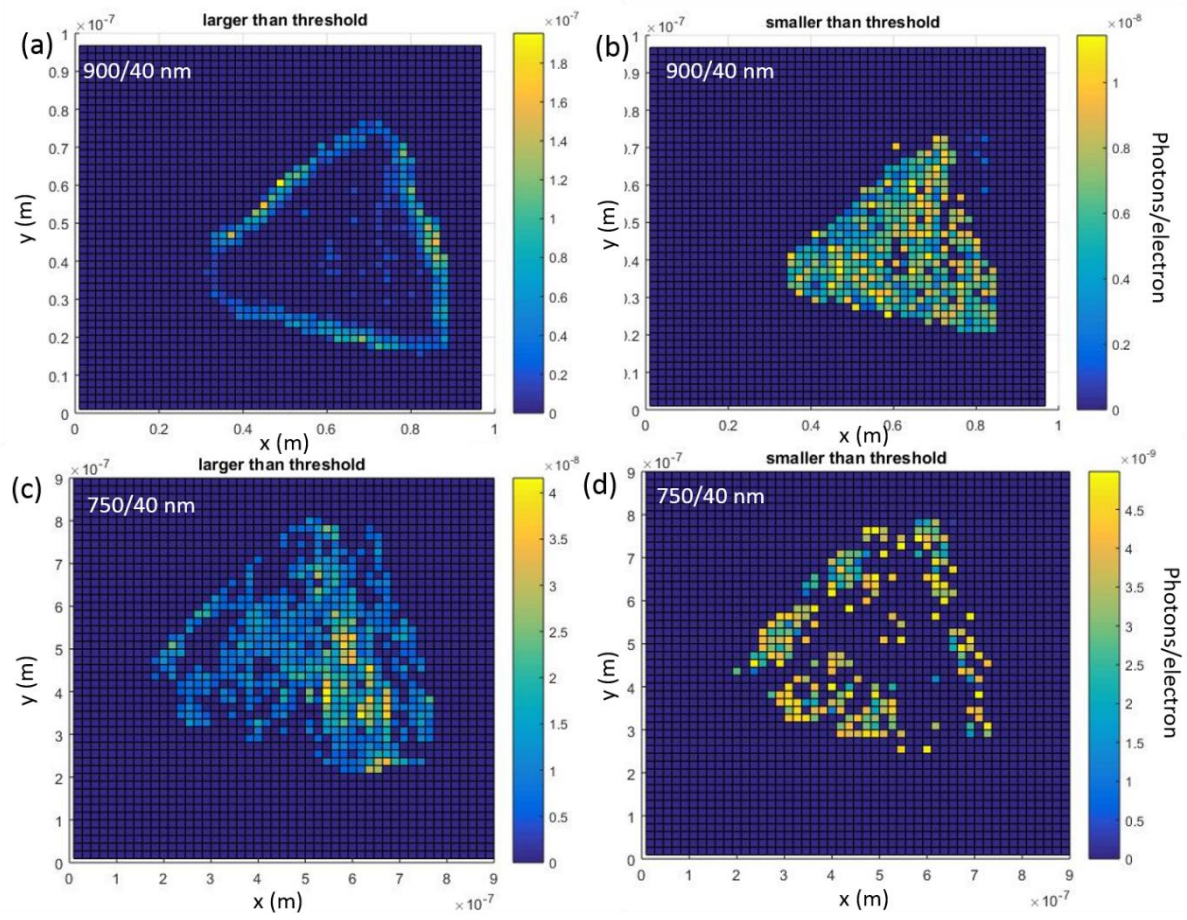

Figure 19. Quantifying the number of photons per electron for the triangular plate with length near 630 nm *and a thickness around* 20 nm. *For the bandpass filter of* 900/40 nm, *the photon yield is respectively (a) larger and (b) smaller than the threshold of 12E-9. For the bandpass filter of* 750/40 nm, *the photon yield is respectively (c) larger and (d) smaller than the threshold of 5E-9.*

In order to attempt to answer our original question of whether the STM-nanosource can map the *optical* LDOS, we will now compare the experimental mapping results with photon mapping simulations (by *Mario Zapata et al.*,). Figure 20 shows the comparison between the experimental ((a)-(c)) and simulation results ((d)-(i)) for the same size triangle (L = 630 nm) for different wavelengths. In the simulation, the inelastic tunnel current is approximated as a vertical oscillating dipole which is moved to different positions on the triangle.

From the simulation at $\lambda = 900$ nm, results (Fig. 20 (i)), we see an edge pattern which is quite similar to the experimental results (Fig. 20 (c)). Additionally, the simulation shows variations in the intensity along the edge which cannot be resolved experimentally.

The pattern evolves as λ decreases but remains localized on the edge until $\lambda = 650$ nm In Fig. 20 (d), a quite similar pattern is seen as in the experiment for the wavelength range $\lambda = 680 - 720$ nm (Fig. 20 (a)). Thus both experiments and simulations show the same trends: for longer wavelengths there is more light emitted when the excitation is on the edge and for shorter wavelengths there is more light when the excitation is in the center. This is a third piece of evidence suggesting that the STM-nanosource is sensitive to the *optical* LDOS.

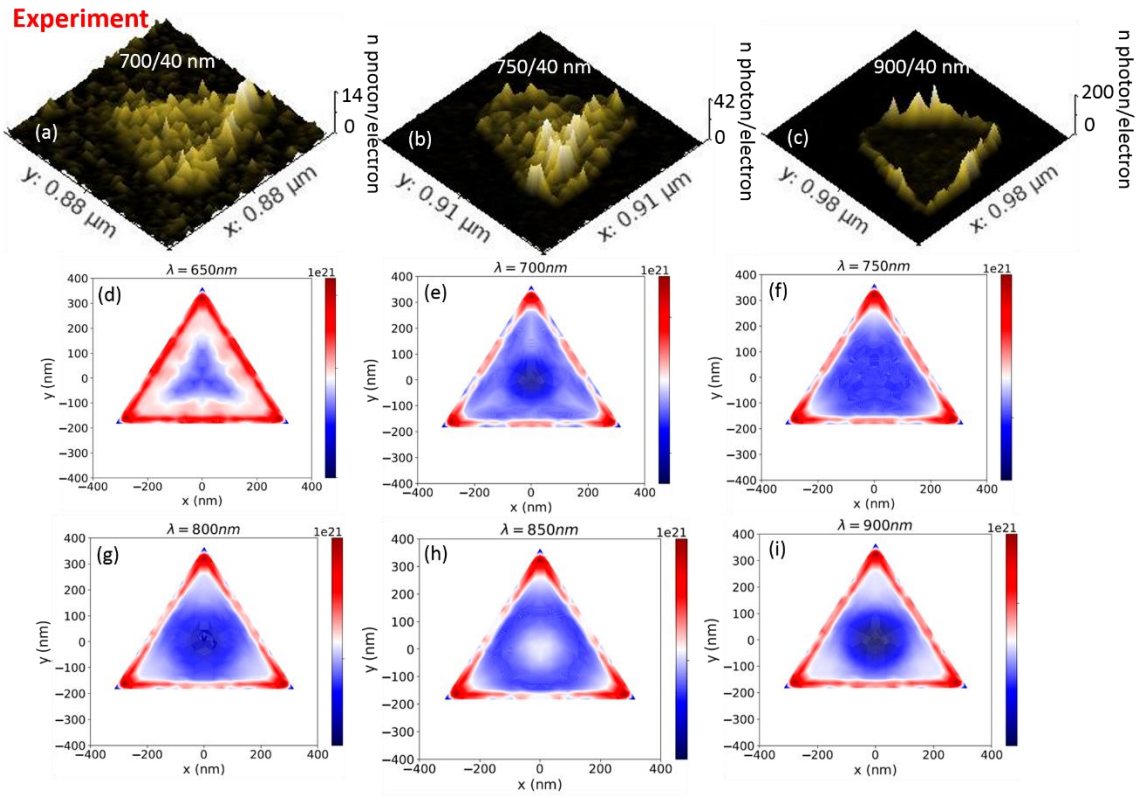

Figure 20. Photon mapping results for experiments ((a)-((c)) and simulations ((d)-(i)) for different wavelengths. The triangle has a side length $L = 630$ nm *and a height of* 20 nm. *In the simulation, a vertical dipole is placed at different positions on the triangle.*

The above results are consistent with each other: the spectral peak positions shift as a function of excitation position with the highest peak at short wavelengths for excitation in the center, and the highest peak at longer wavelengths for excitation on the edge. The photon mapping results show that more light is emitted at shorter wavelengths when the excitation is

in the center while the highest intensity at longer wavelengths is emitted when the excitation is on the edge. The simulation results show the same trends. Thus we conclude that the above evidence supports the idea that the STM-nanosource is sensitive to the *optical* LDOS.

6.2.5 Experimental difficulties

While the above results are encouraging, we cannot unambiguously conclude that the STM-nanosource probes the optical LDOS for several reasons. For example, in Fig. 12, we see that experimentally we have a lack of spectral resolution, probably due to loss in the tip, secondly, in Fig. 18, we see that the signal-to-noise ratio is too low to resolve the intricate pattern seen theoretically in Fig. 20. Possible solutions include using a less lossy tip (but if it is plasmonic, it will perturb the system being studied), and choosing an experimental system whose mapping pattern would be more easily resolved. Other experimental difficulties are discussed below.

First, after performing photon mapping several times on the same nanoplate, the STM may modify the plate slightly; small protrusions may appear. These protrusions may be the result of the photon mapping process because high bias (2.8 V) is applied and this results in an unstable tunnel current (as discussed before). Therefore, experiments cannot be infinitely repeated on the same triangle. Figure 21 shows how the topography is modified by the STM tip after several photon mappings on the same plate. Figure 21 (a) presents the topography acquired during the first photon mapping and Fig. 21 (b) is the 3D representation. Figure 21 (c) shows the topography acquired during the sixth photon mapping on the same plate and Fig. 21 (d) presents its topography in 3D. Comparing Figs. 21 (b) and 21 (d), we clearly see that for the topography in Fig. 21 (d), several small protrusions have appeared as shown in a black circle. These do not exist in Fig. 21 (a).

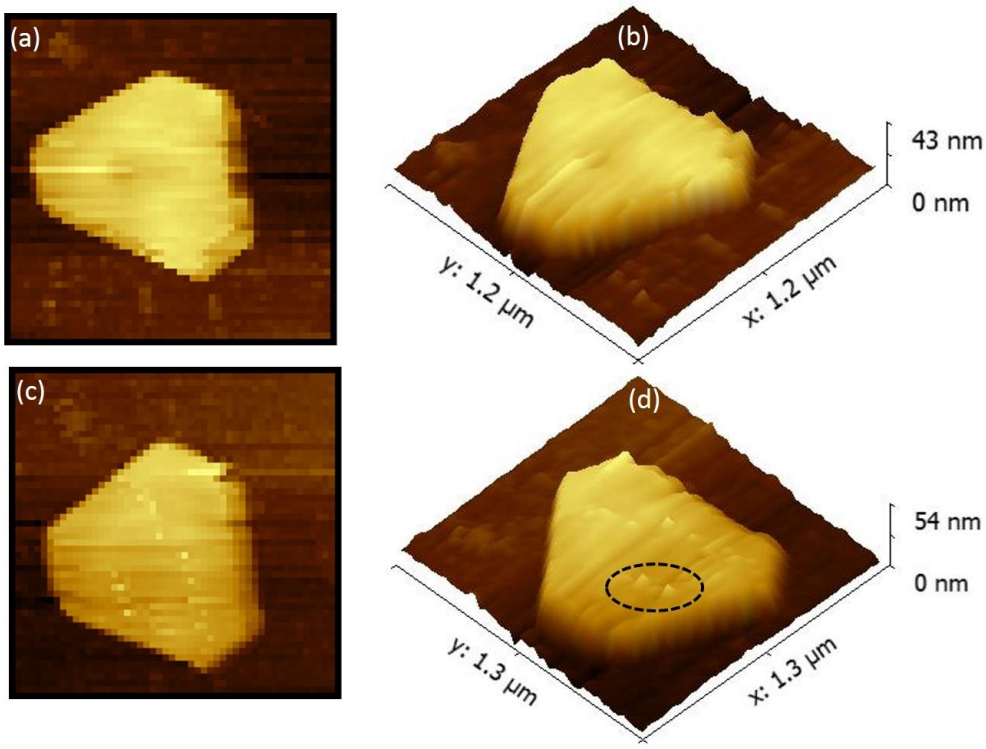

*Figure 21. STM images showing how the topography varies for a nanoplate which has been scanned several times at high voltage (*2.8 V*). (a) STM image acquired during the first photon mapping. (b)* 3D *topography of (a). (c) STM image acquired during the sixth photon mapping. (d) 3D topography of (c).* Here a bias of 2.8 V and a setpoint of 0.1 nA are applied. Note that thermal drift causes apparent the changes in the dimensions seen in parts (a) and (c).

Secondly, it is difficult to control the STM tip light emission efficiently. During the photon mapping process (more than 1 hour for each photon mapping image), photons are collected at each pixel. However, the STM tip plays an important role in photon excitation. We cannot ensure that the STM excitation is equally efficient for each pixel. Therefore, the photon mapping images have extra noise since the tip may slightly vary with time.

Secondly, artifacts may exist due to an edge effect. Figure 22 sketches the situation when the STM tip scans over the triangular plate. Comparing Figs. 22 (a) and 22 (b), we see that when the tip scans across an edge, the inelastic tunnel current is better represented by a tilted than a vertical oscillating dipole. A tilted dipole contains both horizontal and vertical components. Thus, the fact that more photons are emitted when the excitation is at the edge may be due to the fact that the horizontal component excites certain modes more efficiently. The mapping image is then a "mixture" of different projections of the *optical* LDOS if it is correct to consider

the excitation as a tilted dipole at the edge. This idea will be further investigated with simulations.

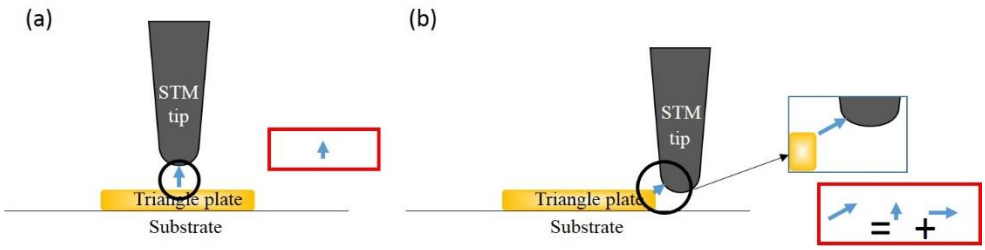

Figure 22. Sketches of the tip location on a triangular plate. (a) The STM tip is in the center of a triangular plate. The inelastic tunnel current may be represented as a vertical dipole. (b) The STM tip is at the edge of the triangular plate. A tilted dipole is the best representation of the inelastic tunnel current.

6.3 Conclusion

In conclusion, in this chapter we have used a biased STM tip to electrically excite individual Au triangular plates. We discuss two aspects of the results.

First, when the STM excitation is centered on the triangular plate, from the recorded Fourier space image, we obtain light source with a broad angular distribution (from $\approx 42°$ to $\approx 72°$) which is quite different from the thin Au film radiation pattern (emission at around $43°$). When we move our excitation to the edge of a triangular plate, directional light emission is obtained. The direction of the light emission is perpendicular to the edge orientation of the plate. The same results can be repeated on an Au hexagonal plate. We propose that the mechanism for directional emission is the excitation of higher order plasmonic modes. Future simulation work can be done to confirm our hypothesis.

Secondly, we have investigated whether the STM-nanosource may be used to map the *optical* LDOS of a triangular plate. The first step is to measure the spectra with the excitation at the center and then at the edge of the triangular plate. The spectra show different features at different locations on the same structure. Next, a series of photon mapping results are shown both in experiment and simulation. Both the experimental and simulation results show the same

trends; more light at shorter wavelengths is obtained when the excitation is in the center of the triangle, and more light is emitted at longer wavelengths when the excitation is at the edge.

Our results are consistent with the idea that the STM-nanosource can probe the optical LDOS. In order to demonstrate this unambiguously losses should be minimized. Also, a sample should be chosen whose modes are well-separated in energy so that they may be easily separated, and whose mapping pattern is easily resolvable.

Above all, our study provides insight into how to maximize the light emission from an STM-excited triangular nanosource (i.e., the excitation should be at the edge) and also suggests a potential technique of using an STM-nanosource to map the *optical* LDOS of individual plasmonic nanostructures.

[1] A. G. Curto, G. Volpe, T. H. Taminiau, M. P. Kreuzer, R. Quidant, and N. F. van Hulst, "Unidirectional emission of a quantum dot coupled to a nanoantenna," *Science*, vol. 329, no. 5994, pp. 930–933, 2010.

[2] T. Kosako, Y. Kadoya, and H. F. Hofmann, "Directional control of light by a nano-optical Yagi – Uda antenna," *Nat. Photonics*, vol. 4, no. 34, p. 312, 2010.

[3] T. Coenen, F. Bernal Arango, A. Femius Koenderink, and A. Polman, "Directional emission from a single plasmonic scatterer," *Nat. Commun.*, vol. 5, p. 3250, 2014.

[4] I. M. Hancu, A. G. Curto, M. Castro-Lopez, M. Kuttge, and N. F. van Hulst, "Multipolar Interference for Directed Light Emission," *Nano Lett.*, vol. 14, no. 1, pp. 166–171, 2014.

[5] J. E. Millstone, S. Park, K. L. Shuford, L. Qin, G. C. Schatz, and C. A. Mirkin, "Observation of a quadrupole plasmon mode for a colloidal solution of gold nanoprisms," *J. Am. Chem. Soc.*, vol. 127, no. 15, pp. 5312–5313, 2005.

[6] P. Jiang *et al.*, "PVP-capped twinned gold plates from nanometer to micrometer," *J. Nanoparticle Res.*, vol. 8, no. 6, pp. 927–934, 2006.

[7] M. Tsuji *et al.*, "Shape-Dependent Evolution of Au @ Ag Core - Shell Nanocrystals by PVP-Assisted N,N-Dimethlformamide Reduction," *crsytal growth Des.*, vol. 8, no. 7, pp. 2528–2536, 2008.

[8] K. H. Drexhage, "Influence of a Dielectric Interface on Fluoresence Decay Time," *J. Lumin.*, vol. 1, no. 2, pp. 693–701, 1970.

[9] C. Chicanne *et al.*, "Imaging the local density of states of optical corrals," *Phys. Rev. Lett.*, vol. 88, no. 9, p. 97402, 2002.

[10] S. Viarbitskaya *et al.*, "Tailoring and imaging the plasmonic local density of states in crystalline nanoprisms," *Nat. Mater.*, vol. 12, no. 5, pp. 426–432, 2013.

[11] J. Nelayah *et al.*, "Mapping surface plasmons on a single metallic nanoparticle," *Nat. Phys.*, vol. 3, no. 5, pp. 348–353, 2007.

[12] F. J. García De Abajo and M. Kociak, "Probing the photonic local density of states with electron energy loss spectroscopy," *Phys. Rev. Lett.*, vol. 100, no. 10, p. 106804, 2008.

[13] R. Carminati and J. Saenz, "Scattering theory of Bardeen's formalism for tunneling: new

approach to near-field microscopy," *Phys. Rev. Lett.*, vol. 84, no. 22, pp. 5156–5159, 2000.

[14] G. Schull, M. Becker, and R. Berndt, "Imaging confined electrons with plasmonic light," *Phys. Rev. Lett.*, vol. 101, no. 13, p. 136801, 2008.

[15] J. Nelayah *et al.*, "Direct imaging of surface plasmon resonances on single triangular silver nanoprisms at optical wavelength using low-loss EFTEM imaging," *Opt. Lett.*, vol. 34, no. 7, pp. 1003–1005, 2009.

[16] A. Losquin *et al.*, "Unveiling nanometer scale extinction and scattering phenomena through combined electron energy loss spectroscopy and cathodoluminescence measurements," *Nano Lett.*, vol. 15, no. 2, pp. 1229–1237, 2015.

[17] J. Nelayah *et al.*, "Two-dimensional quasistatic stationary short range surface plasmons in flat nanoprisms," *Nano Lett.*, vol. 10, no. 3, pp. 902–907, 2010.

[18] A. Campos *et al.*, "Plasmonic Breathing and Edge Modes in Aluminum Nanotriangles," *ACS Photonics*, vol. 4, no. 5, pp. 1257–1263, 2017.

[19] B. Rogez *et al.*, "The mechanism of light emission from a scanning tunnelling microscope operating in air," *Nanotechnology*, vol. 27, no. 46, p. 465201, 2016.

Chapter 7

Conclusion and future work

In conclusion, in my thesis, we use different plasmonic nanostructures to control the emission of electrically excited light. Our electrical emission is from an "STM-nanosource" which uses the inelastic tunnel current between the tip of a scanning tunneling microscope (STM) and a metallic sample, to locally excite both localized and propagating surface plasmon polaritons.

We focus our study on a circular plasmonic lens, an elliptical plasmonic lens, a planar plasmonic multi-layer stack and an individual triangular plate. As compared to a simple thin gold film, we find that a *structured* Au film displays an extraordinary capacity to control and shape the emitted radiation.

The interaction of an STM-nanosource and a *circular* plasmonic lens (a series of concentric slits etched in a thick gold film) produces a radially polarized microsource of light of low angular spread ($\approx \pm 4°$). The operation of the *circular* plasmonic lens may be understood simply as follows: the STM-nanosource excites an SPP circular wave on the central disc of the lens, which then propagates to the slits where the SPPs are scattered into light. The interference of this scattered light results in a nearly collimated beam. The influence of the structural parameters on the angular spread of the resulting microsource is also investigated. In addition, a low angular spread ($< \pm 7°$) for a large wavelength range ($650 - 850\ nm$) is achieved. Thus this electrically-driven microsource of nearly collimated light has a broad spectral response and is optimal over a wide energy range, especially in comparison with other resonant plasmonic structures such as Yagi-Uda nanoantennas. In the future, the STM excitation could be replaced by an integrated planar tunnel junction, leading to a fully integrated opto-electronic device.

The interaction of our STM-nanosource and an *elliptical* plasmonic lens (a single elliptical slit etched in a thick gold film) is also studied. When the STM excitation is located at the focal point position of the elliptical plasmonic lens, a directional light beam of low angular spread is acquired. Moreover, in the experiment we find that by changing the eccentricity of the elliptical plasmonic lens, the emission angle is varied. It is found that the larger the eccentricity of the elliptical lens, the higher the emission angle. This study provides a better understanding of how plasmonic nanostructures shape the emission of light. In future work, a multiple-slit *elliptical*

plasmonic lens could be studied which might lead to directional emission with an even smaller angular spread, thanks to the interference of the light scatter from neighboring slits.

The interaction of STM-excited SPPs and a planar plasmonic multi-layer stack structure is also investigated. It is demonstrated that STM excitation can probe the optical band structure of an Au-SiO_2-Au stack. We find that the thickness of the dielectric layer (SiO_2) plays an important role in changing the coupling between the identified "SPP-like" and "waveguide-like" modes. Possible evidence for strong coupling is obtained for a specific dielectric layer thickness. We also compare the results obtained by both laser and STM excitation of the same stack structure. The results indicate that the STM technique is superior in terms of signal-to-noise for TM modes. These findings highlight the potential of the STM as a sensitive optical nanoscopic technique to probe the optical bands of plasmonic nanostructures.

Finally, the interaction of an STM-nanosource and an individual triangular plate ($L \approx 600\ nm$) is also studied. We find that when the STM excitation is centered on the triangular plate, there is no directional light emission. However, when the STM-nanosource is located on the edge of the triangle, directional light emission is obtained. This study provides us a novel avenue to achieve directional light emission. We also study the possibility of probing the *optical* LDOS of the triangle with the STM-nanosource. The spectra, photon mapping and simulation results are consistent with each other and confirm that the STM-nanosource is sensitive to the *optical* LDOS. In the future, we propose using the STM-nanosource to map the *optical* LDOS on a structure whose modes are well-spaced in energy so that they may be easily separated; and a structure whose low-order mode has its energy in the visible.

Thus, our results show that the manipulation of light is achieved through SPP-matter interactions. Using plasmonic nanostructures, we control the collimation, polarization, and direction of the light originating from the STM-nanosource.

Appendix A

Complementary results for the *elliptical* plasmonic lens study

a.1 Experimental and simulation results when the excitation is located at different positions

In chapter 4, we have seen that when the excitation position is at the focal point of an elliptical slit, we achieve a directional light beam of low angular spread. The direction of the light emission and the angular spread are related to the eccentricity of the elliptical plasmonic lens. Now, we will present the results when the excitation is moved to different positions along the major axis of the elliptical structure.

Figure 1 shows the Fourier space images for various excitation positions on the elliptical structure of $D_1 = 3\ \mu m$, $D_2 = 8.77\ \mu m$. Figure 1 (a)-(e) presents the results when the excitation position is at the left focal point ($F1$), at half of the length $F1$, in the center, half of the length $F2$, at the right focal point ($F2$). Fig. 1 (f) shows schematically the excitation positions on the elliptical plasmonic lens. Focusing on Figure 1 (b)-(d), we see a more complicated pattern with many separated bright spots distributed in the Fourier space images. Fig. 1 (b) and Fig. 1 (d) are relatively symmetrical since the excitation positions are equivalent.

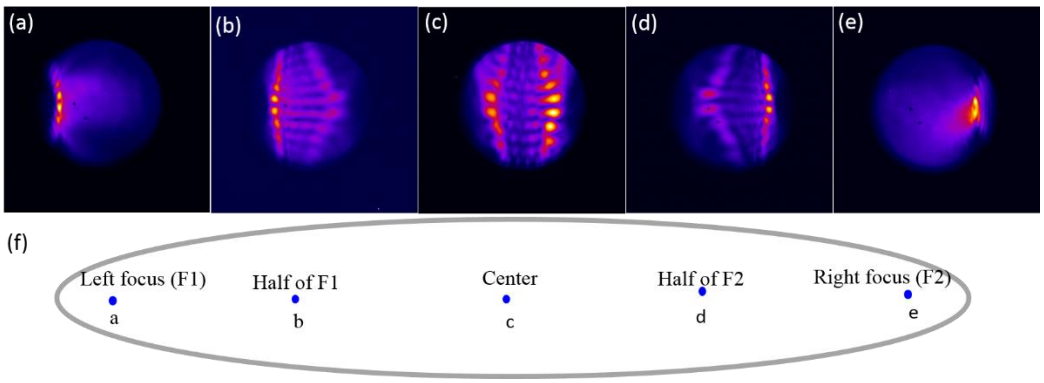

Figure 1. Fourier space images for various tip excitation positions on an elliptical plasmonic lens. (a) Fourier space image when the excitation position is at the left focal point (F1). (b) Fourier space image when the excitation position is at half the length of F1. (c) Fourier space image when the excitation position is in the center. (d) Fourier space image when the excitation position is at half of the length F2. (e) Fourier space image when the excitation position is at

the right focal point (F2). (f) Schematic diagram showing the tip position with respect to the elliptical plasmonic lens.

The next step is to compare these experimental results to a simulation. The simulation is performed by *Aurélien Drezet* from the Institut Neél in Grenoble. He uses a simple analytical model to simulate the Fourier-plane images and determines the theoretical angular spread of the emitted light, as was done for the circular plasmonic lens discussed in chapter 3. The SPPs scattering into photons at the slit are modeled as the radiation of a series of electric dipoles located along the elliptical slit. The dipoles in the model are simulated as horizontally oriented and are normal to the elliptical slit. The complex electric field vector of each dipole is calculated in the far field. The phase delay that exists between the dipoles due to the geometry of the elliptical slit is taken into account. Figure 2 (d)-(e) shows the simulation results for the same excitation locations as in the experiments. The dashed black circle in each Fourier space image of the calculation indicates the $NA = 1.49$ of the objective.

Comparing the experimental and simulation results, we can see that the patterns in Fourier space look quite similar. This confirms that the model takes into account the important physics of the experiment.

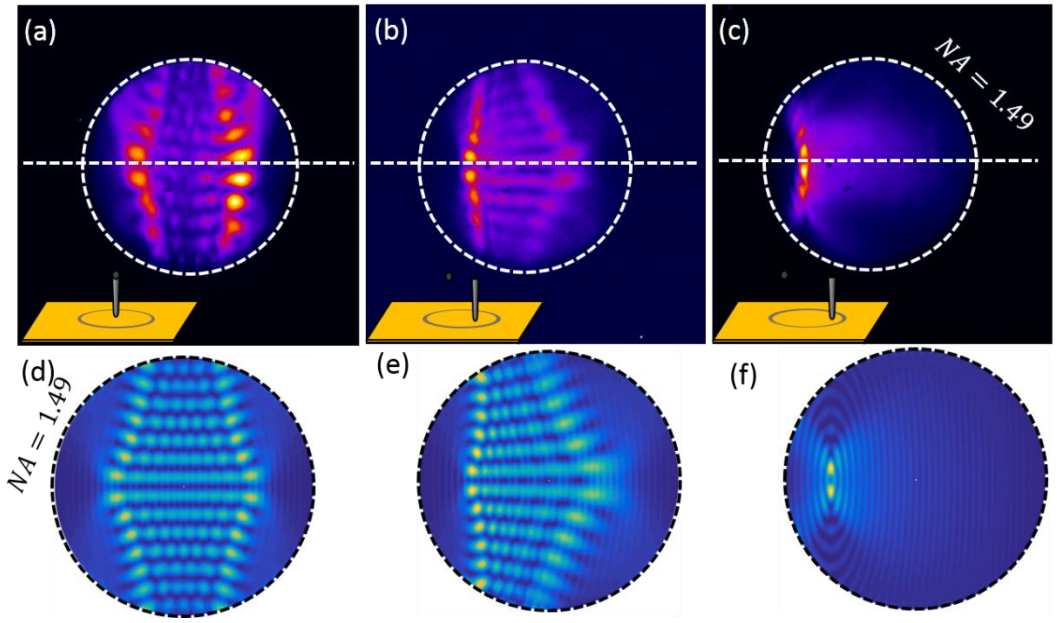

Figure 2. Fourier space images. (a)-(c) Fourier space image as shown before with tip excitation position at center, half of right focal point F_2 and right focal point F_2. (d)-(f) Simulation results for Fourier space images with the same excitation positions as in (a)-(c).

a.2 Experimental results when the excitation is located at different positions for different elliptical plasmonic lenses

After discussing the Fourier space patterns for a particular elliptical plasmonic lens when the excitation position is moved along the major axis of the elliptical plasmonic lens, now we will show the results for different plasmonic lenses. Our results are displayed in Fig. 3. Figure 3 (1)-(5) presents 5 different bright field images of the structures as shown before.

Figure 3 (a)-(e) are the corresponding Fourier space images with the various excitation positons mentioned above: left focal point, half of left focal point, center, half of right focal point and right focal point.

Note how the patterns in Fourier space gradually evolve from the simple circular pattern for the circular slit (Fig.3 (a)) to the more complicated pattern of the ellipse with the highest eccentricity (Fig. 3(c)).

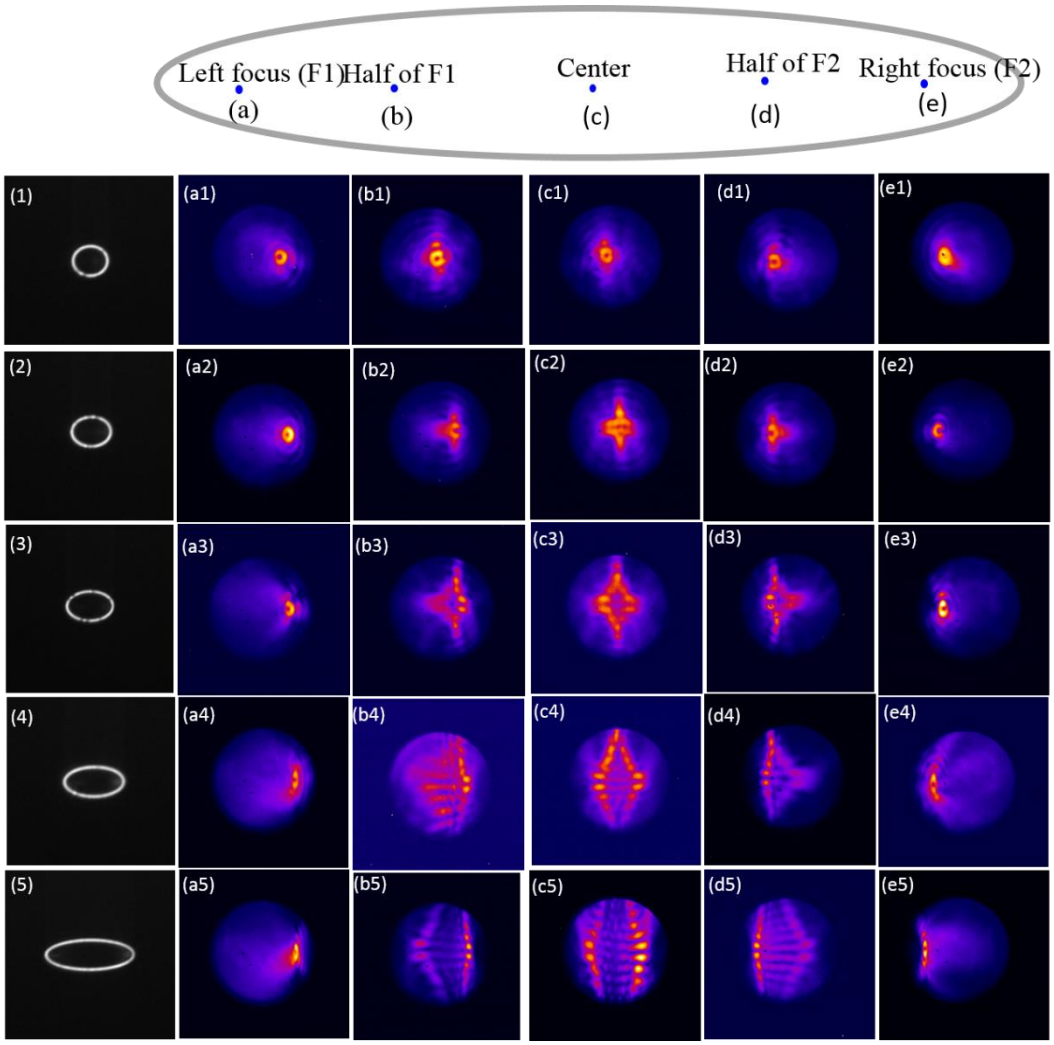

Figure 3. Transmission and Fourier space images for different structures and varying tip excitation positions. (1)-(5) transmission images of the structures with $D_1 = 3\ \mu m$ *and* D_2 *is equals to:* $3.46\ \mu m, 3.92\ \mu m, 4.67\ \mu m, 6\mu m$ *and* $8.77\mu m$*. Fourier space image for different structures when tip is located at the* (a_1) *-*(a_5) *left focal point,* (b_1)*-*(b_5) *half of left focal point,* (c_1)*-*(c_5) *at the center,* (d_1)*-*(d_5) *half of right focal point,* (e_1)*-*(e_5) *right focal point.*

Appendix B

Complementary results for the multi-layer stack structure study

Here we take parts (b) and (c) from Fig. 17 (chapter 5) and we average the spectra over all k_y/k_0. The averaged spectra are presented in Fig.1 (a) (190 nm SiO_2 structure) and 1 (b) (310 nm SiO_2 structure). The processed spectra are separately presented in Figs. 1 (a) and 1 (b). In Fig. 1 (a), we see a dip with a position of around 714 nm which is almost the same dip position as the red curve in Fig. 17 (b) (chapter 5). The dip in the Fig. 1 (b) is not as clear as for the same structure as the blue curve in Fig. 17 (b) (chapter 5).

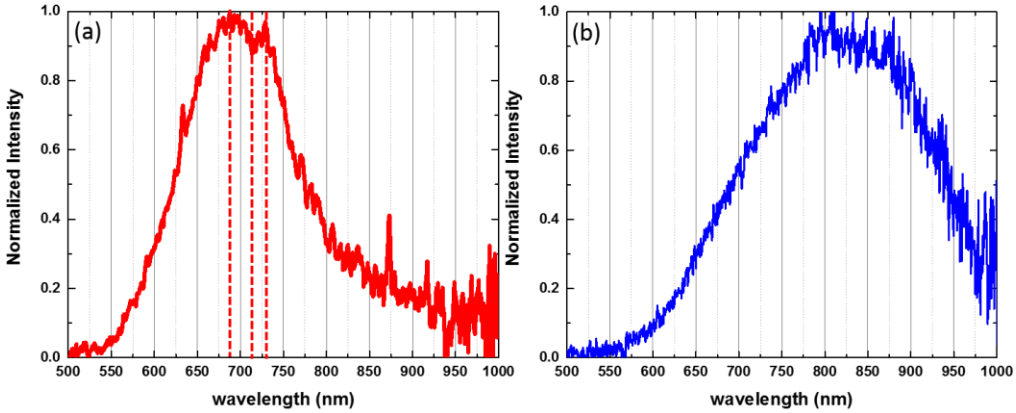

Figure 1. Spectra obtained by averaging over k_y/k_0 in Fig.17 (b) and (c)(chapter 5) for the (a) 190 *nm SiO_2 layer structure and (b)* 310 *nm SiO_2 layer structure. The vertical dotted lines indicate the peak and dip positions. The dip position in the spectrum is at about* 714 *nm.*

Appendix C

Complementary results for the triangular plates study

c.1 Angular distribution of the dipole radiation above a thin Au film on glass

We consider $L \gg \lambda$, i.e., the Fourier space pattern of a vertical oscillating dipole (i.e., inelastic tunnel current) above an air/gold film on glass. The sketch is shown in Fig. 1. Here, the system contains three layers (air-gold-glass) and a vertical oscillating dipole representing the STM excitation. The thickness of the gold layer is d and the height of the dipole above surface is z_0.

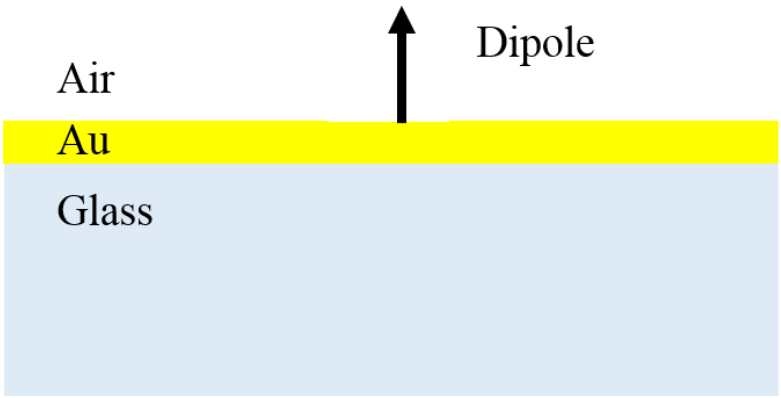

Figure 1. Schematic diagram of a vertical oscillating dipole (i.e., the inelastic tunnel current) above a three layer structure (air, gold and glass).

The angular distribution of the radiation from a vertical dipole through an air-gold –glass sandwich structure can be read as [1]:

$$E(k_{\parallel}) \propto \frac{k_{\parallel} t^{(p)}(k_{\parallel})}{\sqrt{(1-k_{\parallel}^2/k_0^2)}} e^{ik_0 z_0 \sqrt{(1-k_{\parallel}^2/k_0^2)}} \quad \text{(c.1)}$$

When the distance of dipole above the gold layer $z_0 = 0$, the transmitted radiation intensity through the glass layer can be calculated as [1]:

$$I \propto \frac{(k_\parallel)^2 (t^{(p)}(k_\parallel))^2}{(1-k_\parallel^2/k_0^2)} \quad \text{(c.2)}$$

where $k_\parallel$ stands for all the in-plane wavevectors of light which may be collected by the objective, so $k_\parallel = [0, \ldots NA]$ and k_0 is the wavevector of the light in free space. $t^{(p)}$ is the transmission efficiency of three layers structure and can be read as [2]:

$$t^{(p)} = \frac{t_{01}^p t_{12}^p e^{ik_{z1}d}}{1+r_{01}^p r_{12}^p e^{2ik_{z1}d}} \text{ (c.3)}$$

where, t_{01}^p and t_{12}^p are the transmission coefficients at the air/Au and Au/glass interfaces respectively. r_{01}^p and r_{12}^p are the reflection coefficients at the air/Au and Au/glass interfaces respectively. They can be read as [2] :

$$t_{ik}^p = (1 + r_{ik}^p)\sqrt{\varepsilon_i/\varepsilon_k} \text{ (c.4)}$$

$$r_{ik}^p = \frac{\frac{k_{zi}}{\varepsilon_i} - \frac{k_{zk}}{\varepsilon_k}}{\frac{k_{zi}}{\varepsilon_i} + \frac{k_{zk}}{\varepsilon_k}} \text{ (c.5)}$$

$$k_{zi} = \sqrt{k_i^2 - k_\parallel^2} \text{ (c.6)}$$

Using the expression (c.2), a thickness of $d = 20$ nm, a wavelength of $\lambda = 700$ nm and the dielectric constants from Johnson and Christy [3], we get the calculated Fourier space image of Fig. 2.

A bright ring at the leakage radiation angle is seen as expected. There is more intensity at angles higher than the critical angle when compared to the experimental results of the leakage radiation pattern for a 50 nm thick Au film (see Fig. 3 (d), chapter 5). The pattern here is different from what is seen in Fig. 3 (chapter 6) for the triangular plate (about equal intensity for all angles greater than the critical angle).

Another difference presented in the intensity profile is that in Fig. 2 (b), in the region $-1 < n\sin\theta < 1$, the normalized intensity is nearly 0. However, in Fig. 3 (b) (chapter 6), we see that when $-1 < n\sin\theta < 1$, the normalized intensity is around 0.2. This confrims that the radiation pattern from a triangular plate is not well approximated by a thin film.

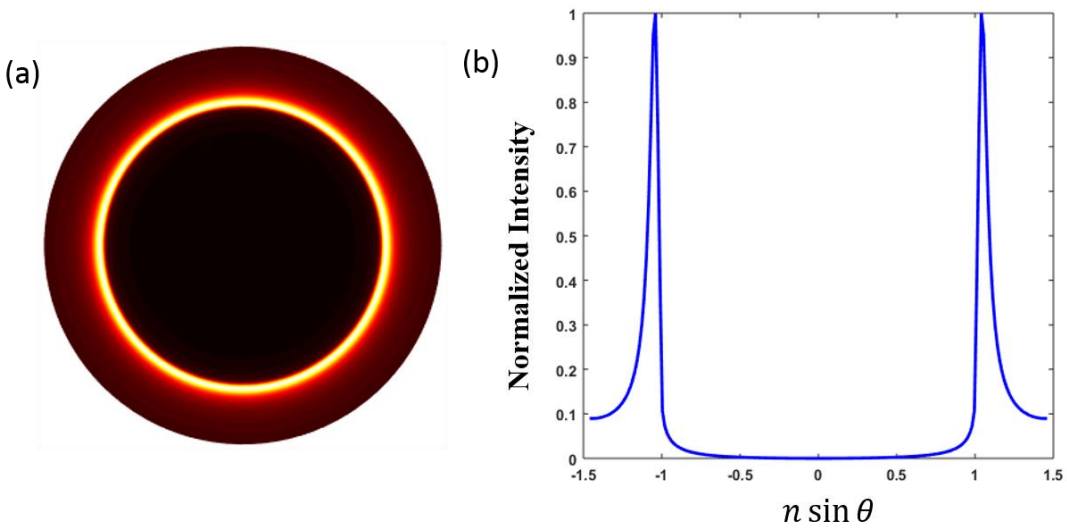

Figure 2. (a) Calculated Fourier space image for a vertical dipole above a gold film on glass. This dipole is at air-gold interface $(z_0 = 0)$. *Film thickness is* 20 nm, *radiation wavelength* $\lambda = 700$ nm, $\varepsilon_{Au}\ (700\ \text{nm}) = -16.5 + 1.1\text{i}$. *(b) Intensity profile through the center of (a).*

Next we will consider the limit where L ≪ λ. In this case, we consider the radiation of a vertical oscillating dipole above a glass substrate. Using the same equation as before but with a film thickness of 0, we get the result shown in Fig. 3 (a). For better comparison, we use a Matlab program to redisplay the experimental results of Fig. 3 (a) (chapter 6) in Fig. 3 (b).

From the intensity profiles in Fig. 3 (c), we see that there is still more light at higher angles than for the thin film results (see Fig. 3 (d), chapter 5). However, there is still no intensity for $-1 < \text{nsin}\theta < 1$, unlike the experimental result for the triangular plate in Fig. 3(d). Thus, expected, the STM-excitation of a triangular plate cannot be approximated as a vertical oscillating dipole above the glass substrate.

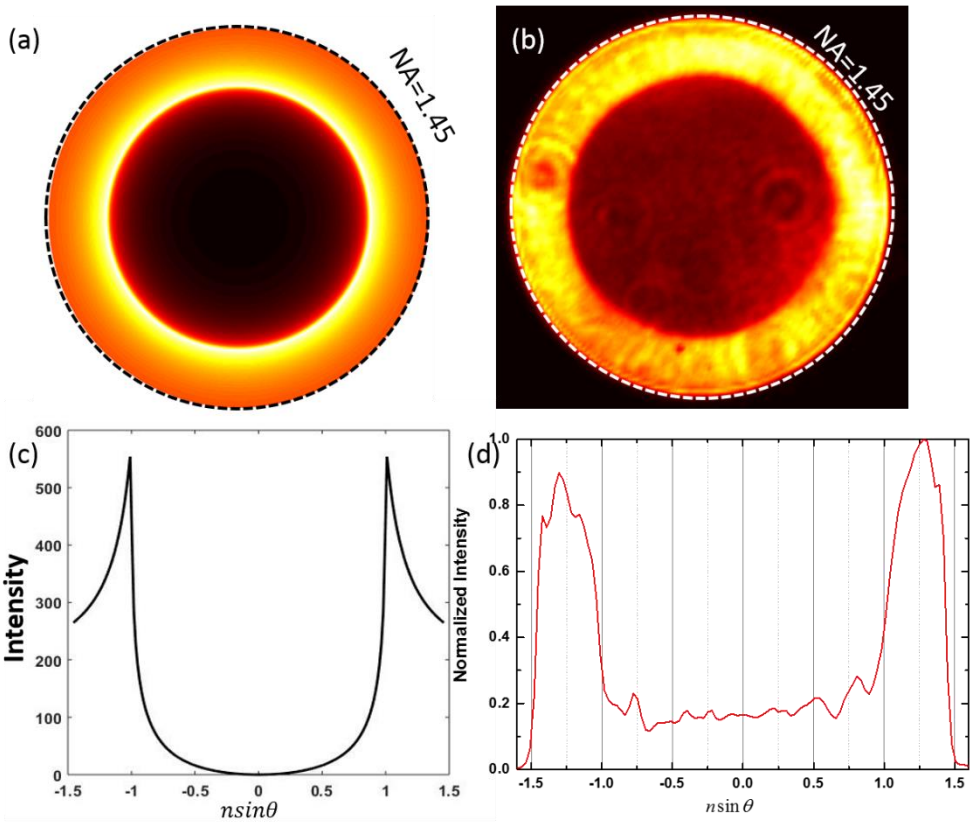

Figure 3. (a) Fourier space image of the emission pattern of a dipole above a glass substrate. Here the radiation wavelength is $\lambda = 700$ nm. *(b) Experiment result from Fig. 3 (a)(chapter 6). Here it is plotted with a Matlab program. (c) Intensity profile of the calculated Fourier space image in (a). (d) Intensity profile of the experimental Fourier space image in (b).*

c.2 Fourier space images when the excitation is at the vertex of the triangle plate

Here is another example for a triangular plate when the excitation is at the vertex and at the edge. Figure 4 (d) shows the STM image of the triangular plate with side length around 650 nm and height around 20 nm. Figs. 4 (a) and 4 (c) are the results for the excitation at the vertex of the triangle plate and Fig. 4 (b) shows the results when the excitation is at the edge.

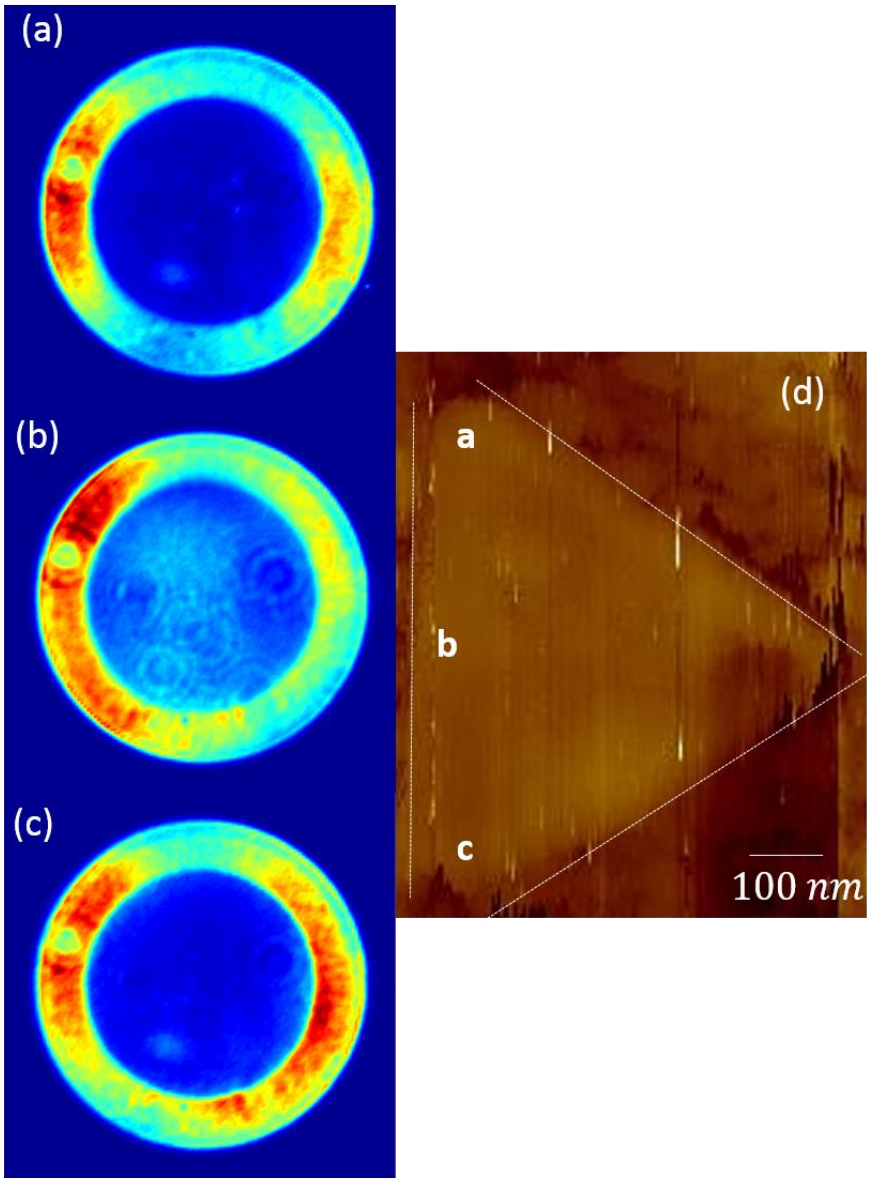

Figure 4. Fourier space images of the STM excitation of a triangular plate with the excitation located at a vertex and on an edge. Fourier space image when the excitation position is (a) at the vertex and (b) at its neighboring edge of the triangular plate, (c) at another vertex. (d) STM image of the triangular plate with side length of 650 nm *and height* 20 nm. *The experimental is performed on the "Veeco" setup. Bias is set at* 2.8 V *and setpoint current is in the range of* 1 nA *to* 4 nA. *Acquisition time is* 300 s.

c.3 More mapping results on triangular plates with bandpass filters

Here we will show another set of experimental results obtained with a more complete series of bandpass filters of 750/40 nm, 800/40 nm, 850/40 nm and 900/40 nm for photon mapping. The triangular plate has a side length of ≈ 750 nm and all the results are shown in Fig. 6.

Figures 6 (a-d), (e-h), (i-l) separately show the topography images, current images and photon yield images for the same triangular plate with different bandpass filters in front of the CCD detector. The topography and current images show the same phenomenon as discussed before. We see that as the collection wavelength is gradually increased (the photon energy decreases), the tendency is that more and more photons appear when the excitation is on the edge.

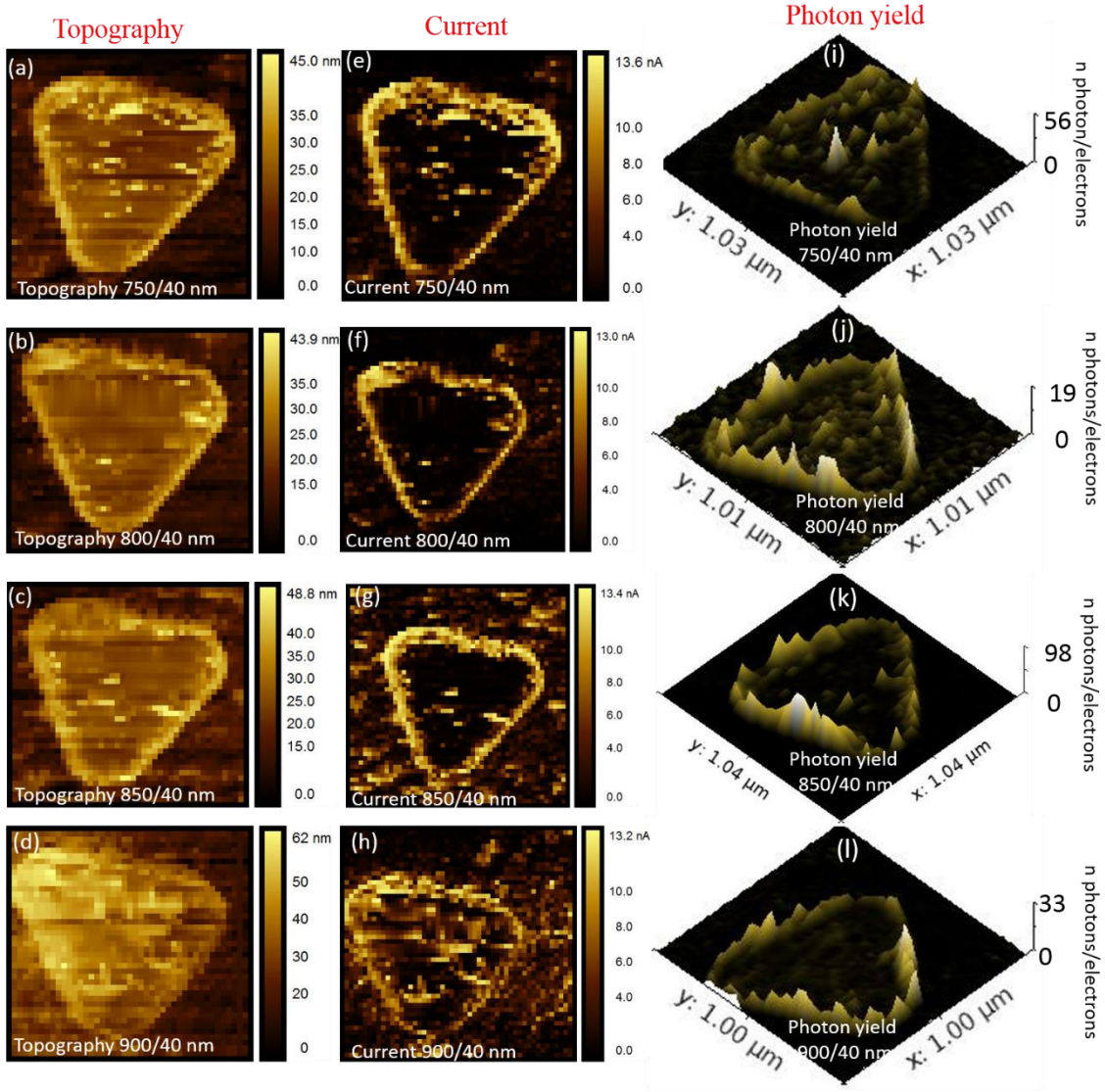

Figure 6. Photon maps obtained with different bandpass filters of $\frac{750}{40}$ nm (1.61 eV to 1.71 e), 800/40 nm (1.51 eV*to*1.59 eV), $\frac{850}{40}$ nm (1.42 eV to 1.49 eV), 900/40 nm (1.35 eV *to* 1.41 eV*). The triangular plate with a size of* ≈ 750 nm *and height around* 20 nm. *(a-d) Topography images. (e-h) Current images. (i-l) Photon yield images. The bias is set at* 2.8 V *and tunnel current is set at* 0.1 nA. *Acquisition time for every image is round* 90 *minutes.*

[1] P. Bharadwaj, A. Bouhelier, and L. Novotny, "Electrical excitation of surface plasmons," *Phys. Rev. Lett.*, vol. 106, no. 22, p. 226802, 2011.

[2] L. Novotny and B. Hecht, *Principles of Nano-Optics*. Cambridge University Press, 2006.

[3] P. B. Johnson and R. W. Christy, "Optical constants of the Noble Metals," *Phys. Rev. B*, vol. 6, no. 12, pp. 4370–4379, 1972.

Résumé

En conclusion, dans ma thèse, nous utilisons différentes nanostructures plasmoniques pour contrôler l'émission de lumière excitée électriquement. Notre émission électrique provient d'une "nanosource STM" qui utilise le courant tunnel inélastique entre la pointe d'un microscope à effet tunnel (STM) et un échantillon métallique, pour exciter localement les polaritons de plasmons de surface localisés et en propagation.

Nous concentrons notre étude sur une lentille plasmonique circulaire, une lentille plasmique elliptique, une pile multicouche planaire plasmonique et une plaque triangulaire individuelle. Par rapport à un simple film d'or mince, nous constatons qu'un film Au structuré affiche une capacité extraordinaire à contrôler et à façonner le rayonnement émis.

L'interaction d'une nanosource STM et d'une lentille plasmonique circulaire (une série de fentes concentriques gravées dans un film d'or épais) produit une microsource radialement polarisée de lumière de faible dispersion angulaire (≈ ± 4 °). Le fonctionnement de la lentille plasmonique circulaire peut être compris simplement comme suit: la nanosource STM excite une onde circulaire SPP sur le disque central de la lentille, qui se propage alors vers les fentes où les SPP sont diffusées dans la lumière. L'interférence de cette lumière diffusée aboutit à un faisceau presque collimaté. L'influence des paramètres structuraux sur la propagation angulaire de la microsource résultante est également étudiée. En outre, une faible dispersion angulaire (<± 7 °) pour une grande plage de longueurs d'onde (650-850 nm) est obtenue. Ainsi, cette microsource entraînée électriquement de lumière presque collimatée a une réponse spectrale large et est optimale sur une large plage d'énergie, en particulier en comparaison avec d'autres structures plasmoniques résonantes telles que Yagi-Uda nanoantennas. Dans le futur, l'excitation STM pourrait être remplacée par une jonction tunnel planaire intégrée, conduisant à un dispositif opto-électronique entièrement intégré.

L'interaction de notre nanosource STM et d'une lentille plasmonique elliptique (une seule fente elliptique gravée dans un film d'or épais) est également étudiée. Lorsque l'excitation STM est située à la position du point focal de la lentille plasmonique elliptique, un faisceau lumineux directionnel à faible propagation angulaire est acquis. De plus, dans l'expérience, nous trouvons qu'en changeant l'excentricité de la lentille plasmique elliptique, l'angle d'émission est varié. On constate que plus l'excentricité de la lentille elliptique est grande, plus l'angle d'émission est élevé. Cette étude permet de mieux comprendre comment les nanostructures plasmoniques

façonnent l'émission de lumière. Dans les travaux futurs, une lentille plasmique elliptique à fentes multiples pourrait être étudiée, ce qui pourrait conduire à une émission directionnelle avec une propagation angulaire encore plus faible, grâce à l'interférence de la diffusion de la lumière provenant des fentes voisines.

L'interaction de SPP excités par STM et d'une structure de pile multicouche planaire plasmonique est également étudiée. Il est démontré que l'excitation STM peut sonder la structure de bande optique d'une pile Au-SiO2-Au. Nous trouvons que l'épaisseur de la couche diélectrique (SiO2) joue un rôle important dans la modification du couplage entre les modes "SPP-like" et "guide d'ondes" identifiés. Une preuve possible d'un couplage fort est obtenue pour une épaisseur de couche diélectrique spécifique. Nous comparons également les résultats obtenus par excitation laser et STM de la même structure de pile. Les résultats indiquent que la technique STM est supérieure en termes de rapport signal sur bruit pour les modes TM. Ces résultats mettent en évidence le potentiel de la STM en tant que technique de nanoscopie optique sensible pour sonder les bandes optiques des nanostructures plasmoniques.

Enfin, l'interaction d'une nanosource STM et d'une plaque triangulaire individuelle (L≈600 nm) est également étudiée. Nous trouvons que lorsque l'excitation STM est centrée sur la plaque triangulaire, il n'y a pas d'émission de lumière directionnelle. Cependant, lorsque la nanosource STM est située sur le bord du triangle, l'émission de lumière directionnelle est obtenue. Cette étude nous fournit une nouvelle voie pour atteindre l'émission de lumière directionnelle. Nous étudions également la possibilité de sonder le LDOS optique du triangle avec la nanosource STM. Les résultats du spectre, de la cartographie photonique et de la simulation sont cohérents entre eux et confirment que la nanosource STM est sensible au LDOS optique.

Thus, our results show that the manipulation of light is achieved through SPP-matter interactions. Using plasmonic nanostructures, we control the collimation, polarization, and direction of the light originating from the STM-nanosource.

université PARIS-SACLAY | ÉCOLE DOCTORALE Ondes et Matière (EDOM)

Titre : Nanostructures plasmoniques pour le contrôle de l'émission de lumière excitée électriquement

Mots clés : microscope à effet tunnel, plasmons de surface, nanosource directionnelle, excitation électrique, lumière à polarisation radiale

Résumé : Cette thèse porte sur l'étude expérimentale de l'interaction entre le courant tunnel inélastique issu d'un microscope à effet tunnel (STM) et diverses nanostructures plasmoniques. Cette source STM est une source locale et à faible énergie générant à la fois des plasmons de surface localisés et propagatifs. Les techniques utilisées sont principalement la microscopie de fuites radiatives, l'imagerie des plans réels et de Fourier ainsi que la spectroscopie. Nous avons trouvé que, contrairement au cas du film continu d'or mince, un film d'or structuré offre la possibilité de contrôler et de mettre en forme la radiation émise.

La réalisation d'une microsource de lumière à polarisation radiale et de faible ouverture angulaire ($\approx \pm 4$ °) est rendue possible en positionnant la source STM au centre d'une lentille plasmonique circulaire consistant en une série d'anneaux concentriques gravés dans un film d'or épais. Nous avons aussi étudié comment les dimensions de cette lentille plasmonique influent sur l'ouverture angulaire du rayon de lumière émis. Nous avons aussi montré que, contrairement à ce qui serait attendu, cette lentille plasmonique produit un faisceau de faible ouverture angulaire pour une large gamme de longueurs d'onde.

Nous avons ensuite étudié l'interaction entre la source STM et une lentille plasmonique elliptique. Une émission de lumière directionnelle, ayant une faible ouverture angulaire, est obtenue lorsque l'excitation est positionnée au niveau de l'un des foyers de la structure elliptique. En variant l'excentricité de la lentille plasmonique elliptique, la direction tout comme l'ouverture angulaire de l'émission peut être contrôlées.

Puis, nous avons montré qu'une nanosource basée sur le STM permet de sonder la structure de bandes optique d'une multi-couche Plasmonique planaire (Au-SiO_2-Au). Nous avons trouvé que l'épaisseur de la couche diélectrique joue un rôle important en modifiant le couplage entre les modes plasmoniques et photoniques. Des résultats comparatifs entre l'excitation STM et l'excitation laser d'une même multi-couche montrent une plus grande sensibilité avec la technique STM.

Enfin, nous nous sommes intéressés à l'excitation STM de feuillets triangulaires d'or d'environ 600 nm de côté. En choisissant soigneusement la position de l'excitation au-dessus du nanotriangle, une nanosource directionnelle avec un indice de directivité jusqu'à 6.8 dB peut être obtenue. De plus, nous avons montré la possibilité d'utiliser la nanosource STM afin de cartographier la densité locale d »états électromagnétiques d'objets plasmoniques individuels.

Université Paris-Saclay
Espace Technologique / Immeuble Discovery
Route de l'Orme aux Merisiers RD 128 / 91190 Saint-Aubin, France

université PARIS-SACLAY | ÉCOLE DOCTORALE Ondes et Matière (EDOM)

Title : Using plasmonic nanostructures to control electrically excited light emission

Keywords : scanning tunneling microscope, surface plasmon polariton, electrical excitation, directional light source, radially polarized beam

Abstract: In this thesis, we experimentally investigating the interaction between the inelastic tunnel current from an STM and various plasmonic nanostructures. This "STM-nanosource" is a local, electrical, low-energy nanosource of both localized and propagating surface plasmons. The main techniques used in this thesis are leakage radiation microscopy, real and Fourier space imaging, and imaging spectroscopy. As compared to a simple thin gold film, we find that a structured Au film displays an extraordinary capacity to control and shape the emitted radiation.

The production of a radially polarized microsource of low angular ($\approx \pm 4°$) is obtained using the STM excitation in the center of a circular plasmonic lens (a series of concentric slits etched in a thick gold film). We also study how the structural parameters of the circular plasmonic lens influence the angular spread of the resulting beam of light. We demonstrate that, contrary to what might be expected, the circular plasmonic lens structure produces a beam of lo angular spread for a large wavelength range. The operation of the circular plasmonic lens may be understood simply as follows: the STM-nanosource excites an SPP circular wave on the central disc of the lens, which then propagates to the slits where the SPPs are scattered into light. The interference of this scattered light results in the nearly collimated beam.

We have investigated the interaction of the STM-excited nanosource and an elliptical plasmonic lens. We obtain directional light emission of low angular spread when the excitation is located at the focal point of the elliptical structure. We find that by changing the eccentricity of the elliptical plasmonic lens, both the direction and angular spread may be controlled.

We also demonstrate that the STM-based nanosource can probe the optical band structure of a planar plasmonic multi-layer Au-SiO_2-Au) stack. We find that the thickness of the dielectric layer (SiO_2) plays in important role in changing the coupling of SPP and photonic modes. Laser and STM excitation results on the same stack structure are compared, indicating that the STM technique is superior in terms of signal-to-noise for TM modes.

Lastly, we have investigated the STM excitation of an individual Au triangular plate ($\approx 600\, nm$ in size). By correctly choosing the excitation position on the triangular plate, we obtain a directional nanosource and the maximum directivity is measured around 6.8 dB. In addition, we investigate the possibility of mapping the electromagnetic local density of states (EM-LDOS) of an individual plasmonic object using the STM-nanosource.

Université Paris-Saclay
Espace Technologique / Immeuble Discovery
Route de l'Orme aux Merisiers RD 128 / 91190 Saint-Aubin, France